Structural Behaviour of CLT Floor Systems in Hybrid Timber Buildings:

Shrinkage-Induced Restraint Forces and the Influence of Diaphragm Stiffness on Stability Response

CIEM0500: Master Thesis

Femke Bon

Delft University of Technology

TU Delft

Structural Behaviour of CLT Floor Systems in Hybrid Timber Buildings:

Shrinkage-Induced Restraint Forces and the Influence of Diaphragm Stiffness on Stability Response

by

Femke Bon

Student number: 4888642

Supervisor:	Dr. ir. G.J.P. Ravenshorst
Supervisor	Prof. dr. ir. J.W.G. van de Kuilen
Supervisor:	Dr. ir. H.R. Schipper
Faculty:	Civil Engineering and Geosciences, Delft
Company involved:	Sweco Architecten- en Ingenieursadviesbureau
Company supervisor:	Ir. N. Castelein
Project Duration:	September, 2025 - March, 2026

Cover:	*Inside Vancouver's Brock Commons, The World's Tallest Mass Timber Building*, 2017 [1].
Style:	TU Delft Report Style, with modifications by Daan Zwaneveld

TU Delft

Summary

The construction sector is under increasing pressure to reduce CO_2 emissions and transition towards a more circular built environment. Within this context, timber is gaining importance as a renewable structural material and is increasingly applied in mid- and high-rise buildings.

The increasing use of timber in mid- and high-rise buildings has created a need for better understanding of the structural behaviour of hybrid systems in which timber floors and frames are combined with a reinforced concrete core. In these buildings, cross-laminated timber (CLT) floor panels do not only carry vertical loads, but also act as diaphragms that transfer horizontal loads from the timber frame to the concrete core. At the same time, CLT is moisture-sensitive and undergoes shrinkage after installation, which may lead to restrained deformations and additional forces in connections. Because the global response of the building depends on diaphragm stiffness, which is governed by the connection stiffness and detailing, and because these connections also govern the restraint against shrinkage, connection detailing has consequences at both local and global level. This thesis therefore investigates how connection stiffness and detailing choices in hybrid concrete core–timber frame buildings influence both shrinkage-induced force development in CLT floor systems and the stability behaviour of the structure.

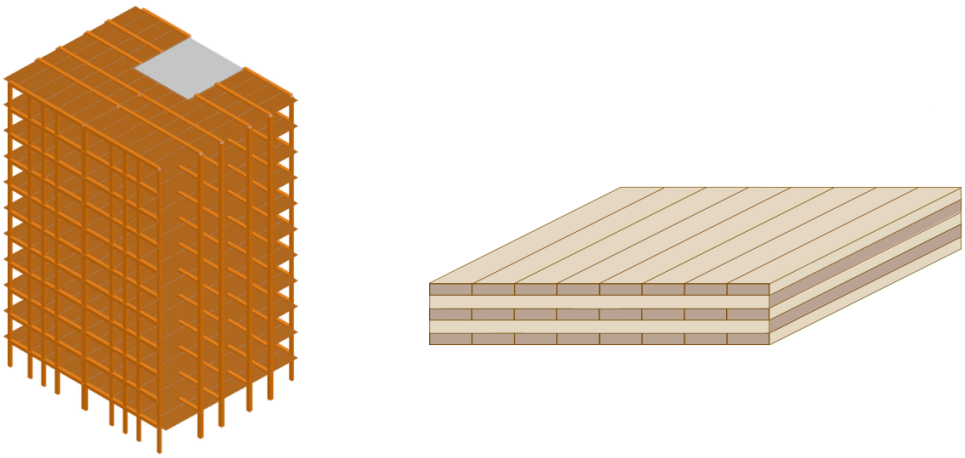

Figure 1: Hybrid concrete–core timber frame structure (left) and cross-laminated timber floor panel (right).

The study is structured into three parts and combines analytical and numerical methods. The first part establishes the material-level basis for the subsequent analyses by examining moisture-driven shrinkage and stress relaxation in CLT. Shrinkage development is evaluated as a function of the shrinkage coefficient and installation moisture content, while a linear generalised Maxwell model is used to describe stress relaxation, and the Boltzmann superposition principle is used to evaluate the resulting stress development over time under time-dependent restrained shrinkage. The results show that the predicted restrained stresses are highly sensitive to the assumed shrinkage coefficient and the installation moisture content, and that viscoelasticity substantially reduces long-term restrained stress compared to a purely elastic prediction.

Figure 2 illustrates this behaviour: while stresses increase rapidly after installation due to restrained shrinkage, a significant portion of the stress relaxes over time due to the viscoelastic behaviour of timber. The retained long-term stress level is governed mainly by the long-term modulus (E_{fin}) of the linear generalised Maxwell model. Based on these findings, a reduced long-term stiffness is adopted in the following parts of the thesis as a practical representation of long-term CLT behaviour.

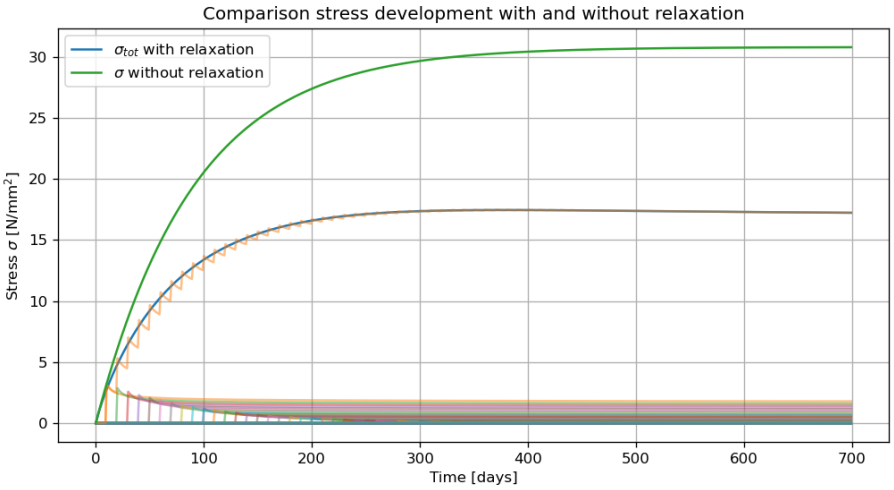

Figure 2: Comparison of stress development in CLT under restrained shrinkage with and without viscoelastic relaxation.

The second part examines how shrinkage deformations are translated into restraint forces in representative CLT connection situations. For this purpose, analytical 1D beam–spring models are developed for several idealised restraint configurations that represent interfaces in hybrid core–frame buildings, followed by parametric studies varying panel length and installation moisture content.

When shrinkage acts across the panel span, that is, perpendicular to the core, restraint forces develop in the screw connections because the floor panel is restrained by the adjacent structure. These forces increase with panel length and with a higher installation moisture content. As a result, higher installation moisture contents require shorter panel lengths to keep the connection forces below the design shear resistance of the screws. In this direction, slotted holes can be introduced as an effective mitigation measure, since they allow slip without significantly reducing diaphragm action.

When shrinkage acts parallel to the core, restraint forces again develop in the screw connections, but their distribution differs from the perpendicular case because the panel remains continuously restrained along the core edge. As illustrated in Figure 3, the resulting screw forces are non-uniform along the interface: they are highest near the ends of the restrained edge and decrease towards the centre of the panel. In this direction, the length of the continuously restrained interface becomes the governing parameter. Reducing this restrained length is therefore the most effective measure to limit high connection forces.

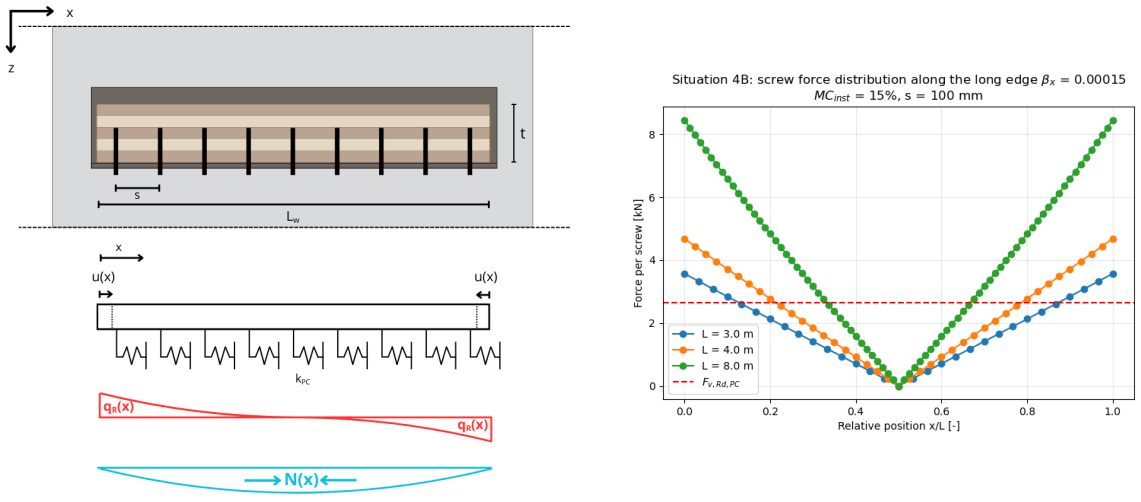

Figure 3: Analytical beam–spring model for restrained CLT edges and resulting screw force distribution along the restrained interface.

The third part investigates the structural implications of diaphragm connection stiffness in a numerical RFEM model of a hybrid concrete core–timber frame case-study building. A set of floor variants is analysed, differing in panel–core stiffness and panel–panel stiffness. The global response is evaluated in both first- and second-order analysis with respect to stability, serviceability, connection demand, and column buckling.

The results show that diaphragm stiffness has a direct influence on the global stability behaviour and on the sensitivity of the structure to second-order effects. When the diaphragm stiffness is insufficient, the frame–core system does not behave as a fully braced structure and global sway instability modes can occur. In these cases, the structure exhibits lower critical load factors and increased drift amplification. Figure 4 schematically illustrates the difference between global sway buckling and member-level column buckling, highlighting the role of diaphragm stiffness in restraining lateral frame deformation.

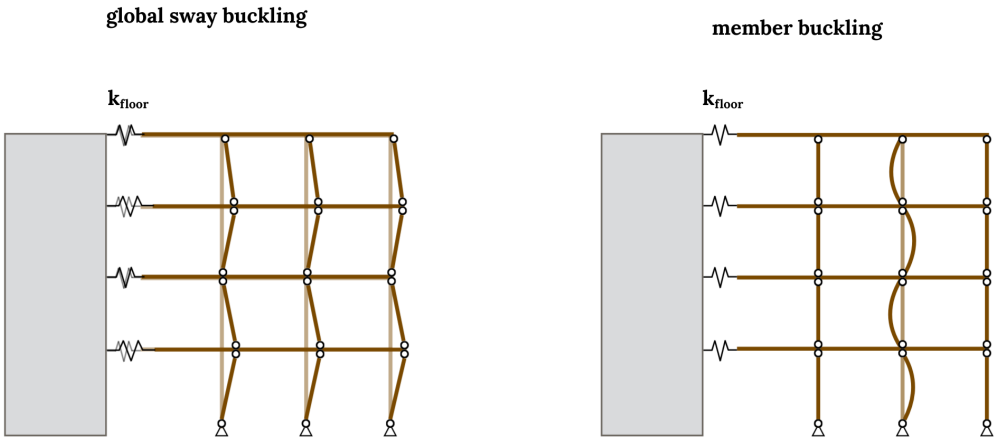

Figure 4: Influence of diaphragm stiffness on global sway buckling and member-level column buckling behaviour.

In general, increasing diaphragm stiffness leads to reduced drift, higher stability margins, and lower fastener demands. The analyses further show that grouting the panel–core interface improves the in-plane diaphragm stiffness by restraining panel rotation about the screws and allowing forces to be partly transferred through compression at the interface. As a result, the global response of the structure becomes less sensitive to sway behaviour.

Taken together, the study shows that connection detailing affects hybrid core–frame buildings at two related levels. At connection level, it influences the degree of restraint against shrinkage and therefore the magnitude and distribution of shrinkage-induced forces. At structural-system level, it influences the effective diaphragm stiffness and therefore the global stability response, deformation demand, and sensitivity to second-order effects. The results indicate a clear design trade-off between these aspects. Measures that reduce shrinkage-induced force build-up, such as shorter panels or lower connection stiffness, may also reduce diaphragm stiffness. Conversely, measures that improve diaphragm action and global stability, such as larger panels and stiffer connections, increase the shrinkage-induced connection forces.

The thesis therefore highlights the need to consider both shrinkage restraint and diaphragm stiffness at an early stage of the design process. In hybrid timber buildings, connection detailing should provide sufficient in-plane stiffness for global stability while also limiting the build-up of shrinkage-induced forces in restrained connections.

Preface

This thesis presents the results of a research on the structural behaviour of hybrid timber–concrete buildings. The work was carried out as part of the Master's programme in Structural Engineering at the Faculty of Civil Engineering and Geosciences of Delft University of Technology.

The research was conducted in collaboration with Sweco Architecture and Engineering Consultancy. Carrying out this thesis in a professional engineering environment was a valuable experience, as it allowed me to connect academic research with engineering practice.

I would like to express my sincere gratitude to my supervisors at TU Delft: Geert Ravenshorst, Jan-Willem van de Kuilen, and Roel Schipper. I am very grateful for all the meetings we had throughout this project, for their guidance, critical feedback, and for the insights they shared during the process. Their different perspectives and expertise greatly helped me to shape this research and deepen my understanding of the topic. Over the course of this thesis, I have learned a great deal in a relatively short time, and this was largely thanks to their support and supervision.

I would also like to thank my company supervisor, Niels Castelein, for the time and attention he dedicated to my graduation project. His practical perspective and willingness to make time for discussions were of great value throughout the process. In addition, I would like to thank all colleagues at Sweco for the pleasant working atmosphere and for making my graduation period an enjoyable and inspiring experience.

Finally, I would like to thank everyone else who contributed to this project in any way. Their support and involvement are greatly appreciated.

Femke Bon
Delft, March 2026

Contents

Summary i

Preface iv

Nomenclature xv

1 Introduction 1
- 1.1 Societal relevance and context . . . 1
- 1.2 Research problem and gap . . . 2
- 1.3 Research aim and objectives . . . 3
- 1.4 Research questions . . . 3
- 1.5 Scope . . . 4
- 1.6 Methodology . . . 5
- 1.7 Reading guide . . . 5

2 Case study 7
- 2.1 General description . . . 7
- 2.2 Geometry and floor plan . . . 8
- 2.3 Materials and members . . . 9
- 2.4 Use of the case-study model . . . 9

I Shrinkage and relaxation in CLT 10

3 Shrinkage and relaxation in CLT 11
- 3.1 Cross-laminated timber . . . 11
  - 3.1.1 Fabrication CLT . . . 11
  - 3.1.2 CLT at the construction site . . . 12
- 3.2 Wood anatomy . . . 13
- 3.3 Moisture in CLT . . . 14
  - 3.3.1 Moisture content . . . 14
  - 3.3.2 Moisture content development over time . . . 15
- 3.4 Shrinkage in CLT . . . 16
  - 3.4.1 Layer-based shrinkage model . . . 17
  - 3.4.2 Shrinkage development over time . . . 18
- 3.5 Restrained shrinkage and relaxation in CLT . . . 19
  - 3.5.1 Visco-elasticity . . . 20
  - 3.5.2 Stress relaxation . . . 21
  - 3.5.3 Linear relaxation models . . . 22
  - 3.5.4 Boltzman superposition principle . . . 24

4 Results 27
- 4.1 Moisture content in CLT . . . 27
  - 4.1.1 Influence of installation moisture content . . . 27
- 4.2 Shrinkage in CLT . . . 29
  - 4.2.1 Layer-based shrinkage model . . . 29
  - 4.2.2 Influence shrinkage coefficient . . . 30
- 4.3 Stress relaxation in CLT . . . 31
  - 4.3.1 Effect of relaxation on restrained stress development . . . 31
  - 4.3.2 Sensitivity to relaxation times . . . 32
  - 4.3.3 Shrinkage rate versus relaxation rate . . . 33
  - 4.3.4 Influence of ageing . . . 33

4.4 Key observations . . . 34

II Shrinkage-induced forces in CLT connections 35

5 Shrinkage-induced forces in CLT connections 36
5.1 Connection types . . . 36
5.2 Stiffness of connections . . . 38
5.2.1 Combined stiffness components . . . 39
5.2.2 Slip behaviour . . . 39
5.2.3 Lateral slip modulus of a screw . . . 40
5.3 Resistance of connections . . . 40
5.3.1 Failure mechanisms of steel-to-timber joints . . . 40
5.3.2 Failure mechanisms of timber-to-timber joints . . . 41
5.4 Shrinkage induced restraint forces . . . 43
5.4.1 Long-term stiffness . . . 43
5.4.2 Situation 1: Fully restrained floor . . . 44
5.4.3 Situation 2: Floor panel between two cores . . . 44
5.4.4 Situation 3: Two floor panels between two cores . . . 46
5.4.5 Situation 4: Floor panel with continuous restraint along the core . . . 47

6 Results 51
6.1 Model parameters . . . 51
6.2 Situation 2: Floor panel between two cores . . . 51
6.3 Situation 3: Two floor panels between two cores . . . 52
6.4 Situation 4: Floor panel with continuous restraint along the core . . . 53
6.4.1 Situation 4A: Shrinkage along the short edge . . . 54
6.4.2 Situation 4B: Shrinkage along the long edge . . . 54
6.5 Slip allowance . . . 56
6.6 Key observations . . . 57

III CLT floor system in structural stability 59

7 CLT floor system in structural stability 60
7.1 Core–frame lateral load path . . . 60
7.2 Diaphragm stiffness and deformation components . . . 61
7.2.1 Deformation components . . . 62
7.3 Diaphragm restraint and stability behaviour . . . 64
7.3.1 Column–spring model . . . 64
7.3.2 Eigenvalue stability analysis in RFEM . . . 66
7.4 Second-order effects . . . 66
7.4.1 Classification . . . 66
7.4.2 First- and second-order analysis . . . 66

8 Results 69
8.1 Verification . . . 69
8.2 Model variants . . . 71
8.2.1 Connection stiffness input . . . 71
8.2.2 Variant matrix . . . 73
8.3 Results: global stability . . . 73
8.4 Results: total drift and inter-storey drift . . . 75
8.5 Results: connection resistance . . . 78
8.6 Results: column stability . . . 79
8.6.1 Column stability results . . . 80
8.7 Verification overview . . . 81
8.8 Key observations . . . 82

9 Discussion **83**
9.1 Part I: Shrinkage and relaxation in CLT . . . 83
9.1.1 Real shrinkage behaviour and the role of the β-coefficient . . . 83
9.1.2 Moisture content at installation and practical controllability . . . 84
9.1.3 Ageing effects and uncertainty in long-term relaxation . . . 84
9.1.4 Viscoelastic model choice . . . 85
9.2 Part II: Shrinkage-induced forces in CLT connections . . . 85
9.2.1 1D idealisation and 2D floor behaviour . . . 85
9.2.2 Interpretation of shrinkage-induced screw slip . . . 86
9.3 Part III: CLT floor system in structural stability . . . 86
9.3.1 Interstorey drift and imperfection modelling . . . 87
9.3.2 Stiffness of the panel–core connection in the RFEM model . . . 88
9.3.3 Explicit shrinkage effects in the RFEM model . . . 88
9.4 Design trade-off: restraint forces and diaphragm stiffness . . . 89

10 Conclusion **90**
10.1 Research questions . . . 90
10.2 Recommendations . . . 92
10.2.1 Practical design recommendations . . . 92

References **94**

A Case study details **96**
A.1 Materials and members . . . 96
A.1.1 Materials . . . 96
A.1.2 Structural members . . . 96
A.2 Connections . . . 97
A.3 Imperfections . . . 97
A.4 Loads . . . 97

B Failure modes **99**
B.1 Connection geometry and screw characteristics . . . 99
B.1.1 Connection layouts . . . 99
B.2 Lateral resistance of dowel-type fasteners . . . 99
B.2.1 Steel-to-timber joints . . . 101
B.2.2 Timber-to-timber joints . . . 101

C Analytical derivation of restraint forces in 1D beam models **102**
C.1 Situation 2: Beam restrained by panel–core connections . . . 102
C.2 Situation 3: Beam restrained by panel–core and panel–beam connections . . . 103
C.3 Situation 4: Continuously restrained beam . . . 105

D Restrained forces verification **108**
D.1 Situation 1: Fully restrained beam. . . . 108
D.2 Situation 2: Beam restrained by panel–core connection. . . . 109
D.3 Situation 3: Beam restrained by panel–core and panel-beam connection. . . . 110
D.4 Situation 4: Continuously restrained beam. . . . 111

E Effective width distributed spring model **114**
E.1 Situation 4a: short edge . . . 114
E.2 Situation 4b: long edge . . . 115

F Critical load spring supported column **117**
F.1 Analytical derivation . . . 117
F.2 Numerical verification column-spring model . . . 118

G Diaphragm deformation mechanisms: rocking, segmentation and grout **119**
G.1 Deformation components . . . 119
G.2 Effect of panel–panel rotational coupling . . . 120
G.3 Effect of grout at the floor–core interface . . . 121

H ULS connection checks **122**

I RFEM case study model verification **125**
I.1 Model verification strategy . . . 125
I.2 Global equilibrium checks . . . 125
I.2.1 Global vertical equilibrium . . . 125
I.2.2 Horizontal equilibrium under wind loading . . . 126
I.3 Load path and reaction distribution . . . 128
I.3.1 Wind load transfer to the stability system . . . 128
I.3.2 Verification of pinned column behaviour . . . 129
I.4 Deformed shape inspection . . . 130
I.4.1 Global displacements . . . 130
I.4.2 Floor out-of-plane deflection . . . 132
I.4.3 Member–surface compatibility . . . 133
I.5 Diaphragm action . . . 133
I.5.1 Diaphragm shear transfer under wind . . . 134
I.6 Second-order analysis . . . 136
I.6.1 Second-order displacements . . . 136
I.6.2 Second-order forces . . . 137

List of Figures

1 Hybrid concrete–core timber frame structure (left) and cross-laminated timber floor panel (right). . . . i
2 Comparison of stress development in CLT under restrained shrinkage with and without viscoelastic relaxation. . . . ii
3 Analytical beam–spring model for restrained CLT edges and resulting screw force distribution along the restrained interface. . . . ii
4 Influence of diaphragm stiffness on global sway buckling and member-level column buckling behaviour. . . . iii

1.1 Engineered timber products, glulam beams (left) and CLT panels (right). . . . 1
1.2 Concrete core with timber frame structure. . . . 2
1.3 Distribution of mass timber buildings worldwide (2022), by number of storeys and structural material combination [8]. . . . 2
1.4 Methodology flowchart 6

2.1 Overview of the case study building. . . . 8
2.2 Floor plan (left) and cross section (right) of the case study building in RFEM. . . . 8
2.3 CLT lay-up used for the floor panels in the case study. . . . 9

3.1 3-layered cross laminated timber with finger joint. . . . 12
3.2 Examples of CLT exposure to outdoor conditions during construction. . . . 12
3.3 Hierarchical structure of wood [11] 13
3.4 Section planes in wood [12] 13
3.5 Free and bound water in wood. . . . 14
3.6 Schematic illustration of CLT moisture exposure during construction and subsequent indoor drying after enclosure. . . . 15
3.7 Relative humidity and temperature measurements and corresponding moisture content by Xiong, Su and Sabri (2009) [15]. . . . 15
3.8 Estimate of moisture content regression, based on data (Xiong, Su and Sabri (2009)) by Willebrands (2017) [14]. . . . 16
3.9 Principal directions CLT panel. . . . 16
3.10 Schematic representation of shrinkage behaviour in CLT, showing the non-uniform deformation of individual layers. . . . 17
3.11 Shrinkage strain development over time. . . . 18
3.12 Free versus restrained shrinkage of a CLT panel. . . . 19
3.13 Schematised linear elastic material and viscous material. . . . 20
3.14 Stress relaxation in timber under constant imposed strain. . . . 21
3.15 Visualisation of the Maxwell and a generalised Maxwell model. . . . 23
3.16 Discretisation of the shrinkage strain over time. . . . 24
3.17 Discretisation of stress development over time using BSP. . . . 25
3.18 Relaxation curves for strain increments introduced at different moments in time, illustrating the effect of material ageing. . . . 26

4.1 Moisture content development over time for different installation moisture contents. . . . 28
4.2 Stress development in a fully restrained element for different installation moisture contents. 28
4.3 Global panel coordinate system (x, y, z) and anatomical directions of a lamella (longitudinal, tangential and radial). . . . 29
4.4 Shrinkage stress development for different shrinkage coefficients obtained using the lay-up method. . . . 30

4.5 Comparison of restrained shrinkage stress development for Eurocode 5 coefficients and the average coefficients from the layer-based lay-up method. 31
4.6 Restrained stress development with and without relaxation. 32
4.7 Influence of the assumed relaxation times in the generalised Maxwell model. 32
4.8 Restrained stress development for gradual (base) versus accelerated shrinkage. 33
4.9 Influence of an age coefficient on restrained stress development. 34

5.1 Floor plan with demarcation of the connection types considered in the case study. . . . 37
5.2 Side and top view of connection details used in the case study. 38
5.3 Schematic load–deformation curve illustrating the definition of the ductility factor D_s and stiffness K_{ser} [24]. 39
5.4 Failure mechanisms for a steel-to-timber joint loaded in shear. 41
5.5 Failure mechanisms for a timber-to-timber joint loaded in single shear. 41
5.6 Principle of shrinkage restraint. 43
5.7 2D schematic representation of the floor panel between two cores. 44
5.8 1D beam–spring model of a CLT floor panel between two cores. 45
5.9 Effective width for 1D beam–spring model of a CLT floor between two cores. 45
5.10 2D schematic representation of two floor panels between two cores. 46
5.11 1D beam–spring model of two interacting CLT floor panels between two cores. 47
5.12 2D schematic representation of a floor panel with continuous restraint along the core edge: (a) restraint along the short side, (b) restraint along the long side. 48
5.13 1D beam-on-elastic-foundation model of a floor panel with continuous core restraint. . . 49
5.14 Effective width for a CLT floor panel with continuous restraint along the core. 50

6.1 Utilisation ratio for a floor panel between two cores (Situation 2) under shrinkage perpendicular to the core. 52
6.2 Utilisation ratio for a floor panel between a steel angle and a glulam beam (Situation 3) under shrinkage perpendicular to the core. 53
6.3 Screw force distribution for shrinkage along the short edge for different panel widths. . 54
6.4 Screw force distribution for shrinkage along the long edge for different panel lengths. . 55
6.5 Schematic representation of slip allowance introduced by slotted holes. 56
6.6 Required slip allowance at both supports to maintain $UC \leq 1$ for Situation 2. 56
6.7 Required slip allowance at the steel support to maintain $UC \leq 1$ for Situation 3. 57

7.1 Cantilevering concrete core in a core–frame system under lateral actions. 60
7.2 Schematic diaphragm action under wind. 61
7.3 Cantilevering segment used for analytical displacement estimates. 62
7.4 Deformation components of the cantilevering segment for a monolithic floor: sliding, rocking, bending and shear. 63
7.5 Column restrained by the floor diaphragm: (left) equivalent storey spring k_{floor}, (middle) member (Euler) buckling for $k_{floor} \to \infty$, (right) sway buckling for finite k_{floor}. 65
7.6 Critical load versus storey restraint stiffness for the column–spring model. 65
7.7 Second-order (P–Δ) effect for a pin-ended column restrained by an equivalent diaphragm stiffness k_{floor}. 67
7.8 Iterative solution of the P–Δ equilibrium equation for a column restrained by a diaphragm spring. 68

8.1 Verification procedure showing which analysis type, imperfections, and checks follow from the critical load factor and governing instability mode. 70
8.2 Connection layout for panel–core (PCa), panel–core + grout (PCb) and panel–panel (PP) connection types. 72
8.3 Variant C0: first buckling mode shape, $\lambda_{cr,ns} = 5.959$. 74
8.4 variant C1a1: first buckling mode shape, $\lambda_{cr,sw} = 1.607$. 74
8.5 First-order lateral displacements in global Y for case C2a3 under the governing SLS combination. 77
8.6 Second-order lateral displacements in global Y for case C2a3 under the governing SLS combination. 77

8.7 Example of the normal-force resultants in local x for C1a1. Left: panel–core normal force n_{PC} and the location of $n_{PC,max}$. Right: panel–panel normal force n_{PP} and the location of $n_{PP,max}$. 78
8.8 Example panel–core resultant in local y, $v_{y,PC}$. Left: non-grouted case (C1a1). Right: grouted case (C1b1). 78
8.9 Selected representative column used for the ULS stability verification. 80

9.1 Schematic illustration of non-uniform moisture distribution, resulting internal stresses perpendicular to the grain, and potential crack formation (Franke et al., 2016) [33]. . . . 84
9.2 RFEM results illustrating the concept of an effective restraint width b_{eff} for shrinkage parallel to the core (Situation 4). 86
9.3 Configuration of imperfections ϕ for horizontal forces on floor diaphragms according to EC3 [31]. 87
9.4 Schematic illustration of first-storey column inclination caused by free shrinkage of the floor panel. 88

A.1 CLT lay-up 97

B.1 Connection geometries and definition of embedment and withdrawal lengths used in the resistance checks. 99

D.1 RFEM check for fully restrained beam. 109
D.2 RFEM check for beam on steel-to-timber connections. 110
D.3 RFEM check for beam on steel-to-timber and timber-to-timber connection. 111
D.4 RFEM check for beam on distributed springs. 112
D.5 RFEM check for beam on distributed springs, discretized. 113

E.1 Effective width for shrinkage along the short edge (situation 4a). 115
E.2 Effective width for shrinkage along the long edge (situation 4b). 116

F.1 Spring-supported column idealisation. 117
F.2 RFEM linear eigenvalue buckling analysis of the spring-supported column. 118

G.1 In-plane displacement u (mm) for (left) a monolithic floor and (right) a segmented floor with rigid panel–panel coupling. 120
G.2 Segmented floors with (left) K_{PP} and (right) K_{PP} = 12000 kN/m^2. Contours show in-plane displacement u (mm). 121
G.3 Effect of grout at the floor–core interface: (left) monolithic floor with grout and (right) segmented floor with grout. Contours show in-plane displacement u (mm). 121

I.1 RFEM: sum of loads and sum of support forces in Z. 126
I.2 RFEM: wind in global Y (LC5) and corresponding support reactions in Y. 127
I.3 RFEM: core support reactions in X and Y under $LC5$, showing a torsional moment about the global Z-axis. 128
I.4 Wind resultant on the first floor level and corresponding torsional moment about the global Z-axis. 129
I.5 RFEM: example moment distribution for $LC1+LC2+LC5$ (visual check of pinned column behaviour). 130
I.6 RFEM: global deformed shape and displacement magnitude under wind in global Y ($LC5$). 131
I.7 RFEM: plan view of the displacement magnitude under $LC5$, illustrating non-uniform deformation across the floor and thus torsion. 131
I.8 RFEM: floor out-of-plane deflection under gravity loading ($LC1 + LC2 + LC3$). 132
I.9 RFEM: example check of member–surface compatibility showing matching vertical displacements on a beam and the connected floor surface. 133
I.10 RFEM: in-plane normal forces N in the panel–core line hinges on the bottom floor under $LC5$. 134

I.11 RFEM: close-up of in-plane normal forces N near the core interface, highlighting local peaks near corners/discontinuities. 135
I.12 RFEM: in-plane shear forces v_y along the panel–core line hinges on the bottom floor under $LC5$. The non-uniform distribution and sign changes indicate torsional diaphragm action. 135
I.13 RFEM: u_y displacements for SLS CO15 (1st-order analysis) for the flexible configuration (PC1a+PP1, PB1). 136
I.14 RFEM: u_y displacements for SLS CO8 (2nd-order analysis) for the flexible configuration (PC1a+PP1, PB1). 137
I.15 RFEM: panel–core line-hinge normal forces N for ULS CO14 (1st order). 138
I.16 RFEM: panel–core line-hinge normal forces N for ULS CO4 (2nd order). 138
I.17 RFEM: panel–panel line-hinge normal forces N for ULS CO14 (1st order). 139
I.18 RFEM: panel–panel line-hinge normal forces N for ULS CO4 (2nd order). 139
I.19 RFEM: panel–core line-hinge shear forces V_y for ULS CO14 (1st order). 140
I.20 RFEM: panel–core line-hinge shear forces V_y for ULS CO4 (2nd order). 140

List of Tables

2.1 General building parameters for Block D. . . . 7
2.2 Material overview for the case-study model. . . . 9
2.3 Structural members and cross-sections used in the case-study model. . . . 9

3.1 Values of the deformation factor k_{def} for selected timber products (FprEN 1995-1-1:2025). 22

4.1 Maximum absolute stress for different initial moisture contents. . . . 28
4.2 Lamella-level shrinkage coefficients adopted from [16]. Tangential and radial coefficients are evaluated at $|\Delta MC| = 7\%$. . . . 29
4.3 Shrinkage coefficients with the lay-up method for different wood species and qualities. . 30
4.4 Effective in-plane shrinkage coefficients used in the comparison of Eurocode 5 and the layer-based lay-up method. . . . 30
4.5 Maximum absolute stress for shrinkage coefficients obtained from Eurocode 5 and from the average values of the layer-based lay-up method. . . . 31

6.1 Fixed parameters used in the parametric study. . . . 51

8.1 Overview of the verification checks adopted for the RFEM variants. . . . 71
8.2 Connection stiffness input used in the RFEM model. . . . 72
8.3 Analysed RFEM cases and connection combinations. . . . 73
8.4 Critical load factors and governing first buckling mode for all investigated variants. . . . 75
8.5 SLS checks per RFEM case for 1st- and 2nd-order analysis. . . . 76
8.6 Connection force demand in ULS per RFEM case for 1st- and 2nd-order analysis. . . . 79
8.7 Governing design forces and utilisation ratio for the selected column. . . . 81
8.8 Summary of compliance per variant for the governing verification categories. . . . 82

A.1 Material properties used in the numerical model . . . 96
A.2 Structural members and cross-sections . . . 96
A.3 Summary of applied loads and wind parameters . . . 98

B.1 Geometric input values for the resistance checks. . . . 99

H.1 Derived fastener-level ULS checks for the **panel–core (PC)** connection (a- and b-series), based on the peak normal-force line resultant $n_{\text{PC,max}}$. . . . 123
H.2 Derived fastener-level ULS checks for the **panel–panel (PP)** connection, based on the peak normal-force line resultant $n_{\text{PP,max}}$. . . . 123
H.3 Derived fastener-level ULS checks for the **panel–core (PC)** shear connection (a-series), based on the peak shear-force line resultant $v_{y,\text{PC,max}}$. . . . 124
H.4 Derived timber bearing stress for grouted panel–core variants (b-series), based on the peak panel–core shear resultant $v_{y,\text{PC,max}}$ from RFEM. . . . 124

I.1 Verification check: global vertical equilibrium. . . . 125
I.2 Verification check: horizontal equilibrium under wind loading. . . . 126
I.3 Verification check: wind load transfer to the core. . . . 128
I.4 Verification check: pinned column behaviour. . . . 129
I.5 Verification check: deformed shape under wind (direction and torsion). . . . 130
I.6 Verification check: floor out-of-plane deflection under gravity. . . . 132
I.7 Verification check: member–surface compatibility (beam–floor coupling). . . . 133
I.8 Verification check: diaphragm shear transfer to the core (line-hinge forces). . . . 134
I.9 Verification check: second-order displacement amplification. . . . 136

I.10 Verification check: second-order amplification of diaphragm interface forces. 137

Nomenclature

Abbreviation	Definition
BSP	Boltzmann superposition principle.
CC2b	Consequence class 2b.
CLT	Cross-laminated timber.
CO	Load combination.
DIC	Digital image correlation.
EC	Eurocode.
EMC	Equilibrium moisture content.
ETA	European Technical Assessment.
FEM	Finite element method.
FSP	Fibre saturation point.
LC	Load case.
LVL	Laminated veneer lumber.
MC	Moisture content.
OSB	Oriented strand board.
PB	Panel–beam.
PC	Panel–core.
PP	Panel–panel.
P–Δ	Second-order effects.
RFEM	Finite element software used for the numerical model.
SLS	Serviceability limit state.
ULS	Ultimate limit state.
UC	Utilisation ratio (unity check).

Symbols

Symbol	Definition	Unit
Geometry and coordinates		
A	Cross-sectional area.	mm^2
A_s	Effective shear area.	mm^2
b_{eff}	Effective restraint width.	mm
$b_{\text{eff,1–3}}$	Effective width for Situations 1–3.	mm
$b_{\text{eff,4A}}$	Effective width for Situation 4A.	mm
$b_{\text{eff,4B}}$	Effective width for Situation 4B.	mm
e_0	Initial bow imperfection.	mm
H	Total building height.	mm
h_i	Storey height.	mm
I	Second moment of area.	mm^4
L	Member length.	mm
L_{con}	Length of restrained connection.	mm
L_{core}	Length of floor–core interface.	mm
L_d	Panel depth perpendicular to restrained edge.	mm
L_{eff}	Effective buckling length.	mm
L_p	Panel length / restrained panel span.	mm
L_w	Length of continuously restrained edge.	mm

Symbol	Definition	Unit
s	Fastener spacing.	mm
t	Thickness.	mm
T_i	Thickness of lamina i.	mm
T_{CLT}	Total CLT thickness.	mm
$T_{d,i}$	Effective deforming thickness of lamina i.	mm
W_{lamina}	Width of a lamina.	mm
W_z	Section modulus about local z-axis.	mm^3
x	Coordinate in global or local x-direction.	mm
x_i	Position of screw i along the connection.	mm
y	Coordinate in global or local y-direction.	mm
z	Coordinate in thickness / local z-direction.	mm
Moisture, shrinkage and material properties		
β	Shrinkage coefficient.	–
β_i	Shrinkage coefficient of lamina i.	–
$\beta_{i,\text{rad}}$	Radial shrinkage coefficient of lamina i.	–
β_{lon}	Longitudinal shrinkage coefficient.	–
β_{tan}	Tangential shrinkage coefficient.	–
β_x	Shrinkage coefficient in major panel direction.	–
β_y	Shrinkage coefficient in minor panel direction.	–
β_z	Shrinkage coefficient in thickness direction.	–
ΔMC	Moisture content change.	%
$\Delta\varepsilon_{\text{sh}}$	Shrinkage strain increment.	–
E	Young's modulus.	N/mm^2
E_{mean}	Mean elastic modulus.	N/mm^2
E_{fin}	Effective long-term modulus.	N/mm^2
$f_{c,0,d}$	Design compressive strength parallel to grain.	N/mm^2
$f_{c,0,k}$	Characteristic compressive strength parallel to grain.	N/mm^2
$f_{m,z,d}$	Design bending strength about local z-axis.	N/mm^2
$G_{xy,\text{mean}}$	Mean in-plane shear modulus.	N/mm^2
$MC(t)$	Moisture content as a function of time.	%
MC_{fin}	Final in-service moisture content.	%
MC_{inst}	Moisture content at installation.	%
m_{dry}	Oven-dry mass.	kg
m_u	Mass at given moisture content.	kg
ρ_{mean}	Mean timber density.	kg/m^3
ρ_1	Density of timber member 1.	kg/m^3
ρ_2	Density of timber member 2.	kg/m^3
ε_{sh}	Free shrinkage strain.	–
Viscoelasticity and relaxation		
$a(t_i)$	Ageing factor.	–
$E(t)$	Relaxation modulus.	N/mm^2
E_i	Modulus of Maxwell element i.	N/mm^2
k_{def}	Deformation factor for long-term effects.	–
m	Ageing exponent.	–
N_{M}	Number of Maxwell elements.	–
s_v	Dummy time variable in convolution integral.	days
t_{ref}	Reference time for ageing model.	days
t_i	Time at which strain increment is applied.	days
Δt	Time increment / time difference.	days
τ	Relaxation time.	days
τ_i	Relaxation time of Maxwell element i.	days
η	Viscosity.	N day/mm^2
$\dot{\varepsilon}$	Total strain rate.	day^{-1}
$\dot{\varepsilon}_m$	Mechanical strain rate.	day^{-1}

Symbol	Definition	Unit
ε_0	Imposed constant strain.	–
ε_m	Mechanical strain.	–
$\varepsilon_{\text{total}}$	Total strain.	–
σ	Normal stress.	N/mm^2
$\dot{\sigma}$	Stress rate.	$\text{N/mm}^2\text{/day}$
σ_{max}	Maximum stress.	N/mm^2
Connection stiffness, resistance and slip		
d_1	Inner thread diameter of screw.	mm
D_s	Ductility factor.	–
F	Applied force.	N
$F_{v,Ed}$	Design shear force in a fastener.	N
$F_{v,Rd}$	Design lateral resistance per fastener per shear plane.	N
$F_{v,Rd,\text{PC}}$	Design shear resistance of panel–core fastener.	N
$F_{v,Rd,\text{PB}}$	Design shear resistance of panel–beam fastener.	N
$F_{v,Rd,\text{PP}}$	Design shear resistance of panel–panel fastener.	N
$F_{v,Rk}$	Characteristic lateral resistance per fastener per shear plane.	N
g	Required slip allowance at support.	mm
k	Smeared stiffness per unit length.	N/mm^2
k_{line}	Line stiffness of a connection.	N/mm^2
K_A	Translational connection stiffness for sliding.	N/mm
K_{anchors}	Stiffness contribution of anchors.	N/mm
K_{CLT}	Stiffness contribution of CLT member.	N/mm
K_{fin}	Effective long-term connection stiffness.	N/mm
K_{mean}	Mean slip stiffness of a connection.	N/mm
$K_{\text{PB,fin}}$	Effective long-term stiffness of panel–beam connection.	N/mm
$K_{\text{PC,fin}}$	Effective long-term stiffness of panel–core connection.	N/mm
K_{plate}	Stiffness contribution of steel plate.	N/mm
K_{PP}	Rotational stiffness of panel–panel connection.	Nmm/rad
K_R	Rotational stiffness of connection rocking.	Nmm/rad
K_{SLS}	Serviceability slip modulus.	N/mm
$K_{SLS,v,i}$	Lateral slip modulus per fastener per shear plane.	N/mm
$K_{SLS,v,i}^{st}$	Lateral slip modulus for steel-to-timber connection.	N/mm
K_{screws}	Stiffness contribution of screw group.	N/mm
K_{tot}	Total connection stiffness from component method.	N/mm
k_{mod}	Modification factor for load duration and moisture condition.	–
γ_M	Partial safety factor.	–
u	Relative slip / displacement.	mm
u_u	Ultimate slip.	mm
u_y	Slip at onset of yielding.	mm
Restraint-force models and diaphragm behaviour		
F_h	Applied horizontal floor force.	kN
k_{floor}	Effective floor restraint stiffness.	kN/mm
k_{PC}	Distributed stiffness of panel–core connection.	N/mm^2
$k_{\text{PC,fin}}$	Distributed long-term line stiffness of panel–core connection.	N/mm^2
k_{req}	Required storey restraint stiffness for member buckling to govern.	kN/mm
k_{tot}	Equivalent stiffness of beam–spring series system.	N/mm
λ	Foundation parameter.	1/mm
M	Bending moment.	Nmm
N	Axial force.	kN
$N(x)$	Axial force distribution along restrained edge.	kN

Symbol	Definition	Unit
n_{PC}	Axial force per unit length in panel–core connection.	kN/m
$n_{\text{PC,max}}$	Maximum panel–core normal resultant per unit length.	kN/m
n_{PP}	Axial force per unit length in panel–panel connection.	kN/m
$n_{\text{PP,max}}$	Maximum panel–panel normal resultant per unit length.	kN/m
q	Line load.	kN/m
q_R	Distributed restraint reaction.	kN/m
$q_R(x)$	Distributed reaction force along restrained edge.	kN/m
Q_m	Horizontal diaphragm force due to imperfections.	kN
R	Restraint reaction force.	kN
R_H	Horizontal restoring force from diaphragm.	kN
R_i	Force in screw i.	kN
R_{PB}	Reaction force at panel–beam support.	kN
R_{PC}	Reaction force at panel–core support.	kN
$u(x)$	Axial displacement along restrained edge.	mm
u_A	In-plane displacement due to connection sliding.	mm
u_B	In-plane displacement due to panel bending.	mm
u_R	In-plane displacement due to connection rocking.	mm
u_S	In-plane displacement due to panel shear.	mm
$u_{s,i}$	Slip of individual screw i.	mm
u_{sh}	Free shrinkage shortening.	mm
$u_{\text{sh,global}}$	Global free shrinkage deformation of a floor panel.	mm
u_{tot}	Total in-plane diaphragm displacement.	mm
v_y	In-plane shear force per unit length.	kN/m
$v_{y,\text{PC,max}}$	Maximum panel–core resultant perpendicular to the interface.	kN/m
θ	Rotation angle.	rad
ϕ	Imperfection angle.	rad
Stability, analysis and verification		
α_{cr}	Critical load factor.	–
K_G	Geometric stiffness matrix.	–
K_L	Linear elastic stiffness matrix.	–
k_c	Buckling reduction factor.	–
λ_{cr}	Buckling eigenvalue factor.	–
$\lambda_{\text{cr,ns}}$	Critical load factor for non-sway member buckling.	–
$\lambda_{\text{cr,sw}}$	Critical load factor for sway buckling.	–
$M_{z,Ed}$	Design bending moment about local z-axis.	kNm
$M_{z,1,Ed}$	First-order design bending moment about local z-axis.	kNm
$M_{z,2,Ed}$	Second-order design bending moment about local z-axis.	kNm
N_{Ed}	Design axial force.	kN
$N_{1,Ed}$	Design axial force from first-order analysis.	kN
$N_{2,Ed}$	Design axial force from second-order analysis.	kN
N_{cr}	Elastic critical axial force.	kN
P_h	Horizontal component of axial force.	kN
P_{cr}	Critical buckling load.	kN
$P_{\text{cr,E}}$	Euler critical load.	kN
$P_{\text{cr,ns}}$	Critical non-sway buckling load.	kN
$P_{\text{cr,sway}}$	Critical sway buckling load.	kN
u_i	Inter-storey displacement.	mm
$u_{i,\text{max}}$	Maximum inter-storey displacement.	mm
$u_{i,\text{max,1}}$	Maximum inter-storey displacement from first-order analysis.	mm
$u_{i,\text{max,2}}$	Maximum inter-storey displacement from second-order analysis.	mm
u_{top}	Top displacement of the building.	mm

Symbol	Definition	Unit
$u_{\text{top},1}$	Top displacement from first-order analysis.	mm
$u_{\text{top},2}$	Top displacement from second-order analysis.	mm
$u_{\text{top,lim}}$	Limit value for top displacement.	mm
$u_{i,\text{max,lim}}$	Limit value for inter-storey displacement.	mm
UC	Utilisation ratio.	–
$\boldsymbol{\phi_b}$	Buckling mode shape vector.	–

1

Introduction

1.1. Societal relevance and context

The construction sector is one of the most environmentally impactful industries worldwide, largely due to the extensive use of concrete and steel [2]. To meet climate targets, the Dutch government aims for a fully circular built environment by 2050 [3]. This requires a strong reduction in CO_2 emissions and a shift towards renewable and low-carbon materials.

Timber is therefore increasingly used as a structural material. To create structural elements with sufficient strength and stiffness, wood is processed into so-called engineered timber products. These products consists of smaller timber boards (lamella) that are bonded together to form larger components.

A common example is glue-laminated timber (glulam), which is made by bonding timber lamellas with the grain oriented in the same direction (Figure 1.1a). Glulam is commonly used for beams and columns. It provides higher and more consistent strength and stiffness than sawn timber of comparable dimensions. Its high strength-to-weight ratio enables long spans, and the manufacturing process allows tailored cross-sections, including tapered and curved elements [4]. Another widely used product is cross-laminated timber (CLT), which consists of multiple timber layers glued together with alternating grain directions (Figure 1.1b). CLT is used as large surface panels for floors and walls. The large cross-sections provide high load-bearing capacity and stiffness, both in-plane and out-of-plane. As a result, CLT panels can also contribute to the global stability of the building [5].

(a) Glulam beams [6].

(b) CLT panels [7].

Figure 1.1: Engineered timber products, glulam beams (left) and CLT panels (right).

In mid- and high-rise buildings, engineered timber products are often used in hybrid structural systems, where timber is combined with another primary material. A common layout is a timber frame with timber floors connected to a concrete core (Figure 1.2). Timber is used to reduce environmental impact,

while the concrete core provides the primary lateral stiffness, resists horizontal loads such as wind, and ensures overall stability.

Figure 1.2: Concrete core with timber frame structure.

These hybrid buildings are already widely realised in practice. A global survey of timber buildings of eight storeys and higher shows that concrete–timber hybrids form a substantial share of completed projects, and that hybrid solutions become more common as building height increases (Figure 1.3).

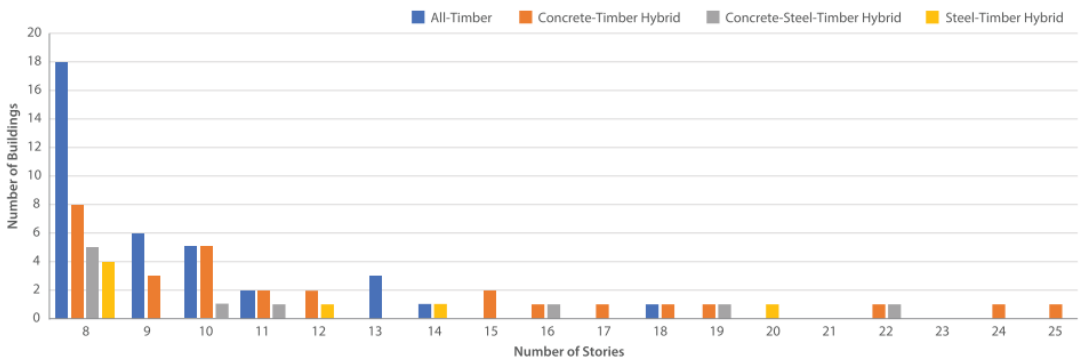

Figure 1.3: Distribution of mass timber buildings worldwide (2022), by number of storeys and structural material combination [8].

The continued growth of concrete–timber hybrid construction increases the need for reliable design and assessment methods. Although many projects have been completed, practical guidance is still evolving.

1.2. Research problem and gap

The hybrid core-frame system described in the previous section is a commonly used structural concept for tall timber structures. In this configuration, a stiff reinforced concrete core provides the primary lateral stability against horizontal loads such as wind, while a timber frame carries the vertical loads. Besides carrying vertical loads, the CLT floors are part of the overall stabilising concept: they couple the frame to the core and act as diaphragms that transfer horizontal actions from the timber system towards the concrete core.

The hybrid timber system cannot be designed in the same way as a conventional concrete core–slab building. The floor system differs fundamentally in both material behaviour and structural performance. First, timber is moisture-sensitive and exhibits time-dependent deformations. After installation, the moisture content of CLT elements reduces towards an indoor equilibrium. This reduction causes shrinkage in the CLT panel, and can lead to progressive in-plane shortening over time. Such deformations require explicit consideration in timber design.

Second, CLT floors are not monolithic. They are assembled from prefabricated panels connected on site with mechanical fasteners. As a result, the in-plane deformation of a CLT floor is governed not

only by the panel stiffness, but also by the stiffness of the present connections. Compared to cast-in-situ concrete slabs, diaphragm behaviour is therefore more sensitive to connection detailing and can vary significantly between design choices.

These characteristics lead to two uncertainties in hybrid core–frame buildings that are not yet well addressed in an integrated way.

The first uncertainty concerns restrained shrinkage. When CLT panels shrink, their free movement may be partly or fully restrained by connections. If shrinkage is restrained, internal stresses develop in the floor panels and additional forces develop in the connection and in the element. In practice, it is not yet well understood how large these shrinkage-induced forces can become, which parameters govern them, and under what conditions they become critical for design and detailing.

The second uncertainty concerns the effective diaphragm stiffness and its influence on global stability. The CLT floor couples the timber frame to the concrete core and therefore plays a key role in the distribution of horizontal loads. A central question is how sensitive the global response is to the assumed diaphragm stiffness. In particular, it must be assessed when the stiffness becomes sufficiently low to affect the building's stability, and whether a first-order analysis (analysis on the undeformed geometry) remains adequate or a second-order analysis is required (analysis on the deformed geometry).

Finally, it has not yet been examined whether shrinkage-induced restraint forces and diaphragm stiffness influence each other, and whether their combined effect governs connection demand or global behaviour.

This thesis addresses these issues by studying the development of shrinkage-induced forces due to restraint in CLT floor systems and the interaction between diaphragm stiffness and the stability response of a hybrid core–frame building, using a combined analytical and numerical approach.

1.3. Research aim and objectives

This thesis aims to improve the understanding and assessment of CLT floor systems in concrete core–timber frame buildings. It focuses on shrinkage restraint and the resulting forces in connections, and on how diaphragm stiffness affects global stability and the need for first- or second-order analysis.

To achieve this, the following objectives are pursued:

1. Describe the shrinkage behaviour of CLT over time and how stresses can reduce due to time-dependent material behaviour (stress relaxation).
2. Develop analytical models that convert shrinkage deformation into restraint forces for representative floor restraint situations in hybrid core–frame buildings.

   the parameters that govern shrinkage-induced force development and determine under which conditions these forces become critical for detailing and design.
3. Evaluate how different connection stiffness configurations influence the global structural response under SLS and ULS criteria, and determine the differences between first-order (linear) and second-order (geometrically non-lineair) analysis outcomes.
4. Translate the findings into practical guidance on connection stiffness and detailing measures to limit shrinkage-induced forces and conditions under which second-order analysis should be considered.

1.4. Research questions

The main research question guiding this thesis is:

> *How do connection stiffness in CLT floor systems of hybrid concrete core–timber frame buildings influence shrinkage-induced forces and the global stability behaviour of the structure?*

To address this main question, the study is structured into three research parts (Figure 1.4). Each part is associated with a set of sub-questions.

Part I: Shrinkage and relaxation of CLT

1. How does moisture-driven shrinkage in CLT develop over time, and which material and environmental parameters govern its magnitude and rate?
2. How does viscoelastic stress relaxation influence the evolution of stresses in CLT subjected to restrained shrinkage, and how can this effect be represented in a practical long-term modelling approach?

Part II: Shrinkage-induced forces in CLT connections

1. How do common CLT–core and CLT–timber connection configurations provide restraint against shrinkage deformations, and which parameters govern the resulting restraint forces?
2. Under which geometric and moisture-related conditions do shrinkage-induced forces become critical for connection utilisation, and what measures can be taken to keep the demand within acceptable limits?

Part III: Influence of CLT connections on structural stability

1. How does the in-plane stiffness of the CLT floor diaphragm affect system response under SLS and ULS criteria in first- and second-order analysis?
2. Under which conditions does first-order analysis no longer provide a reliable assessment of the system response, and when is second-order analysis required to capture the governing response of the structure?

1.5. Scope

This thesis focuses on the structural implications of CLT floor behaviour in a hybrid concrete core–timber frame system, with particular emphasis on shrinkage-induced restraint forces and the role of diaphragm stiffness in global system response.

In scope

- Analytical evaluation of shrinkage-induced restraint forces in CLT floor systems using a set of idealised restraint situations representative for hybrid core–frame connections; one situation matches the boundary conditions of the case-study building.
- Numerical analysis of the selected hybrid concrete core–timber frame case-study building in RFEM to assess the influence of assumed CLT diaphragm stiffness on the global response under governing SLS and ULS load combinations. SLS is assessed using global displacement limits and interstorey drift limits, while ULS is assessed using connection force demand and column buckling checks.
- Global stability evaluation of the case study based on first- and second-order analysis to quantify the relevance of geometric non-linearity.
- Connection modelling using representative linear translational stiffness values: the study does not model individual fasteners.
- Within the case study, the design variants are limited to connector spacing and the addition of grout (same connection type and layout concept)

Out of scope

- Explicit modelling of shrinkage as an imposed deformation/load case in the global RFEM model.
- Fastener-level connection modelling and detailed capacity verification beyond the linear stiffness representations used for analysis.
- Generalisation to other building geometries and layouts beyond the selected case study.
- Seismic response, dynamic loading and vibration-related behaviour.
- Building physics and non-structural performance aspects, including fire safety, acoustics and thermal performance.

1.6. Methodology

The methodology follows the three-part structure of the thesis (Figure 1.4), progressing from material behaviour, to connection mechanics, and finally to structural system response in a case study.

Part I: Shrinkage and relaxation of CLT
A theoretical framework is established for moisture-driven shrinkage and time-dependent stress development in CLT. Shrinkage is described using moisture-related input parameters and representative shrinkage coefficients. Viscoelastic behaviour is incorporated to account for stress relaxation over time, leading to a practical long-term representation of the material response in terms of an effective long-term modulus. The resulting parameter set and long-term material representation form the basis for the subsequent connection force assessment.

Part II: Shrinkage-induced forces in CLT connections
Analytical models are developed to translate shrinkage deformations into restraint forces in idealised CLT floor restraint situations that represent typical interfaces in hybrid core–frame buildings. The shrinkage input and time-dependent material representation established in Part I are adopted as model input, enabling an estimation of long-term restraint forces. The governing parameters are evaluated through parametric studies, which identify critical combinations of panel geometry and installation moisture. Detailing measures are assessed to limit restraint forces.

Part III: Influence of CLT connections on structural stability
A numerical model of the case-study hybrid core–frame building is developed in RFEM to assess how assumed diaphragm connection stiffness affects the global structural response. Connection stiffnesses are represented by linear elastic translational springs derived from Part II. Both first-order (linear) and second-order analyses are performed to evaluate sensitivity to geometric non-linearity across the investigated configurations. The comparison focuses on global drift, internal forces, column stability, and overall stability performance.

Discussion, conclusion and recommendations
The analytical and numerical results are combined to clarify the trade-offs between accommodating restraint shrinkage forces and maintaining sufficient diaphragm restraint for stability and force transfer. In addition, the study derives practical insights into the appropriate choice of analysis type by linking connection stiffness and structural response to the need for second-order assessment. This forms the basis for design recommendations on feasible connection stiffness levels and detailing strategies, as well as guidance on when second-order analysis should be considered essential.

1.7. Reading guide

The thesis follows the structure shown in Figure 1.4. After introducing the societal context, research problem, and guiding research questions in this chapter (Chapter 1), Chapter 2 presents the case-study building, which serves as the reference example throughout the remainder of the thesis. Part I (Chapter 3-4) establishes the material-level framework for moisture-driven shrinkage and time-dependent stress development in CLT. Part II (Chapter 5-6) develops analytical models to quantify shrinkage-induced restrained forces in representative connection situations and evaluates the role of key parameters and detailing measures. Part III (Chapter 7-8) assesses the structural implications in the numerical case study, including the influence of diaphragm connection assumptions and the need for first- and second-order analysis. Chapter 9 interprets the results, discusses limitations, and outlines broader implications, while Chapter 10 concludes the thesis and presents the main recommendations.

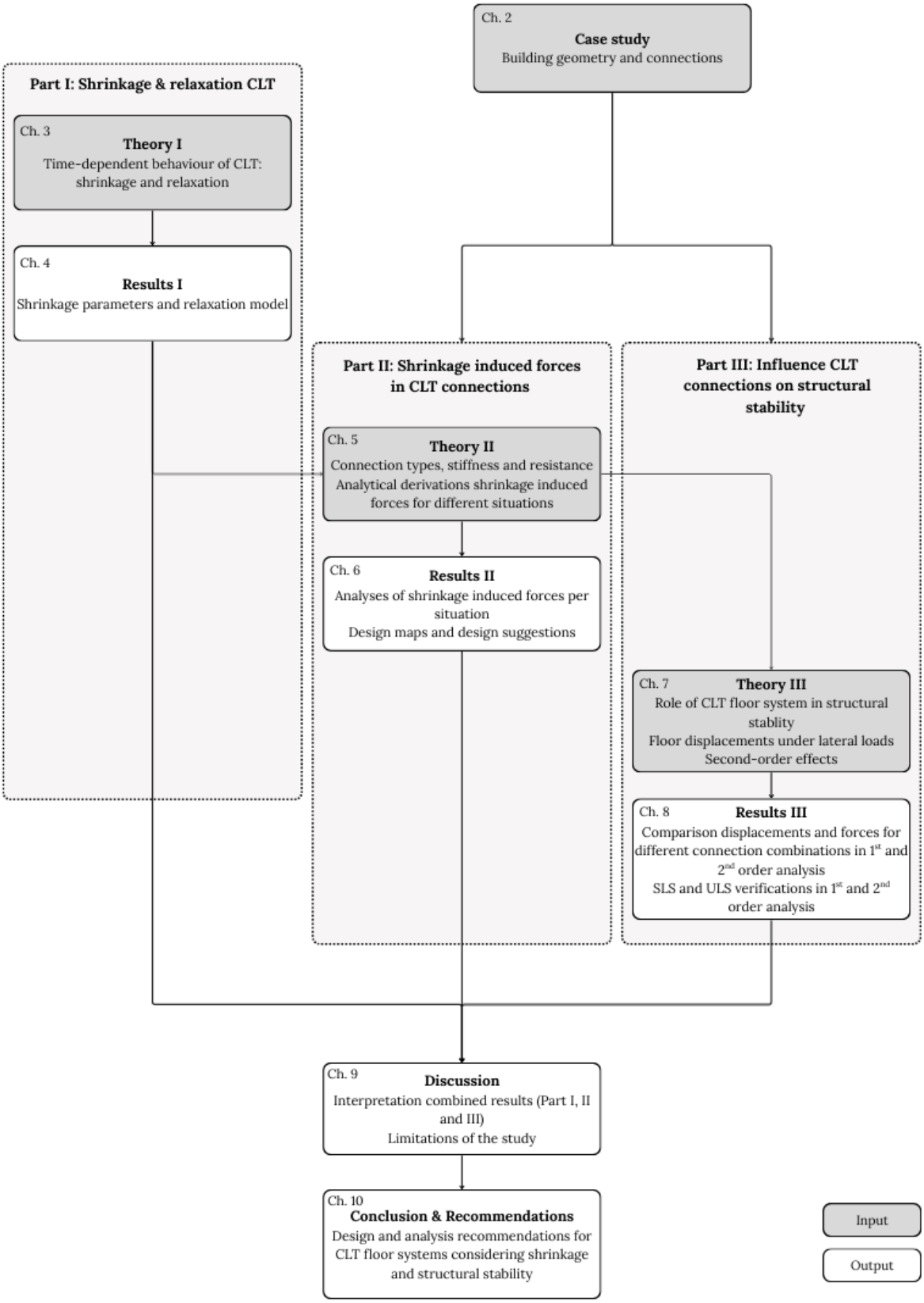

Figure 1.4: Methodology flowchart

2

Case study

2.1. General description

To investigate the structural implications of CLT floor behaviour in hybrid core–frame buildings, a residential project in Roosendaal, the Netherlands, is adopted as a case study. The project consists of five building blocks: the analyses in this thesis focus on Block D (Figure 2.1a).

Block D comprises eleven storeys. In the realised project, the ground floor has a commercial function and is constructed in reinforced concrete, while the storeys above are built in a prefabricated timber system consisting of CLT floor panels supported by glulam beams and columns. Global lateral stability is provided by a reinforced concrete core.

For modelling simplicity, the case-study model idealises the superstructure as a timber system over all eleven storeys, so the lowest storey is also modelled as a timber storey. The reinforced concrete ground floor is therefore not represented explicitly in the numerical model.

The selected case study is also structurally relevant for the topics addressed in this thesis. A substantial length of the CLT floor panels is connected to the concrete core, which can lead to significant restraint of moisture-driven shrinkage and corresponding force demand in the panel–core interface. Moreover, the floor plan is asymmetric and the core is not located centrally. Horizontal loading can therefore induce a torsional response, which increases sensitivity to instability mechanisms.

The case study serves two purposes in this thesis. First, it provides realistic boundary conditions for the analytical restraint situations used to study shrinkage-induced force development. Second, it forms the basis for a global numerical assessment in RFEM, in which diaphragm connection stiffness and analysis type (first- and second-order) are evaluated.

Table 2.1 summarises general building parameters relevant for the design context and numerical modelling.

Table 2.1: General building parameters for Block D.

Parameter	Value
Function	Residential
Number of storeys	11
Design service life class	Class 3
Design service life	50 years
Reliability class	RC2
Consequence class	CC2b
Service class	Class 1
Lateral stability system	Concrete core

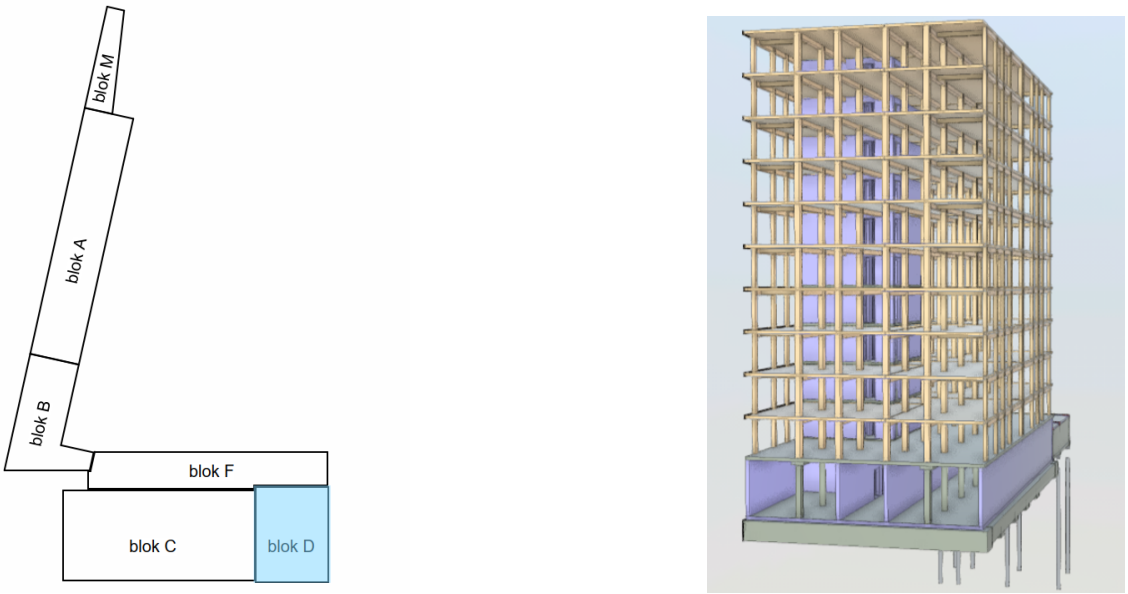

(a) Project overview.

(b) Materialisation of Block D.

Figure 2.1: Overview of the case study building.

2.2. Geometry and floor plan

Figure 2.2 shows the floor plan (left) and a cross section (right) of the case-study building as implemented in the RFEM model. The plan measures approximately 19 m in the x-direction and 24 m in the y-direction. The floor plan is asymmetric in the y-direction due to the position of the reinforced concrete core.

The CLT floor system is arranged such that the panels span in the x-direction. The panels are supported by glulam beams, resulting in multiple support lines and a segmented floor layout with panel–panel interfaces. The floor diaphragm is connected to the concrete core along the floor–core boundary. Depending on the floor field, the core connection occurs either along the long edge of the panels or at the short edge.

The cross section indicates eleven storeys with a typical storey height of 3.2 m, resulting in a total structural height of approximately 35.2 m.

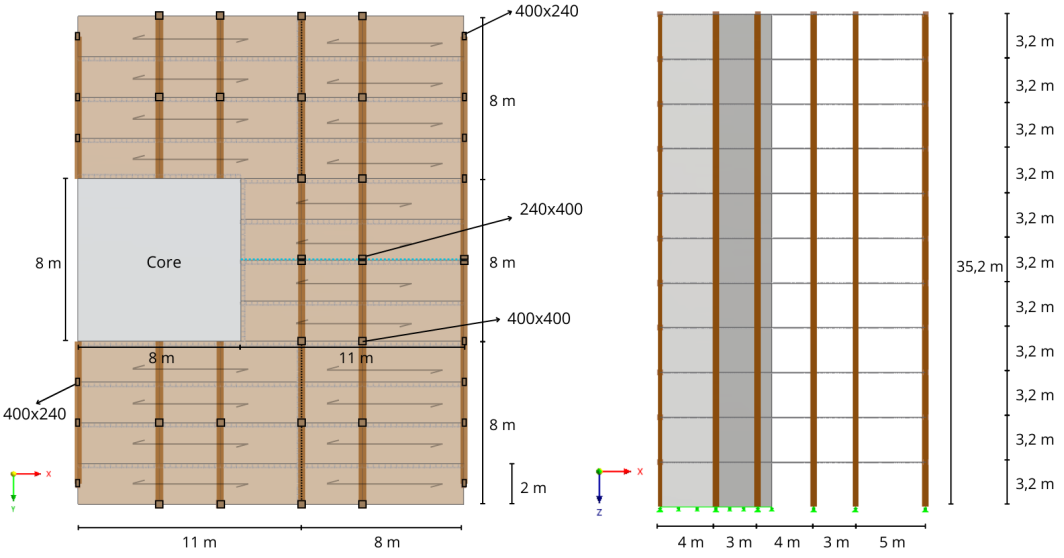

Figure 2.2: Floor plan (left) and cross section (right) of the case study building in RFEM.

For acoustic reasons, the column line is split into two separate columns (2 × 240×400) instead of a single 400×400 column (marked as AC in Figure 2.2). Local coupling of the floors across the separation is provided to maintain in-plane load transfer towards the concrete core.

2.3. Materials and members

The numerical model consists of a reinforced concrete core, glulam beams and columns, and CLT floor slabs. All materials are modelled as linear elastic. Material grades and member dimensions are summarised in Table 2.2 and Table 2.3. Detailed material properties adopted in the RFEM model are provided in Appendix A.

Table 2.2: Material overview for the case-study model.

Material	Grade / product	Application
Concrete	C30/37	Core walls
Glulam	GL24h	Beams and columns
CLT	Stora Enso (5-layer)	Floor panels

Table 2.3: Structural members and cross-sections used in the case-study model.

Member type	Location / function	Dimension
Columns	Typical	400 × 400 mm
Columns	Façade	400 × 240 mm
Columns	At AC	240 × 400 mm
Beams	Floor beams	360 × 360 mm
Concrete core	Core walls	t = 300 mm
CLT floors	Floor panels	t = 200 mm

CLT floor panels

The floor system consists of five-layer CLT panels with a total thickness of 200 mm. Each layer has a thickness of 40 mm, resulting in the lay-up 0°–90°–0°–90°–0° as shown in Figure 2.3. The CLT slabs are modelled as orthotropic linear-elastic surface elements to represent the directional stiffness relevant for diaphragm behaviour.

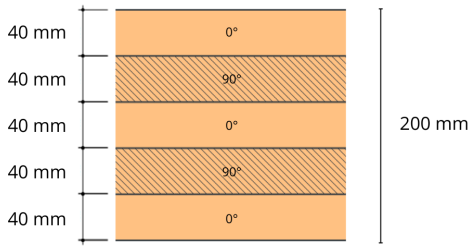

Figure 2.3: CLT lay-up used for the floor panels in the case study.

2.4. Use of the case-study model

The case-study model defined in this chapter is used as a reference framework throughout the thesis. It provides representative geometry and boundary conditions for the analytical restraint situations developed in Part I and Part II, and forms the basis for the global RFEM assessments in Part III.

Additional modelling details, including adopted material stiffness parameters, loads and imperfection assumptions, are provided in Appendix A. The investigated connection typologies and stiffness assumptions are introduced in chapter 5.

Part I

Shrinkage and relaxation in CLT

3

Shrinkage and relaxation in CLT

This chapter provides the theoretical background required to understand the shrinkage and time-dependent behaviour of CLT floor panels. It first introduces CLT as a structural product and explains why moisture-related deformation is relevant in practice. The chapter then describes how changes in moisture content lead to shrinkage strains and how these strains can generate stresses when deformation is restrained. Finally, the time-dependent (viscoelastic) behaviour of timber and stress relaxation are introduced, forming the basis for the analytical models developed in Part II.

Throughout this thesis, shrinkage- and time-dependent design parameters are taken from the *draft* revision of Eurocode 5 (FprEN 1995-1-1:2025) [9], unless stated otherwise. The theoretical background in this chapter is primarily based on the book Timber Engineering Prinsiples for Design by Blaß and Sandhaas [10], complemented with CLT-specific guidance from the Swedish Wood CLT handbook [5].

3.1. Cross-laminated timber

This section gives insight into how CLT is produced and how moisture conditions may vary from fabrication to installation. Understanding this process is necessary to define realistic shrinkage input parameters.

3.1.1. Fabrication CLT

Cross-laminated timber (CLT) is a layered engineered wood product in which boards are stacked in multiple layers with alternating grain orientation and bonded together using structural adhesives. This crosswise arrangement changes the panel response compared to unidirectional timber products: CLT behaves as a plate-like structural element capable of carrying loads both in-plane and out-of-plane, making it suitable for floors, walls and diaphragms in multi-storey timber buildings.

CLT panels are manufactured from strength-graded boards that are finger-jointed to form continuous lamellas and assembled into layers with alternating grain direction. Common configurations consist of an odd number of layers (e.g. 3, 5 or 7), with typical lamella thicknesses in the range of 20–45 mm [5]. Product requirements and declared properties are documented by the manufacturer (e.g. under EN 16351 and/or European Technical Assessment, ETA).

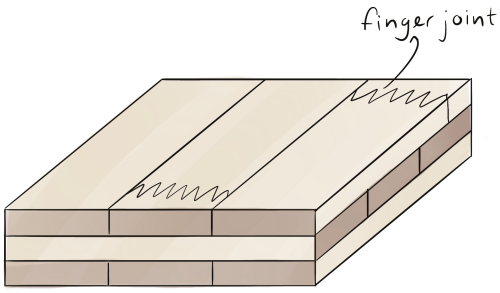

Figure 3.1: 3-layered cross laminated timber with finger joint.

Moisture content is a key production parameter because it affects both bond quality and subsequent moisture-related movement. During manufacturing, boards are typically glued within a controlled moisture range (approximately 8–15%), with limited variation between adjacent boards to ensure reliable bonding and to reduce the risk of splitting during subsequent drying or moisture uptake [5]. After production and packaging, CLT elements are commonly delivered at moisture contents in the order of ≤16% [5]. These ranges provide a practical reference for the initial moisture state of panels before transport, storage and installation, which is further discussed in the next subsection.

3.1.2. CLT at the construction site

Between delivery and enclosure of the building, CLT elements may be exposed to outdoor climate conditions during transport, temporary storage and erection. Although panels are typically wrapped for protection, the wrapping is not necessarily vapour-tight and may be damaged during handling. In addition, once packages are opened and elements are installed, surfaces can be exposed to precipitation, snow or condensation before the building envelope is closed. Figure 3.2 illustrates situations in which CLT is stored outdoors under temporary cover and where floor panels experience direct exposure during erection.

(a) CLT panels stored outdoors under temporary protection.

(b) CLT floor panels during erection.

Figure 3.2: Examples of CLT exposure to outdoor conditions during construction.

Such exposure can increase the moisture content at or near the surfaces and may also lead to locally elevated moisture levels at vulnerable regions such as end-grain surfaces and panel edges. Practical guidance therefore emphasises minimising exposure time and prioritising rapid encasement or effective temporary weather protection, combined with on-site acceptance checks of the moisture content [5]. For the modelling in this thesis, these site conditions motivate treating the moisture content at installation MC_{inst} as a variable input rather than a fixed value.

3.2. Wood anatomy

Wood behaves differently from many common structural materials because it reacts to moisture and because part of its mechanical response is time-dependent. Wood can absorb and release moisture from the surrounding air (*hygroscopic* behaviour), which causes swelling and shrinkage. In addition, stresses and deformations in wood can change gradually over time (*viscoelastic* behaviour). This section provides background to interpret moisture-driven deformation in CLT (Section 3.3) and stress relaxation under restrained shrinkage (Section 3.5). It introduces the hierarchical structure of wood and the principal material directions used in the modelling approach of this thesis.

The anatomical structure of wood forms the basis for its mechanical behaviour. Wood has a hierarchical structure, ranging from the macroscale of structural elements to annual growth rings, individual cells and the molecular arrangement of the cell wall (Figure 3.3).

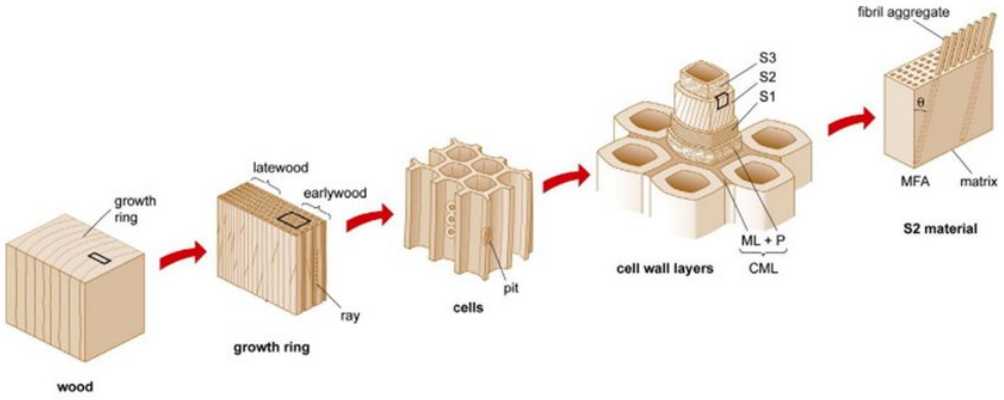

Figure 3.3: Hierarchical structure of wood [11]

On the macroscale, wood grows outward from the pith by forming annual growth rings consisting of earlywood and latewood. Earlywood contains thin-walled, low-density cells, whereas latewood consists of thicker-walled, denser cells. This growth pattern leads to variations in density and stiffness within a single cross-section.

The growth structure gives rise to three principal material directions:

- **Longitudinal**: parallel to the fibres,
- **Radial**: perpendicular to the growth rings,
- **Tangential**: tangential to the growth rings.

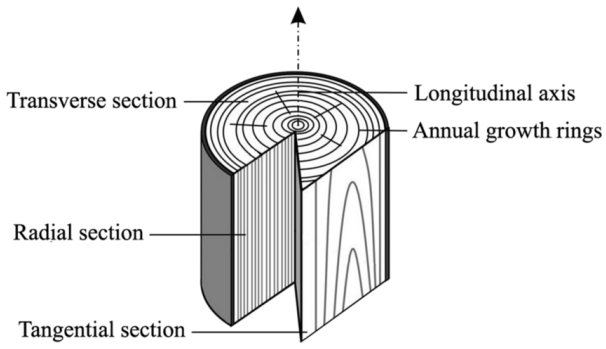

Figure 3.4: Section planes in wood [12]

At the microscale, wood consists mainly of elongated tubular cells. The mechanical behaviour of these cells is governed by the layered structure of the cell wall, consisting of the S1, S2 and S3 layers. The S2

layer is the thickest and contains highly oriented cellulose microfibrils, which dominate stiffness and strength parallel to the grain. The orientation of these microfibrils, often expressed by the microfibril angle, strongly influences elastic properties, creep behaviour and shrinkage.

As a direct consequence of its anatomical structure, timber is commonly idealised as an orthotropic material, meaning that its properties differ along three mutually perpendicular principal directions. Stiffness and strength parallel to the grain are significantly higher than those perpendicular to the grain, where stiffness is much lower and deformation behaviour is governed by the transverse directions.

For the remainder of this thesis, this orthotropic character is mainly relevant because moisture-induced deformation differs strongly between the longitudinal, radial and tangential directions.

3.3. Moisture in CLT

Moisture content is the driving variable for shrinkage in timber. This section therefore defines moisture content, introduces equilibrium moisture content (EMC) as the reference level for indoor service conditions, and adopts a time-dependent moisture evolution model used in further analyses.

3.3.1. Moisture content

The moisture content MC of wood is defined as

$$MC = 100 \cdot \frac{m_u - m_{\text{dry}}}{m_{\text{dry}}}, \tag{3.1}$$

where m_u is the mass at moisture content MC and m_{dry} is the oven-dry mass, obtained by drying at 105°C until constant weight [13].

Moisture in wood exists in two forms. *Free water* is located in the cell cavities (lumina) and has negligible influence on mechanical properties or dimensional changes. *Bound water* is held within the cell wall by hydrogen bonds and governs hygroscopic behaviour, including swelling, shrinkage and moisture-dependent mechanical properties.

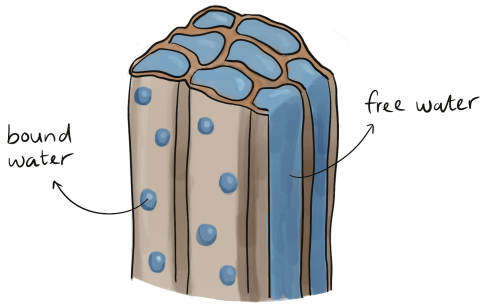

Figure 3.5: Free and bound water in wood.

The point at which the cell walls are fully saturated with bound water is known as the *fibre saturation point* (FSP), typically between 25–30% moisture content. Above the FSP, additional moisture exists only as free water and does not lead to further swelling or changes in stiffness. Below the FSP, changes in bound water content result directly in dimensional changes and variations in mechanical behaviour.

Because moisture-driven swelling and shrinkage are governed by changes in bound water content below the FSP, moisture variations in this range are of primary importance for structural applications.

Equilibrium moisture content (EMC)

Wood exchanges moisture with the surrounding air until it approaches an *equilibrium moisture content* (EMC), which depends mainly on the ambient relative humidity and temperature. If the indoor climate were constant, the EMC would be the moisture level reached after a sufficiently long time. In this thesis, this long-term indoor reference level is represented by the final in-service moisture content MC_{fin} used in the moisture evolution model of Section 3.3.2.

3.3.2. Moisture content development over time

Timber elements are delivered with a moisture content specified by the manufacturer. In practice, the moisture content at installation may differ from this delivery value, as elements can be exposed to ambient weather conditions between delivery and enclosure. After installation and closure of the building envelope, the moisture content generally decreases as the timber adjusts to the indoor climate.

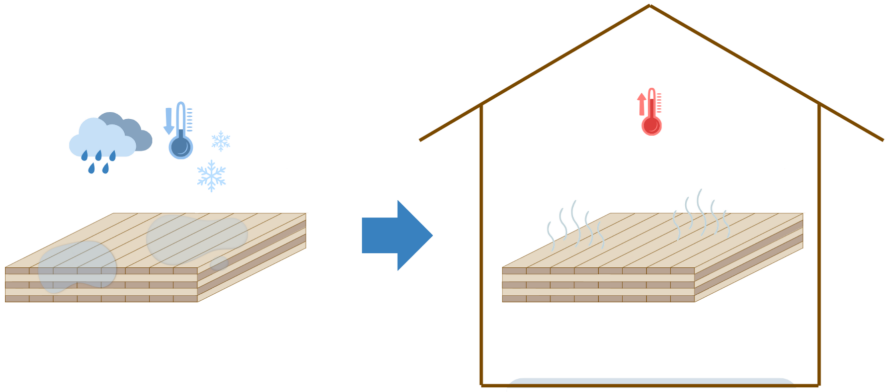

Figure 3.6: Schematic illustration of CLT moisture exposure during construction and subsequent indoor drying after enclosure.

In structural applications, the average moisture content evolution is often of interest, as it governs shrinkage and moisture-related time-dependent effects. To obtain a realistic representation, the experimental data reported by Xiong, Su and Sabri (2009), as analysed in the MSc thesis of Willebrands (2017) [14], are adopted in this study. In that work, daily average relative humidity and temperature were measured on the second and seventh storeys of a mid-rise timber building, and the corresponding moisture content was derived from these measurements. The resulting time series showed a similar trend on both storeys, characterised by an initial drying phase, followed by seasonal fluctuations driven by changes in the indoor climate.

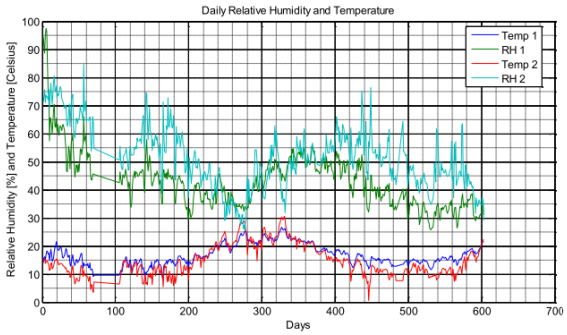

(a) Relative humidity and temperature on second and seventh floor.

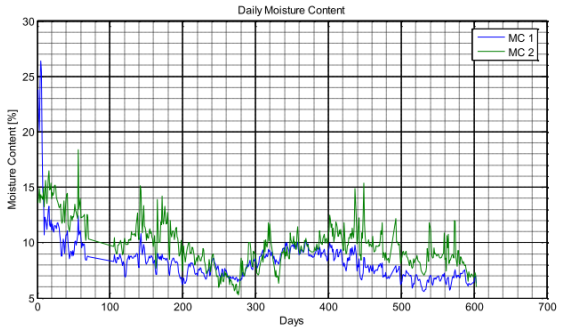

(b) Moisture content on the second and seventh floor.

Figure 3.7: Relative humidity and temperature measurements and corresponding moisture content by Xiong, Su and Sabri (2009) [15].

For modelling purposes, Willebrands (2017) fitted a smooth trend curve to the calculated moisture content data to represent the overall drying behaviour, rather than short-term seasonal variability. This trend is approximated by an exponential decay from the moisture content at installation MC_{inst} toward a final in-service value MC_{fin}:

$$MC(t) = \Delta MC \cdot \mathrm{e}^{-0.011t} + MC_{\text{fin}}, \tag{3.2}$$

with $\Delta MC = MC_{\text{inst}} - MC_{\text{fin}}$, where t is time in days and the coefficient 0.011 represents an empirically fitted drying rate.

In Willebrands' regression, this trend describes a decrease from approximately 15% at installation toward about 8% over time. The exponential form reflects typical timber drying behaviour, with a

relatively rapid moisture decrease in the initial phase followed by a gradual convergence toward a long-term mean level.

Equation (3.2) should be interpreted as a smoothed representation of the average moisture content evolution. In reality, moisture content continues to fluctuate around this mean due to seasonal variations in indoor climate.

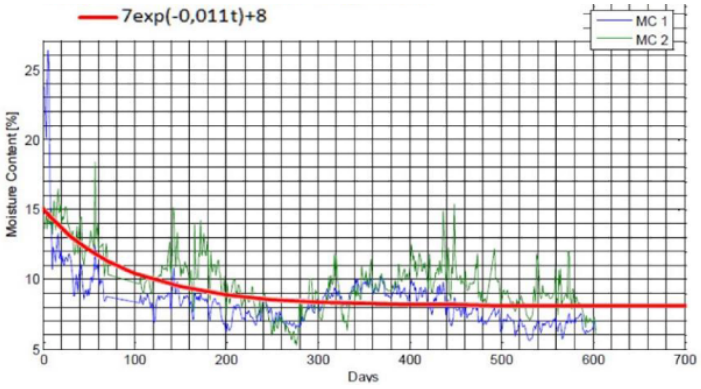

Figure 3.8: Estimate of moisture content regression, based on data (Xiong, Su and Sabri (2009)) by Willebrands (2017) [14].

3.4. Shrinkage in CLT

Shrinkage in timber is expressed as a strain resulting from a change in moisture content below the fibre saturation point. For a given material direction, the *total free shrinkage strain* associated with a moisture change ΔMC is written as

$$\varepsilon_{\text{sh}} = \beta \cdot \Delta MC, \tag{3.3}$$

where β is the shrinkage coefficient in the considered direction (in % strain per % moisture content). Here, ε_{sh} denotes the *total shrinkage strain* corresponding to the total moisture change ΔMC.

Shrinkage of CLT can be estimated using Equation 3.3 together with the shrinkage coefficients provided in Eurocode 5 (FprEN 1995-1-1:2025). For CLT, shrinkage coefficients are distinguished for the two in-plane directions of the panel and for the thickness direction.

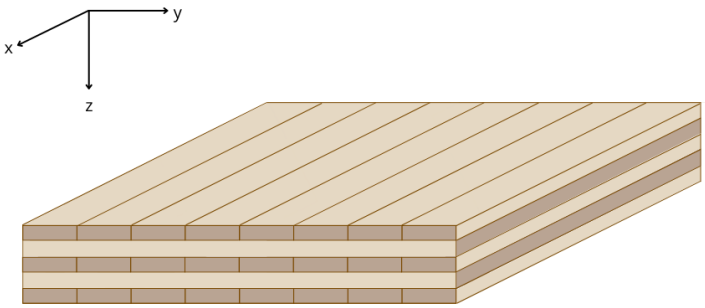

Figure 3.9: Principal directions CLT panel.

For in-plane directions, the recommended shrinkage coefficients are

$$\beta_x = 0.02\,\%/\%, \tag{3.4}$$

$$\beta_y = 0.04\,\%/\%, \tag{3.5}$$

where the x-direction denotes the major panel direction (outer lamellas oriented parallel to x) and the y-direction denotes the minor panel direction, as illustrated in Figure 3.9.

Shrinkage perpendicular to the panel plane, i.e. in the thickness direction (z-direction), is significantly larger and is given by

$$\beta_z = 0.24\,\%/\%. \tag{3.6}$$

This approach treats CLT as a homogenised material with fixed shrinkage coefficients, independent of wood species, number of layers, lamella thickness or layup configuration. While this provides a practical first estimate, it does not explicitly reflect the layered nature of CLT.

In reality, CLT consists of individual lamellas with different fibre orientations that restrain each other during moisture-induced deformation. Consequently, the shrinkage behaviour depends on the properties and geometry of the individual layers. A prediction method based on lamina-level shrinkage coefficients therefore allows a more accurate description of dimensional changes in CLT.

Pang and Jeong [16] demonstrated that the Eurocode-based approach may both overestimate and underestimate shrinkage strains, depending on panel configuration. Based on experimental results, they proposed a layer-based prediction method that explicitly accounts for lamina-level behaviour and showed improved agreement with measured shrinkage strains.

3.4.1. Layer-based shrinkage model

The layer-based shrinkage model assumes that the shrinkage behaviour of CLT can be derived from the shrinkage behaviour of its individual lamellas. The model accounts for the fibre orientation of each lamina, the relative lamella thicknesses, the number of layers, and the restraint imposed by adjacent layers. The resulting non-uniform shrinkage deformation is illustrated in Figure 3.10.

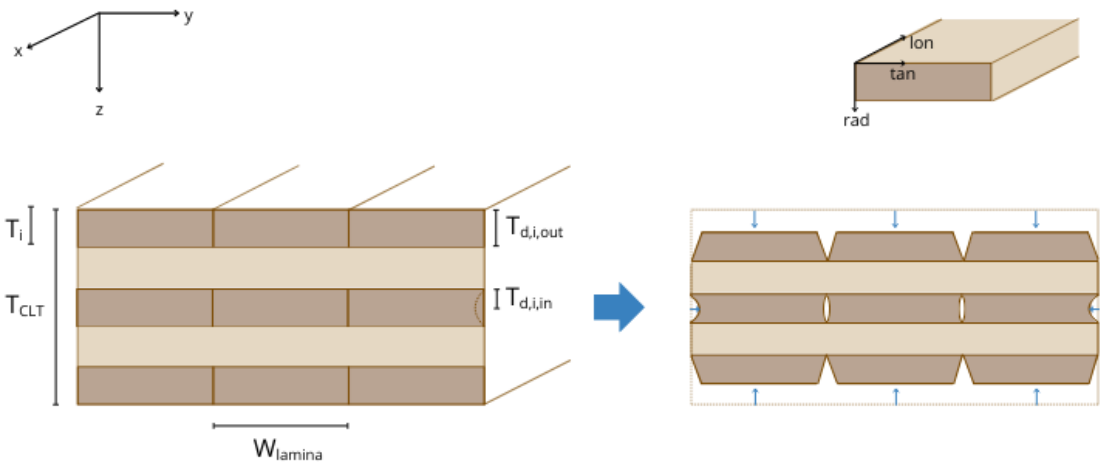

Figure 3.10: Schematic representation of shrinkage behaviour in CLT, showing the non-uniform deformation of individual layers.

All lamellas undergo moisture-induced shrinkage. Figure 3.10 illustrates that shrinkage within each lamella is partially restrained near the glue lines by adjacent layers with a different fibre orientation, while deformation can develop more freely toward exposed surfaces. The figure represents a CLT configuration in which the joints between boards within a lamella are not edge-glued.

For in-plane directions, the effective CLT shrinkage coefficient is obtained by summing the layer contributions:

$$\beta_{x,y} = \sum_{i=1}^{n} \left(\beta_i \, \frac{T_{d,i}}{W_{\text{lamina},i}} \, \frac{T_i}{T_{\text{CLT}}} \right). \tag{3.7}$$

where β_i is the shrinkage coefficient of lamina i in the relevant direction. Depending on the fibre orientation, β_i represents either longitudinal or tangential shrinkage. The term $T_{d,i}/W_{\text{lamina}}$ accounts for the non-uniform shrinkage distribution within a lamina, reflecting reduced deformation near glue lines. The ratio T_i/T_{CLT} describes the contribution of each lamina to the total panel deformation.

Example: 3-layer CLT panel. Consider a three-layer CLT panel in which the outer layers are oriented parallel to the x-direction and the middle layer is oriented parallel to the y-direction (Figure 3.10). The

effective shrinkage coefficient in the y-direction then follows from

$$\beta_y = \left(\beta_{\tan} \frac{T_{d,1}}{W_{\text{lamina}}} \frac{T_1}{T_{\text{CLT}}}\right) + \left(\beta_{\text{lon}} \frac{T_{d,2}}{W_{\text{lamina}}} \frac{T_2}{T_{\text{CLT}}}\right) + \left(\beta_{\tan} \frac{T_{d,3}}{W_{\text{lamina}}} \frac{T_3}{T_{\text{CLT}}}\right). \tag{3.8}$$

In this configuration, the outer layers contribute with tangential (across-grain) shrinkage in the y-direction, whereas the middle layer contributes with longitudinal (parallel-to-grain) shrinkage. For the outer layers ($i = 1, 3$), the effective deforming width is taken equal to the full lamella thickness, i.e. $T_{d,1} = T_1$ and $T_{d,3} = T_3$, since one side is adjacent to a free surface. For the inner layer ($i = 2$), shrinkage is restrained on both sides by adjacent layers, and therefore $T_{d,2}$ is taken as half the lamella thickness.

This example illustrates that the overall panel shrinkage differs between the x- and y-directions because the relative share of layers contributing with tangential (across-grain) shrinkage differs between the two directions.

The shrinkage coefficient perpendicular to the panel plane is governed by the radial direction of the lamellas and is calculated as

$$\beta_z = \frac{1}{n} \sum_{i=1}^{n} \beta_{i,\text{rad}} \tag{3.9}$$

Compared to the Eurocode approach, the layer-based model allows the effective shrinkage behaviour of CLT to vary with wood species, layup and panel geometry. The influence of the resulting shrinkage coefficients on restrained stress levels is analysed in subsection 4.2.2.

3.4.2. Shrinkage development over time

The shrinkage strain defined in Equation 3.3 represents the total strain associated with a given change in moisture content. In practice, however, moisture transport in timber is a gradual process, and shrinkage therefore develops progressively in time.

The time-dependent moisture content is described using the exponential regression introduced in Equation 3.2. By combining this relation with the shrinkage coefficient, the time-dependent shrinkage strain follows as

$$\Delta\varepsilon_{sh}(t) = \beta \cdot \Delta MC(t), \qquad \Delta MC(t) = MC_{\text{inst}} - MC(t) \tag{3.10}$$

Figure 3.11 illustrates the resulting shrinkage strain development over time, for a shrinkage coefficient of $\beta = 0.0004$. The strain increases rapidly during the initial drying phase, when the moisture gradient is largest, and gradually converges toward an asymptotic value as the moisture content approaches its final in-service level.

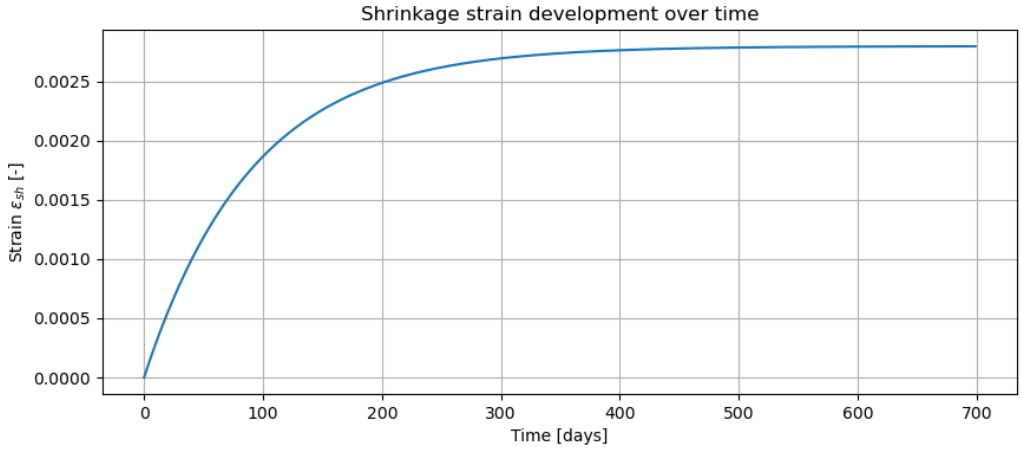

Figure 3.11: Shrinkage strain development over time.

3.5. Restrained shrinkage and relaxation in CLT

Moisture-driven shrinkage causes CLT to shorten by a free shrinkage strain ε_{sh}. If the panel is allowed to deform freely, this strain results only in a change in length and no stresses develop. In a structural floor system, however, shrinkage is often restrained by connections to adjacent panels, beams or a concrete core (Figure 3.12). In that case, part of the shrinkage deformation is prevented and internal stresses arise.

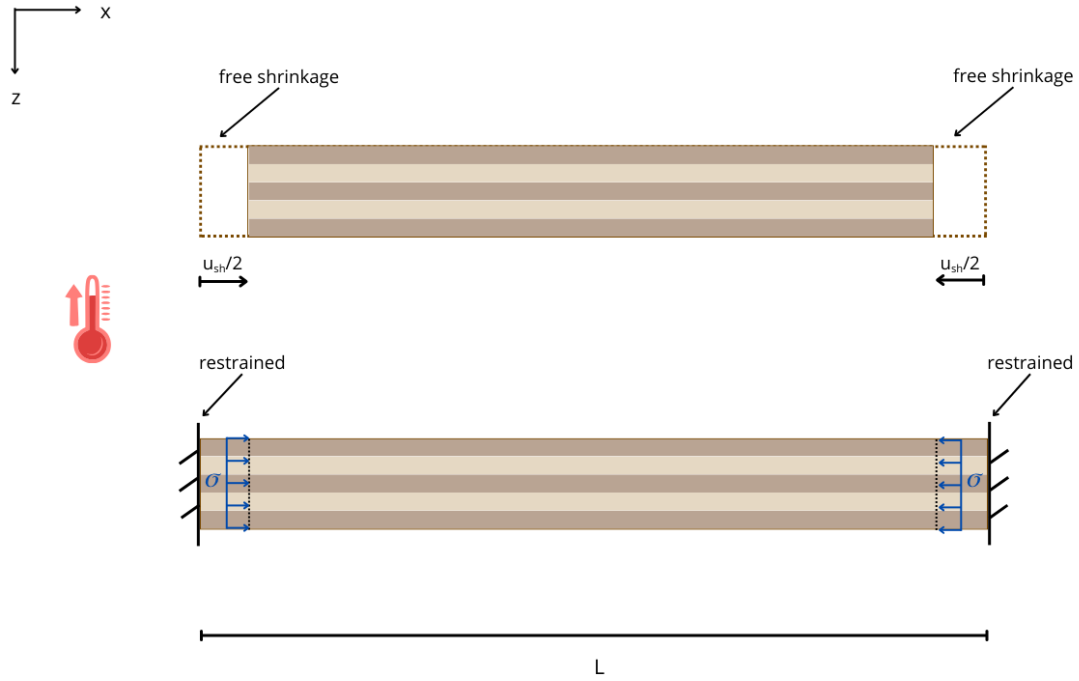

Figure 3.12: Free versus restrained shrinkage of a CLT panel.

To illustrate the basic mechanism, consider the case of *full restraint* and an instantaneous linear-elastic material response. Stress σ (force per unit area) is proportional to the mechanical strain ε_m through the elastic modulus E_{mean} (Young's modulus):

$$\sigma = E_{mean}\, \varepsilon_m. \tag{3.11}$$

The total strain can be written as the sum of mechanical and shrinkage strain,

$$\varepsilon_{total} = \varepsilon_m + \varepsilon_{sh}.$$

Under full restraint, the total strain is zero, so the mechanical strain must counteract the shrinkage strain,

$$\varepsilon_m = -\varepsilon_{sh}. \tag{3.12}$$

Substituting gives

$$\sigma = -E_{mean}\, \varepsilon_{sh}.$$

Timber, however, is not purely elastic. Due to time-dependent processes in the cell wall and the movement of bound water, part of the imposed shrinkage deformation can be accommodated over time. As a result, restrained shrinkage is not necessarily fully converted into stress, and the stress level can decrease even if the deformation remains restrained (*stress relaxation*). To quantify this behaviour for time-dependent shrinkage strains, a viscoelastic framework is introduced in the following sections.

In this part of the thesis, the fully restrained case is used as a reference to quantify how much viscoelastic stress relaxation reduces the maximum shrinkage-induced stress over time. In Part II, this relaxation framework is then used as material input when analysing more realistic, *partly restrained* connection configurations.

3.5.1. Visco-elasticity

As shown in the previous section, restrained shrinkage can convert an imposed shrinkage strain into stress. This simple elastic interpretation, however, is not sufficient for timber. Besides an immediate elastic response, timber shows time-dependent behaviour due to processes in the cell wall and the interaction with bound water. As a result, stresses and deformations evolve with time.

In this thesis, timber is modelled as a *linear viscoelastic* material within the serviceability range. To introduce this concept, the following section first explains the two idealised components that make up viscoelastic behaviour: an elastic response and a viscous response.

Elastic and viscous components

The time-dependent behaviour of timber can be understood by considering two idealised material responses: purely elastic and purely viscous behaviour. These ideal cases form the conceptual basis for viscoelastic modelling.

A linear elastic material responds instantaneously to loading (Figure 3.13). Stress and mechanical strain are related by Hooke's law,

$$\sigma = E_{\text{mean}}\, \varepsilon_{\text{m}}, \tag{3.13}$$

where E_{mean} denotes the short-term (instantaneous) Young's modulus. The deformation is fully recoverable upon unloading. Elastic behaviour therefore represents an immediate, time-independent response.

In contrast, a purely viscous (Newtonian) material exhibits a time-dependent response governed by

$$\dot{\varepsilon}_{\text{m}} = \frac{\sigma}{\eta}, \tag{3.14}$$

where η denotes the viscosity and the dot above a symbol represents a time derivative (rate of change with respect to time). Under constant stress, deformation increases continuously over time and does not recover after unloading (Figure 3.13), reflecting irreversible flow.

Timber does not behave according to either idealisation alone. Instead, its mechanical response combines instantaneous elastic deformation with delayed, time-dependent processes. Viscoelastic models are therefore required to capture both the immediate stiffness and the gradual evolution of deformation and stress.

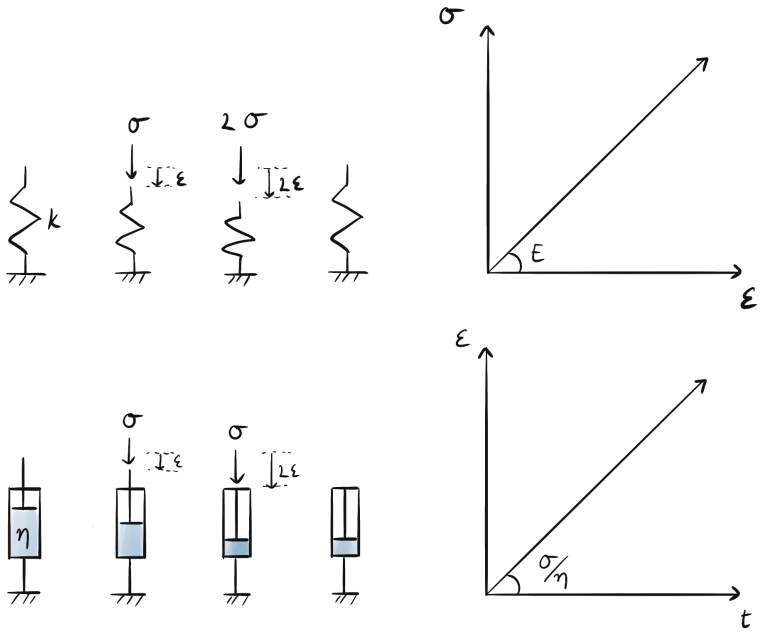

Figure 3.13: Schematised linear elastic material and viscous material.

3.5.2. Stress relaxation

The viscoelastic mechanisms described above become visible under different boundary conditions. Under sustained stress, timber continues to deform over time (*creep*). Under sustained deformation, the internal stress decreases over time (*stress relaxation*). Both responses originate from the same underlying material behaviour.

In the context of restrained shrinkage, shrinkage acts as an imposed deformation. When this deformation is restrained, the total strain is fixed and the material is forced to develop a mechanical strain that generates stress. Due to viscoelastic processes in the cell wall, part of this stress is gradually redistributed, leading to a reduction of stress over time.

Stress relaxation is defined as the decrease of stress under a sustained (imposed) mechanical strain. For the case of a constant imposed strain ε_0, the stress response can be written as

$$\sigma(t) = E(t)\,\varepsilon_0, \tag{3.15}$$

where $E(t)$ is the *relaxation modulus*. This time-dependent modulus represents the effective stiffness governing stress under constant strain. Immediately after imposing the strain, the stress equals $E(0)\varepsilon_0$, where $E(0) = E_{\text{mean}}$ corresponds to the instantaneous elastic modulus. As time progresses, $E(t)$ decreases due to viscoelastic effects, resulting in a gradual reduction of stress (Figure 3.14).

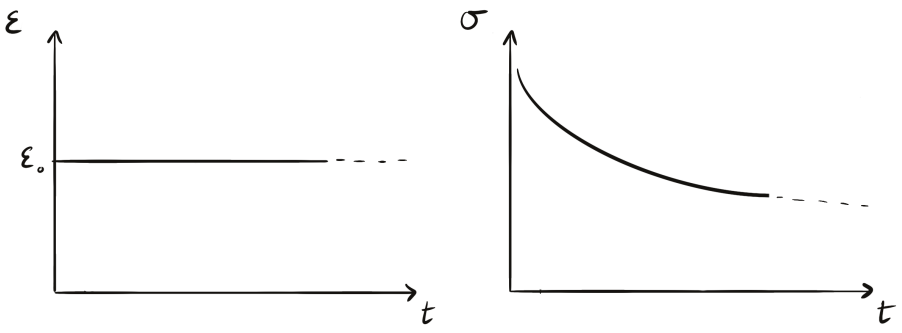

Figure 3.14: Stress relaxation in timber under constant imposed strain.

In design practice, Eurocode 5 (FprEN 1995-1-1:2025) accounts for time-dependent behaviour through the deformation factor k_{def}, which depends on the service class and therefore reflects the moisture environment during use. Typical values are summarised in Table 3.1. Higher service classes correspond to higher average moisture levels and larger moisture fluctuations, which enhance viscoelastic and mechano-sorptive processes in the cell wall. The use of k_{def} is introduced in Eurocode 5 to estimate long-term effects on effective material stiffness.

Accordingly, a practical *final-state* modulus can be defined as

$$E_{\text{fin}} = \frac{E_{\text{mean}}}{1 + k_{\text{def}}}, \tag{3.16}$$

where E_{mean} is the mean elastic modulus and E_{fin} represents the residual stiffness after long-term viscoelastic effects.

The decrease of $E(t)$ does not imply a physical degradation of the material stiffness. It represents a time-dependent effective modulus that governs the stress response under sustained deformation. For short-duration loading, the appropriate instantaneous modulus E_{mean} remains applicable.

Table 3.1: Values of the deformation factor k_{def} for selected timber products (FprEN 1995-1-1:2025).

Material	SC1	SC2	SC3
Structural timber (ST)	0.60	0.80	2.00
Glued laminated timber (GL)	0.60	0.80	2.00
Cross-laminated timber (CLT)	0.80	1.00	–
LVL (parallel veneers)	0.60	0.80	2.00
Plywood (PW)	0.80	1.00	2.50
OSB/3, OSB/4	1.50	2.25	–
Fibreboard, hard (HB)	2.25	3.00	–

It is important to note that E_{fin} represents a simplified end-state approximation and does not describe the rate at which relaxation occurs. In contrast, the relaxation modulus $E(t)$ explicitly describes the time-dependent decay of stress. For moisture-driven shrinkage, the imposed strain does not occur instantaneously: shrinkage increases gradually during the drying process. As a result, stresses accumulate while shrinkage develops, but simultaneously relax due to viscoelastic behaviour.

Capturing this interaction between increasing imposed strain and stress relaxation requires a time-dependent formulation of $E(t)$ rather than a single end-state value. This motivates the use of Maxwell-type viscoelastic models and the Boltzmann superposition principle introduced in the following sections.

3.5.3. Linear relaxation models

The time-dependent behaviour of timber and engineered wood products has been studied in the literature [17, 18, 19, 20, 21]. Experimental and numerical investigations have been performed on solid wood, adhesives and CLT under a wide range of loading conditions, moisture states and time scales. These studies consistently show that creep and stress relaxation are inherent features of timber behaviour, while also demonstrating a strong dependence of the measured response on test conditions and material state.

A common limitation of many experimental studies is the relatively short duration of tests. Creep and relaxation experiments often span minutes to days, whereas structural applications require predictions over months or years. Material models are therefore calibrated using short-term data and extrapolated to longer time scales, which introduces uncertainty. As a result, no single constitutive model has been shown to accurately describe timber behaviour for all materials, loading modes and environmental conditions.

Despite this variability, linear viscoelastic formulations are widely adopted in both research and engineering practice. In this context, *linear* implies that stress is proportional to strain and that the material response is assumed to be independent of load magnitude, provided stress levels remain within the serviceability range.

The principal advantage of linear viscoelastic models is their compatibility with the Boltzmann superposition principle, which allows the response to a complex loading or deformation history to be obtained by summing the contributions of individual strain increments. This property is essential for structural analyses involving time-dependent imposed strains, such as moisture-induced shrinkage. Linear viscoelastic models therefore provide a practical balance between physical realism and analytical transparency.

In the present thesis, linear viscoelasticity is adopted as the governing framework for modelling stress relaxation in CLT. This choice enables a transparent treatment of shrinkage-induced strain histories while remaining consistent with commonly used design-oriented approaches. The Maxwell model and its generalised extensions are introduced in the following section.

Maxwell and generalised maxwell

The idealised spring–dashpot models introduced earlier represent the two fundamental components of viscoelastic behaviour: instantaneous elastic response and time-dependent viscous deformation. Timber exhibits both mechanisms simultaneously, requiring models that combine elastic and viscous elements.

A basic model capable of representing stress relaxation is the *Maxwell model*, consisting of a spring and dashpot connected in series (Figure 3.15a). Since both elements carry the same stress and their strains are additive, the constitutive relationship is given by

$$\dot{\varepsilon} = \frac{\dot{\sigma}}{E} + \frac{\sigma}{\eta}, \tag{3.17}$$

where a dot denotes a time derivative ($\dot{\varepsilon} = \mathrm{d}\varepsilon/\mathrm{d}t$ and $\dot{\sigma} = \mathrm{d}\sigma/\mathrm{d}t$), E is the elastic modulus of the spring and η is the viscosity of the dashpot.

For a constant imposed strain ε_0 (i.e. $\dot{\varepsilon} = 0$), the stress decays exponentially:

$$\sigma(t) = E(t)\,\varepsilon_0, \qquad E(t) = E\,\mathrm{e}^{-t/\tau}, \tag{3.18}$$

with the characteristic relaxation time

$$\tau = \frac{\eta}{E}.$$

Here, $E(t)$ represents the *relaxation modulus*, a time-dependent effective stiffness governing the stress response under sustained deformation.

Although the Maxwell model captures the basic mechanism of stress relaxation, a single exponential decay is insufficient to describe the behaviour of timber. Experimental relaxation curves typically exhibit multiple phases, with an initial rapid stress reduction followed by progressively slower processes. These phases are associated with different viscoelastic mechanisms acting on distinct time scales.

To account for this behaviour, timber is commonly modelled using a *linear generalised Maxwell model*, in which multiple Maxwell elements are connected in parallel (Figure 3.15b). The relaxation modulus is then expressed as

$$E(t) = E_{\mathrm{fin}} + \sum_{i=1}^{N} E_i \mathrm{e}^{-t/\tau_i}, \tag{3.19}$$

where E_i and τ_i denote the modulus and relaxation time of the i-th Maxwell element, respectively. The term E_{fin} represents the long-term effective modulus, corresponding to the residual stiffness after viscoelastic relaxation has taken place.

In this study, the long-term modulus E_{fin} is defined in accordance with Equation 3.16.

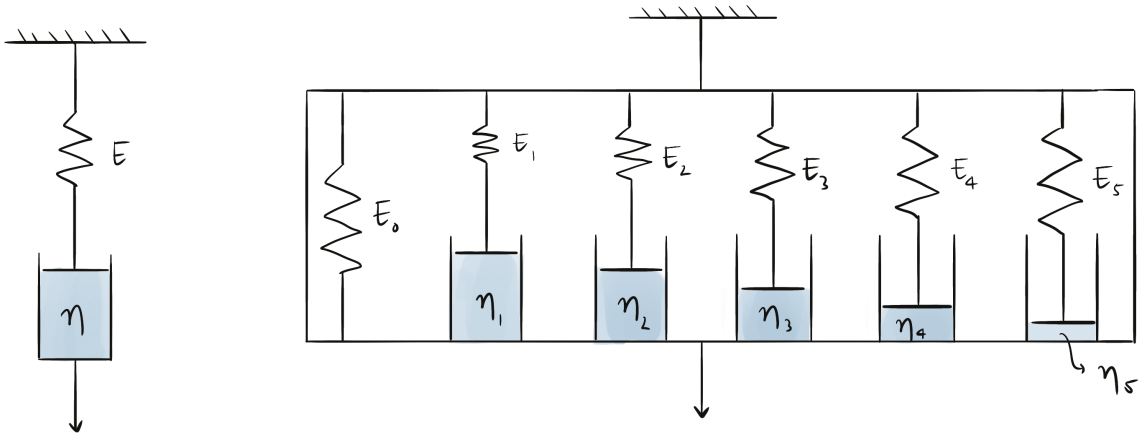

(a) Maxwell model.

(b) Generalised Maxwell model with N = 5.

Figure 3.15: Visualisation of the Maxwell and a generalised Maxwell model.

3.5.4. Boltzman superposition principle

The spring–dashpot models introduced in the previous sections describe the response to idealised loading cases, such as a sudden step in stress or strain. In structural applications, however, deformations rarely occur as instantaneous inputs. Timber elements are subjected to time-dependent deformation due to moisture-induced shrinkage, which evolve continuously over time. Consequently, the stress at any moment depends on the entire history of the imposed strain rather than on a single loading event.

The *Boltzmann superposition principle* provides the framework for modelling such behaviour. It states that the total response of a linear viscoelastic material can be obtained by summing the contributions of all past strain increments, each weighted by the relaxation function that governs how its contribution decays over time.

For stress relaxation problems, where the strain history is prescribed, the stress response is given by

$$\sigma(t) = \int_0^t E(t-s)\,\mathrm{d}\varepsilon_{\mathrm{sh}}(s), \tag{3.20}$$

where $E(t)$ denotes the relaxation function. In this thesis, $E(t)$ is represented using a linear generalised Maxwell model.

This principle is essential for modelling moisture-induced shrinkage in timber. The shrinkage strain $\varepsilon_{\mathrm{sh}}(t)$ develops gradually: it is relatively rapid at early times when moisture transport is high and slows down as the material approaches its equilibrium moisture content.

A key implication of the Boltzmann superposition principle is that relaxation must be applied to individual *strain increments*, not to the total strain. Each incremental increase in shrinkage is treated as a separate loading event, with its own relaxation history. The total stress can therefore be written as

$$\sigma(t) = \sum_{i=1}^{N} E(t-t_i)\,\Delta\varepsilon_{\mathrm{sh}}(t_i) \tag{3.21}$$

where $\Delta\varepsilon_{\mathrm{sh}}(t_i)$ denotes the incremental shrinkage introduced at time t_i.

This procedure is illustrated in Figures 3.16 and 3.17. Figure 3.16 shows the discretisation of the continuously evolving shrinkage strain $\varepsilon_{\mathrm{sh}}(t)$ into a series of small strain increments $\Delta\varepsilon_{\mathrm{sh}}(t_i)$. Each increment represents a separate loading event in the Boltzmann superposition framework.

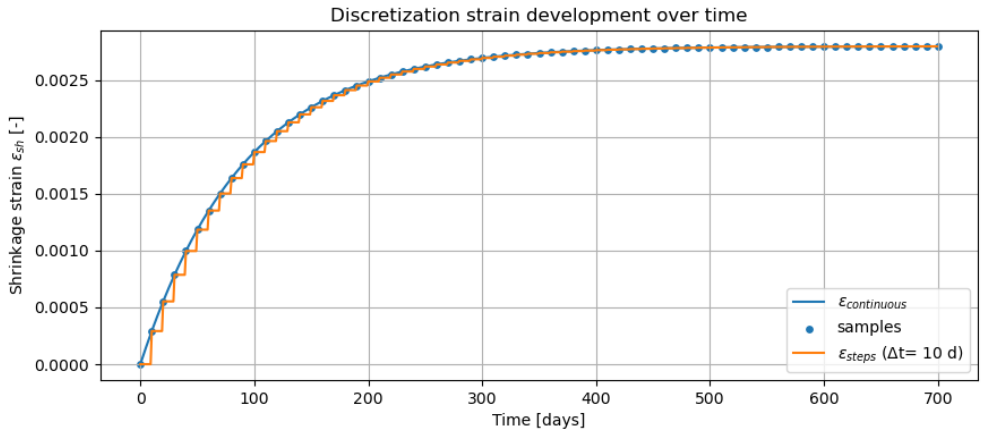

Figure 3.16: Discretisation of the shrinkage strain over time.

Figure 3.17 illustrates the corresponding stress response. Each coloured curve represents the stress contribution generated by a single shrinkage increment, which initially increases and subsequently relaxes over time according to the relaxation modulus. The blue curve shows the total stress, obtained by summing all individual contributions at each time step.

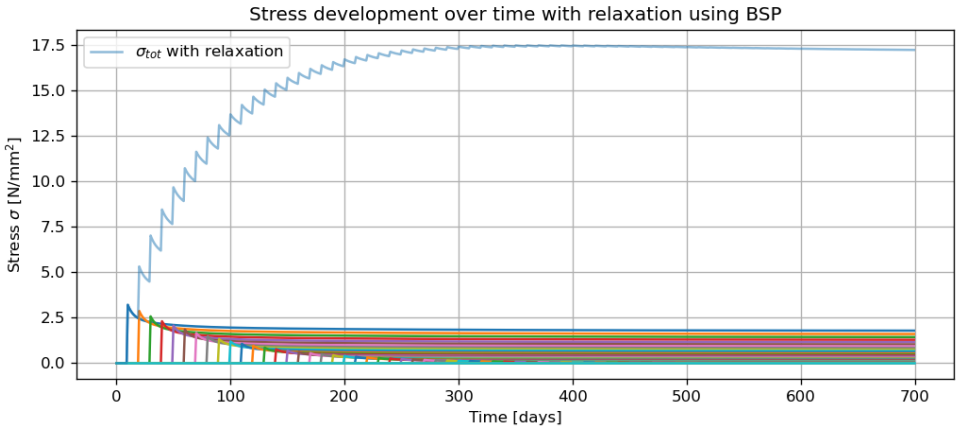

Figure 3.17: Discretisation of stress development over time using BSP.

During the shrinkage phase, stresses accumulate because new strain increments are added before earlier contributions have fully relaxed. After shrinkage has ceased, no new increments are introduced and the total stress gradually converges as the individual contributions continue to relax.

Age coefficient

Within the Boltzmann superposition framework adopted in this thesis, the total stress is obtained by superposing the stress contributions associated with individual strain increments. In the standard linear formulation, the material is assumed to be time-invariant, such that each strain increment relaxes according to the same relaxation modulus $E(\Delta t)$, independent of the time t_i at which the increment occurs.

Timber, however, exhibits *ageing*: as the material becomes older, its ability to creep or relax decreases. Consequently, the relaxation behaviour is not strictly time-invariant, and the relaxation modulus depends not only on the time since the strain increment Δt, but also on the age of the material at the moment of loading t_i.

A similar need to account for ageing arises in the viscoelastic analysis of concrete. In concrete mechanics, ageing effects are commonly incorporated through so-called *age-adjusted* formulations (Trost–Bažant approach), in which an *age-adjusting coefficient* modifies the effective time scale of the viscoelastic response. Wang and Gong [22] describe this concept and introduce an explicit age-adjusting coefficient to account for ageing in viscoelastic modulus formulations.

In the present thesis, this concept is adopted only in a *simplified* form: rather than using a full age-adjusted formulation, ageing is represented by a pragmatic time-scaling factor applied to the relaxation function:

$$a(t_i) = \left(\frac{t_i + t_{\text{ref}}}{t_{\text{ref}}} \right)^m , \tag{3.22}$$

where t_{ref} is a reference time introduced to avoid singular behaviour at $t_i = 0$, and m is an ageing exponent controlling the strength of the effect. The age-dependent relaxation modulus is then evaluated by time-scaling the generalised Maxwell relaxation function:

$$E(\Delta t, t_i) = E\left(\frac{\Delta t}{a(t_i)} \right). \tag{3.23}$$

Here, $\Delta t = t - t_i$ denotes the time elapsed since the strain increment introduced at time t_i.

The influence of ageing on the relaxation behaviour is illustrated in Figure 3.18. The figure shows relaxation curves corresponding to strain increments introduced at different moments in time. As t_i increases, the relaxation curves decay more slowly and remain at higher modulus levels, indicating a reduced relaxation capacity for later strain increments.

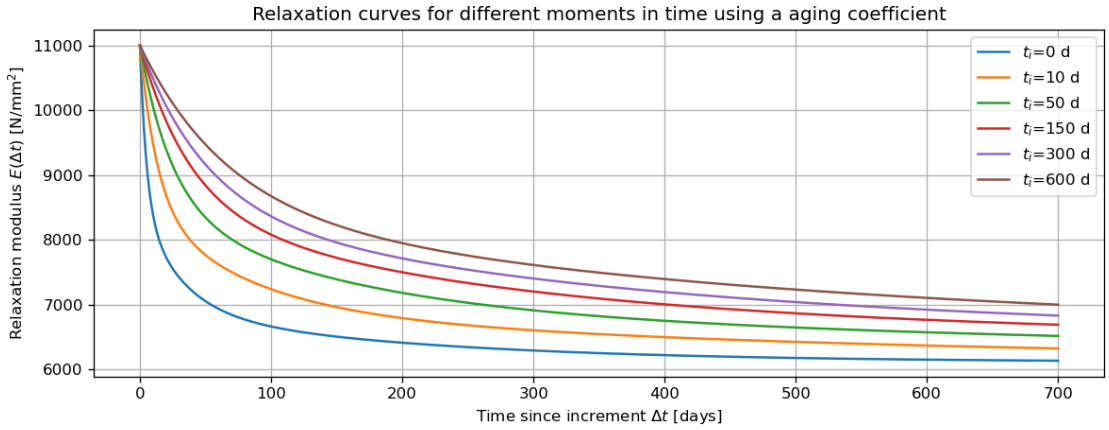

Figure 3.18: Relaxation curves for strain increments introduced at different moments in time, illustrating the effect of material ageing.

For $m = 0$, the ageing factor reduces to $a(t_i) = 1$ and the standard time-invariant formulation is recovered. For $m > 0$, $a(t_i)$ increases with t_i, meaning that later strain increments are evaluated at a smaller effective time increment $\Delta t / a(t_i)$. As a result, these increments relax less and contribute to a higher retained stress level.

4

Results

This chapter presents results for moisture-driven shrinkage and the associated stress development in timber under complete displacement restraint. Under full restraint (Figure 3.12), shrinkage strain development over time is prescribed as $\Delta\varepsilon_{\text{sh}}(t) = \beta \cdot \Delta MC(t)$, and stresses follow from either a purely elastic relation $\sigma(t) = E_{mean}\ \varepsilon_{\text{sh}}(t)$ or with a linear viscoelastic model that accounts for stress relaxation using the Boltzmann superposition principle.

The results are organised as follows. First, the moisture content evolution is evaluated, focusing on the influence of the installation moisture content. Next, the shrinkage coefficient β is established using a layer-based lay-up method for CLT and its influence on restrained stress is quantified. Finally, viscoelastic relaxation is introduced using a generalised Maxwell model, including sensitivity analyses for relaxation times, the interaction between shrinkage rate and relaxation rate, and the potential influence of ageing. The chapter concludes with key observations that inform the subsequent parts of the thesis.

4.1. Moisture content in CLT

In this section, the influence of moisture content on shrinkage-induced stress is analysed. Stress relaxation is not considered, in order to isolate the effects of moisture-related input parameters. Two key variables are examined: the moisture content at installation MC_{inst} and the shrinkage coefficient β.

When analysing the influence of the installation moisture content, the shrinkage coefficient is kept constant at its upper bound given by Eurocode 5, $\beta = 0.0004$.

4.1.1. Influence of installation moisture content

In this analysis, the installation moisture content is varied between MC_{inst} = 9–15%, while the final moisture content is fixed at MC_{fin} = 8%. The moisture content development over time is computed using Equation 3.2, and the corresponding stresses are obtained from the restrained shrinkage relation given in Equation 3.10.

Figure 4.1 shows the moisture content evolution for different values of MC_{inst}. In all cases, the moisture content decreases monotonically and converges towards the final value. Differences between the curves are most pronounced at early times and gradually diminish. After approximately 300 days, all curves are close to MC_{fin} = 8% and remain nearly constant thereafter.

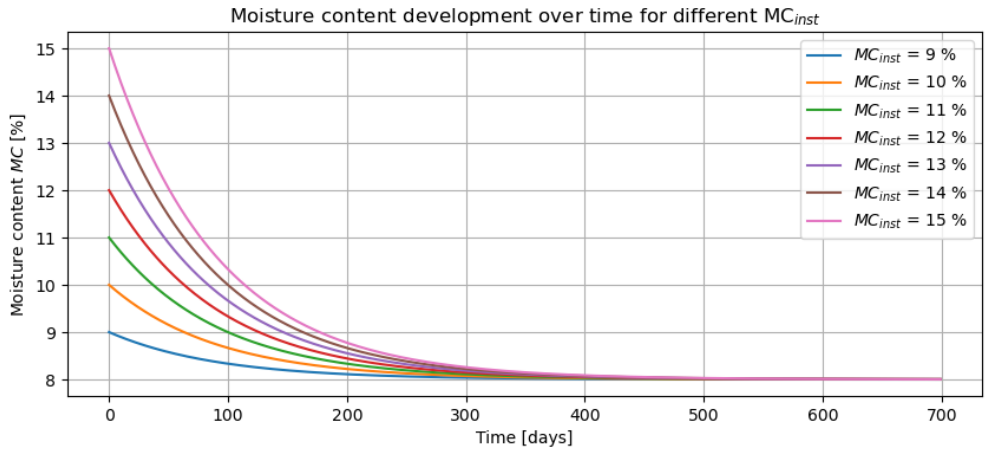

Figure 4.1: Moisture content development over time for different installation moisture contents.

Figure 4.2 presents the corresponding stress development in a fully restrained element. For all installation moisture contents, the stress starts from zero and increases over time towards an asymptotic value. Higher installation moisture contents lead to higher stress levels throughout the entire time range.

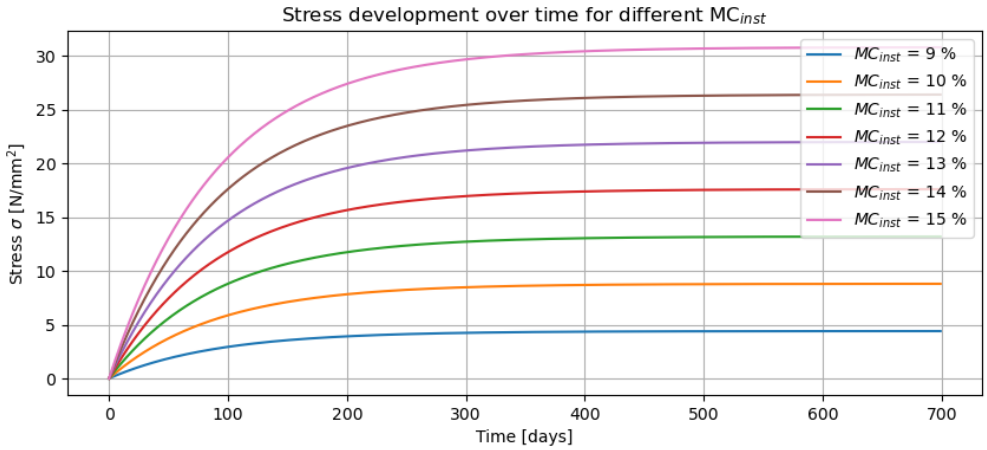

Figure 4.2: Stress development in a fully restrained element for different installation moisture contents.

The maximum stress increases almost linearly with MC_{inst}, as summarised in Table 4.1. The peak stress rises from $\sigma_{\max} = 4.40\,\text{N/mm}^2$ for $MC_{\text{inst}} = 9\%$ to $\sigma_{\max} = 30.79\,\text{N/mm}^2$ for $MC_{\text{inst}} = 15\%$, highlighting the strong sensitivity of restrained shrinkage stress to the moisture condition at installation.

Table 4.1: Maximum absolute stress for different initial moisture contents.

MC_{inst} [%]	$\sigma_{\max}$ [N/mm^2]
9	4.40
10	8.80
11	13.19
12	17.59
13	21.99
14	26.39
15	30.79

4.2. Shrinkage in CLT

In this section, first, the effective panel-level coefficients are derived using a layer-based lay-up method for a representative 5-layer CLT configuration (Section 4.2.1). Second, the influence of the shrinkage coefficient on restrained stress is quantified by comparing the lay-up based coefficients with Eurocode values (Section 4.2.2).

When analysing the influence of the shrinkage coefficient, the installation moisture content is kept constant at $MC_{\text{inst}} = 15\%$ (unfavourable installation condition), while the final moisture content is fixed at $MC_{\text{fin}} = 8\%$. Stress relaxation is not considered.

4.2.1. Layer-based shrinkage model

The layer-based lay-up method (Section 3.4.1) is used to determine effective panel-level shrinkage coefficients for the CLT floor panel in the case-study building (Chapter 2). The panel is modelled as a five-layer lay-up with uniform lamella thickness $T_i = 40$ mm, resulting in a total panel thickness of $T_{\text{CLT}} = 200$ mm. Following the modelling assumption, the effective deforming thickness is taken as $T_{d,i} = T_i$ for the outer lamellas and $T_{d,i} = T_i/2$ for the inner lamellas.

The global panel coordinate system (x, y, z) and the anatomical directions of a single lamella (longitudinal, tangential and radial) are illustrated in Figure 4.3. The longitudinal direction is parallel to the grain, the tangential direction is perpendicular to the grain within the lamella plane, and the radial direction is oriented through the thickness of the lamella. The effective panel-level shrinkage coefficients β_x and β_y result from the combination of these anatomical shrinkage components depending on the fibre orientation of each layer in the lay-up.

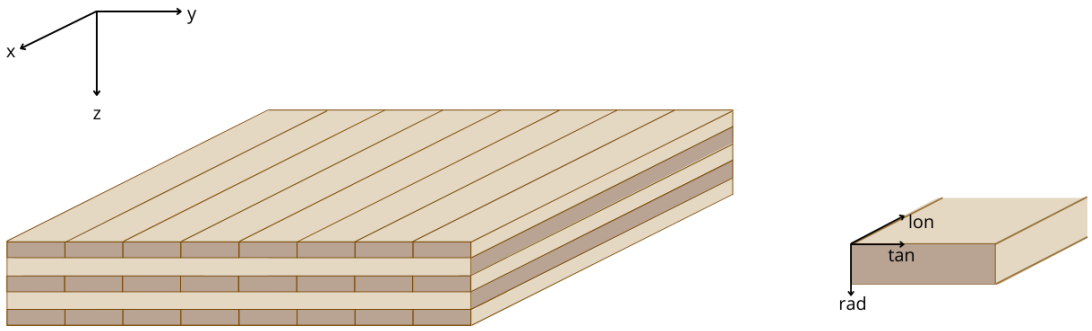

Figure 4.3: Global panel coordinate system (x, y, z) and anatomical directions of a lamella (longitudinal, tangential and radial).

The wood species and strength grading of the lamellas in the case-study panel are not specified. Therefore, lamella-level shrinkage properties are adopted from [16], which reports swelling and shrinkage coefficients measured using digital image correlation (DIC) for commercially common lamella grades of Korean larch (E12, E8) and Korean pine (E10, E6). Where E8 grade defines elastic modulus of lumber between 8GPa and 8.9GPa.

Table 4.2: Lamella-level shrinkage coefficients adopted from [16]. Tangential and radial coefficients are evaluated at $|\Delta MC| = 7\%$.

Lamella type	β_{tan} [-]	β_{rad} [-]	β_{lon} [-]
Larch E12	0.000901	0.000865	−0.000008
Larch E8	0.001491	0.000426	0.000021
Pine E10	0.001077	0.000259	0.000131
Pine E6	0.000950	0.000735	0.000042

The coefficients in Table 4.2 serve as input to the lay-up calculation to obtain effective panel-level coefficients. For each lamella property set (Larch E12, Larch E8, Pine E10 and Pine E6), the layer-based method is applied to the full five-layer configuration, resulting in effective panel-level shrinkage

coefficients in the global panel directions β_x and β_y, which are of interest in this thesis. Finally, representative values β_x and β_y are obtained by averaging the resulting panel-level coefficients across the four lamella property sets.

Table 4.3: Shrinkage coefficients with the lay-up method for different wood species and qualities.

Lamella type	β_x	β_y
Larch E12	0.000272	0.000684
Larch E8	0.000123	0.000300
Pine E10	0.000112	0.000226
Pine E6	0.000084	0.000193
Average	**0.000148**	**0.000351**

Figure 4.4 shows the restrained stress development obtained with the shrinkage coefficients derived from the layer-based lay-up method. For all lamella property sets, the stress increases from zero as shrinkage strain accumulates and converges towards an asymptotic value at long times. Larger effective shrinkage coefficients lead to higher stress levels over the entire time range.

For each lamella property set, the stresses associated with β_y are consistently higher than those corresponding to β_x. This reflects the larger effective shrinkage coefficient in the y-direction, which results from the lay-up: in the y-direction a larger share of layers contributes with tangential (across-grain) shrinkage, whereas in the x-direction a larger share of the deformation is governed by longitudinal (along-grain) shrinkage.

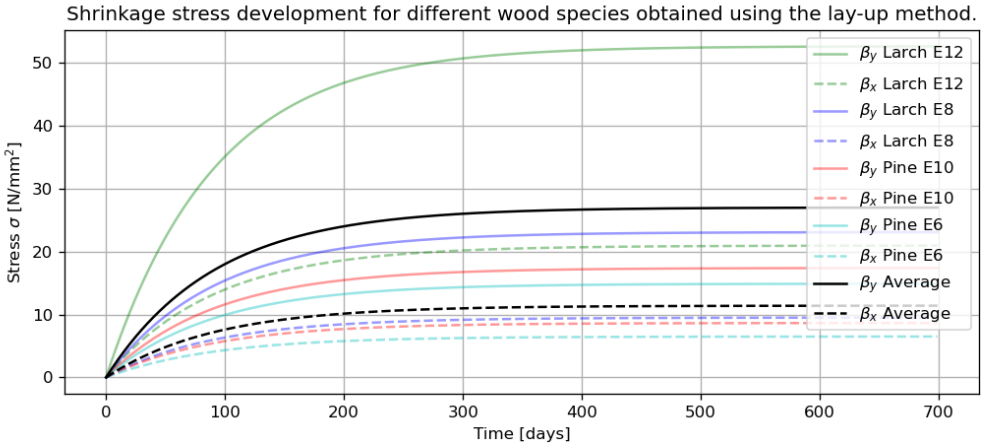

Figure 4.4: Shrinkage stress development for different shrinkage coefficients obtained using the lay-up method.

4.2.2. Influence shrinkage coefficient

This subsection compares restrained stress development obtained with shrinkage coefficients from Eurocode 5 and with the effective coefficients derived from the layer-based lay-up method. The installation moisture content is kept constant at $MC_{\text{inst}} = 15\%$ and stress relaxation is not considered, such that differences in stress response follow directly from the selected β-values.

Table 4.4 summarises the coefficients adopted for both approaches. The lay-up based coefficients are slightly lower than the Eurocode values in both directions.

Table 4.4: Effective in-plane shrinkage coefficients used in the comparison of Eurocode 5 and the layer-based lay-up method.

Method	β_x [-]	β_y [-]
Eurocode 5	0.000200	0.000400
Lay-up method (average)	0.000148	0.000351

Figure 4.5 compares the corresponding restrained stress development. For both approaches, the stress evolution follows the same temporal trend because the moisture history is identical; however, the stress magnitude is governed by the selected shrinkage coefficient. As expected, the Eurocode coefficients lead to higher predicted stresses, while the lay-up based coefficients show lower stress levels throughout the time range.

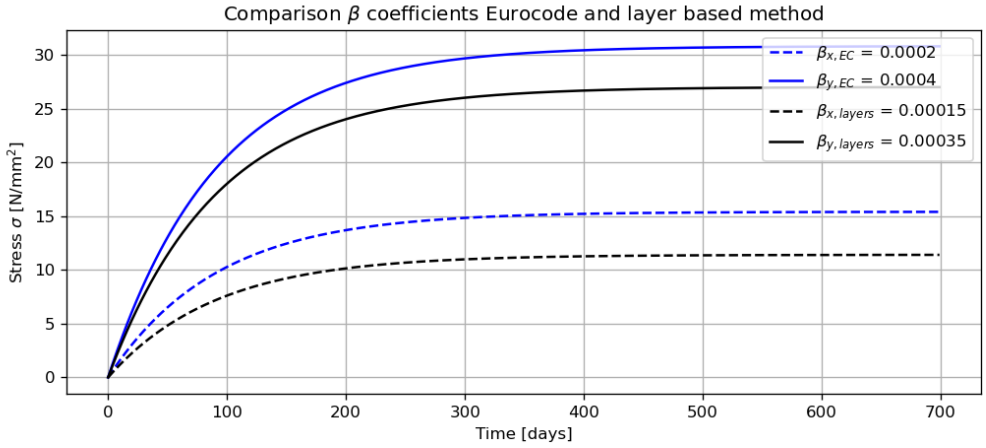

Figure 4.5: Comparison of restrained shrinkage stress development for Eurocode 5 coefficients and the average coefficients from the layer-based lay-up method.

The resulting maximum stresses are summarised in Table 4.5. In the x-direction, using the lay-up based coefficient reduces the peak stress from 15.39 N/mm^2 to 11.40 N/mm^2. In the y-direction, the peak stress reduces from 30.79 N/mm^2 (Eurocode) to 26.99 N/mm^2 (lay-up). This confirms that the choice of shrinkage coefficient has a direct and significant influence on the predicted restrained stresses.

Table 4.5: Maximum absolute stress for shrinkage coefficients obtained from Eurocode 5 and from the average values of the layer-based lay-up method.

Method	Direction	β [-]	$\sigma_{\max}$ [N/mm^2]
Lay-up (average)	x	0.000148	11.40
Lay-up (average)	y	0.000351	26.99
Eurocode 5	x	0.000200	15.39
Eurocode 5	y	0.000400	30.79

4.3. Stress relaxation in CLT

To account for stress relaxation, timber is modelled as a linear viscoelastic material using a generalised Maxwell model (Section 3.5.3). The stress response under time-varying shrinkage strain is evaluated using the Boltzmann superposition principle, such that the contribution of successive shrinkage strain increments is accumulated over time.

Given the variability in viscoelastic material models reported in the literature and the absence of models calibrated for the present moisture-driven loading conditions, a simplified yet representative model is adopted. A generalised Maxwell model with $N = 3$ Maxwell elements is selected, providing a balance between model complexity and interpretability. The relaxation times are chosen to represent fast, intermediate and slow processes in wood: $\tau_1 = 5$ days, $\tau_2 = 30$ days and $\tau_3 = 200$ days. The influence of this choice is assessed through a sensitivity analysis in Section 4.3.2.

4.3.1. Effect of relaxation on restrained stress development

Figure 4.6 compares restrained stress development with and without viscoelastic relaxation for $\beta = 0.0004$ and $MC_{\text{inst}} = 15\%$.

In both cases, stress increases from zero as shrinkage strain develops over time. Without relaxation, stress continues to build up and converges towards a high asymptotic value governed by the elastic modulus. When viscoelastic behaviour is included through the Boltzmann superposition principle, the initial trend is similar, but the response approaches a substantially lower long-term stress level.

The difference between both responses becomes more pronounced with increasing time. While the purely elastic response retains the full stress induced during shrinkage, the viscoelastic response converges towards a value governed by the equilibrium modulus E_{fin} of the generalised Maxwell model. This illustrates the potential reduction in restrained shrinkage stress due to stress relaxation.

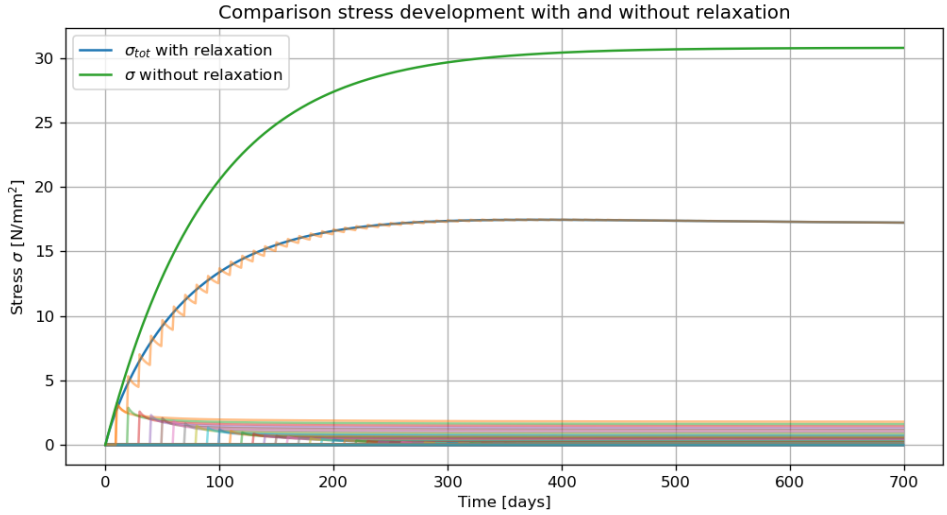

Figure 4.6: Restrained stress development with and without relaxation.

4.3.2. Sensitivity to relaxation times

To assess sensitivity to the assumed relaxation spectrum, the stress response is evaluated for modified sets of relaxation times in which all τ_i are taken twice as fast and twice as slow compared to the base case. The equilibrium modulus E_{fin} is kept constant.

Figure 4.7 compares the resulting stress development. Varying the relaxation times mainly affects the transient response: faster relaxation leads to a more gradual stress build-up and lower intermediate stress levels, whereas slower relaxation results in a stiffer early-time response and slightly higher transient stresses.

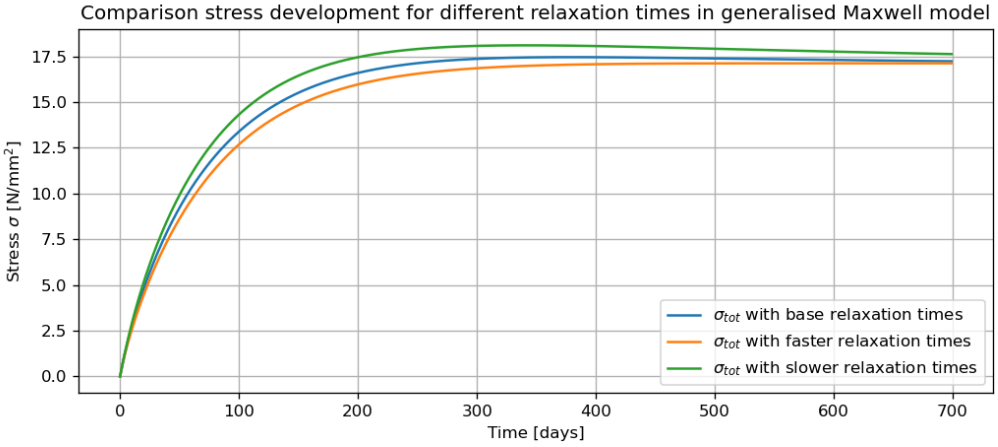

Figure 4.7: Influence of the assumed relaxation times in the generalised Maxwell model.

Despite differences during the early and intermediate stages, all curves converge towards the same long-term stress level. This demonstrates that, as long as an equilibrium modulus is present, the restrained stress at long times is governed by E_{fin} and is relatively insensitive to the precise choice of relaxation times. The relaxation times therefore primarily influence the transient evolution rather than the final stress level.

4.3.3. Shrinkage rate versus relaxation rate

The interaction between the rate of shrinkage development and the rate of viscoelastic relaxation is examined by comparing the base-case moisture evolution with an artificially accelerated shrinkage process. When shrinkage develops rapidly, large increments of shrinkage strain are imposed over short time intervals, leaving limited time for relaxation before additional shrinkage occurs.

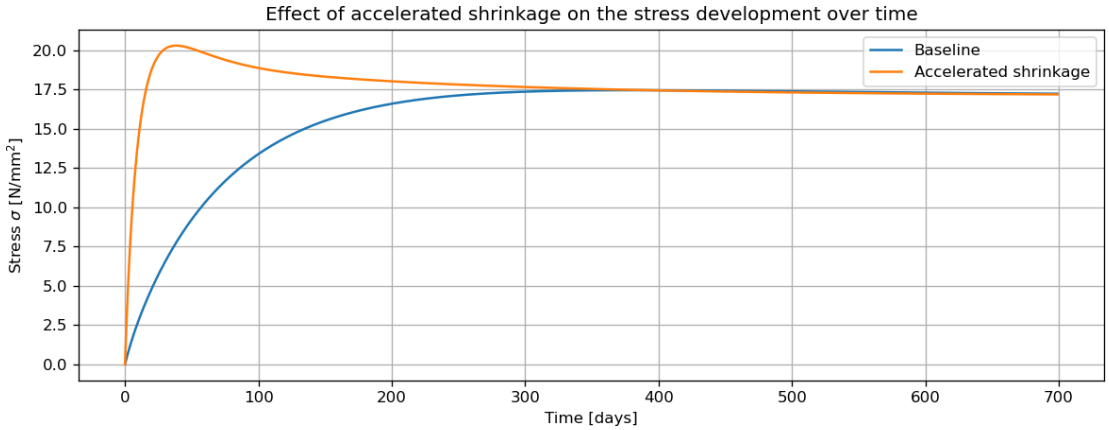

Figure 4.8: Restrained stress development for gradual (base) versus accelerated shrinkage.

Figure 4.8 shows that accelerated shrinkage produces a pronounced transient stress peak, caused by the accumulation of shrinkage strain before significant viscoelastic relaxation can take place. After shrinkage has largely completed, relaxation progressively reduces the stress towards the long-term level governed by E_{fin}.

The accelerated case does not represent realistic timber behaviour; in practice, moisture-driven shrinkage is governed by diffusion and environmental equilibration and develops gradually over extended periods. The accelerated case is therefore included as a conceptual scenario to demonstrate that transient peaks may occur when deformation develops faster than relaxation. For realistic shrinkage rates, the response is expected to evolve more smoothly, with limited overshoot and a closer correspondence between peak and long-term stress. This supports the use of E_{fin} for estimating long-term restrained shrinkage stresses when shrinkage develops gradually.

4.3.4. Influence of ageing

As discussed in Section 3.5.4, the age of timber affects its capacity to relax. This effect can be approximated by introducing an age coefficient that reduces the relaxation capacity of strain increments occurring at later ages.

Figure 4.9 compares stress development without ageing ($m = 0$) and with increasing ageing effects ($m = 0.25$ and $m = 0.4$). With increasing m, higher stress levels are observed both during the transient phase and at long times.

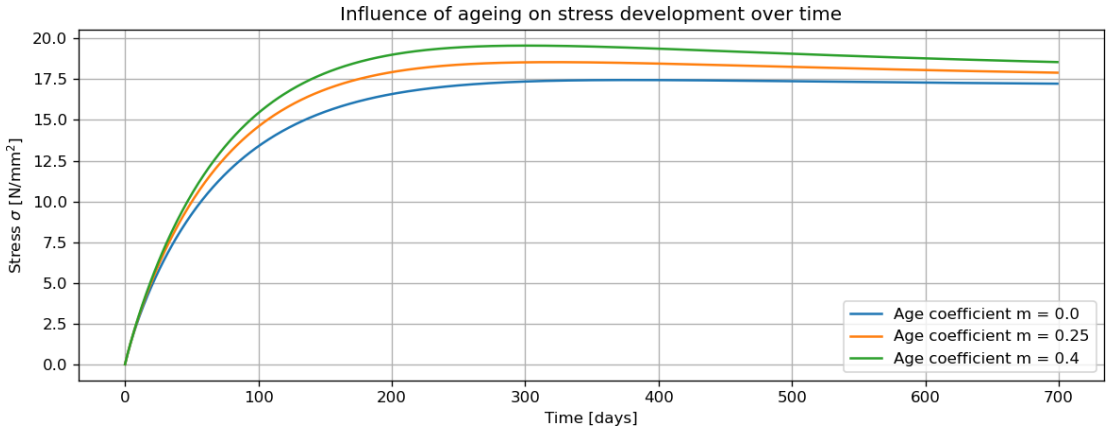

Figure 4.9: Influence of an age coefficient on restrained stress development.

This behaviour follows from the interaction between shrinkage strain development and relaxation. Each incremental increase in shrinkage strain $\Delta\varepsilon_{sh}$ generates an immediate stress contribution governed by the relaxation modulus. When ageing is included, strain increments occurring later experience reduced relaxation, such that a larger portion of the stress generated during the shrinkage phase is retained. Consequently, both the transient response and the retained long-term stress increase, and the final stress exceeds the value predicted using the equilibrium modulus E_{fin} without ageing.

4.4. Key observations

The following observations are drawn from the analysis of moisture-driven restrained shrinkage in timber under complete displacement restraint:

- Restrained shrinkage stresses are strongly governed by hygroscopic input parameters. In particular, higher installation moisture contents MC_{inst} and larger shrinkage coefficients β directly lead to higher predicted stress levels.
- The selection of β has a significant influence on the predicted stresses. Eurocode-based coefficients show higher stresses than the effective coefficients obtained with the layer-based lay-up method for the considered CLT configuration.
- Including viscoelasticity through a linear generalised Maxwell model and the Boltzmann superposition principle results in a substantial reduction of long-term restrained stresses compared to purely elastic predictions.
- For long-term conditions, the retained stress level is governed by the equilibrium modulus E_{fin} of the Maxwell model. In the present formulation, the long-term stress scales with E_{fin}/E_{mean}.
- The relaxation times mainly influence the transient stress evolution. Provided that an equilibrium modulus is present, the final stress level is largely insensitive to the precise relaxation parameters.
- A mismatch between shrinkage rate and relaxation rate can generate transient stress peaks. For realistic diffusion-controlled moisture evolution, the response is smoother and the peak stress approaches the long-term level.
- Ageing reduces the relaxation capacity of strain increments occurring at later times, increasing both transient and retained stresses. However, the effect depends on uncertain ageing parameters. Therefore, ageing is not included in the subsequent analyses.

Based on these results, E_{fin} is adopted in the subsequent chapters to represent long-term behaviour when estimating shrinkage-induced forces in structural systems with compliant connections. This choice provides a consistent and physically motivated basis for long-term assessment while avoiding undue sensitivity to uncertain transient modelling assumptions.

Part II

Shrinkage-induced forces in CLT connections

5

Shrinkage-induced forces in CLT connections

Connections are essential elements in a building structure. They join members into a coherent load-bearing system by providing force transfer, alignment and continuity between structural components. Their stiffness and strength influence how loads are distributed, how much relative deformation can occur between members, and how the global structural response develops.

Unless stated otherwise, the background information, stiffness formulations and resistance models presented in this chapter are based on the draft version of the new Eurocode 5 (FprEN 1995-1-1:2025).

This chapter describes the connection types in the case study and establishes representative stiffness and resistance values for later modelling. Connection stiffness is introduced using the load–slip concept, and screw resistance is evaluated using the European Yield Model. The resulting parameters are then used in simplified restraint models to quantify shrinkage-induced forces for the considered support configurations.

5.1. Connection types

Figure 5.1 shows the floor plan of the case study considered in this thesis. The case-study building is described in Chapter 2. The connection types relevant to this thesis are indicated in the plan. Typical connection details are presented in Figure 5.2, while additional screw characteristics are provided in Appendix B. The connection types are described below.

Type 1: Panel-to-core connections
Panel-to-core connections transfer diaphragm forces from the CLT floor into the concrete core, which provides the global lateral stability of the building. In the case study, the connection consists of a steel angle bracket anchored to the concrete wall and connected to the CLT panel by self-drilling wood screws.

Two variants are considered:

- **Type 1a:** screwed steel angle connection without grout,
- **Type 1b:** screwed steel angle connection with grout at the interface.

Both variants provide the same global function, but the load-transfer mechanism differs. For the ungrouted detail, forces are transferred mainly through slip in the fasteners. When grout is applied, load transfer may additionally occur through compression and shear contact once the interface is closed, which can increase the effective stiffness after contact is established.

Type 2: Panel-to-panel connections
Panel-to-panel connections provide continuity between adjacent CLT panels and enable diaphragm action by transferring in-plane shear across panel joints. In the case study, a half-lap joint combined with self-drilling wood screws is used at the panel interface.

Types 3–4: Panel-to-beam connections
Types 3 and 4 denote the fastening details between the CLT panels and the supporting glulam beams. They are included as boundary conditions that may provide translational restraint in the floor plane.

Two support situations are distinguished:

- **Type 3:** two adjacent floor panels on the same beam (green zones in Figure 5.1),
- **Type 4:** edge beam supporting a single panel (pink zones in Figure 5.1).

In addition to Types 3–4, the CLT panels are also fastened to the intermediate glulam beams within the panel span. In the RFEM case-study model, these intermediate panel-to-beam fasteners are not explicity modelled. Such that RFEM idealises these connections as fully tied connections. As a result, no relative in-plane slip can occur between panel and beam at these locations, i.e. the beams are assumed to follow the same in-plane displacements as the floor panels. This modelling simplification is adopted to reduce model complexity.

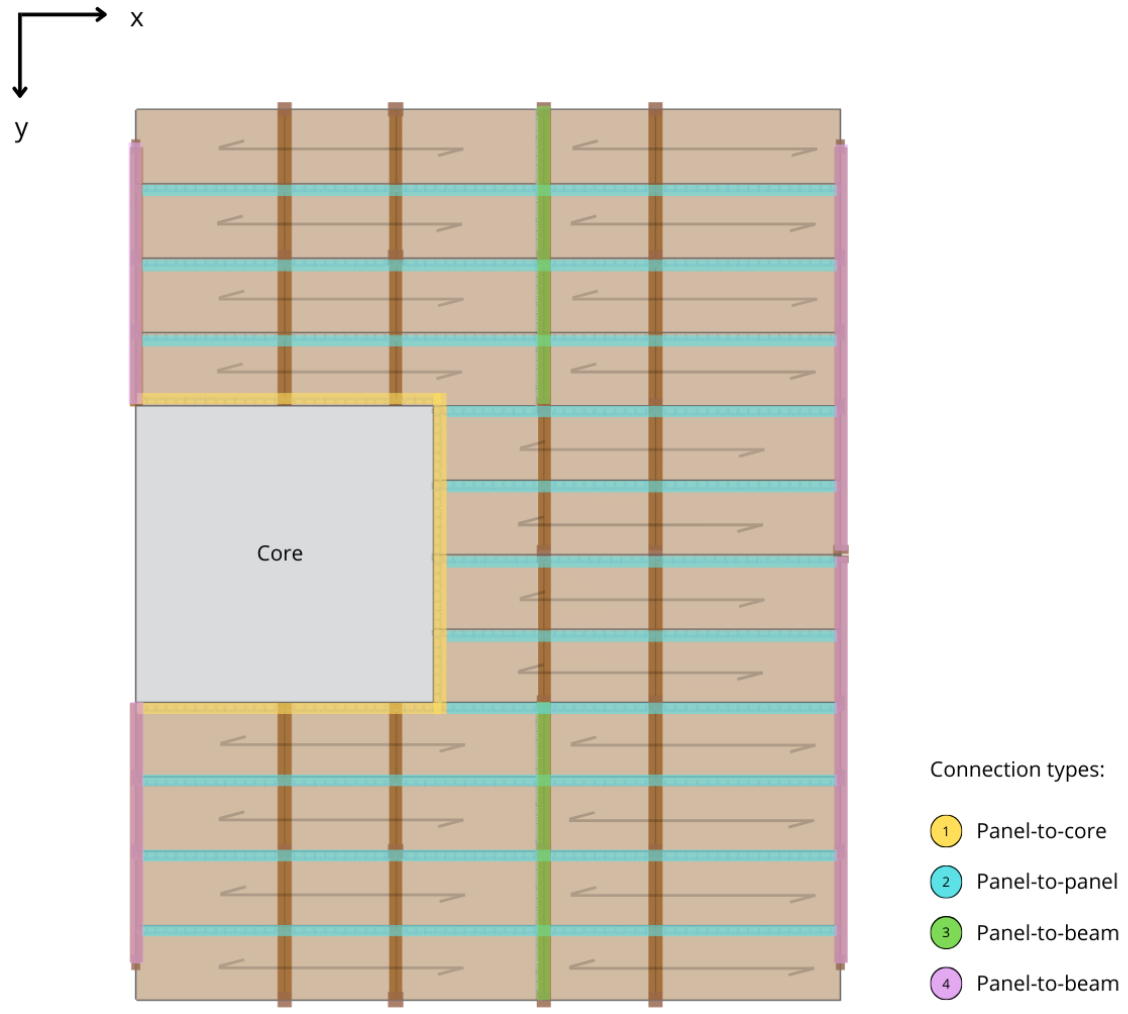

Figure 5.1: Floor plan with demarcation of the connection types considered in the case study.

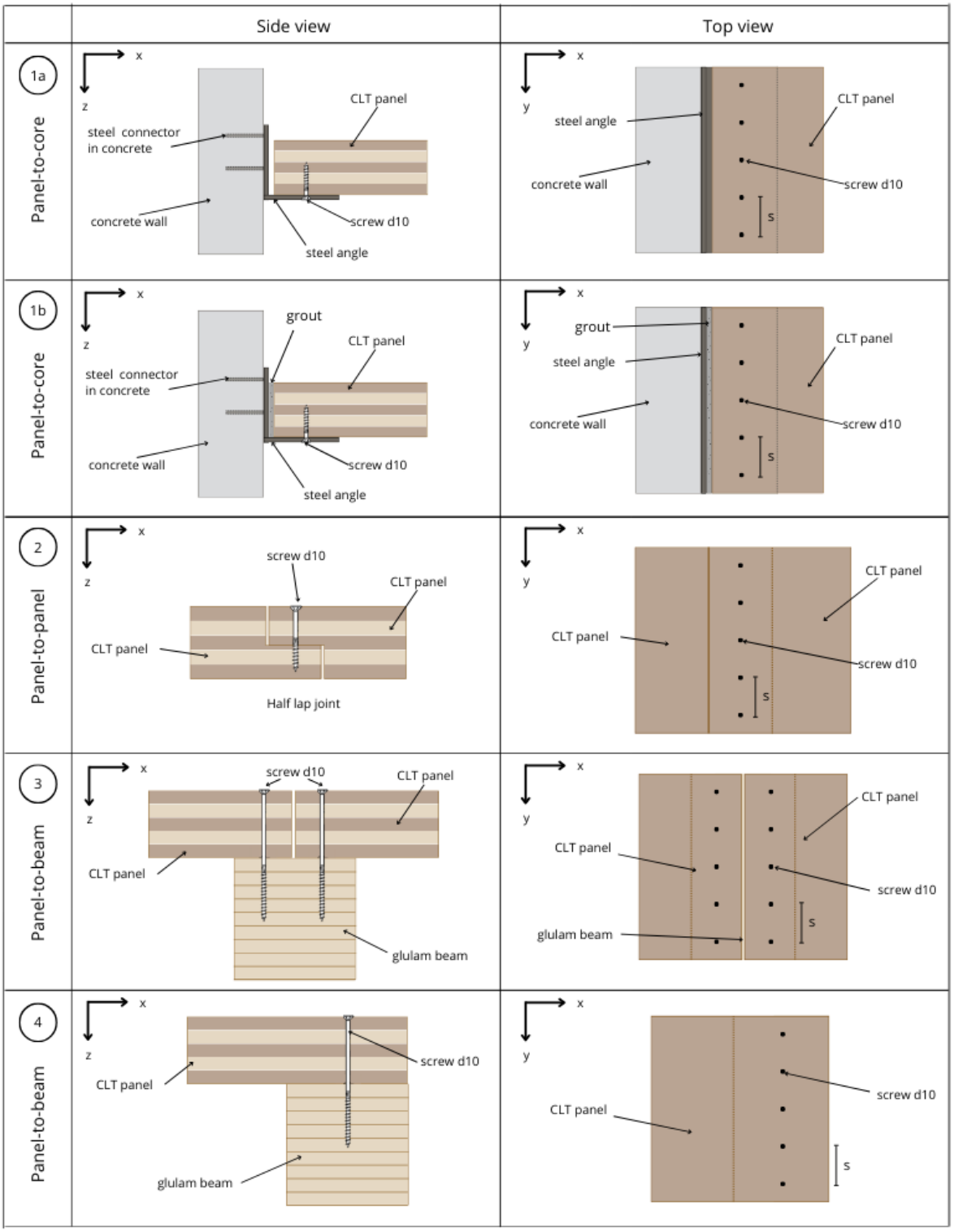

Figure 5.2: Side and top view of connection details used in the case study.

5.2. Stiffness of connections

This section defines representative connection stiffness values for use in the analytical and numerical models presented later in this thesis.

5.2.1. Combined stiffness components

Connection stiffness can be evaluated using a *component method*, in which the total slip is decomposed into the deformation of individual connection components. Each component is idealised as a linear spring, and the total stiffness follows from a series arrangement:

$$\frac{1}{K_{\text{tot}}} = \frac{1}{K_{\text{CLT}}} + \frac{1}{K_{\text{screws}}} + \frac{1}{K_{\text{plate}}} + \frac{1}{K_{\text{anchors}}}. \tag{5.1}$$

Feng et al. [23] applied this approach to CLT wall-to-foundation connections (hold-downs and angle brackets) strengthened with self-tapping screws. Their model accounted for deformation of the CLT, slip and rotation of the screw group, deformation of the steel plate, and deformation of the anchor bolts. They demonstrated that, when the steel plate and anchorage are sufficiently stiff, the overall connection slip is governed by the deformation of the screw group.

Based on these findings, this thesis focuses on the stiffness of the screwed connection as the governing component for the floor–to–core restraint behaviour. Other sub-components are assumed sufficiently stiff and are therefore not analysed.

5.2.2. Slip behaviour

The mechanical response of a timber connection is characterised by its load–slip relationship, the relation between the applied force F and the relative slip u between the connected members.

The load–slip behaviour of dowel-type connections is inherently non-linear. At low load levels, relatively large deformations may occur due to initial slip, for example caused by tolerances or hole clearance. With increasing load, the response becomes approximately linear over an intermediate range, after which the stiffness gradually decreases as plastic deformation develops in the fastener and the surrounding timber.

As a result, the stiffness of a connection is not a unique material property, but depends on the load level at which it is evaluated. In this context, a distinction can be made between the *tangential stiffness*, which is the local slope of the load–slip curve at a given point, and the *secant stiffness*, which is the average slope between two load levels. In Eurocode 5, the serviceability stiffness is represented by the slip modulus K_{SLS} (often denoted K_{ser}), which is taken as a secant stiffness in the serviceability range, typically between $0.1F_{\text{max}}$ and $0.4F_{\text{max}}$. Within this range, the behaviour may be approximated as linear for design purposes.

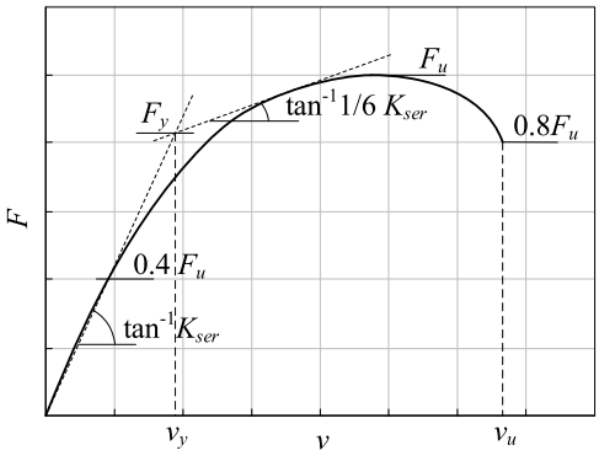

Figure 5.3: Schematic load–deformation curve illustrating the definition of the ductility factor D_s and stiffness K_{ser} [24].

In addition to stiffness, the deformation capacity of the connection is of importance. This is commonly expressed by the ductility factor D_s, defined as the ratio between the ultimate slip u_u and the slip at the start of yielding u_y:

$$D_s = \frac{u_u}{u_y} \tag{5.2}$$

As illustrated in Figure 5.3, ductile connections are able to undergo significant additional deformation beyond the initial elastic range without a proportional increase in force. For dowel-type fasteners, this behaviour is typically associated with plastic hinge formation in the fastener. The existence of such post-yield deformation capacity is particularly relevant for displacement-driven problems, since imposed deformations do not necessarily lead directly to connection failure once the elastic range is exceeded.

5.2.3. Lateral slip modulus of a screw

In this thesis, the lateral slip modulus of a screw is determined using the formulation adopted in Eurocode 5 (FprEN 1995-1-1:2025). The serviceability-level lateral slip modulus per fastener per shear plane is given by:

$$K_{\mathrm{SLS},v,i} = 60\, d_1^{1.7} \left(\frac{\rho_{\mathrm{mean}}}{420}\right)^{1.1}, \tag{5.3}$$

where d_1 is the inner thread diameter of the screw and ρ_{mean} is the mean density of the timber in kg/m^3. The expression shows that the slip stiffness increases with both timber density and screw diameter.

For **steel-to-timber** and **concrete-to-timber** connections, where the fastener is clamped against a rigid non-timber member, Eurocode 5 recommends doubling the lateral slip modulus:

$$K^{\mathrm{st}}_{\mathrm{SLS},v,i} = 2\, K_{\mathrm{SLS},v,i}. \tag{5.4}$$

For **timber-to-timber** connections, the lateral slip modulus depends on the properties of both timber members. An effective mean density is therefore adopted:

$$\rho_{\mathrm{mean}} = \sqrt{\rho_1\, \rho_2}, \tag{5.5}$$

where ρ_1 and ρ_2 are the mean densities of the connected timber members. This definition reflects the contribution of both members to the embedment deformation governing the slip behaviour.

Smeared stiffness

The *smeared stiffness* k is defined as the stiffness per unit length and is obtained by dividing the slip modulus of a single fastener by the fastener spacing s:

$$k = \frac{K}{s}. \tag{5.6}$$

5.3. Resistance of connections

This section describes the ultimate load-carrying behaviour of the connection types considered in this thesis, focusing on laterally loaded self-drilling screws. For timber-to-timber joints, the resistance models follow FprEN 1995-1-1:2025 [9], whereas for steel-to-timber joints EN 1995-1-1 [25] is adopted, since steel-to-timber joint provisions are not explicitly provided in the draft. For clarity, the present section discusses the underlying failure mechanisms only. The corresponding resistance expressions, together with the adopted connection geometries and screw properties, are provided in Appendix B.

5.3.1. Failure mechanisms of steel-to-timber joints

In steel-to-timber joints, lateral forces are transferred through embedment deformation of the timber member and bending of the screw. Depending on the thickness of the steel plate, different idealised failure mechanisms may govern the ultimate resistance.

For thin steel plates, failure is typically governed by embedment of the timber, with limited or no plastic deformation of the fastener. For thick steel plates, more ductile mechanisms may develop, characterised by one or more plastic hinges in the screw. In these cases, axial tension in the screw may contribute to the lateral resistance through the rope effect.

The failure mechanisms considered are illustrated in Figure 5.4. Each failure mode is associated with a specific resistance expression. The characteristic lateral resistance of the connection is obtained as the minimum resistance over all relevant failure modes.

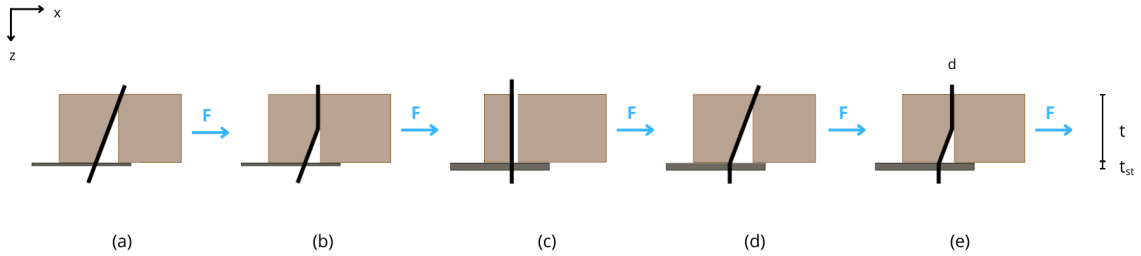

Figure 5.4: Failure mechanisms for a steel-to-timber joint loaded in shear.

The failure modes shown in Figure 5.4 represent the following physical mechanisms:

(a) Timber embedment failure with a thin steel plate, without plastic hinging of the fastener.

(b) Timber embedment failure combined with plastic hinging of the fastener for a thin steel plate.

(c) Timber embedment failure with a thick steel plate, without plastic hinging of the fastener.

(d) Timber embedment failure combined with a single plastic hinge in the fastener for a thick steel plate.

(e) Fully ductile failure with plastic deformation of the fastener for a thick steel plate, characterised by two plastic hinges.

5.3.2. Failure mechanisms of timber-to-timber joints

In timber-to-timber joints, lateral forces are transferred through embedment deformation of both timber members and bending of the screw. The governing failure mechanism depends on the relative embedment strengths and thicknesses of the connected members.

For single-shear connections, failure may occur through embedment of either timber member, through combined embedment and plastic hinging of the fastener, or through fully ductile plastic hinging of the screw.

The failure mechanisms considered are illustrated in Figure 5.5. As for steel-to-timber joints, each failure mode corresponds to a specific resistance expression. The characteristic lateral resistance of the connection is obtained as the minimum resistance over all applicable failure modes.

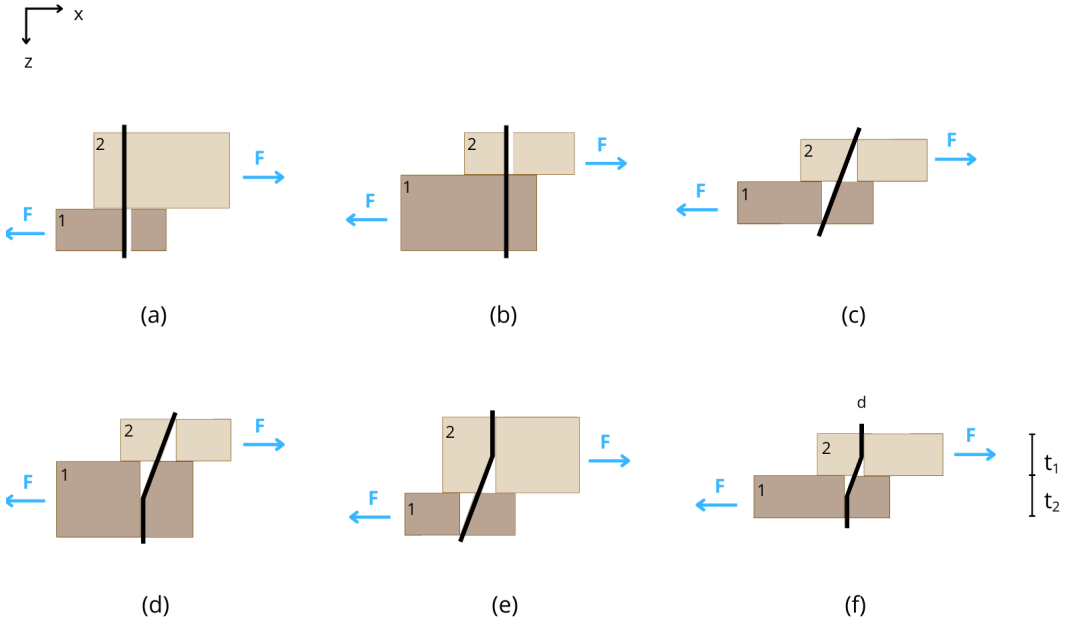

Figure 5.5: Failure mechanisms for a timber-to-timber joint loaded in single shear.

The failure modes shown in Figure 5.5 represent the following physical mechanisms:

(a) Embedment failure in member 1, without plastic hinging of the fastener.

(b) Embedment failure in member 2, without plastic hinging of the fastener.

(c) Embedment failure in member 1 and 2 without plastic hinging of the fastener.

(d) Embedment failure in member 2 combined with plastic hinging of the fastener and embedment deformation in member 1.

(e) Embedment failure in member 1 combined with plastic hinging of the fastener and embedment deformation in member 2.

(f) Fully ductile failure with plastic deformation of the fastener, characterised by two plastic hinges.

The expressions given in Appendix B provide the *characteristic* lateral resistance $F_{v,Rk}$ per fastener per shear plane. The design lateral resistance per fastener per shear plane is:

$$F_{v,Rd} = \frac{k_{\text{mod}}}{\gamma_M} F_{v,Rk}. \tag{5.7}$$

For CLT connections under permanent (shrinkage) loading, $k_{\text{mod}} = 0.6$ and $\gamma_M = 1.3$, resulting in:

$$F_{v,Rd} \approx 0.46\, F_{v,Rk}. \tag{5.8}$$

The design resistance $F_{v,Rd}$ is used for ultimate limit state verification.

5.4. Shrinkage induced restraint forces

Moisture-driven shrinkage causes a CLT floor panel to shorten in its plane. In Part I, this mechanism was studied in its most extreme form: a fully restrained member, where shrinkage strain is directly converted into axial stress. Real buildings, however, are rarely *fully* restrained. The detailing of floor panel connections provides a *finite* restraint stiffness.

Figure 5.6 recalls the basic principle. Under free shrinkage, the panel would contract by a total amount u_{sh}. If this contraction is partially or fully restrained, an axial normal force N develops in the panel, accompanied by reaction forces R in the restraints. In this chapter, the focus therefore shifts from stress (σ) to force resultants: the normal force in the panel (N) and the associated support reactions (R), which are directly relevant for connection design and detailing.

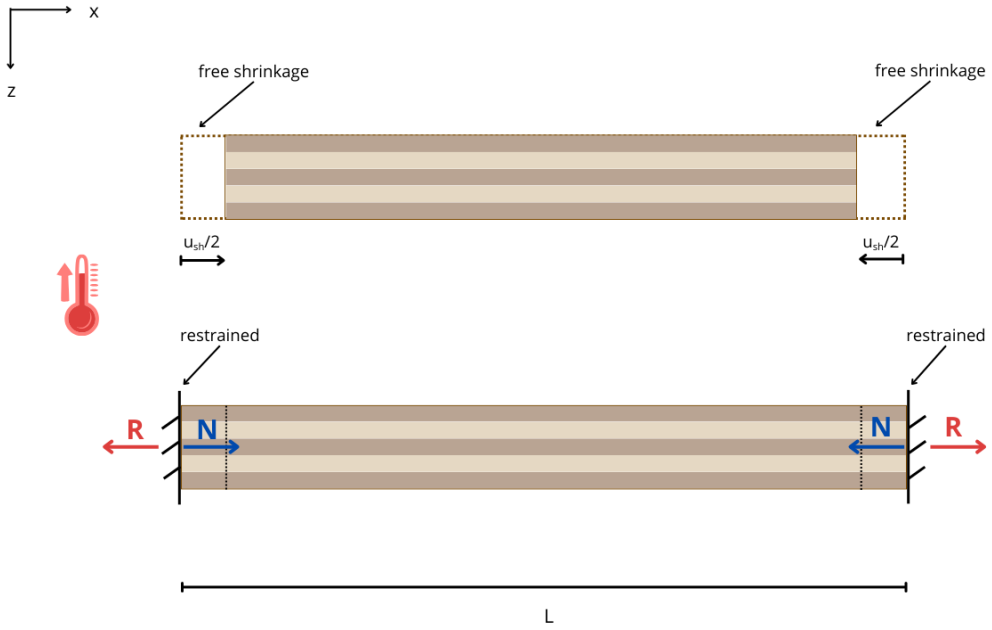

Figure 5.6: Principle of shrinkage restraint.

In the following, shrinkage-induced restraint forces are analysed using simplified one-dimensional beam–spring models. First, the material and shrinkage parameters used in the formulations are defined. Subsequently, four restraint situations are considered in increasing order of structural complexity, representing connection scenarios in hybrid core–frame buildings. Appendix C shows the analytical derevations of the formulas and Appendix D presents a numerical verification for each situation from RFEM.

5.4.1. Long-term stiffness

The development of shrinkage-induced restraint forces depends on the axial stiffness of the panel, the stiffness of the connections, and the imposed shrinkage strain. As demonstrated in the previous chapter, shrinkage-induced stresses evolve over time and reach their maximum in the final equilibrium state, after stress relaxation has taken place. For this reason, effective long-term stiffness properties are used in all restraint-force formulations presented in this section.

The effective long-term modulus of the timber is defined as:

$$E_{\text{fin}} = \frac{E_{\text{mean}}}{1 + k_{\text{def}}}, \tag{5.9}$$

where E_{mean} is the mean elastic modulus and k_{def} is the deformation factor accounting for the viscoelastic deformation of timber under long-term loading.

Similarly, the effective long-term connection stiffness is defined as:

$$K_{\text{fin}} = \frac{K_{\text{mean}}}{1 + 2\,k_{\text{def}}}, \tag{5.10}$$

where K_{mean} is the mean slip stiffness of the connection. The factor $2\,k_{\text{def}}$ reflects the more pronounced time-dependent deformation in mechanical timber connections compared to the timber material itself.

This approach is consistent with experimental findings reported by Van de Kuilen (2008), who derived deformation factors for mechanical timber joints for implementation in Eurocode 5, showing that connections exhibit higher long-term deformation [26].

5.4.2. Situation 1: Fully restrained floor

The free shrinkage strain is defined as

$$\Delta\varepsilon_{sh} = \beta\,\Delta MC, \tag{5.11}$$

where β is the shrinkage coefficient and $\Delta MC = MC_{\text{fin}} - MC_{\text{inst}}$ is the change in moisture content between the initial and final equilibrium state. In the absence of restraint, this results in a free shortening

$$u_{sh} = \Delta\varepsilon_{sh} L, \tag{5.12}$$

without inducing internal stresses.

The first configuration represents the limiting case of a fully restrained floor panel, as shown in Figure 5.6. Since axial shortening is fully prevented, the free shrinkage strain is entirely converted into axial stress. The resulting axial force follows directly from Hooke's law:

$$N = -E_{\text{fin}} A\,\Delta\varepsilon_{sh}, \tag{5.13}$$

where $A = b_{\text{eff}} t$ is the cross-sectional area of the considered strip. The support reactions are equal in magnitude and opposite in sign, i.e. $R = -N$.

5.4.3. Situation 2: Floor panel between two cores

The second configuration considers a floor panel located between two concrete cores, as shown in Figure 5.7. The panel is supported along both edges by steel angles and connected to the cores by screws (detail 1 in Figure 5.2). Shrinkage occurs perpendicular to the cores, along the span between the two supports. The influence of the supporting beams is not considered.

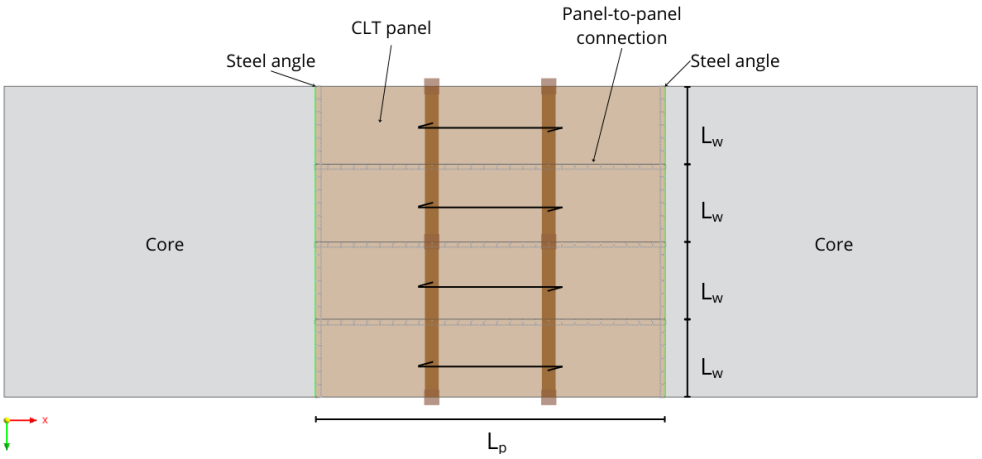

Figure 5.7: 2D schematic representation of the floor panel between two cores.

In contrast to the fully restrained case, the connections to the cores have finite stiffness. As a result, shrinkage is only partially restrained and the developed axial force depends on both the panel stiffness and the connection stiffness.

The system can be idealised as a one-dimensional beam subjected to uniform shrinkage and connected at both ends to axial springs with equal stiffness $K_{PC,\text{fin}}$, representing the effective long-term stiffness of the panel–core connections (see Figure 5.8).

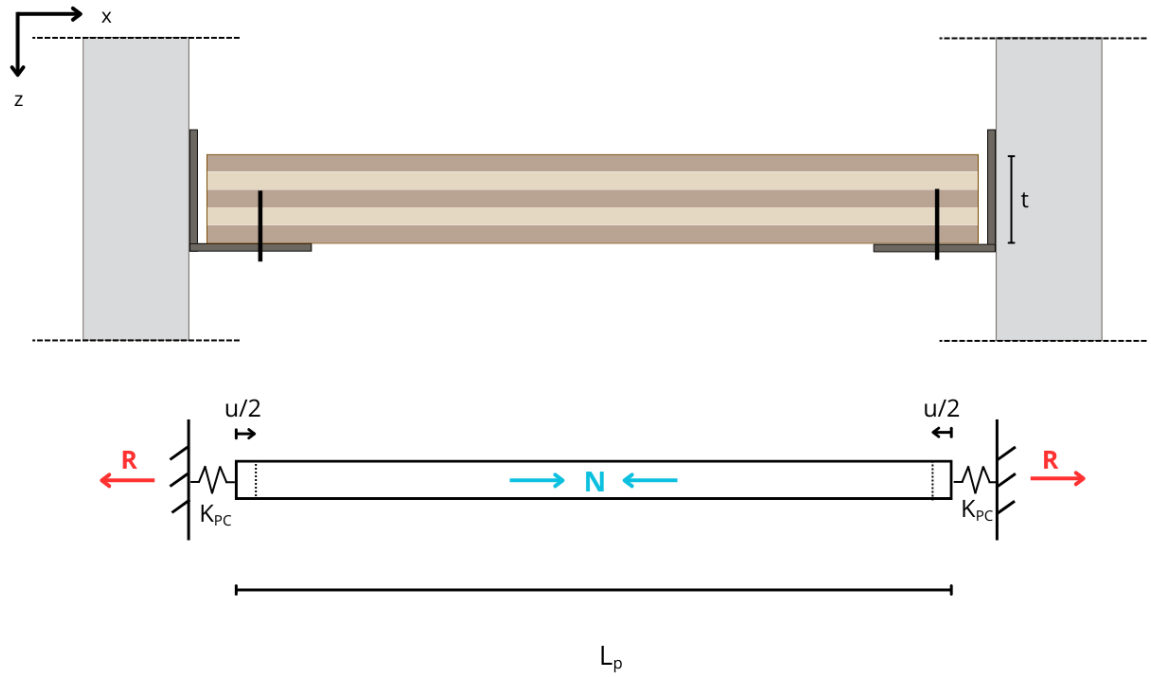

Figure 5.8: 1D beam–spring model of a CLT floor panel between two cores.

To determine the force in an individual screw, the panel is considered as a strip with an effective width equal to the screw spacing. The cross-sectional area of this strip is defined as

$$A = b_{\text{eff}}\, t,$$

where b_{eff} equals the screw spacing and t is the panel thickness.

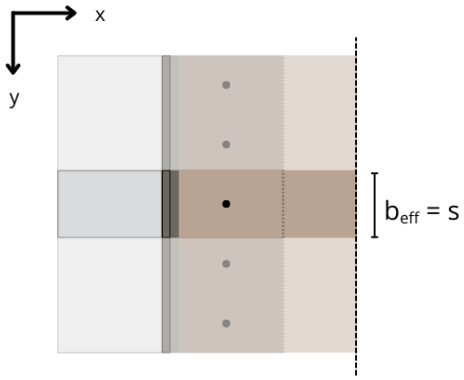

Figure 5.9: Effective width for 1D beam–spring model of a CLT floor between two cores.

Following the derivation in Appendix C, the axial force in the panel is given by

$$N = -\frac{\Delta\varepsilon_{sh} L_p}{\dfrac{2}{K_{PC,\text{fin}}} + \dfrac{L_p}{E_{\text{fin}} A}}, \tag{5.14}$$

where L_p is the panel length between the two cores. The reaction force in each end spring is equal in magnitude to the axial force, i.e. $R = -N$.

This expression shows that the restraint force is governed by the relative stiffness of the panel and the connections. It may also be interpreted using Hooke's law, with the free shrinkage imposing a shortening $u = \Delta\varepsilon_{sh} L_p$ on a series system consisting of the beam and the two end connections. The equivalent stiffness of this system is

$$\frac{1}{k_{\text{tot}}} = \frac{1}{K_{PC,\text{fin}}} + \frac{1}{K_{PC,\text{fin}}} + \frac{L_p}{E_{\text{fin}} A}, \tag{5.15}$$

so that the axial force follows directly as $N = k_{\text{tot}} u$. The limiting cases illustrate the physical behaviour:

- *As* $K_{PC,\text{fin}} \to \infty$, the contribution of the end connections vanishes and the response approaches the fully restrained case of Situation 1.
- *As* $K_{PC,\text{fin}} \to 0$, the system offers no restraint, the panel shortens freely, and no axial force develops.

5.4.4. Situation 3: Two floor panels between two cores

The third configuration considers two CLT floor panels located between two concrete cores, meeting at a glulam beam positioned between the cores (see Figure 5.10). Each panel is connected to a core at one end and supported by the glulam beam at the other (detail 3 in Figure 5.2). The influence of the supporting beams is not considered.

If both panels have equal length and undergo the same shrinkage strain, the system is symmetric. In that case, the glulam beam remains approximately stationary due to the opposing shrinkage forces from the two panels. The behaviour of the system can therefore be analysed by considering one half of the configuration.

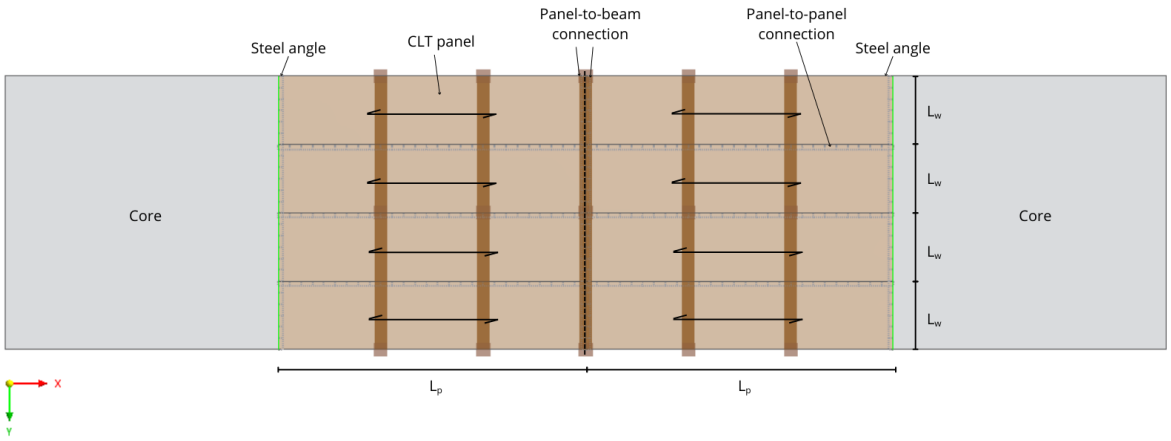

Figure 5.10: 2D schematic representation of two floor panels between two cores.

For one panel, shrinkage occurs perpendicular to the cores, along the span between the core and the glulam beam. In contrast to Situation 2, the panel is now restrained by two different supports: the concrete core and the glulam beam. These restraints generally have different effective stiffnesses.

The system is idealised as a one-dimensional beam subjected to uniform shrinkage and connected at its ends to two axial springs with stiffnesses $K_{PC,\text{fin}}$ and $K_{PB,\text{fin}}$, representing the effective long-term stiffness of the panel–core connection and the panel–beam connection, respectively (see Figure 5.11).

The cross-sectional area of the considered strip is defined as

$$A = b_{\text{eff}}\, t,$$

where b_{eff} equals the screw spacing and t is the panel thickness (Figure 5.9).

Following the derivation in Appendix C, the axial force in the panel is given by

$$N = -\frac{\Delta\varepsilon_{sh} L_p}{\dfrac{1}{K_{PC,\text{fin}}} + \dfrac{1}{K_{PB,\text{fin}}} + \dfrac{L_p}{E_{\text{fin}} A}}, \tag{5.16}$$

where L_p is the panel length between the core and the glulam beam. The reaction forces in the two springs are equal in magnitude to the axial force, i.e. $R_{PC} = R_{PB} = N$.

This expression shows that the restraint force depends on the relative stiffness of the panel and both supports. As in Situation 2, the response may be interpreted in terms of a series system, now consisting of the beam stiffness and two different connection stiffnesses.

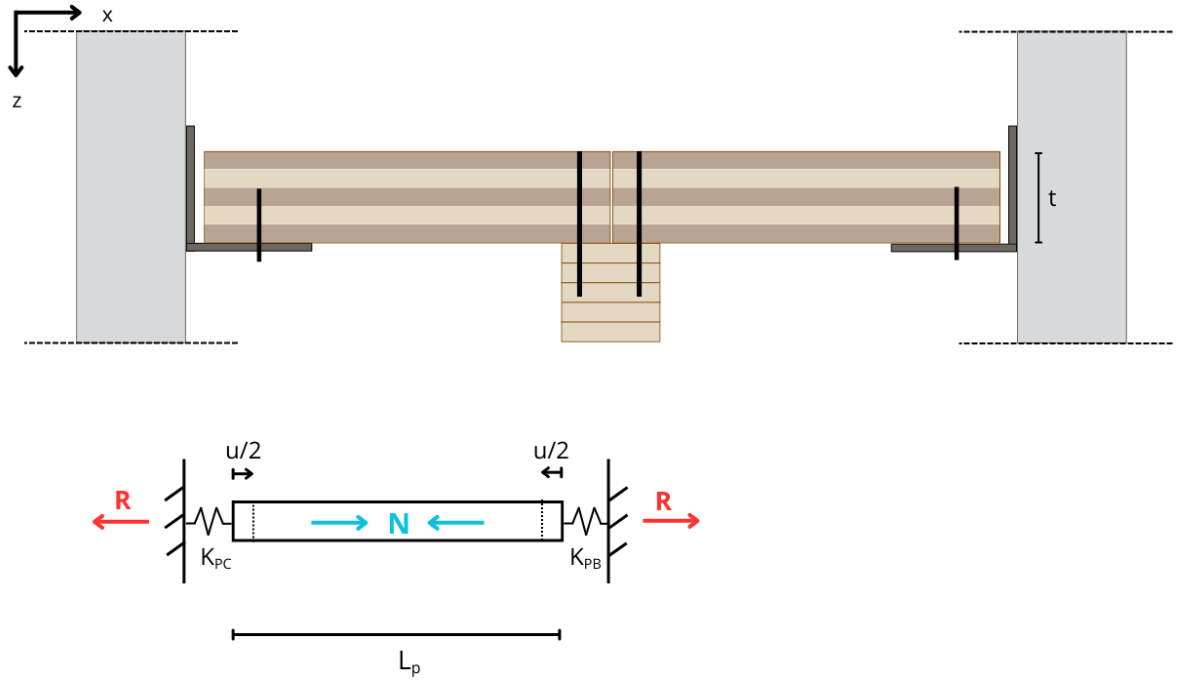

Figure 5.11: 1D beam–spring model of two interacting CLT floor panels between two cores.

5.4.5. Situation 4: Floor panel with continuous restraint along the core

The fourth configuration considers shrinkage parallel to the core. Here, the panel edge along the core is modelled as a continuous line connection, which represents a series of discrete steel-angle connections with screws distributed along the core-side edge. Shrinkage develops parallel to this restrained edge, either along the short or the long panel direction depending on the floor layout (see Figure 5.12).

In contrast to the previous situations, the restraint is not concentrated at discrete points but distributed continuously along the edge. Consequently, the load-transfer mechanism differs from the end-spring models considered in Situations 2 and 3.

The system is idealised as a one-dimensional beam subjected to uniform shrinkage and supported by a continuous elastic foundation with effective line stiffness $k_{PC,\text{fin}}$, representing the long-term stiffness of the screw connection per unit length (see Figure 5.13).

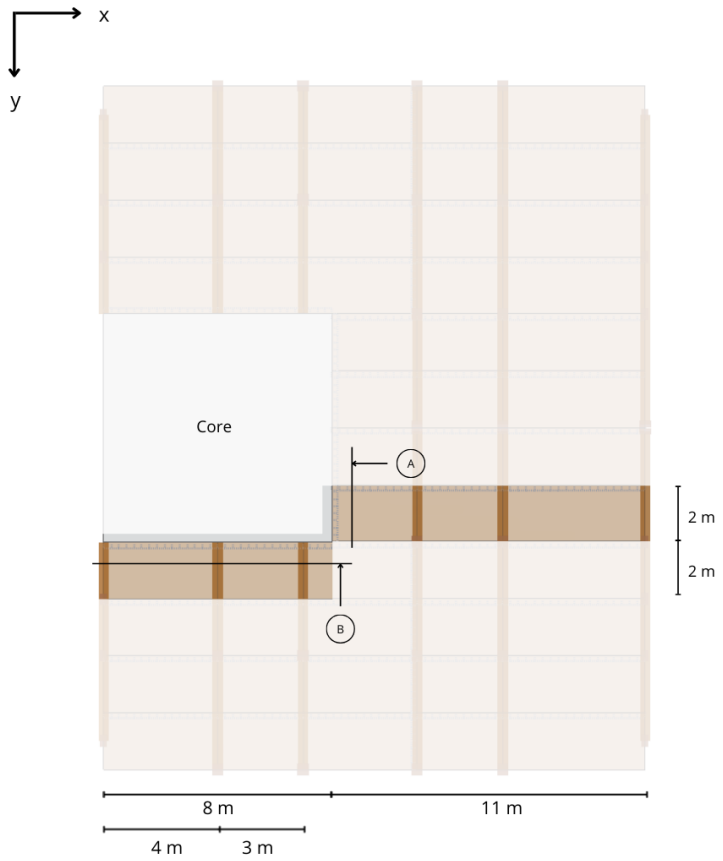

Figure 5.12: 2D schematic representation of a floor panel with continuous restraint along the core edge: (a) restraint along the short side, (b) restraint along the long side.

The governing differential equation for a shrinking beam on an elastic foundation is

$$E_{\text{fin}} A\, u''(x) - k_{PC,\text{fin}}\, u(x) = 0, \tag{5.17}$$

where $u(x)$ denotes the axial displacement along the restrained edge. Similar load transfer mechanisms occur in other engineering problems such as reinforcement bond in concrete, shear-lag in composite members, and piles interacting with soil, all described by a differential equation governing the interaction between an axially loaded member and a distributed elastic restraint [27].

With boundary conditions $N(0) = N(L_w) = 0$ and

$$\lambda = \sqrt{\frac{k_{PC,\text{fin}}}{E_{\text{fin}} A}}, \tag{5.18}$$

the displacement field becomes (see Appendix C)

$$u(x) = \frac{\Delta\varepsilon_{sh}}{\lambda} \frac{\sinh\left(\lambda\left(\frac{L_w}{2} - x\right)\right)}{\cosh\left(\frac{\lambda L_w}{2}\right)}. \tag{5.19}$$

The corresponding distributed reaction force and axial force distribution are

$$q_R(x) = k_{PC,\text{fin}} \frac{\Delta\varepsilon_{sh}}{\lambda} \frac{\sinh\left(\lambda\left(\frac{L_w}{2} - x\right)\right)}{\cosh\left(\frac{\lambda L_w}{2}\right)}, \tag{5.20}$$

$$N(x) = -E_{\text{fin}} A\, \Delta\varepsilon_{sh} \left[1 - \frac{\cosh\left(\lambda\left(\frac{L_w}{2} - x\right)\right)}{\cosh\left(\frac{\lambda L_w}{2}\right)}\right]. \tag{5.21}$$

The axial force is zero at the ends of the restrained edge and reaches a maximum at midspan, while the distributed reaction force is largest near the edges and decreases towards the centre.

To relate the continuous foundation model to the discrete screw connection, the distributed reaction $q_R(x)$ may be interpreted as the shear flow transferred into the steel angle. For a screw spacing s, the force in a screw at position x_i is approximated as

$$R_i \approx q_R(x_i)\, s. \tag{5.22}$$

The largest screw forces therefore occur near the edges of the restrained length.

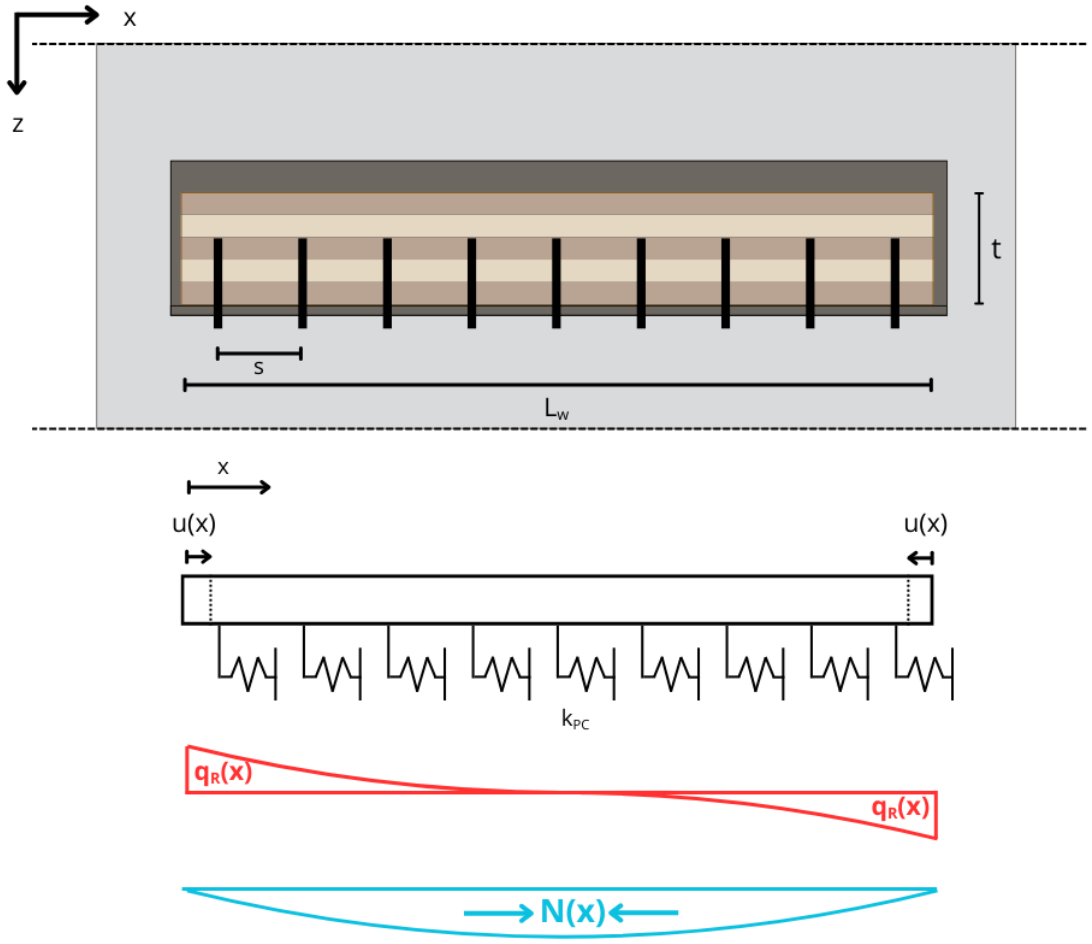

Figure 5.13: 1D beam-on-elastic-foundation model of a floor panel with continuous core restraint.

The determination of the effective width associated with this distributed load-transfer mechanism is addressed separately in the following subsection.

Effective width

In Situations 1–3, the effective width in the one-dimensional model was taken as the screw spacing. In those cases, the axial force in the strip could be directly related to the force in an individual screw.

For shrinkage parallel to the core (Situation 4), the load-transfer mechanism is fundamentally different. Although the connection to the core is continuous along its full length, the axial force that develops in the panel is not confined to a strip of predefined width. Instead, due to the two-dimensional plate behaviour, the force spreads into the panel. As a result, the width over which the axial stiffness should be considered in the one-dimensional model is not known beforehand.

To determine a representative effective width for this configuration, numerical analyses were performed in RFEM. The panel was connected to the concrete core along one edge by a continuous line spring, while the remaining edges were free to shrink, consistent with the case study configuration (Figure 5.12).

Using the analytical expression for the distributed spring reaction (see Equation 5.19 and Equation 5.20), an equivalent effective width was back-calculated. The effective width is defined here as the panel width that reproduces the maximum line reaction obtained from the numerical model. It therefore represents a calibrated one-dimensional approximation of the two-dimensional plate behaviour.

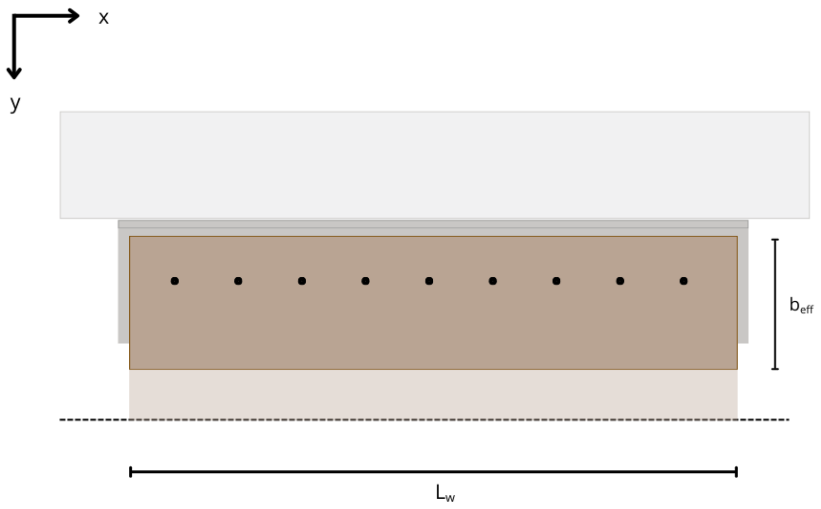

Figure 5.14: Effective width for a CLT floor panel with continuous restraint along the core.

Numerical results are provided in Appendix E. In this thesis, the effective widths obtained from the RFEM analyses are used for the specific configurations considered and subsequently applied in the analytical model to calculate the forces in the screws.

6

Results

The analytical formulations derived in the previous chapter are applied to evaluate the forces in the screw connections for varying panel geometries and moisture conditions.

In this thesis, the panel length L_p and the installation moisture content MC_{inst} are treated as variable parameters. The shrinkage coefficients β_x and β_y, the screw spacing, and the connection stiffness are kept constant.

For each combination of panel length and installation moisture content, the resulting restraint force in the connection is calculated and compared to the design shear capacity of the screw. This allows identification of parameter combinations for which the connection force exceeds the screw capacity, as well as combinations that remain within safe limits.

The results are presented separately for shrinkage acting perpendicular to the core (Situations 2 and 3) and shrinkage acting parallel to the core (Situation 4).

6.1. Model parameters

Table 6.1 summarises the parameters that are kept constant throughout the parametric study.

Table 6.1: Fixed parameters used in the parametric study.

Category	Parameter	Value	Unit
Geometry	Screw spacing s	100	mm
	Panel thickness t	200	mm
Moisture & shrinkage	Final moisture content MC_{fin}	8	%
	Shrinkage coefficients (β_x, β_y)	$(0.00015,\ 0.00035)$	–
Material & stiffness	Effective modulus E_{fin}	6111	MPa
	Connection stiffness (panel–core) $K_{PC,\text{fin}}$	2313.2	N/mm
	Connection stiffness (panel–beam) $K_{PB,\text{fin}}$	1156.6	N/mm
	Distributed line stiffness (panel-core) $k_{PC,\text{fin}}$	23.13	N/mm^2
Effective width	Situations 1–3: $b_{\text{eff},1-3}$	100 (= s)	mm
	Situation 4A: $b_{\text{eff,4A}}$	190	mm
	Situation 4B: $b_{\text{eff,4B}}$	655	mm
Screw capacities	Steel-to-timber shear capacity $F_{v,Rd,PC}$ (mode e)	2645	N
	Timber-to-timber shear capacity $F_{v,Rd,PB}$ (mode f)	2819	N

6.2. Situation 2: Floor panel between two cores

This section presents the results for a CLT floor panel located between two concrete cores, corresponding to Situation 2 defined in section 5.4. The results shown here concern shrinkage perpendicular to the core, modelled using the spring-ends formulation with equal connection stiffness at both supports.

Figure 6.1 shows the utilisation ratio

$$UC = \frac{F_{v,\mathrm{Ed}}}{F_{v,\mathrm{Rd,PC}}},$$

as a function of panel length L_p and installation moisture content MC_{inst}, for the parameter set given in Table 6.1. The red contour indicates the limit state $UC = 1$. Combinations below this contour satisfy the design requirement, whereas combinations above it lead to exceedance of the screw shear capacity.

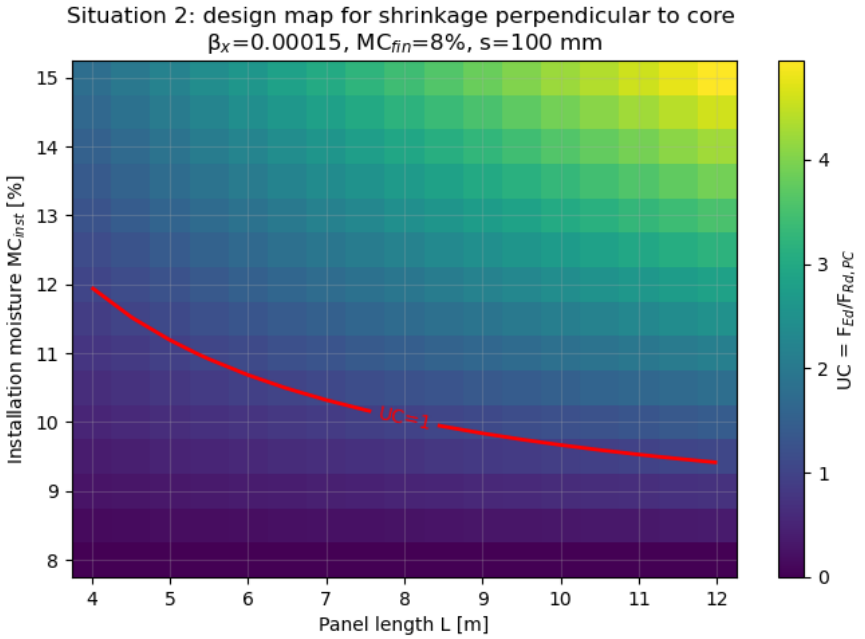

Figure 6.1: Utilisation ratio for a floor panel between two cores (Situation 2) under shrinkage perpendicular to the core.

The contour plot shows that the utilisation ratio increases with both panel length and installation moisture content. The red curve represents the design limit (UC = 1). Its downward slope indicates that as panel length increases, the allowable installation moisture content decreases.

In practical terms, long panels require a low moisture content at installation to remain within design limits. Conversely, if the installation moisture content is high, only shorter panel lengths remain feasible without exceeding the utilisation limit.

6.3. Situation 3: Two floor panels between two cores

This section presents the results for two CLT floor panels located between two concrete cores and meeting at a glulam beam, corresponding to Situation 3 defined in section 5.4. The results shown here concern shrinkage perpendicular to the core. The system is modelled using the spring-ends formulation with unequal support stiffnesses: a steel–timber connection at the core and a timber–timber connection at the glulam beam.

Figure 6.2 shows the utilisation ratio

$$UC = \frac{F_{v,\mathrm{Ed}}}{F_{v,\mathrm{Rd,PC}}},$$

as a function of panel length L_p and installation moisture content MC_{inst}, for the parameter set in Table 6.1. The governing check is the *panel–core* connection for the considered parameter set.

The contour plot shows that utilisation increases with both panel length and installation moisture content. The red curve indicates the design boundary ($UC = 1$): its downward slope means that longer

panels require a lower installation moisture content to remain within the design limit. Conversely, for higher MC_{inst}, only shorter panel lengths remain feasible.

Compared to Situation 2, the presence of the glulam beam introduces a more compliant support at one end. Because the timber–timber connection is less stiff than the panel–core connection ($K_{PB,\text{fin}} < K_{PC,\text{fin}}$), a larger share of the shrinkage deformation is accommodated by slip at the beam-side support. This reduces the restraint force that develops for a given shrinkage strain (see Equation 5.16). As a result, the $UC = 1$ boundary shifts towards larger ranges of (L_p, MC_{inst}) compared to Situation 2, indicating reduced demand in the governing panel–core connection.

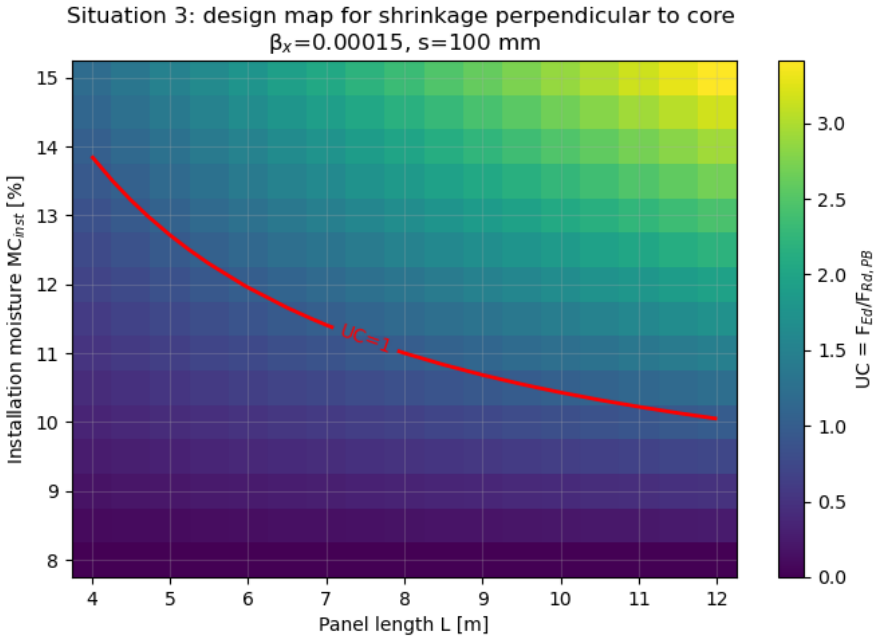

Figure 6.2: Utilisation ratio for a floor panel between a steel angle and a glulam beam (Situation 3) under shrinkage perpendicular to the core.

6.4. Situation 4: Floor panel with continuous restraint along the core

This section presents the results for shrinkage parallel to the core in a configuration where the floor panel remains continuously connected along the full length of the interface. In contrast to Situations 2 and 3, where the evaluated results concern restraint perpendicular to the core, the present case focuses on restraint acting parallel to the core edge.

For this configuration, the governing behaviour is not characterised by a single support reaction, but by a non-uniform distribution of restraint along the continuously connected edge. It is therefore more informative to present the force distribution over the individual screws along the restrained interface than to summarise the response by a single resultant force.

The results presented below correspond to a moisture change from $MC_{\text{inst}} = 15\%$ to $MC_{\text{fin}} = 8\%$. For Situation 4A, the shrinkage coefficient $\beta_y = 0.00035$ is used, while for Situation 4B $\beta_x = 0.00015$ is applied. The effective widths adopted in the analytical model are obtained from the RFEM calibration described in Appendix E.

For the case-study geometry, Situation 4A corresponds to a restrained width of 2 m, while Situation 4B corresponds to a continuously restrained length of 8 m. Additional dimensions are shown to illustrate the influence of restrained length on the force distribution.

The force distributions presented in this section follow from the linear elastic restrained-shrinkage

model with distributed connection stiffness $k_{PC,\text{fin}}$. The resulting variation in screw force therefore reflects the non-uniform load transfer along the restrained edge. Nonlinear behaviour of the individual screws is not included explicitly in the analytical model.

6.4.1. Situation 4A: Shrinkage along the short edge

Figure 6.3 shows the distribution of the shrinkage-induced force per screw along the connection for Situation 4A. The horizontal axis represents the relative position x/L, where x is the distance measured along the connection and L is the total restrained length. Thus, $x/L = 0$ and $x/L = 1$ correspond to the outermost screws, while $x/L = 0.5$ represents the midpoint.

A V-shaped force distribution is obtained: the screw force is zero at midspan and increases towards the edges, reflecting the cumulative restraint effect of the distributed connection. The red dashed line indicates the design shear resistance $F_{v,Rd,PC}$. Screws located above this line exceed their design resistance, which indicates that the linear elastic representation is no longer expected to remain fully valid at those locations.

Panel widths of 1 m, 2 m and 3 m are considered. The 2 m case corresponds to the case-study geometry. With increasing restrained width, the maximum screw force increases and a larger number of outer screws exceed $F_{v,Rd,PC}$, while the central screws remain only lightly loaded.

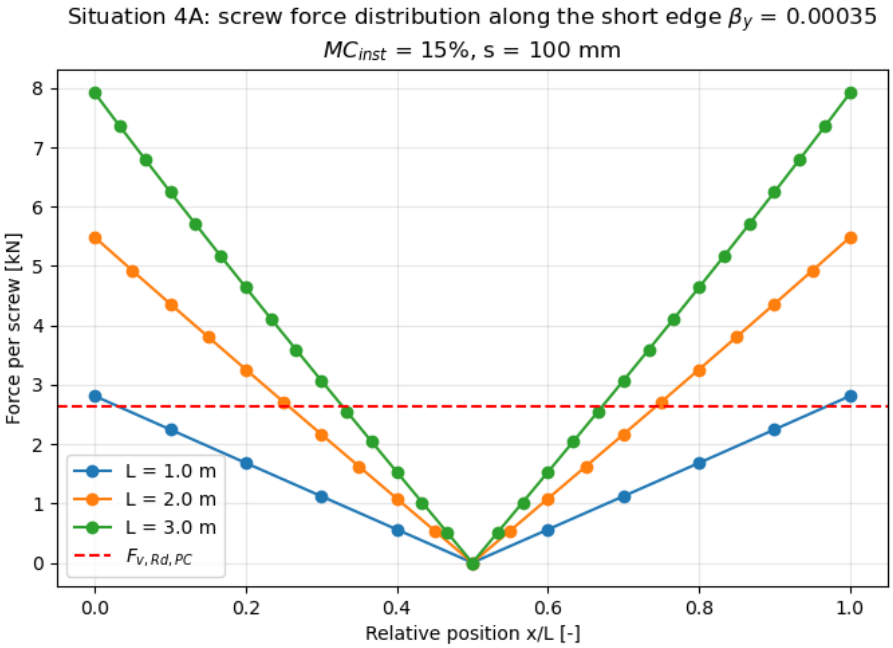

Figure 6.3: Screw force distribution for shrinkage along the short edge for different panel widths.

6.4.2. Situation 4B: Shrinkage along the long edge

Figure 6.4 presents the screw force distribution for shrinkage along the long edge of the panel. The same V-shaped distribution is obtained, with zero force at midspan and maximum forces at the outermost screws.

As in Situation 4A, the restraint force is therefore concentrated near the ends of the continuously restrained interface, while the screws in the central region carry relatively little force. Direct comparison of the absolute force levels between Situations 4A and 4B should be made with care, since the two cases differ not only in restrained length and effective width, but also in the shrinkage coefficient used in the analysis (β_y for Situation 4A and β_x for Situation 4B).

The panel lengths shown in Figure 6.4 represent different structural layouts. The case $L = 8$ m corresponds to the case-study configuration, in which a single floor panel is continuously connected to

the core along its full length. The additional cases $L = 4$ m and $L = 3$ m are shown to illustrate how reducing the continuously restrained length decreases the shrinkage-induced screw forces.

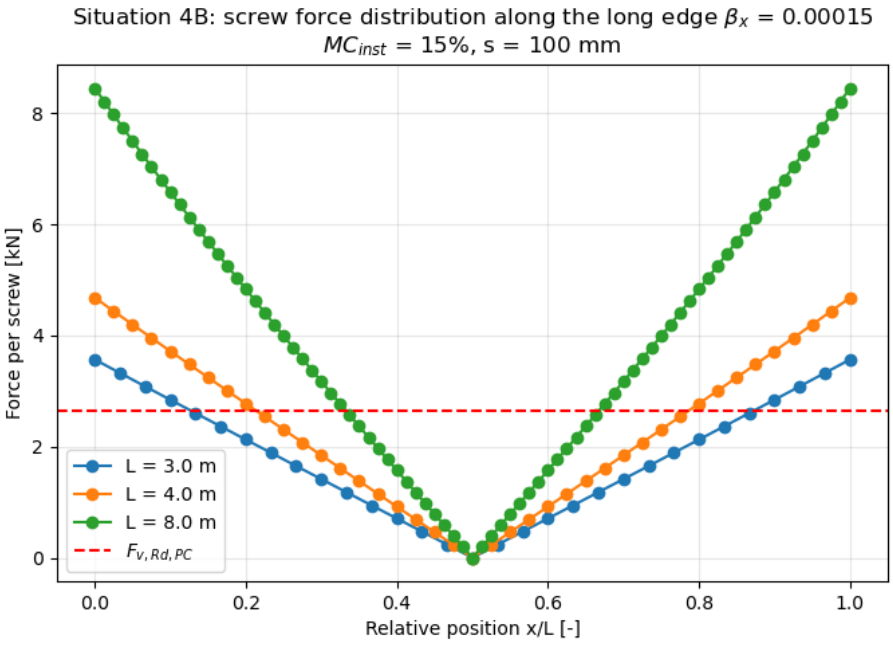

Figure 6.4: Screw force distribution for shrinkage along the long edge for different panel lengths.

For increasing panel length, not only does the maximum force increase, but also the number of screws exceeding the design resistance grows. In the most unfavourable case considered, a substantial part of the outer screws exceeds $F_{v,Rd,PC}$, whereas the central screws remain below this level. Reducing the continuous connection length along the core decreases the maximum shrinkage-induced screw force.

The increase in panel length not only raises the maximum screw force, but also the associated local deformation demand. Using the adopted long-term connection stiffness, the slip in an individual screw may be estimated as

$$u_i = \frac{R_i}{K_{fin}}. \tag{6.1}$$

For the case-study configuration with a continuously restrained length of $L = 8$ m, the outermost screws reach a slip of approximately $u_{\max} \approx 3.7$ mm.

For comparison, the slip corresponding to the onset of yielding may be estimated as

$$u_y \approx \frac{F_{v,Rk}}{K_{SLS}} \approx 0.95 \text{ mm}. \tag{6.2}$$

The calculated slip therefore clearly exceeds the initial elastic range of the connection, indicating that the outer screws are expected to enter a non-linear response regime. This implies that the assumption of purely linear-elastic connection behaviour is no longer appropriate for the most highly loaded screws.

This does not imply immediate connection failure. As discussed in subsection 5.2.2, screwed timber connections can exhibit significant ductility and may accommodate additional imposed deformation through plastic slip. Whether this deformation demand is still compatible with the ductile deformation capacity of screwed connections is discussed further in Chapter 9, with reference to values reported in the literature.

6.5. Slip allowance

For shrinkage perpendicular to the core, slip allowance can be introduced without compromising the intended diaphragm load transfer towards the core. This makes slotted holes a feasible mitigation measure for the restraint considered in Situations 2 and 3.

For shrinkage parallel to the core, however, the same connection line is required to transfer in-plane shear forces. In that direction, global slip allowance cannot be introduced without affecting the assumed load path. As a result, slip allowance is not a viable measure to relieve restrained shrinkage parallel to the core.

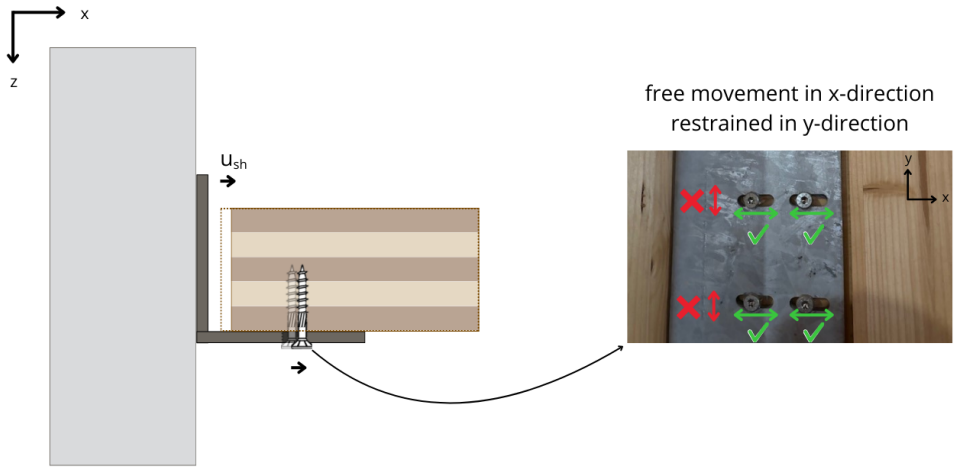

Figure 6.5: Schematic representation of slip allowance introduced by slotted holes.

Situation 2

For the restraint perpendicular to the core considered in Situation 2, slip allowance can be introduced at both supports. This movement allowance permits part of the shrinkage deformation to occur before axial restraint develops. Figure 6.6 shows the required slip allowance g at both supports to ensure $UC \leq 1$ for combinations of L_p and MC_{inst}.

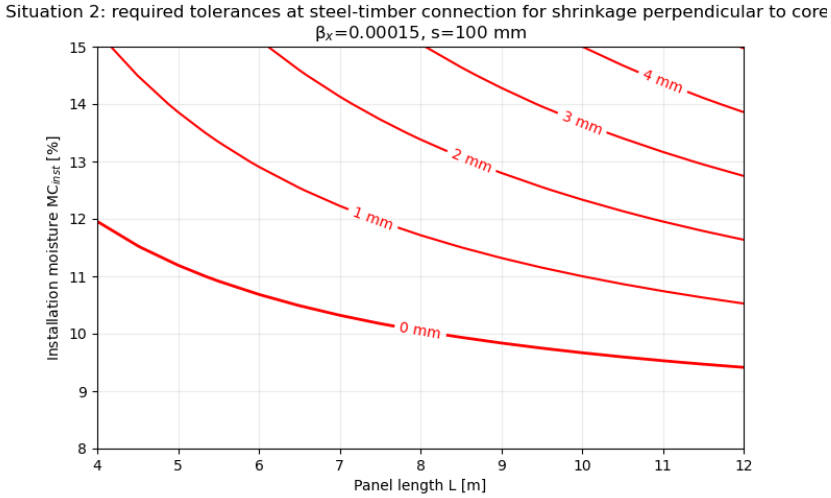

Figure 6.6: Required slip allowance at both supports to maintain $UC \leq 1$ for Situation 2.

For short panel lengths and low installation moisture contents, no additional slip allowance is required. For increasing panel length and higher installation moisture content, however, the required slip

allowance increases. This reflects the larger shrinkage deformation that must be accommodated before critical restraint forces develop in the connection.

Situation 3

For the restraint perpendicular to the core considered in Situation 3, slip allowance is introduced at the steel support only. No additional slip allowance is considered at the timber–timber connection. Figure 6.7 shows the required slip allowance g at the steel support to ensure that neither connection exceeds its design resistance.

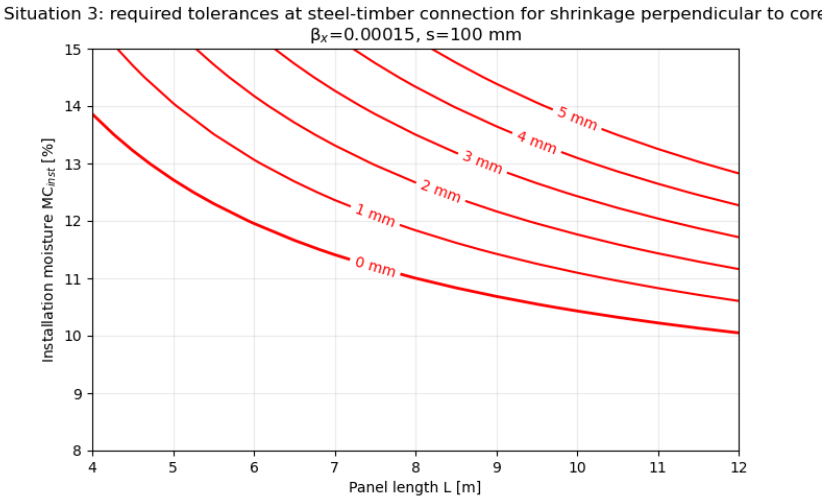

Figure 6.7: Required slip allowance at the steel support to maintain $UC \leq 1$ for Situation 3.

For short panel lengths and low installation moisture contents, no additional slip allowance is required. With increasing L_p and MC_{inst}, the required slip allowance increases.

6.6. Key observations

The following key observations are drawn from the parametric evaluation of shrinkage-induced restraint forces in the screw connections:

- For the cases evaluated with shrinkage perpendicular to the core (Situations 2 and 3), the utilisation increases with both panel length L_p and installation moisture content MC_{inst}. The $UC = 1$ boundary illustrates a clear trade-off: longer panels require lower MC_{inst} to remain within design limits, whereas higher MC_{inst} restricts the feasible panel length.
- Compared to Situation 2, Situation 3 develops lower restraint forces in the governing panel–core connection. Because the panel–beam connection is less stiff than the panel–core connection ($K_{PB,\text{fin}} < K_{PC,\text{fin}}$), a larger share of the shrinkage deformation is accommodated at the beam-side support, which shifts the $UC = 1$ boundary to larger ranges of (L_p, MC_{inst}).
- For shrinkage perpendicular to the core, slip allowance is an effective mitigation measure. The required slip allowance increases with increasing L_p and MC_{inst}, because a larger free shrinkage deformation must be accommodated before significant restraint forces develop.
- For the cases evaluated with shrinkage parallel to the core (Situation 4), the restraint forces are distributed along the connection and show a V-shaped pattern: screw forces are lowest near midspan and reach their maximum near the ends of the restrained length.
- Within both Situation 4A and Situation 4B, increasing the continuously restrained length increases the peak screw force and the number of screws exceeding the design resistance. The additional cases shown alongside the case-study geometries illustrate that reducing the restrained length is an effective way to reduce shrinkage-induced force demand.

- In Situation 4, part of the connection may exceed the elastic design resistance $F_{v,Rd,PC}$. This does not imply an immediate loss of load transfer, but it does indicate increased slip and reduced incremental stiffness in the affected fasteners. Plastic deformation is expected to initiate first in the outer screws, while the central part of the connection remains elastic.
- For consistency, utilisation is evaluated against the elastic design resistance as a conservative criterion. Post-yield redistribution and the associated stiffness degradation are not modelled in this study.

These results show that the applicability of slip allowance depends on the direction of restrained shrinkage relative to the diaphragm load path. For shrinkage perpendicular to the core, slip allowance can be introduced without interfering with the required in-plane force transfer and therefore offers an effective means of reducing restraint forces. For shrinkage parallel to the core, however, the connection must continue to transfer diaphragm shear forces, so global slip allowance is not a viable solution. In that direction, the most direct way to reduce shrinkage-induced connection forces is therefore to limit the continuously restrained length along the core.

Part III

CLT floor system in structural stability

7

CLT floor system in structural stability

This chapter provides the conceptual background for Part III of this thesis. Part III evaluates how the stiffness of the CLT floor system influences the structural response of the case-study building. In particular, the study focuses on the stiffness of panel–core and panel–panel connections, and investigates how these choices affect global displacements and the force demand in the relevant interfaces. The chapter also motivates why second-order effects are considered, and under which circumstances they become important for the assessment.

The chapter is structured as follows: first the core–frame load path is introduced, followed by the diaphragm deformation mechanisms that govern the in-plane displacement response. The resulting effective diaphragm restraint is then linked to global stability mechanisms and second-order (P–Δ) effects. Finally, the implications for column stability are formulated using the lateral buckling format of Eurocode 5 (FprEN 1995-1-1:2025).

7.1. Core–frame lateral load path

The structural system considered in this thesis consists of a reinforced concrete core surrounded by a timber post-and-beam frame. At each storey, the CLT floor panels act as horizontal diaphragms and are connected to the stiff core, supporting the frame.

Under lateral actions (e.g. wind), the core provides the lateral resistance and behaves as a vertical cantilever fixed at foundation level (Figure 7.1). Façade loads are collected by the perimeter frame, transferred to the floor level, and transmitted to the core through in-plane diaphragm action. The core then resists these forces through storey shear forces and overturning moments.

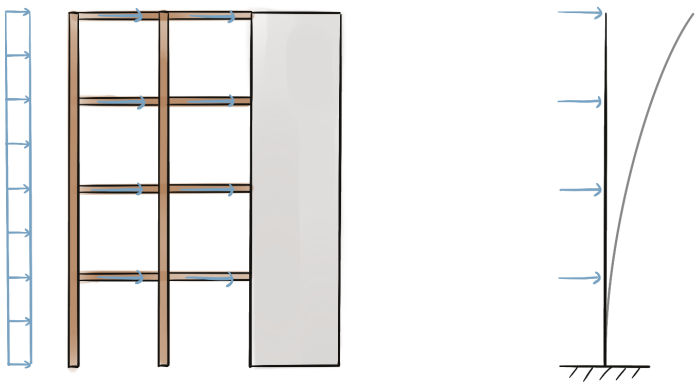

Figure 7.1: Cantilevering concrete core in a core–frame system under lateral actions.

In the case-study building, the floor plan is asymmetric. As a result, lateral loads do not only induce an in-plane translation of the floor diaphragm, but can also create torsion of the floor field around the core. The diaphragm therefore needs to transfer a combination of in-plane shear and torsion into the core through the floor–core interface. This makes the effectiveness of the panel–core coupling particularly important: insufficient diaphragm stiffness can lead to increased deformations.

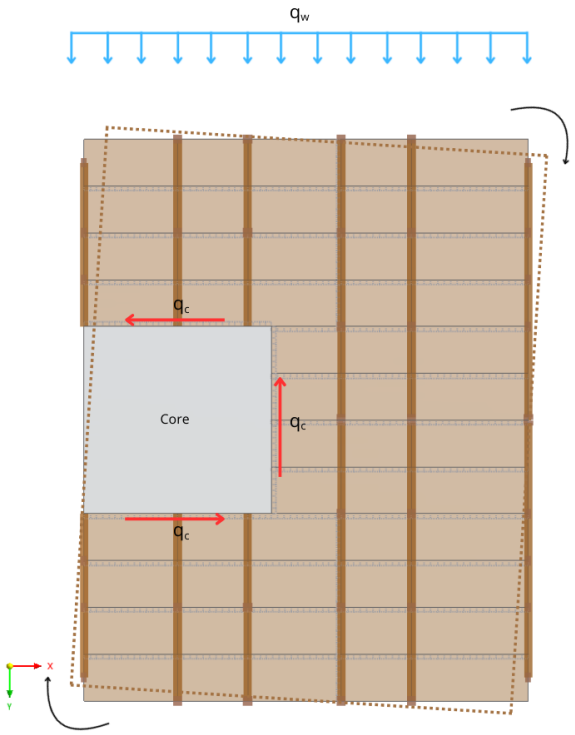

Figure 7.2: Schematic diaphragm action under wind.

The effectiveness of load transfer to the core depends on the in-plane stiffness of the floor diaphragm and its connections. A more flexible diaphragm requires larger in-plane deformations to transfer the same horizontal loads, which increases displacements and can change the lateral load path and internal force distribution. The following section introduces the deformation mechanisms that contribute to in-plane diaphragm displacements.

7.2. Diaphragm stiffness and deformation components

To quantify the influence of connection stiffness, the in-plane response is described in terms of in-plane floor displacements u. This displacement governs both the global lateral drift of the building and the forces in the connections, as larger in-plane deformations are required to transfer the same lateral actions.

To obtain expressions for the displacement components, the case-study floor plan is simplified as a local *cantilevering* segment connected to the core along one edge (Figure 7.3). For this simplified segment, expressions can be derived for a monolithic diaphragm assumption. These expressions are used to identify which mechanisms dominate the in-plane deformation and to support interpretation of the numerical results for the full case study. In the full plan, panels may continue past the core boundary and interlock with adjacent panels.

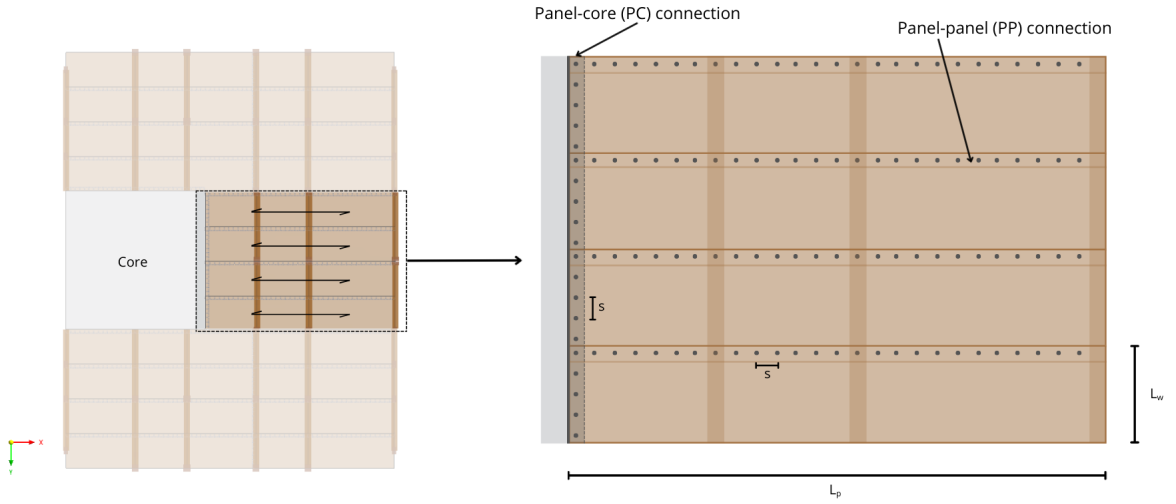

Figure 7.3: Cantilevering segment used for analytical displacement estimates.

7.2.1. Deformation components

For the cantilever segment, the total in-plane displacement is decomposed into connection sliding, connection rocking, panel bending and panel shear (Figure 7.4),

$$u_{\text{tot}} = u_A + u_R + u_B + u_S. \tag{7.1}$$

Assuming a uniformly distributed in-plane line load q acting over a segment length L_p (with resultant shear $F = qL_p$), the individual displacement components are

$$u_A = \frac{F}{K_A} = \frac{qL_p}{K_A}, \tag{7.2}$$

$$u_R = \theta L_p = \frac{M}{K_R} L_p = \frac{qL_p^3}{2K_R}, \tag{7.3}$$

$$u_B = \frac{qL_p^4}{8EI}, \tag{7.4}$$

$$u_S = \frac{qL_p^2}{2\,G_{xy,\text{mean}}\,A_s}. \tag{7.5}$$

Here, u_A, u_R, u_B and u_S represent the sliding, rocking, bending and shear displacement components, respectively. EI denotes the bending stiffness of the diaphragm segment, $G_{xy,\text{mean}}$ the in-plane shear modulus of the CLT, and A_s the effective shear area.

For the monolithic idealisation, the rocking component can be related to the floor–core interface behaviour by modelling the interface as a continuous line of translational springs with stiffness k_{PC} [N/mm^2] distributed over the interface width L_{core}. Assuming symmetric rocking about the mid-width, the equivalent rotational stiffness becomes

$$K_R = k_{PC}\,\frac{L_{\text{core}}^3}{12}. \tag{7.6}$$

The analytical expressions above are evaluated for a monolithic diaphragm assumption in Appendix G. That evaluation shows that rocking contributes a major share of the total in-plane displacement. This indicates that the deformation of the cantilevering floor segment is governed primarily by rotation at the floor–core interface, while bending and in-plane shear of the panel are of secondary importance.

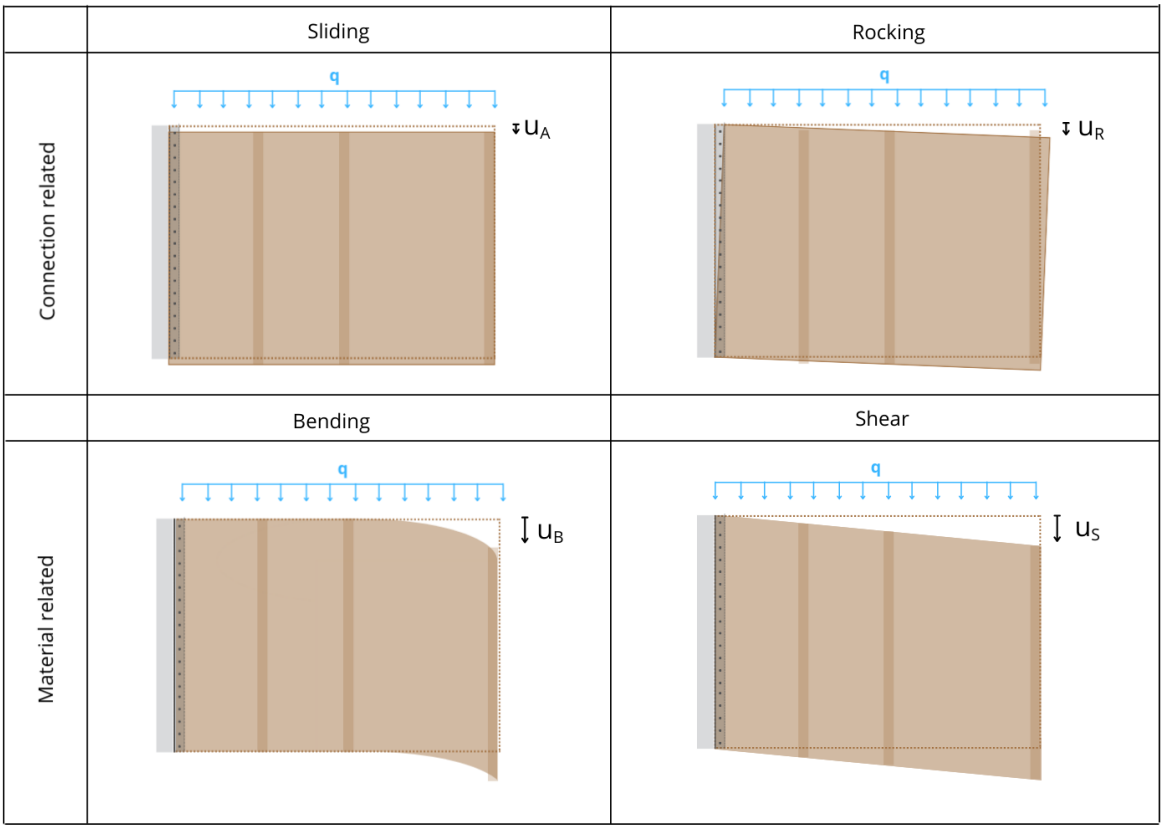

Figure 7.4: Deformation components of the cantilevering segment for a monolithic floor: sliding, rocking, bending and shear.

Monolithic versus segmented diaphragm behaviour

A monolithic floor idealisation assumes full in-plane compatibility between adjacent panels, such that the diaphragm response is governed mainly by the elastic deformation of the floor and by deformation at the floor–core interface. In contrast, a segmented floor introduces additional compliance through the panel–panel joints, allowing relative slip and rotation between adjacent panels. As a result, connection-related deformation becomes more important and the in-plane stiffness of the diaphragm decreases.

This distinction is consistent with recent numerical studies on CLT diaphragms under in-plane loading. Fakhrzarei et al. showed that diaphragm deformation is strongly influenced by connection behaviour and panel layout, and that changes in panel installation pattern affect both stiffness and force distribution when the load is applied perpendicular to the panel length [28]. Other numerical studies likewise show that subdividing a monolithic CLT floor into smaller panels connected by panel–panel joints reduces the in-plane stiffness and increases diaphragm deformation due to slip in the connections [29].

Rocking: effect of segmentation

A segmented diaphragm introduces an additional deformation mode that is absent in a monolithic floor: *relative rotation between adjacent panels*. In the numerical model, this effect can be studied by varying the rotational stiffness of the panel–panel line hinges, K_{PP}, see Appendix G. For $K_{PP} \rightarrow \infty$ the floor behaves monolithically and the deformation is dominated by one global rocking mode of the floor field. For finite K_{PP}, adjacent panels are able to rotate relative to each other, which reduces the effective coupling across the diaphragm and increases the overall rocking contribution to the in-plane displacement.

Segmentation therefore changes not only the magnitude of the displacement, but also the deformation pattern. Instead of one global rocking mode, multiple local rotations may develop, depending on the level of panel–panel rotational stiffness. This reduces the effective lever arm over which the diaphragm can mobilise a restoring couple against rotation at the core.

Segmentation also changes how forces are transmitted through the diaphragm. When panel coupling is

reduced, a larger part of the load transfer must be carried locally by the panel–panel connections rather than being shared over a wider floor field. As a result, force concentrations in the line hinges increase as K_{PP} decreases. The associated deformation patterns and force concentrations are illustrated with RFEM results in Appendix G.

Rocking restraint: effect of grout at the floor–core interface

The rocking idealisations described above assume sufficient clearance for the panel to rotate relative to the concrete core, while the restoring action at the interface is governed primarily by fastener deformation. This is representative for the ungrouted connection detail (Type 1a), see section 5.1. In that case, rocking of the diaphragm is resisted mainly by deformation of the screws and by the associated force couple in the mechanical connection.

When the gap between the panel and the concrete core is filled with grout (Type 1b), the interface behaviour changes. Rotation of the floor relative to the core activates compression contact at the interface, causing the panel edge to bear against the grout. A compression zone then forms along the core boundary. This contact provides an additional and comparatively stiff restoring couple against rotation, such that part of the rocking demand is transferred by direct compression rather than by fastener deformation alone.

Grout therefore does not primarily change the global load path from diaphragm to core, but increases the rotational restraint at the floor–core interface. Its main effect is to reduce rocking deformation of the floor diaphragm and thereby to increase the effective diaphragm stiffness. RFEM results illustrating this mechanism are provided in Appendix G.

7.3. Diaphragm restraint and stability behaviour

Besides transferring lateral loads to the core, the floor system provides lateral restraint to the columns. The stability behaviour of the building therefore depends on how strongly the floor diaphragm restrains storey translation. Numerical verification of the analytical models are given in Appendix F.

7.3.1. Column–spring model

Consider a pin-ended column of height L that is laterally restrained at the storey level by the floor diaphragm. The diaphragm restraint is idealised as a translational spring with stiffness k_{floor} acting at the column top. This simplified model captures how diaphragm stiffness influences column stability.

Two limiting buckling modes can be distinguished. If the diaphragm is infinitely stiff ($k_{\text{floor}} \to \infty$), storey translation is suppressed and the column exhibits classical member buckling between its end restraints. For a pin-ended column, the corresponding Euler critical load is

$$P_{\text{cr,ns}} = \frac{\pi^2 EI}{L^2}, \tag{7.7}$$

where EI is the column bending stiffness about the relevant axis.

If the diaphragm has finite stiffness, storey translation is possible and the column–floor interaction may instead be governed by a global *sway buckling* mode. For the column–spring model, the corresponding critical load reads

$$P_{\text{cr,sw}} = k_{\text{floor}}\, L, \tag{7.8}$$

with derivation provided in Appendix F. Equations (7.7) and (7.8) therefore bound the stability behaviour: for high k_{floor} member buckling governs, whereas for low k_{floor} sway buckling governs and P_{cr} scales linearly with the available storey restraint.

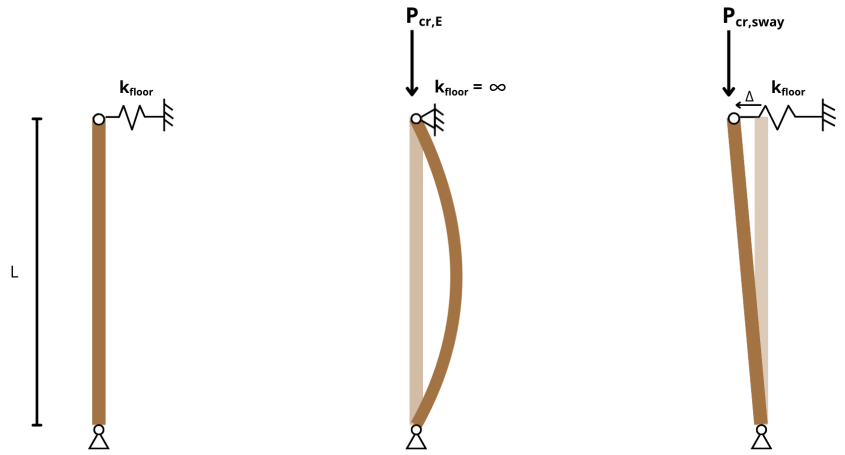

Figure 7.5: Column restrained by the floor diaphragm: (left) equivalent storey spring k_{floor}, (middle) member (Euler) buckling for $k_{\text{floor}} \to \infty$, (right) sway buckling for finite k_{floor}.

The required storey restraint stiffness for member (Euler) buckling to govern follows from $P_{\text{cr,ns}} = P_{\text{cr,sw}}$, and reads

$$k_{\text{req}} = \frac{\pi^2 EI}{L^3}. \tag{7.9}$$

For $k_{\text{floor}} \gtrsim k_{\text{req}}$ member buckling governs, whereas for $k_{\text{floor}} < k_{\text{req}}$ the stability margin is controlled by sway buckling.

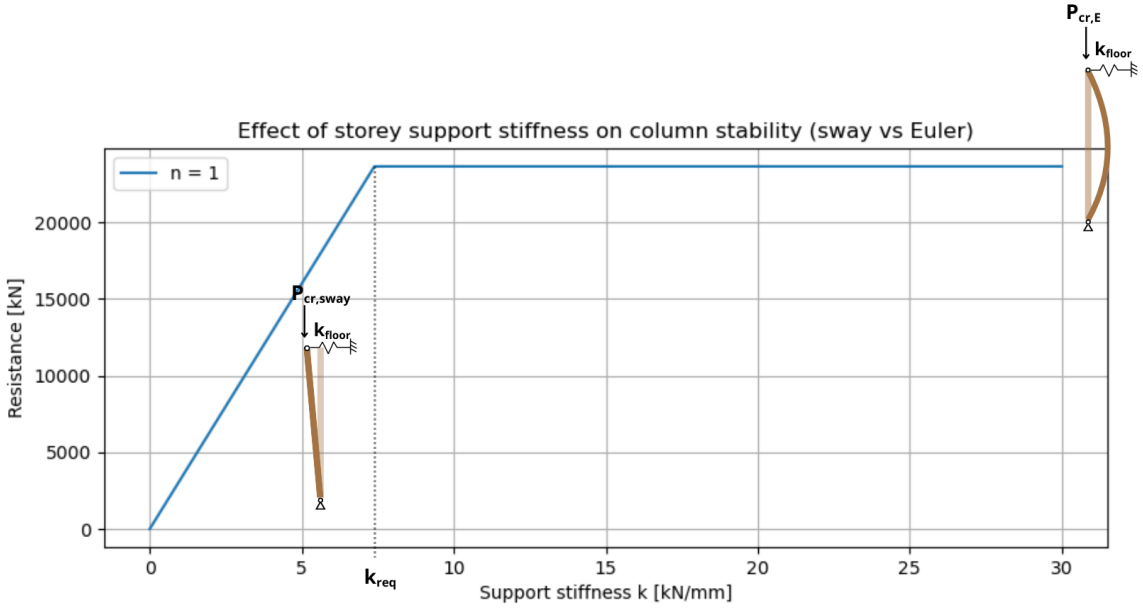

Figure 7.6: Critical load versus storey restraint stiffness for the column–spring model.

As illustrated in Figure 7.6, the column response transitions from sway-controlled to Euler-type buckling when the available diaphragm stiffness exceeds k_{req}. For lower stiffness values, the stability capacity is directly governed by the diaphragm stiffness, with P_{cr} scaling linearly with k_{floor}.

This behaviour can be interpreted in terms of a cantilever: the floor spans from the core outwards, and its deformation increases with distance from the core (Figure 7.4). As a result, columns located further away from the core experience a lower effective lateral restraint, making the in-plane stiffness of the diaphragm a governing parameter for their stability.

7.3.2. Eigenvalue stability analysis in RFEM

The column–spring model provides a simplified interpretation of how diaphragm stiffness can influence column stability. In the real building, however, the storey restraint is not provided by a single spring acting on an individual column or column row. Instead, the lateral restraint emerges from the combined response of the entire structural system, including the diaphragm, the panel connections, the concrete core, and the interaction between multiple column lines.

In RFEM, stability is assessed using a global eigenvalue (linear buckling) analysis. First, the structural response under the applied load combination is calculated, which determines the axial force distribution in the columns. Based on this *pre-stressed* state, the software then evaluates which deformation pattern would cause the structure to lose stability if the loads were increased.

This is formulated as an eigenvalue problem of the form [30]

$$[\mathbf{K}_L + \lambda_{\text{cr}}\, \mathbf{K}_G]\, \boldsymbol{\phi} = \mathbf{0}, \tag{7.10}$$

where $\mathbf{K}_L$ is the linear elastic stiffness matrix of the structure (core, diaphragm and connections), $\mathbf{K}_G$ is the geometric stiffness matrix generated by the axial force state, λ_{cr} is the critical load factor, and $\boldsymbol{\phi}$ is the corresponding buckling mode shape.

The mode shape $\boldsymbol{\phi}$ can be interpreted as the deformation pattern that requires the least additional load to trigger instability. The critical load factor λ_{cr} indicates by which factor the applied load combination would have to be multiplied to reach the elastic buckling limit.

Although the simplified column–spring model cannot reproduce the exact critical load of the full system, it helps to interpret trends in the RFEM results. In particular, reducing diaphragm stiffness lowers the effective global lateral restraint (i.e. reduces $\mathbf{K}_L$), which promotes global sway-buckling modes and reduces the critical load factor. This implies lower member critical forces and therefore a larger effective buckling length L_{eff}. Moreover, the first mode often localises in the lower storeys because the geometric stiffness contribution $\mathbf{K}_G$ is governed by the axial force level, which is highest near the base of the building.

7.4. Second-order effects

Second-order effects arise when structural deformations influence the internal force equilibrium. These effects become important when axial forces interact with lateral displacements, which may lead to amplification of both displacements and internal forces.

7.4.1. Classification

Eurocode 3 [31] and Eurocode 5 [25] provide criteria to assess whether second-order effects must be considered in the structural analysis. A common indicator is the critical load factor λ_{cr}, obtained from eigenvalue stability analysis. This factor represents the multiplier that would cause the structure to reach its elastic buckling limit.

If the critical load factor is sufficiently large, the structure is considered stable against global buckling and second-order effects may be neglected. However, when the stability margin becomes smaller, geometric non-linear effects must be taken into account.

In practice, structures are classified according to the value of λ_{cr}. When

$$\lambda_{\text{cr}} < 10 \tag{7.11}$$

the structure is generally considered *sway-sensitive*, and second-order effects should be included in the analysis.

7.4.2. First- and second-order analysis

In a first-order (linear) analysis, equilibrium is evaluated with respect to the initial (undeformed) geometry of the structure. A lateral load produces a corresponding lateral displacement, and the internal forces are determined from this displacement assuming that the geometry of the structure does not change during the analysis. In other words, the effect of the deformation on the equilibrium equations is neglected.

In a second-order (geometrically non-linear) analysis, equilibrium is evaluated on the deformed configuration of the structure. A lateral load first produces a lateral displacement, which causes the columns to become inclined. Because the members carry axial forces, this inclination introduces additional horizontal force components that further increase the lateral displacement. This interaction between axial forces and lateral displacements is commonly referred to as the P–Δ effect, it is illustrated in Figure 7.7.

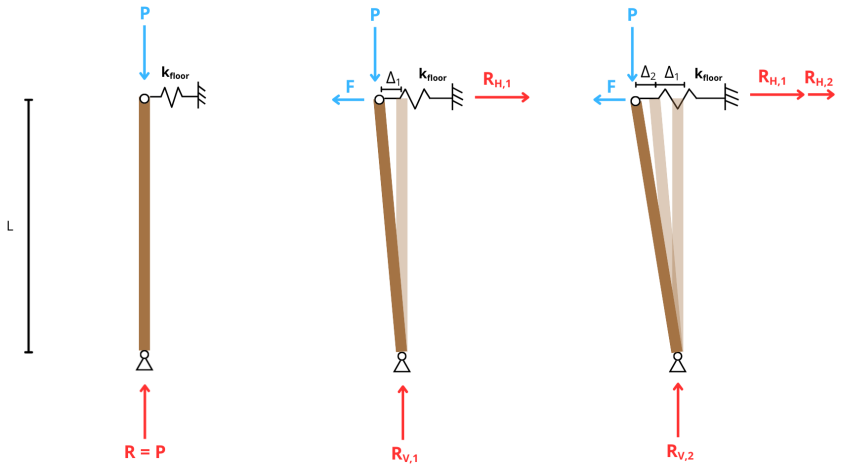

Figure 7.7: Second-order (P–Δ) effect for a pin-ended column restrained by an equivalent diaphragm stiffness k_{floor}.

The mechanism illustrated in Figure 7.7 uses a pin-ended column of height L carrying an axial force P and subjected to a lateral load F at floor level. The floor diaphragm is represented by an equivalent translational spring of stiffness k_{floor}.

For a lateral displacement Δ, the diaphragm provides the restoring reaction

$$R_H = k_{\text{floor}}\,\Delta. \tag{7.12}$$

For small rotations $\theta \approx \Delta/L$, the axial force introduces an additional horizontal component

$$P_h \approx P\,\frac{\Delta}{L}. \tag{7.13}$$

Horizontal equilibrium gives

$$k_{\text{floor}}\,\Delta = F + P\,\frac{\Delta}{L}, \tag{7.14}$$

and the amplified displacement follows as

$$\Delta = \frac{F}{k_{\text{floor}} - P/L}. \tag{7.15}$$

Equation (7.15) shows that second-order amplification increases as P/L approaches k_{floor}. In the limit, $P \to P_{\text{cr,sway}} = k_{\text{floor}}L$, the denominator approaches zero and the displacement tends to infinity, indicating loss of stability.

The equilibrium expressed by Eq. (7.14) can be solved iteratively by updating the displacement and the corresponding horizontal force components. For load levels below the critical value $P_{\text{cr,sway}}$, the iterations converge to a finite displacement. At the critical load, however, the iterations no longer converge, which reflects the onset of instability. This behaviour is illustrated in Figure 7.8.

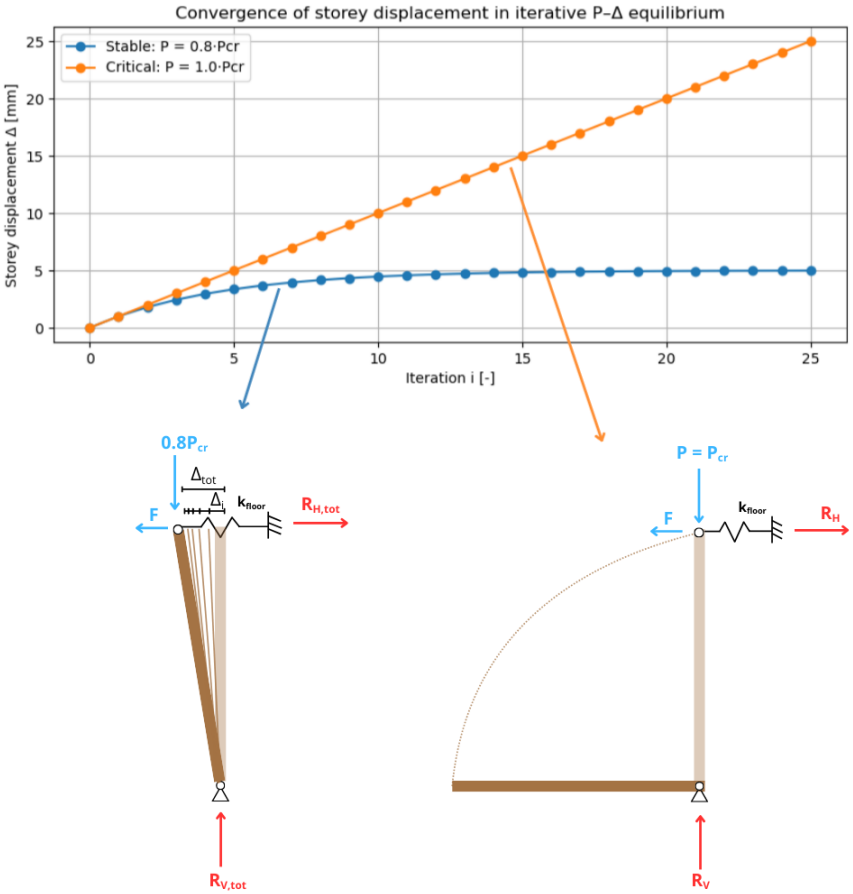

Figure 7.8: Iterative solution of the P–Δ equilibrium equation for a column restrained by a diaphragm spring.

8

Results

This chapter presents the results of Part III, which evaluates how the in-plane stiffness of the CLT floor system influences the structural response of the case-study building.

A set of RFEM model variants is analysed in which the stiffness of the panel–core and panel–panel connections is varied, and grout at the panel–core interface is either included or excluded. The results are evaluated in terms of global stability, displacement response, connection forces, and column verification.

For each variant, both first-order and second-order results are reported in order to show the influence of geometric non-linearity on the structural response. The chapter first defines the verification procedure and load combinations, then introduces the investigated model variants, and finally presents the results for the considered verification categories.

8.1. Verification

To define a consistent verification procedure, the analysis philosophy of Eurocode 3 [31], formulated for steel frames, is adopted to distinguish between global sway instability and member buckling. In EC3, this distinction is made through the elastic critical load factors for global sway buckling and non-sway member buckling. These critical load factors indicate how sway-sensitive the structure is and, therefore, how sensitive it is to second-order effects. They are used to determine the required analysis order and the imposed imperfections.

The same distinction is used here to select the appropriate analysis route for the case-study building, while the member verification itself is based on Eurocode 5. According to EC5, second-order effects may either be accounted for implicitly by reduction factors or explicitly by including geometrical non-linearity and imperfections in the analysis. In the present RFEM models, the explicit route is adopted for the global system response. The response is therefore evaluated by means of first- and second-order analysis, with imposed sway and bow imperfections of $\phi = 1/200$ and $e = 1/1000$, respectively.

A distinction is made between cases governed by member buckling and cases governed by global sway buckling. When the governing instability mode corresponds to member buckling, the column is verified as an individual compression member. In that case, the first-order axial force is used together with the EC5 buckling format, including the buckling reduction factor k_c and an effective buckling length equal to the storey height. Since the columns are pinned and do not transfer end moments, this verification is based on axial compression only.

When the governing instability mode corresponds to global sway buckling, the instability is not governed by Euler buckling of an individual column, but by the sway deformation of the structural system. In those cases, the columns remain approximately straight and participate in the global frame deformation. Therefore, no separate buckling reduction factor k_c or effective buckling length is introduced for the column verification. Instead, the column check is based directly on the design internal forces obtained from the selected global analysis, since the stability effects are already represented through the analysis order and the imposed imperfections.

The verification procedure is summarised in Figure 8.1. It starts with an eigenvalue stability analysis under vertical loading only, from which the first buckling mode and the corresponding critical load factor are obtained. Depending on whether the governing mode is identified as global sway buckling or member buckling, the system is classified as sway-sensitive or non-sway. This classification is then used to select the appropriate analysis order and imposed imperfections.

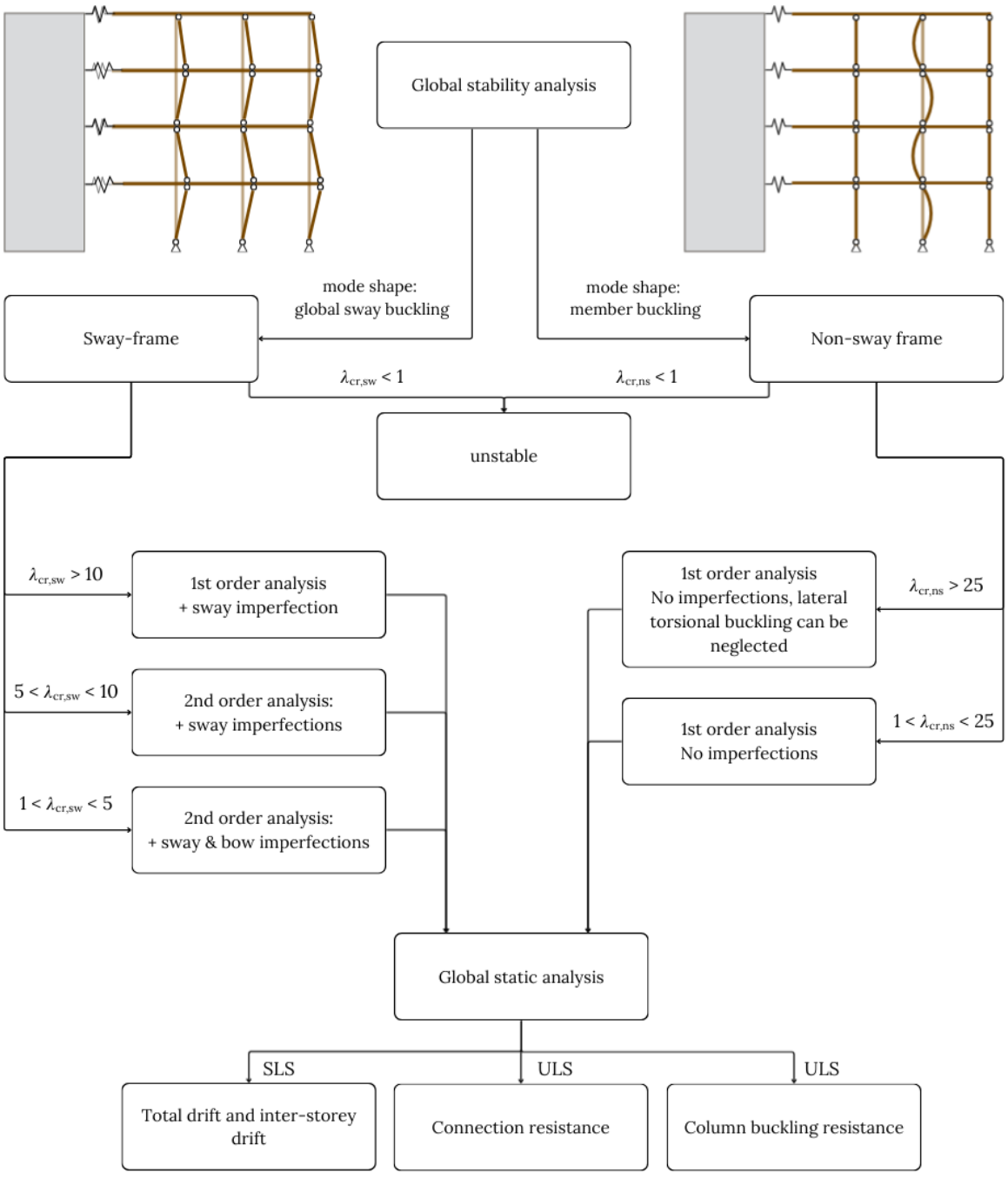

Figure 8.1: Verification procedure showing which analysis type, imperfections, and checks follow from the critical load factor and governing instability mode.

For sway-sensitive variants, the critical load factor determines whether first-order analysis with sway imperfections is sufficient or whether second-order (geometrically non-linear) analysis is required, with sway imperfections only or with both sway and bow imperfections. Based on this classification, the

corresponding analysis type and imperfections are applied in the RFEM model, after which a global static analysis is carried out from which the design response quantities are obtained.

The resulting response is evaluated in three verification categories. Serviceability is assessed through the overall top displacement and the inter-storey drift. At ultimate limit state, the diaphragm connections are verified for the governing connection forces. The column verification is also carried out at ultimate limit state, but depends on the governing instability mode. For member buckling cases, the column is verified as an individual compression member using the first-order axial force $N_{1,Ed}$, the buckling reduction factor k_c, and an effective buckling length equal to the storey height. For sway-governed cases, the column is verified directly from the internal forces obtained from the global analysis: using $N_{1,Ed}$ for first-order analysis with sway imperfection, $N_{2,Ed}$ for second-order analysis with sway imperfection, and $N_{2,Ed}$ together with $M_{2,Ed}$ when both sway and bow imperfections are included.

Table 8.1: Overview of the verification checks adopted for the RFEM variants.

Check	Load combination	Verification
Global stability	$LC1 + LC2 + LC3$	$\lambda_{\text{cr}} \geq 1$
Displacements	$LC1 + LC2 + LC5 + 0.40\,LC3$	Overall top displacement: $u_{\text{top}} \leq H/500$ Inter-storey displacement: $u_i \leq h_i/300$
Connection resistance	$1.20\,LC1 + 1.20\,LC2 + 1.50\,LC5 + 0.60\,LC3$	Panel–panel fasteners: $\dfrac{F_{Ed}}{F_{Rd,PP}} \leq 1$ Panel–core fasteners: $\dfrac{F_{Ed}}{F_{Rd,PC}} \leq 1$ Timber bearing: $\dfrac{\sigma_{c,t,Ed}}{f_{c,t,d}} \leq 1$
Column buckling resistance	$1.20\,LC1 + 1.20\,LC2 + 1.50\,LC5 + 0.60\,LC3$	Member buckling cases: $\dfrac{N_{Ed}}{k_c\,A\,f_{c,0,d}} \leq 1$ Sway-governed cases without bow imperfection: $\dfrac{N_{Ed}}{A\,f_{c,0,d}} \leq 1$ Sway-governed cases with bow imperfection: $\dfrac{N_{Ed}}{A f_{c,0,d}} + \dfrac{M_{z,Ed}}{W_z f_{m,z,d}} \leq 1$

Note: LC = load case; LC1 = self-weight, LC2 = additional permanent load, LC3 = imposed load, and LC5 = wind load in global Y-direction. The governing SLS and ULS load combinations are based on the combination rules of EN 1990 [32].

8.2. Model variants

Material properties and member dimensions are taken from the case study description in Chapter 2. The investigated variants differ only in the assumed in-plane stiffness of the floor connections that couple the timber frame to the concrete core and connect adjacent CLT panels.

8.2.1. Connection stiffness input

Table 8.2 lists the connection stiffness values adopted in the RFEM model. For the panel–core connections, two stiffness values are defined: k_{SLS} and k_{fin}. The value k_{SLS} represents the connection stiffness before shrinkage and relaxation have taken place, whereas k_{fin} represents a reduced stiffness after these

processes.

In the present case-study models, the panel–core connections are assigned the stiffness k_{fin}. This was done to represent a reduced connection stiffness after shrinkage has taken place. Due to shrinkage, the fasteners may already have undergone some slip before lateral loading occurs. As a result, the stiffness available for subsequent diaphragm action may be lower than the initial stiffness.

In the present modelling approach, this reduction is approximated using the long-term effective stiffness based on k_{def}. This should be regarded as a practical modelling assumption rather than as a directly validated representation of the connection behaviour under short-term lateral loading after prior shrinkage. Strictly speaking, for short-duration lateral actions such as wind, k_{SLS} would be the more appropriate stiffness parameter. However, it is currently uncertain to what extent prior shrinkage reduces the effective connection stiffness in such a loading situation, and further research would be required to establish a more realistic stiffness model for this post-shrinkage condition. The implications of this assumption for the interpretation of the results are discussed further in Chapter 9.

The reduction to k_{fin} is not applied to timber–timber interfaces, because these joints are not subjected to shrinkage-induced restraint forces and therefore no comparable relaxation effect is considered.

Table 8.2: Connection stiffness input used in the RFEM model.

Connection	Type	Grout	Spacing s [m]	k_{SLS} [kN/m^2]	k_{fin} [kN/m^2]
PC0	Panel–core	Yes	–	fixed	fixed
PC1a	Panel–core	No	0.1	60142	23132
PC1b	Panel–core	Yes	0.1	60142	23132
PC2a	Panel–core	No	0.2	30071	11566
PC2b	Panel–core	Yes	0.2	30071	11566
PC3a	Panel–core	No	0.3	20047	7711
PC3b	Panel–core	Yes	0.3	20047	7711
PP0	Panel–panel	n/a	–	fixed	n/a
PP1	Panel–panel	n/a	0.1	30071	n/a
PP2	Panel–panel	n/a	0.2	15036	n/a
PP3	Panel–panel	n/a	0.3	10024	n/a
PP4	Panel–panel	n/a	0.4	7518	n/a
PB0	Panel–beam	n/a	-	fixed	n/a
PB1	Panel–beam	n/a	0.1	30071	n/a

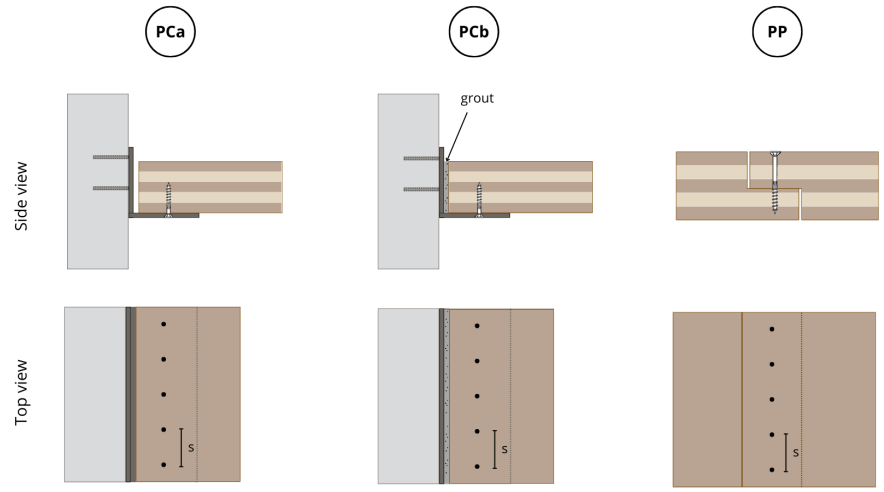

Figure 8.2: Connection layout for panel–core (PCa), panel–core + grout (PCb) and panel–panel (PP) connection types.

8.2.2. Variant matrix

Table 8.3 summarises the analysed RFEM cases. Case C0 is a reference case with fixed connections. All other cases represent segmented floor with connections with finite stiffness and combine a selected panel–core connection type (PC1–PC3, with or without grout) with a panel–panel connection type (PP1–PP4). The qualitative labels *stiff*, *medium*, *weak* and *very weak* describe the relative stiffness levels within the investigated set.

Table 8.3: Analysed RFEM cases and connection combinations.

Variant	Panel–core (PC)	Panel–panel (PP)	Description
C0	PC0	PP0	fixed connections
C1a1	PC1a	PP1	stiff PC + stiff PP
C1b1	PC1b	PP1	stiff PC + grout + stiff PP
C1a2	PC1a	PP2	stiff PC + medium PP
C1b2	PC1b	PP2	stiff PC + grout + medium PP
C1a3	PC1a	PP3	stiff PC + weak PP
C1b3	PC1b	PP3	stiff PC + grout + weak PP
C1a4	PC1a	PP4	stiff PC + very weak PP
C1b4	PC1b	PP4	stiff PC + grout + very weak PP
C2a1	PC2a	PP1	medium PC + stiff PP
C2b1	PC2b	PP1	medium PC + grout + stiff PP
C2a2	PC2a	PP2	medium PC + medium PP
C2b2	PC2b	PP2	medium PC + grout + medium PP
C2a3	PC2a	PP3	medium PC + weak PP
C2b3	PC2b	PP3	medium PC + grout + weak PP
C2a4	PC2a	PP4	medium PC + very weak PP
C2b4	PC2b	PP4	medium PC + grout + very weak PP
C3a1	PC3a	PP1	weak PC + stiff PP
C3b1	PC3b	PP1	weak PC + grout + stiff PP
C3a2	PC3a	PP2	weak PC + medium PP
C3b2	PC3b	PP2	weak PC + grout + medium PP
C3a3	PC3a	PP3	weak PC + weak PP
C3b3	PC3b	PP3	weak PC + grout + weak PP
C3a4	PC3a	PP4	weak PC + very weak PP
C3b4	PC3b	PP4	weak PC + grout + very weak PP

8.3. Results: global stability

This section presents the global stability results of the investigated variants. In line with the verification procedure defined in Section 8.1, a distinction is made between critical load factors associated with member buckling, denoted $\lambda_{cr,ns}$, and those associated with global sway buckling, denoted $\lambda_{cr,sw}$. The objective is to identify how the floor diaphragm stiffness influences the governing instability mechanism, the sway sensitivity of the system, and the resulting choice of analysis order and imposed imperfections.

A clear distinction is observed between the reference case C0 with fixed connections and the variants with finite diaphragm stiffness. Only C0 shows a first mode governed by member buckling, as illustrated in Figure 8.3. Its reported critical load factor is therefore $\lambda_{cr,ns} = 5.959$. In contrast, all other variants exhibit a global sway first buckling mode, similar to that shown for C1a1 in Figure 8.4. For these variants, the reported critical load factors are therefore interpreted as $\lambda_{cr,sw}$. This indicates that reducing diaphragm stiffness shifts the governing instability mechanism from member buckling towards global sway buckling.

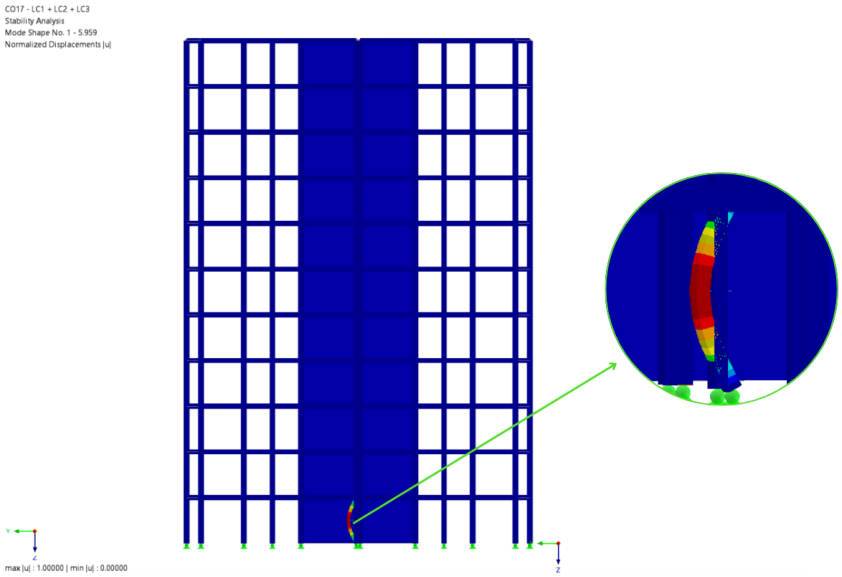

Figure 8.3: Variant C0: first buckling mode shape, $\lambda_{cr,ns} = 5.959$.

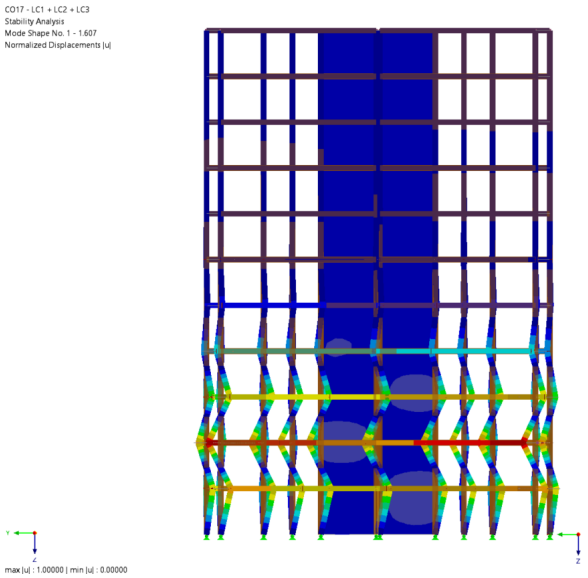

Figure 8.4: variant C1a1: first buckling mode shape, $\lambda_{cr,sw} = 1.607$.

The critical load factor must therefore be interpreted together with the corresponding mode shape. For the variants with a global sway first mode, a low $\lambda_{cr,sw}$ indicates a reduced global stability margin and a strong sensitivity to second-order effects. For C0, by contrast, the first mode is governed by member buckling rather than by storey sway, and its value of $\lambda_{cr,ns} = 5.959$ therefore reflects member instability rather than global sway sensitivity.

The most flexible configurations show the lowest global stability reserve. Variants C2a2, C2a3, C2a4, C3a1, C3a2, C3a3 and C3a4 have $\lambda_{cr,sw} < 1$, indicating that the applied load level exceeds the elastic stability limit for the governing sway mode.

A consistent trend is observed between corresponding non-grouted (a) and grouted (b) variants. For the same connection stiffnesses, the b-variants systematically show higher critical load factors than the corresponding a-variants, indicating that grout increases the effective diaphragm stiffness and improves the global stability margin. For example, $\lambda_{cr,sw}$ increases from 1.607 for C1a1 to 3.049 for C1b1, from

1.339 for C1a2 to 2.366 for C1b2, and from 0.869 for C3a1 to 2.591 for C3b1. In the investigated set, all b-variants have $\lambda_{cr,sw} > 1$, whereas several a-variants fall below the elastic stability limit.

The eigenvalue results therefore show that reduced diaphragm stiffness leads not only to lower critical load factors, but also to a change in the governing instability mechanism from member buckling to global sway buckling. This distinction directly affects the required analysis route. For all variants with a global sway first mode, second-order analysis is required in combination with sway and bow imperfections, in accordance with the adopted verification procedure.

Table 8.4: Critical load factors and governing first buckling mode for all investigated variants.

Variant	First mode	Critical load factor	[-]
C0	Member buckling	$\lambda_{cr,ns}$	5.959
C1a1	Global sway	$\lambda_{cr,sw}$	1.607
C1b1	Global sway	$\lambda_{cr,sw}$	3.049
C1a2	Global sway	$\lambda_{cr,sw}$	1.339
C1b2	Global sway	$\lambda_{cr,sw}$	2.366
C1a3	Global sway	$\lambda_{cr,sw}$	1.174
C1b3	Global sway	$\lambda_{cr,sw}$	1.985
C1a4	Global sway	$\lambda_{cr,sw}$	1.059
C1b4	Global sway	$\lambda_{cr,sw}$	1.761
C2a1	Global sway	$\lambda_{cr,sw}$	1.106
C2b1	Global sway	$\lambda_{cr,sw}$	2.743
C2a2	Global sway	$\lambda_{cr,sw}$	0.965
C2b2	Global sway	$\lambda_{cr,sw}$	2.153
C2a3	Global sway	$\lambda_{cr,sw}$	0.870
C2b3	Global sway	$\lambda_{cr,sw}$	1.833
C2a4	Global sway	$\lambda_{cr,sw}$	0.800
C2b4	Global sway	$\lambda_{cr,sw}$	1.622
C3a1	Global sway	$\lambda_{cr,sw}$	0.869
C3b1	Global sway	$\lambda_{cr,sw}$	2.591
C3a2	Global sway	$\lambda_{cr,sw}$	0.776
C3b2	Global sway	$\lambda_{cr,sw}$	2.045
C3a3	Global sway	$\lambda_{cr,sw}$	0.712
C3b3	Global sway	$\lambda_{cr,sw}$	1.747
C3a4	Global sway	$\lambda_{cr,sw}$	0.662
C3b4	Global sway	$\lambda_{cr,sw}$	1.551

8.4. Results: total drift and inter-storey drift

Following the global stability assessment in Section 8.1, this section evaluates the serviceability response of the building under lateral loading. Whereas the eigenvalue analysis identified the sway sensitivity of the variants, the present section examines how this sensitivity translates into actual deformations under the governing SLS load combination.

The influence of diaphragm stiffness is quantified through the overall top displacement u_{top} and the maximum inter-storey drift $u_{i,max}$. Results are reported for both first- and second-order analyses. The results are assessed against a total displacement limit of $H/500$ and an inter-storey drift limit of $h_i/300$. With a building height $H = 11 \times 3200 = 35{,}200$ mm, this gives $u_{top,lim} = 70.4$ mm. With a storey height $h_i = 3200$ mm, the drift limit becomes $u_{i,max,lim} = 10.7$ mm.

Table 8.5 reports u_{top} and $u_{i,max}$ for all variants. Cases for which no second-order result was available are indicated by a dash. These correspond to variants for which the second-order analysis did not converge, consistent with the instability sensitivity identified in the global stability assessment.

Table 8.5: SLS checks per RFEM case for 1st- and 2nd-order analysis.

Variant	$u_{\text{top},1}$ [mm]	$u_{i,\max,1}$ [mm]	$u_{\text{top},2}$ [mm]	$u_{i,\max,2}$ [mm]
C0	6.8	0.7	6.9	0.7
C1a1	8.0	1.9	8.1	2.3
C1b1	7.5	1.5	7.6	1.6
C1a2	8.4	2.4	8.5	3.0
C1b2	7.9	1.8	8.0	2.1
C1a3	8.9	2.6	9.0	3.6
C1b3	8.3	2.1	8.4	2.4
C1a4	9.3	3.1	9.2	4.8
C1b4	8.5	2.4	8.5	3.0
C2a1	8.7	2.7	8.8	3.9
C2b1	7.9	1.8	7.9	2.0
C2a2	9.1	3.1	9.2	5.5
C2b2	8.2	2.1	8.3	2.6
C2a3	9.7	3.5	9.5	10.3
C2b3	8.5	2.5	8.6	3.1
C2a4	9.8	3.9	–	–
C2b4	8.8	2.7	8.8	3.7
C3a1	9.3	3.3	9.3	9.7
C3b1	8.0	1.9	8.1	2.3
C3a2	9.7	3.8	–	–
C3b2	8.4	2.3	8.5	2.9
C3a3	10.0	4.2	–	–
C3b3	8.7	2.6	8.8	3.6
C3a4	10.4	4.4	–	–
C3b4	9.0	3.0	9.0	4.3

Across all converged variants, both the overall top displacement and the inter-storey drift remain within the specified limits. The top displacement is consistently small compared to the limit of $H/500$ and is therefore not governing. The inter-storey drift is more sensitive to the diaphragm stiffness and to the inclusion of second-order effects.

The influence of second-order effects is most pronounced in the weaker diaphragm configurations. In these cases, a clear amplification of $u_{i,\max}$ is observed in second-order analysis. The maximum drift occurs in the lowest storey, where the axial force level is highest and geometric non-linearity has the largest influence.

Although all converged variants satisfy the drift limit of $h_i/300$, two variants (C2a3 and C3a1) approach this limit in second-order analysis, with $u_{i,\max} = 10.3$ mm and 9.7 mm, respectively. This indicates that these configurations are close to the serviceability boundary and are sensitive to further reductions in diaphragm stiffness.

Several of the weakest variants (C2a4, C3a2, C3a3, and C3a4) do not converge in the second-order analysis. This behaviour is consistent with the global stability assessment and indicates that these configurations are governed by instability before reaching the SLS drift limit.

Comparing corresponding non-grouted (a) and grouted (b) variants shows a consistent reduction in both u_{top} and $u_{i,\max}$ when grout is present, indicating a stiffer floor–core coupling. Overall, the results show that diaphragm stiffness primarily influences the serviceability response through inter-storey drift and second-order amplification effects, rather than through absolute displacement levels.

Figure 8.5 shows the first-order deformed shape for case C2a3, which results in a relatively smooth drift profile over the building height.

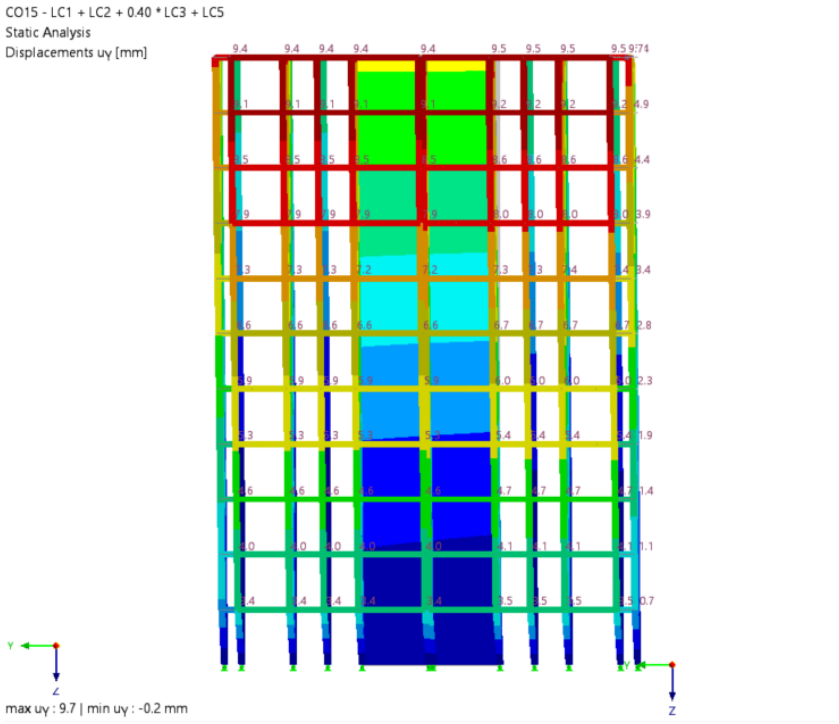

Figure 8.5: First-order lateral displacements in global Y for case C2a3 under the governing SLS combination.

Figure 8.6 shows the corresponding second-order deformed shape. In second-order analysis, the deformation becomes more concentrated in the lower storeys, leading to a clear amplification of the inter-storey drift. This is consistent with the sway sensitivity identified in the eigenvalue analysis and illustrates that reduced diaphragm restraint increases the sensitivity of the building response to second-order effects.

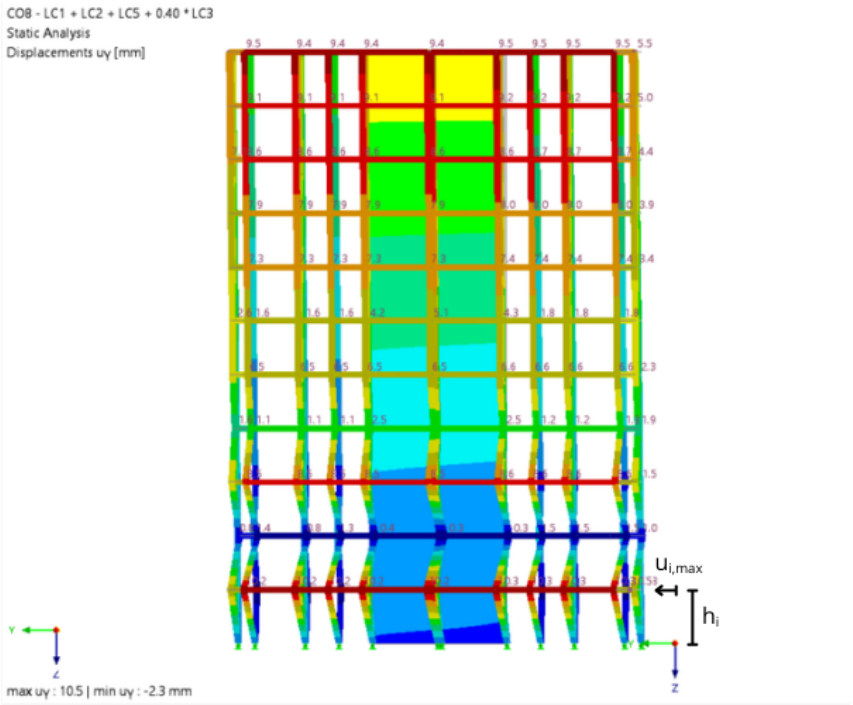

Figure 8.6: Second-order lateral displacements in global Y for case C2a3 under the governing SLS combination.

8.5. Results: connection resistance

Following the global stability and serviceability assessment, this section examines how diaphragm stiffness and second-order effects influence the ULS force demand in the diaphragm connections. The extracted quantities are the governing panel–core normal resultant per unit length, $n_{\mathrm{PC,max}}$, acting along the panel–core interface, and the resultant perpendicular to this interface, $v_{y,\mathrm{PC,max}}$. For the panel–panel interface, the governing normal resultant per unit length is reported as $n_{\mathrm{PP,max}}$. These line resultants are used as input for the fastener-level checks presented in Appendix H.

Figures 8.7 and 8.8 illustrate the extracted quantities. The quantity $v_{y,\mathrm{PC}}$ represents the resultant force perpendicular to the panel–core interface obtained from the line hinge. In the grouted variants this resultant becomes highly localised, reflecting the development of a compression contact zone at the interface (see Appendix G).

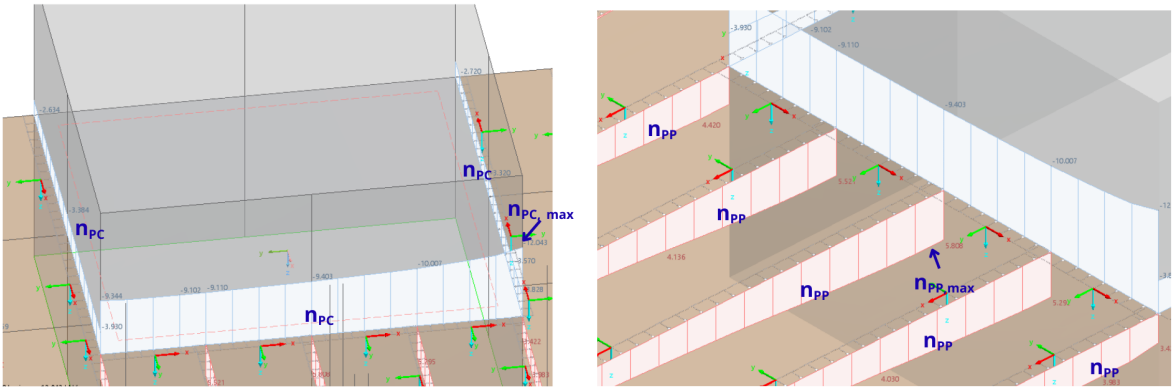

Figure 8.7: Example of the normal-force resultants in local x for C1a1. Left: panel–core normal force n_{PC} and the location of $n_{\mathrm{PC,max}}$. Right: panel–panel normal force n_{PP} and the location of $n_{\mathrm{PP,max}}$.

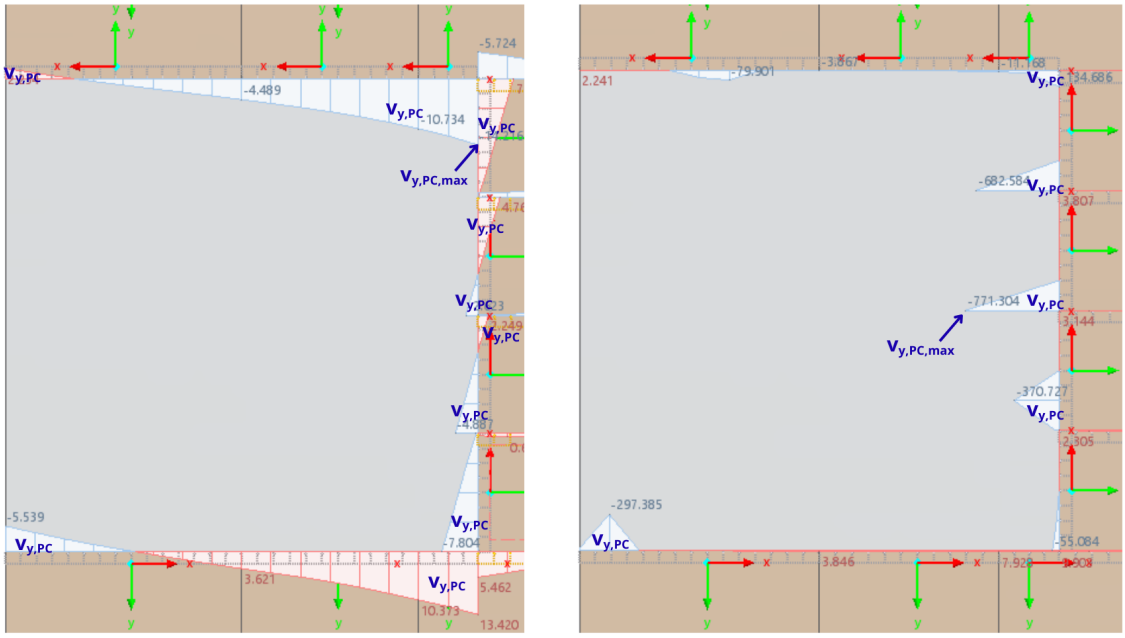

Figure 8.8: Example panel–core resultant in local y, $v_{y,\mathrm{PC}}$. Left: non-grouted case (C1a1). Right: grouted case (C1b1).

A dash in Table 8.6 indicates that no second-order result was available for that variant. This occurs where the second-order ULS analysis did not converge.

Table 8.6: Connection force demand in ULS per RFEM case for 1st- and 2nd-order analysis.

Variant	$n_{PC,max,1}$ [kN/m]	$v_{y,PC,max,1}$ [kN/m]	$n_{PP,max,1}$ [kN/m]	$n_{PC,max,2}$ [kN/m]	$v_{y,PC,max,2}$ [kN/m]	$n_{PP,max,2}$ [kN/m]
C0	-33.7	-56.2	10.1	-34.5	-56.3	10.1
C1a1	-10.5	-15.3	6.5	-13.0	-18.7	8.4
C1b1	-8.0	-821.8	5.4	-8.5	-821.8	6.4
C1a2	-10.0	-16.8	5.6	-13.7	-22.9	8.2
C1b2	-8.1	-1175.4	4.3	-9.3	-1177.8	5.4
C1a3	-9.7	-17.9	8.0	-15.7	-28.9	8.9
C1b3	-8.2	-1416.3	6.6	-10.0	-1423.8	8.2
C1a4	-9.5	-18.9	4.6	–	–	–
C1b4	-8.1	-1625.1	3.5	-11.1	-1635.7	5.2
C2a1	-10.3	-12.8	6.8	-27.2	-34.8	20.4
C2b1	-6.8	-853.3	5.0	-8.0	-853.3	6.4
C2a2	-10.0	-13.8	6.0	–	–	–
C2b2	-7.3	-1254.1	4.8	-9.3	-1254.1	7.0
C2a3	-9.7	-14.6	5.4	–	–	–
C2b3	-7.5	-1526.7	4.1	-10.8	-1531.2	6.4
C2a4	-9.6	-15.2	5.0	–	–	–
C2b4	-7.5	-1747.8	3.7	-13.0	-2095.7	7.1
C3a1	-10.0	-11.8	6.9	–	–	–
C3b1	-6.0	-857.5	5.0	-7.4	-857.4	6.8
C3a2	-9.9	-12.5	6.1	–	–	–
C3b2	-6.6	-1275.3	5.2	-9.3	-1275.3	6.9
C3a3	-9.8	-13.0	5.6	–	–	–
C3b3	-6.8	-1559.6	4.1	-12.0	-2227.3	8.8
C3a4	-9.6	-13.5	5.2	–	–	–
C3b4	-4.6	-1287.7	2.5	–	–	–

Table 8.6 shows two main trends. First, grout changes the load-transfer mechanism at the panel–core interface. Compared with the non-grouted (a) variants, the grouted (b) variants generally show lower panel–core normal-force resultants $n_{PC,max}$, while the resultant perpendicular to the interface, $v_{y,PC,max}$, becomes much larger due to a local compression contact peak.

Second, second-order analysis increases the connection force demand, particularly in the variants that were already identified as sway-sensitive in the global stability assessment. This is most evident in the more flexible non-grouted series. For example, in C2a1 the panel–core normal-force resultant increases from −10.3 kN/m to −27.2 kN/m, the panel–core shear resultant from −12.8 kN/m to −34.8 kN/m, and the panel–panel normal resultant from 6.8 kN/m to 20.4 kN/m. This confirms that reduced diaphragm stiffness can substantially amplify diaphragm connection demand in second-order analysis.

The red values in Table 8.6 indicate where the corresponding fastener-level checks become non-compliant. Because the design checks are performed per fastener, similar line resultants do not necessarily lead to the same verification outcome: for larger fastener spacing, the force per fastener becomes higher. As a result, weaker connection layouts may fail even when the global line resultants are of a similar order.

Three governing failure mechanisms can be distinguished. The first is insufficient panel–core normal-force resistance, which becomes critical mainly for the weakest panel–core layouts and for cases with strong second-order amplification. The second is insufficient panel–core shear resistance in the non-grouted variants, which governs several medium and weak a-variants. The third is insufficient panel–panel resistance, although this is less critical overall and becomes decisive only in isolated cases such as C2b4.

Overall, the results show that reduced diaphragm stiffness does not only increase sway sensitivity at global level, but also raises the ULS force demand in the diaphragm connections. The panel–panel connection mainly affects the response indirectly through its influence on diaphragm stiffness, while the panel–core connection is more directly involved in the governing ULS checks. Detailed fastener-level derivations and utilisation ratios are given in Appendix H.

8.6. Results: column stability

This section evaluates the ULS stability verification of the timber frame columns using the design approach defined earlier in this chapter, i.e. based on the governing member forces obtained from the

imperfect global model with second-order analysis. In line with the adopted verification procedure, sway imperfections and member bow imperfections are included in the ULS analysis.

To examine whether the diaphragm variants influence the member-level stability verification of the timber frame, one representative *governing* column is considered across all variants. The selected member is critical because it experiences the highest axial compression level and is therefore the most relevant column for the combined compression and bending check.

Figure 8.9 shows the location of the selected column in the floor plan. The column has a cross-section of 240×400 mm.

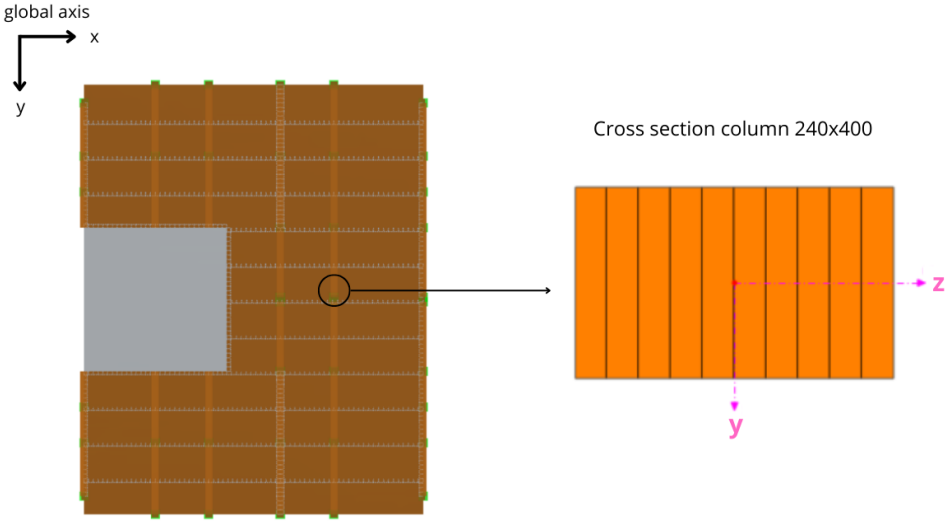

Figure 8.9: Selected representative column used for the ULS stability verification.

8.6.1. Column stability results

For the selected column, RFEM gives essentially the same governing design forces for all sway-governed variants that converge in the ULS second-order analysis. The first-order analysis gives approximately $N_{1,Ed} = 800$ kN and $M_{z,1,Ed} = 2.56$ kNm, while the second-order analysis with sway and bow imperfections gives approximately $N_{2,Ed} = 801$ kN and $M_{z,2,Ed} = 3.28$ kNm.

This limited variation between the converged variants indicates that the column verification is only weakly affected by the diaphragm assumptions within the present study. In contrast to the global stability assessment, where the variant-dependent sway sensitivity led to clear differences in critical load factor and convergence behaviour, the ULS verification of the governing column for the sway-governed variants is based directly on the internal forces from the imperfect global analysis. For all variants that remain stable enough to converge, these forces are nearly identical.

The influence of second-order effects is limited. The axial force remains practically unchanged between first- and second-order analysis, while the bending moment increases only slightly, from 2.56 kNm to 3.28 kNm. This indicates that P–Δ effects are relatively small for the governing column in the considered configurations. As a result, the column verification is governed primarily by axial compression, with bending providing only a minor additional contribution.

Accordingly, for all sway-governed variants that converge in the ULS second-order analysis, the governing column check can be based on one representative set of design forces:

$$UC = \frac{N_{2,Ed}}{A\, f_{c,0,d}} + \frac{M_{z,2,Ed}}{W_z\, f_{m,z,d}}. \tag{8.1}$$

Using these values results in a utilisation ratio of approximately $UC \approx 0.53$, which is very similar to the value obtained from the first-order analysis ($UC \approx 0.52$). This further confirms that the effect of second-order behaviour on the column check is limited.

Table 8.7: Governing design forces and utilisation ratio for the selected column.

Analysis type	Axial force [kN]	Bending moment [kNm]	UC [-]
First-order	$N_{1,Ed} = 800$	$M_{z,1,Ed} = 2.56$	0.52
Second-order	$N_{2,Ed} = 801$	$M_{z,2,Ed} = 3.28$	0.53

Variant C0 is treated separately, since its governing instability mode corresponds to member buckling rather than global sway buckling. For this variant, the column is verified as an individual compression member using the first-order axial force $N_{1,Ed}$, the buckling reduction factor k_c, and an effective buckling length equal to the storey height, in accordance with the procedure described in Section 8.1. This results in a comparable utilisation ratio ($UC \approx 0.53$), indicating that also in this case the column capacity is not governing.

The main conclusion is therefore that column stability is not the governing mechanism by which diaphragm stiffness affects the structural response in the sway-governed variants considered here. The influence of diaphragm detailing is much more pronounced in the global stability behaviour, the SLS drift response, and the ULS connection demand. Variants with insufficient diaphragm stiffness tend to become critical in these aspects first, and in the weakest cases they do not converge in the ULS second-order analysis at all. For the remaining converged sway-governed variants, the governing column forces and corresponding utilisation remain nearly unchanged.

8.7. Verification overview

Table 8.8 summarises the governing verification outcome per variant. A check mark indicates compliance, a cross indicates that the corresponding check was evaluated but not satisfied, and a dash indicates that no meaningful result was available for that verification step, for example because the second-order analysis did not converge.

A clear distinction exists between the reference case C0 and the segmented floor variants. Case C0 remains fully compliant and is the only variant for which the governing instability mode is member buckling rather than global sway. Among the segmented floor variants, the grouted *b*-series performs consistently better than the corresponding non-grouted *a*-series. All grouted variants remain globally stable, whereas several of the more flexible non-grouted variants have $\lambda_{\mathrm{cr}} < 1$ and therefore fail already at the global stability level.

For the converged variants, serviceability is generally not critical. All converged cases satisfy the drift limit of $h_i/300$, although variants C2a3 and C3a1 approach this limit in second-order analysis. The SLS response is therefore mainly useful as an indicator of sensitivity to second-order effects, rather than as the decisive governing check.

At ULS, the governing checks are mainly found at the diaphragm connections. The panel–core connection is the most critical interface, particularly in the more flexible variants and in cases where second-order amplification increases the line resultants. The panel–panel connection is less often decisive and governs only in isolated cases. By contrast, the column verification remains non-governing throughout the investigated set: the utilisation ratio is about 0.53 both for the sway-governed variants and for the member-buckling reference case C0.

Overall, the verification overview confirms that diaphragm detailing affects the structural response primarily through global sway sensitivity, drift amplification, and ULS connection demand. Its influence on the column verification is limited in the present case study.

Table 8.8: Summary of compliance per variant for the governing verification categories.

Variant	Global stability	SLS drift	ULS connections	ULS column
C0	✓	✓	✓	✓
C1a1	✓	✓	✓	✓
C1b1	✓	✓	✓	✓
C1a2	✓	✓	✓	✓
C1b2	✓	✓	✓	✓
C1a3	✓	✓	✗	✓
C1b3	✓	✓	✓	✓
C1a4	✓	✓	–	–
C1b4	✓	✓	✓	✓
C2a1	✓	✓	✗	✓
C2b1	✓	✓	✓	✓
C2a2	✗	✓	–	–
C2b2	✓	✓	✓	✓
C2a3	✗	✓	–	–
C2b3	✓	✓	✓	✓
C2a4	✗	–	–	–
C2b4	✓	✓	✗	✓
C3a1	✗	✓	–	–
C3b1	✓	✓	✓	✓
C3a2	✗	–	–	–
C3b2	✓	✓	✗	✓
C3a3	✗	–	–	–
C3b3	✓	✓	✗	✓
C3a4	✗	–	–	–
C3b4	✓	✓	–	–

8.8. Key observations

The following main observations can be drawn from the RFEM case study:

- All segmented diaphragm variants exhibit a global sway mode as the first instability mode, whereas only the monolithic reference case C0 shows a member-buckling first mode.
- Reduced diaphragm stiffness lowers the global stability margin. Several of the more flexible non-grouted a-variants have $\lambda_{cr} < 1$, indicating insufficient global sway stability.
- All converged variants satisfy the SLS drift limit of $h_i/300$. However, variants C2a3 and C3a1 approach this limit in second-order analysis, showing increased sensitivity to reduced diaphragm stiffness and second-order effects.
- Grouting the panel–core interface consistently improves the global response. Compared with the corresponding non-grouted variants, the grouted b-series gives higher critical load factors and lower drift values.
- The ULS connection checks are governed mainly by the panel–core interface. In the more flexible variants, second-order effects can substantially increase the connection force demand.
- The panel–panel connection is less often decisive than the panel–core connection and governs only in isolated cases.
- Column verification is not governing in the present case study. For the converged sway-governed variants, the governing column forces are nearly identical and the utilisation remains low ($UC \approx 0.53$). The reference case C0 gives a similar utilisation.
- Overall, the main influence of diaphragm detailing is found at system level and connection level: it governs the global sway sensitivity, the drift response, and the ULS connection demand much more strongly than the column verification.

Overall, the RFEM study shows that diaphragm stiffness is a governing parameter in the structural behaviour of the case-study building. Its influence is expressed mainly at global and connection level, through the sway stability, drift response, and connection force demand, whereas the column verification remains non-governing in the present case.

9

Discussion

This chapter discusses the main findings of the thesis and places them in a broader design context. For each part, the most relevant assumptions, uncertainties and implications are addressed, followed by an overall discussion of the trade-off between shrinkage-induced restraint forces and the diaphragm stiffness required for global stability.

9.1. Part I: Shrinkage and relaxation in CLT

Part I examined the prediction of moisture-driven shrinkage and the role of stress relaxation in restrained CLT elements. The discussion below focuses on how the shrinkage demand is defined, how representative the adopted moisture and viscoelastic assumptions are, and which uncertainties remain when translating these simplified material-level models to practical design situations.

9.1.1. Real shrinkage behaviour and the role of the β-coefficient

An important modelling choice in this thesis is how the shrinkage demand is described through the shrinkage coefficient β. In design standards such as Eurocode 5, β is usually given as a general value for a wide range of timber products and situations. This is practical and easy to use, but it does not account for differences between CLT lay-ups, timber species, or the role of the individual lamellae.

In this study, a layer-based lay-up method is used to determine an effective shrinkage coefficient for the specific CLT panel considered. This method takes into account the timber properties, the share of lamellae in each direction, and the restraining effect of the glued interfaces. As a result, the effective β is expected to represent the in-plane shrinkage behaviour of the panel more realistically than one general design value. The results of Part I also show that this choice has a clear influence on the predicted restraint stresses.

At the same time, this approach is still a simplification. The layered CLT behaviour is reduced to one effective shrinkage coefficient for each panel direction. This means that it does not describe how moisture content and shrinkage vary through the thickness of the panel. Experimental studies have shown that moisture content can develop differently near the surface than in the inner layers [33]. In thicker timber elements, the inner zones usually react more slowly and less strongly to climate changes than the outer zones. This can lead to moisture gradients and internal stresses, which are not captured explicitly when a single effective shrinkage coefficient is used.

This mechanism is illustrated schematically in Figure 9.1, where a non-uniform moisture distribution causes internal tensile stresses perpendicular to the grain and may lead to cracking.

In addition, using a shrinkage coefficient also assumes that shrinkage is uniform within the panel, not only through the thickness but also along the panel length. Numerical and experimental studies show that moisture diffusion does not always follow an ideal linear pattern, especially during drying [33]. The effective β approach therefore gives a practical estimate of the overall panel shrinkage for a given moisture change, but it does not describe local differences in shrinkage within the panel.

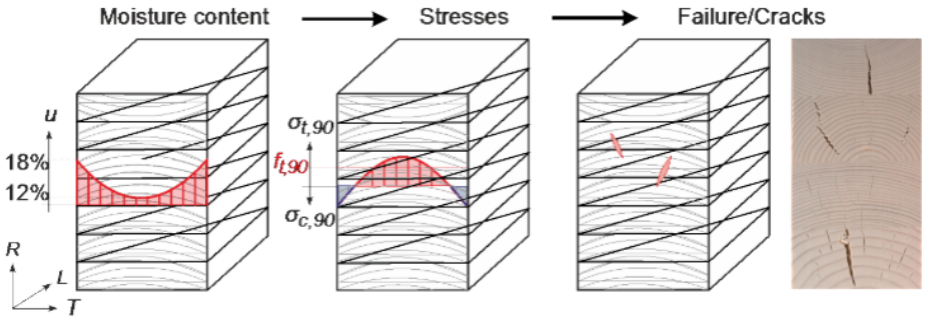

Figure 9.1: Schematic illustration of non-uniform moisture distribution, resulting internal stresses perpendicular to the grain, and potential crack formation (Franke et al., 2016) [33].

For design purposes, this simplification is often acceptable and useful, because it keeps the model clear and manageable. However, if the aim is to study stresses in individual lamellae or local effects near connections, a more detailed model would be needed in which moisture diffusion and the separate layers are represented explicitly.

9.1.2. Moisture content at installation and practical controllability

A main outcome of the parametric evaluations is the strong sensitivity of restraint forces to the moisture content at the time of installation MC_{inst}. This is physically intuitive: the larger the subsequent moisture reduction, the larger the shrinkage strain demand, and therefore the larger the forces that develop when shrinkage is restrained. In practice, however, MC_{inst} is not a "design choice" but the result of production, transport, temporary storage, and on-site exposure. Even if elements leave the factory at a controlled moisture level, moisture gradients can develop on site due to changing ambient conditions. This makes it difficult to guarantee a single, well-defined installation moisture content for all panels and all locations in a building.

This leads to two practical considerations for design practice. First, shrinkage-related checks should not be based on a single value of MC_{inst}, but on a plausible range that reflects realistic exposure scenarios. Second, where feasible, construction sequencing may offer a practical way to reduce shrinkage restraint: the screws that provide strong in-plane restraint in the panel–core connection, especially the outer screws, could be inserted and fully fastened only once they are structurally required. This would allow the floor panels to partially adapt to indoor climate conditions before full restraint is introduced.

9.1.3. Ageing effects and uncertainty in long-term relaxation

This study uses a linear viscoelastic model to describe stress relaxation under restrained shrinkage. This is suitable for studying how stresses develop over time, but one aspect is not included: *ageing*. Ageing means that creep and relaxation depend on the age of the material when a strain increment occurs. In ageing materials, strain increments that occur later in time usually relax less than those that occur earlier. As a result, the remaining stress after a long period may be higher.

For concrete, ageing is a well-established topic and is included in commonly used prediction models and design-oriented approaches. The concept of ageing creep has been developed in viscoelastic theory and forms the basis of practical methods for predicting long-term behaviour [22]. This gives designers guidance on how stresses and strains develop over time depending on the age at loading.

For timber and CLT, this knowledge base is still more limited. Time-dependent behaviour such as creep and relaxation is recognised as important, but there is only limited long-term data that specifically describes ageing effects in engineered wood products. For that reason, ageing is not included in this thesis. Including it would require additional parameters that cannot be justified well enough for the CLT product considered.

Neglecting ageing may lead to an underestimation of the long-term residual stress, because older material is expected to relax less. The calculated long-term stresses should therefore be interpreted with some caution. A useful topic for future work would be experimental research on ageing in CLT

under representative moisture histories, so that ageing functions can be developed for specific products and applications, similar to what already exists for concrete.

9.1.4. Viscoelastic model choice

In this thesis, stress relaxation is described with a linear generalised Maxwell model. This choice was mainly practical. The model is commonly used, relatively easy to implement, and makes it possible to describe relaxation with a limited number of stiffness values and relaxation times.

At the same time, the results depend on this model choice. The relaxation model used here was not calibrated specifically for the CLT product, lay-up, and in-plane shrinkage case considered in this thesis. If a different viscoelastic model had been used, the predicted stress development could also have been different. For example, a pure Maxwell model would eventually relax to zero stress, whereas the present model retains a remaining stress level through the equilibrium modulus. More generally, different linear viscoelastic models can lead to differences in both the rate of relaxation and the final retained stress.

Within the model used here, the results show that the long-term stress is mainly controlled by the equilibrium modulus E_{fin}, while the relaxation times mainly affect how quickly that level is approached. However, this conclusion applies only to the chosen model. Further research would be needed to determine which viscoelastic model best represents the behaviour of CLT under moisture-driven in-plane shrinkage, and how sensitive the results are to that choice.

9.2. Part II: Shrinkage-induced forces in CLT connections

Part II considered how shrinkage translates into force demand in restrained CLT connections. The discussion focuses on the limitations of the analytical idealisation and on the interpretation of the calculated screw slip under shrinkage, including its possible implications for the connection behaviour.

9.2.1. 1D idealisation and 2D floor behaviour

The analytical models in this thesis describe restrained shrinkage with a one-dimensional beam–spring model. This is useful to identify the main trends, but it remains a simplification of the real behaviour of a floor diaphragm. In reality, shrinkage and restraint develop in two dimensions. The forces are not transferred through one line only, but through a plate with distributed stiffness, multiple boundaries, and several connections. As a result, the restraint forces are not spread uniformly over the full panel width.

This is especially important for shrinkage *parallel* to the core in the continuously restrained case (Situation 4). The RFEM results show that not the full floor width contributes equally to the force transfer into the core. Instead, most of the restrained deformation is concentrated in a zone close to the restrained edge. In this thesis, this zone is described by an effective restraint width b_{eff}. Within this width, the plate contributes most strongly to the connection force demand, while the influence decreases further away from the core. This is illustrated in Figure 9.2, where the response clearly decays with distance from the restrained edge.

In the present study, b_{eff} was not derived from plate theory. Instead, it was estimated from the RFEM results and then used in the 1D beam–spring model. This gave a practical way to include the 2D plate behaviour in a simplified analytical model.

The RFEM results also suggest that b_{eff} is not a fixed geometric property. It appears to depend on the relative stiffness of the connections, on the boundary conditions, and on the geometry of the floor. In addition, it may vary with the shrinkage demand itself, for example through β and MC_{inst}, and with the ratio between restrained connection length and panel depth, L_{con}/L_d. This means that a single fixed value of b_{eff} can be useful for the present idealisation, but it should not automatically be assumed to apply to other layouts or connection details.

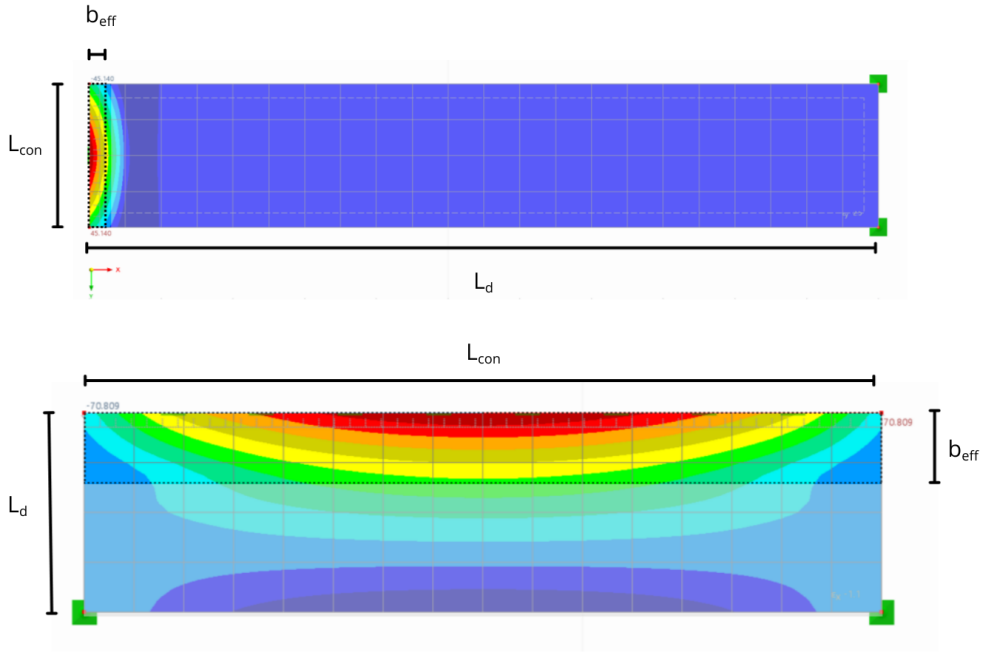

Figure 9.2: RFEM results illustrating the concept of an effective restraint width b_{eff} for shrinkage parallel to the core (Situation 4).

9.2.2. Interpretation of shrinkage-induced screw slip

The results for Situation 4 show that the highest deformation demand occurs in the outermost screws along a continuously restrained edge. For the case-study configuration with a restrained length of 8 m, the calculated slip reaches approximately 3.7 mm. This clearly exceeds the initial linear-elastic range of the connection and indicates that the response of these screws is expected to become non-linear.

As discussed in subsection 5.2.2, this does not necessarily imply immediate connection failure. Dowel-type timber connections can exhibit significant ductility, allowing additional deformation beyond the elastic range through plastic slip in the fastener and surrounding timber.

Insight into the magnitude of possible slip can be obtained from experimental studies. Mirra et al. [34] investigated the load–slip behaviour of screwed timber connections in diaphragm systems and observed that the peak load was reached at slip values of more than 10 mm, with further deformation occurring before a significant loss of resistance. Although the connection configuration in that study differs from the present steel–timber detail, the results indicate that several millimetres of slip do not necessarily correspond to immediate failure.

The calculated slip demand of approximately 3.7 mm therefore indicates that the connection response is likely to enter a ductile regime, rather than immediately reaching a brittle failure state. However, this has important implications for the structural behaviour.

Plastic deformation in the outer screws may lead to a reduction in the effective connection stiffness. As a result, the force distribution assumed in the linear model may no longer remain valid, and part of the shrinkage-induced forces will be redistributed to adjacent screws or reduced due to additional slip.

9.3. Part III: CLT floor system in structural stability

Part III evaluated how diaphragm connection stiffness affects the global response of the case-study building. The discussion below addresses the practical meaning of the required diaphragm stiffness, possible alternative stiffening strategies, and the limitations of the numerical model due to the fact that shrinkage was not included explicitly as an imposed deformation.

9.3.1. Interstorey drift and imperfection modelling

In timber frame–core buildings, it is often assumed in design that the floor diaphragm provides sufficient in-plane stiffness to transfer lateral loads to the core and to provide adequate lateral restraint to the timber frame. The results of Part III show that this assumption should not be made without verification.

For the analysed case-study building, the presence of the concrete core keeps the overall lateral displacement of the building well within acceptable limits. The main concern is therefore not the global top displacement of the building, but the extent to which the floor diaphragm provides sufficient lateral support to the timber columns.

As indicated by the first mode shape of the system, the governing instability behaviour is not a purely local column buckling mode, but a global deformation mode in which the frame deforms laterally relative to the core. In this mode, adjacent columns do not necessarily move in the same direction. Instead, the response is characterised by relative horizontal movements between storeys. In combination with the high vertical loads in the columns, this increases the sensitivity to second-order effects, particularly in the lower storeys. For the present case study, the critical issue is therefore the interstorey drift rather than the overall building drift.

If interstorey deformation and diaphragm action govern the response, the assumed imperfection pattern also becomes important. In the RFEM model used in this thesis, the imperfections were applied in a single direction over the full building height. This was adopted to represent an unfavourable configuration for the global lateral displacement of the building under wind loading. However, this is not the most unfavourable configuration for the force demand in the floor diaphragm itself.

Eurocode 3 gives a different imperfection configuration for the determination of horizontal forces in floor diaphragms of a braced system. In that approach, adjacent storeys are displaced in opposite directions, as illustrated in Figure 9.3. This results in local diaphragm forces associated with the axial forces in the stabilised members, expressed through $Q_m = 2\phi N_{Ed}$.

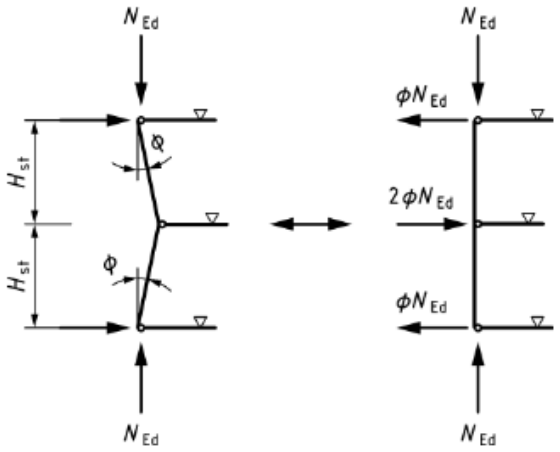

Figure 9.3: Configuration of imperfections ϕ for horizontal forces on floor diaphragms according to EC3 [31].

Although this Eurocode approach is introduced for the evaluation of diaphragm forces rather than for drift assessment, it is also relevant for the present study. The first instability mode obtained from the RFEM analysis shows a deformation pattern in which the horizontal displacements change direction over the building height, rather than developing as a uniform global sway. An alternating imperfection pattern is therefore of particular interest, as it resembles the deformation pattern observed in the RFEM analysis and may provide a more unfavourable loading pattern for the assessment of diaphragm forces, connection forces, and interstorey deformations.

A useful extension of the present analysis would therefore be to repeat the analyses with alternating storey imperfections, in order to evaluate how sensitive the diaphragm forces, connection forces, and interstorey drifts are to the assumed imperfection shape.

9.3.2. Stiffness of the panel–core connection in the RFEM model

A modelling question in Part III is which stiffness should be assigned to the panel–core connections in the RFEM model when evaluating the building response under short-term lateral loading.

In principle, the appropriate stiffness for short-term loading would be k_{SLS}, since this represents the initial connection stiffness under service-type loading. From that perspective, the reduction of shrinkage-induced forces due to relaxation does not imply that the initial stiffness under later short-term loading should also be reduced.

In the present study, however, the reduced stiffness k_{fin} was assigned to the panel–core connections. This was intended as a modelling assumption to represent a possible reduction in effective stiffness due to prior shrinkage-induced slip and local plastic deformation. Even so, this choice should be viewed critically, because k_{fin} does not directly represent the initial stiffness under subsequent short-term loading.

At the same time, the use of k_{SLS} is also questionable. Due to shrinkage-induced slip, the outer screws may already have undergone plastic deformation before the building is subjected to short-term lateral loading. In that case, additional slip may occur already at an early stage of reloading, meaning that a reduced effective stiffness could be more representative than the original k_{SLS}.

A brief comparison with models using k_{SLS} showed, as expected, lower displacements, lower connection forces, and higher critical load factors. However, the general structural behaviour remained the same: the floor diaphragm still provided limited lateral support to the columns, and the governing instability mode remained a global sway-type deformation mode in the lower storeys. The use of k_{fin} therefore appears to have made the results more unfavourable, without changing the main qualitative conclusion of Part III.

The key uncertainty is therefore how much stiffness reduction is actually caused by shrinkage-induced plastic deformation in the screws and surrounding timber. Further research is needed to determine whether post-shrinkage connection behaviour under short-term lateral loading is better represented by k_{SLS}, by a reduced stiffness, or by a different load–slip model altogether.

9.3.3. Explicit shrinkage effects in the RFEM model

In the RFEM case-study model, shrinkage is not included explicitly as an imposed deformation. A possible next step would be to include it directly in the global model, for example as a prescribed strain.

Such an approach would provide direct insight into the structural response of the case-study building under shrinkage. In particular, it would allow the evaluation of the force development in the connections at locations where shrinkage is restrained, and the shortening of the floor where shrinkage can occur freely. For the present case study, this shortening is especially relevant in the lowest storey, where the column bases are restrained by the foundation and cannot follow the floor shortening. In that case, shrinkage introduces an initial inclination of the first-storey columns, potentially increasing the sensitivity to second-order effects (Figure 9.4).

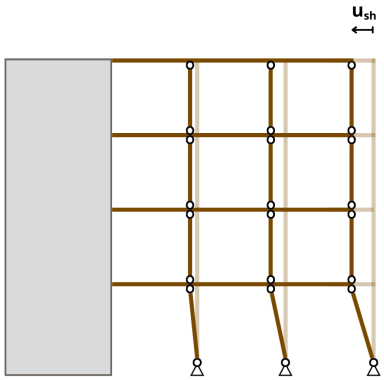

Figure 9.4: Schematic illustration of first-storey column inclination caused by free shrinkage of the floor panel.

To illustrate the order of magnitude, the free shrinkage deformation of an 11 m floor panel, from the case study, for $\beta = 0.00015$ and $\Delta MC = 7\%$ is approximately 11.6 mm.

Such a global analysis would still remain a simplification. If shrinkage is introduced explicitly in a linear-elastic model, the resulting forces represent the force build-up caused by restrained shortening, but stress relaxation is not included automatically. The results of Part I can then be used to give an indication of how much these elastically predicted forces may reduce over time due to relaxation.

9.4. Design trade-off: restraint forces and diaphragm stiffness

The results from Part I–III show a clear trade-off between limiting shrinkage-induced restraint forces and providing sufficient diaphragm stiffness for the global stability of a timber frame–core building. If the aim is to reduce shrinkage-induced forces in the connections, this can be achieved by reducing the degree of restraint, for example by limiting the continuously restrained length along the core or by introducing more compliance in the connection layout where this is structurally possible. However, such measures also reduce the effective diaphragm stiffness and therefore weaken the coupling between core and frame.

If, on the other hand, the aim is to improve global stability, this generally requires a stiffer diaphragm and a stronger connection between floor, frame, and core. This improves lateral load transfer and reduces sensitivity to sway behaviour and second-order effects. At the same time, it also increases the restraint against shrinkage and may therefore lead to higher force demand in the connections.

The trade-off is therefore between local shrinkage behaviour and global structural response. A detailing choice that is favourable from the point of view of shrinkage may be unfavourable from the point of view of stability, while a choice that improves global stability may lead to less favourable shrinkage behaviour in the connections.

At the same time, some uncertainty remains regarding how unfavourable these higher shrinkage-induced forces are in practice. Screwed timber connections can show ductile behaviour, which means that exceeding the elastic range does not necessarily lead directly to a sudden loss of load transfer. Instead, increased slip and a reduction in effective connection stiffness may occur. The exact influence of this behaviour on the diaphragm response after shrinkage is still not fully clear, and this interaction requires further research.

Even so, the results already provide clear design lessons. The analyses show that the restrained length along the core and the overall diaphragm stiffness are key parameters. Where possible, it is therefore sensible to keep the continuously restrained length along the core as small as possible, provided that this does not lead to unfavourable effects on stability. At the same time, the floor diaphragm stiffness should be considered explicitly in the stability design of the building, rather than being assumed sufficient without verification. If the required floor stiffness cannot be achieved through the diaphragm connections alone, this should already be recognised in the design stage. In that case, other ways of increasing the stiffness of the system should also be considered, such as a stiffer diaphragm layout, additional collectors, or a larger contribution of the timber frame itself to the overall stability of the building.

10

Conclusion

This chapter answers the research questions of this thesis, summarises the main findings, and reflects on their scientific and practical relevance.

10.1. Research questions

Sub−research questions

How does moisture-driven shrinkage in CLT develop over time, and which material and environmental parameters govern its magnitude and rate?

Moisture-driven shrinkage in CLT develops progressively as the moisture content decreases towards the indoor equilibrium level. Its magnitude is governed primarily by the installation moisture content MC_{inst} and the shrinkage coefficient β: higher values of either parameter directly lead to larger shrinkage strains and, under restraint, to higher stresses. For the studied CLT lay-up, the choice of β proved decisive. Eurocode-based shrinkage coefficients led to higher predicted stresses than the effective coefficients obtained from the layer-based approach, showing that shrinkage assessment is highly sensitive to the adopted parameterisation and is best represented using lay-up-specific parameters when the lay-up is known.

How does viscoelastic stress relaxation influence the evolution of stresses in CLT subjected to restrained shrinkage, and how can this effect be represented in a practical long-term modelling approach?

Viscoelastic stress relaxation substantially reduces restrained shrinkage stresses compared with purely elastic predictions. In the adopted linear generalised Maxwell model, the retained long-term stress is governed by the equilibrium modulus E_{fin}, whereas the relaxation times adopted in the model mainly affect the transient stress development. For realistic diffusion-controlled moisture changes, this development is smooth and peak stresses remain close to the long-term level. On that basis, E_{fin} provides a practical and physically motivated parameter for representing long-term restraint effects in subsequent analyses of shrinkage-induced connection forces.

How do common CLT–core and CLT–timber connection configurations provide restraint against shrinkage deformations, and which parameters govern the resulting restraint forces?

The shrinkage-induced forces in the studied connection configurations are governed by the imposed shrinkage deformation and by the relative stiffness of the surrounding restraints. For shrinkage acting over the panel span between restrained supports, the force demand increases with panel length L_p and installation moisture content MC_{inst}, because both increase the free shrinkage deformation that must be restrained. For shrinkage along the panel–core connection line, the restraint forces are distributed non-uniformly along the connection line, with peak screw forces occurring near the ends of the restrained length. In that case, the effective restrained length along the core is a key governing parameter.

Under which geometric and moisture-related conditions do shrinkage-induced forces become critical for connection utilisation, and what measures can be taken to keep the demand within acceptable limits?

Shrinkage-induced forces become critical for combinations of large panel lengths, high installation moisture contents, and stiff or continuous restraint. For shrinkage across the panel span between restrained edges, slip allowance is an effective mitigation measure, and the required allowance increases with L_p and MC_{inst}. For shrinkage along the panel–core connection line, however, global slip allowance is generally not compatible with the diaphragm shear transfer that must be maintained at this interface. In that direction, reducing the continuously restrained length is the most direct way to limit peak connection forces. Although local exceedance of the elastic resistance does not necessarily imply immediate loss of load transfer, it does indicate increased slip and reduced incremental stiffness, and was therefore treated conservatively in this study.

How does the in-plane stiffness of the CLT floor diaphragm affect system response under SLS and ULS criteria in first- and second-order analysis?

The RFEM case study shows that the in-plane stiffness of the CLT floor diaphragm has a direct influence on the stability behaviour and overall feasibility of the building. Reduced diaphragm stiffness lowers the global stability margin, increases sway sensitivity, and leads to larger interstorey drift and higher diaphragm connection forces. Increasing the diaphragm stiffness, for example by grouting the panel–core interface, consistently improves the structural response.

In the present case study, the influence of diaphragm stiffness is most significant at system level and connection level. At SLS, the overall top displacement remains within acceptable limits in all converged cases, while interstorey drift is the more relevant indicator of structural sensitivity. At ULS, the governing checks are found mainly in the diaphragm connections, particularly at the panel–core interface. Column verification remains non-governing in the analysed variants.

Under which conditions does first-order analysis no longer provide a reliable assessment of the system response, and when is second-order analysis required to capture the governing response of the structure?

First-order analysis becomes insufficient when the in-plane stiffness of the floor diaphragm is insufficient for the structural response to remain governed by member buckling rather than global sway buckling. In such cases, reduced diaphragm stiffness lowers the critical load factor, increases sensitivity to geometric non-linearity, and can substantially amplify interstorey drift and diaphragm connection demand. This effect is most pronounced in the more flexible variants, for which several cases become critical or fail to converge in geometrically non-linear second-order analysis.

Second-order analysis is therefore required for diaphragm configurations that provide only limited lateral support to the timber frame. This is particularly important in the lower storeys, where axial forces are highest and drift amplification is most pronounced. The results show that first-order analysis alone may underestimate, or even fail to capture, the governing response of flexible diaphragm variants.

Main research question

How do connection stiffness in CLT floor systems of hybrid concrete core–timber frame buildings influence shrinkage-induced forces and the global stability behaviour of the structure?

Connection stiffness and detailing choices govern both the degree of restraint against moisture-driven shrinkage and the in-plane stiffness of the floor diaphragm required for global stability. As a result, the same design choices influence both the magnitude of shrinkage-induced forces in the connections and the global structural response of the building.

Measures that reduce shrinkage-induced forces, such as limiting the continuously restrained length or introducing more compliant detailing, reduce the degree of restraint but also decrease diaphragm stiffness and may adversely affect stability. Conversely, measures that improve diaphragm action and increase stiffness enhance global stability but increase restraint against shrinkage and therefore lead to higher connection force demand.

The influence of connection detailing on hybrid core–frame buildings is therefore characterised by a fundamental design trade-off between shrinkage behaviour and structural stability. This means that connection detailing should not be treated as a local design issue only, but as a system-level choice that affects both connection behaviour and overall structural performance.

10.2. Recommendations

The findings of this thesis lead to several recommendations for the assessment and design of hybrid core–frame buildings in which shrinkage effects and diaphragm action interact.

First, shrinkage-induced forces in restrained CLT connections should be assessed explicitly rather than neglected or represented only qualitatively. The framework developed in this thesis shows how shrinkage strain, connection stiffness, and viscoelastic stress relaxation can be combined into one consistent assessment approach. Although the numerical results presented here are based on specific assumptions, the method itself can be adapted to project-specific material properties, geometries, restraint situations, and relaxation models. It is therefore recommended to use this approach either directly as an indicative assessment or as a basis for more refined project-specific analyses.

Second, viscoelastic stress relaxation should be considered when estimating long-term restraint forces. The results show that relaxation can reduce a substantial part of the initially generated shrinkage-induced forces. Ignoring this effect may lead to overly conservative estimates, while incorporating it can provide a more realistic basis for structural assessment. At the same time, the magnitude of this reduction remains dependent on modelling assumptions and available material data, and should therefore be interpreted with appropriate caution. The viscoelastic behaviour of timber over time is not yet sufficiently established to define this effect with high confidence, and additional long-term experimental research is needed to improve its characterisation and application in structural modelling.

Third, the in-plane stiffness of the floor diaphragm should be verified explicitly in the stability design of hybrid core–frame buildings. The case study shows that the timber frame cannot automatically be assumed to be adequately braced by the floor system. Where diaphragm stiffness is insufficient, the governing structural response may shift towards global sway buckling behaviour, and first-order analysis may no longer provide a reliable verification. In such cases, geometrically non-linear analysis is recommended.

Finally, particular care is needed when selecting the stiffness of panel–core connections in global models after shrinkage has already occurred. The present study indicates that this stiffness may be reduced by prior slip and local plastic deformation, but the extent of this reduction under subsequent short-term or cyclic lateral loading remains uncertain. It is therefore recommended to treat post-shrinkage connection stiffness as an important modelling uncertainty and to consider its influence explicitly when evaluating global stability.

These recommendations form the basis for the practical design considerations presented below.

10.2.1. Practical design recommendations

Based on the findings of this thesis, a number of practical considerations can be formulated for the design and execution of hybrid core–frame buildings. These considerations aim to support a balanced assessment of shrinkage effects, diaphragm stiffness, and their interaction.

Design

- **Check diaphragm stiffness early in design.** Assess at an early stage whether the floor diaphragm is likely to provide sufficient in-plane stiffness for the required lateral support of the timber frame. If not, identify which design measures are needed to achieve adequate stiffness, such as a stiffer diaphragm layout, stronger connection detailing, additional collectors, or a larger contribution of the timber frame to the global stability system.
- **Assess diaphragm stiffness explicitly.** Do not assume that the floor system provides sufficient lateral support to the timber frame. Where diaphragm stiffness is limited, the structural response may become governed by global sway behaviour, and second-order effects may be critical, particularly in the lower storeys.
- **Panel orientation and layout.** Consider panel orientation and segmentation such that critical restrained lengths at the panel–core connection line are limited. Where feasible, aim for relatively short restrained segments along this line while maintaining sufficient in-plane stiffness of the diaphragm.

- **Panel–core stiffness.** Ensure that the panel–core interface provides sufficient stiffness to achieve the required global response, including drift and torsional control. At the same time, recognise that higher stiffness increases restraint against shrinkage and therefore increases connection force demand.
- **Panel–panel stiffness.** Provide sufficient panel–panel coupling to maintain diaphragm action and to avoid weakly restrained configurations. Shrinkage-induced restraint forces are generally not critical at these connections, since adjacent panels deform in the same overall shrinkage direction.
- **Compare first- and second-order response.** For diaphragm configurations where the global response depends strongly on the in-plane stiffness of the floor diaphragm, first-order analysis alone may be insufficient. Variants that appear acceptable in first-order analysis can become governing when geometric non-linearity is included.
- **Consider shrinkage in the stability assessment.** Where relevant, account for the implications of shrinkage, such as reduced effective stiffness at critical interfaces and potential additional deformations or imperfections.
- **Slip allowances.** Where the load path allows it, slip allowance (e.g. slotted holes) can effectively reduce shrinkage-induced restraint forces, particularly for shrinkage across the panel span between restrained edges. For shrinkage along the panel–core connection line, however, slip allowances are generally not compatible with the required diaphragm shear transfer and alternative strategies are needed, such as limiting the continuously restrained length.

Execution

- **Limit exposure and protect panels.** Reduce on-site exposure time and apply protective measures to limit moisture uptake during construction.
- **Building sequence.** Where feasible, install the most critical restraints (e.g. outer screws along the panel–core connection line) as late as structurally permissible. This allows partial adaptation of the panels to indoor conditions before full restraint is introduced.
- **Monitor moisture content.** Use moisture measurements to document installation conditions and to support realistic assumptions for MC_{inst} in design verification and quality control.

References

[1] *Inside Vancouver's Brock Commons, the World's Tallest Mass Timber Building*. 2017. URL: https://www.archdaily.com/879625/inside-vancouvers-brock-commons-the-worlds-tallest-timber-structured-building.

[2] Yale Center for Ecosystems + Architecture United Nations Environment Programme. *Building Materials and the Climate: Constructing a New Future*. 2023-09. URL: https://wedocs.unep.org/20.500.11822/43293.

[3] *Circulair bouwen*. URL: https://www.rvo.nl/onderwerpen/circulaire-economie/circulair-bouwen.

[4] Swedish Wood. *The Glulam Handbook Project design of glulam structures Volume 2*. EDITION 1:2024. Vol. Volume 2. Mar. 2024.

[5] Eric Borgström et al. *The CLT Handbook*. May 2019, pp. 3–184. URL: www.traguiden.se.

[6] Kalesnikoff Mass Timber Lumber. *GLULAM - Glue Laminated Beams / Columns - Mass Timber - Kalesnikoff*. July 21, 2025. URL: https://kalesnikoff.com/products/mass-timber-glulam-beams/.

[7] Bob Grande. *CLT-hout: een duurzame bouwmethode voor woningen en gebouwen*. Feb. 27, 2025. URL: https://www.timbertitanen.nl/clt-hout-een-duurzame-bouwmethode-voor-woningen-en-gebouwen/.

[8] Daniel Safarik, Jacob Elbrecht, and William Miranda. *The State of Tall Timber: A Global Audit*. 2022. URL: https://www.ctbuh.org/mass-timber-data.

[9] CEN. *prEN 1995-1-1:2023 Eurocode 5 – Design of timber structures – Part 1-1: General rules and rules for buildings*. Draft for public enquiry (2nd generation Eurocode 5). Brussels: European Committee for Standardization, 2023.

[10] Hans Joachim Blaß and Carmen Sandhaas. *Timber Engineering Principles for Design*. Tech. rep.

[11] Julia Parlatore Lancha. "A multiscale approach to understand and predict the effects of hydrothermal treatment on lignocellulosic biomass". PhD thesis. July 2020.

[12] André Geus et al. "An analysis of timber sections and deep learning for wood species classification". In: *Multimedia Tools and Applications* 79 (Dec. 2020). DOI: 10.1007/s11042-020-09212-x.

[13] Hans Joachim Blaß, Carmen Sandhaas, and Rainer Görlacher. *Principles for Design*. 2017. DOI: 10.5445/KSP/1000069616.

[14] Okke Willebrands. "Differential vertical shortening in timber-concrete high-rise structures". Nov. 2017.

[15] Zeng Xiong Yu, Ren Su Xin, and Omar Sabri. "Vertical Displacements in a Medium-rise Timber Building". 2009.

[16] Sung-Jun Pang and Gi Young Jeong. "Swelling and shrinkage behaviors of cross-laminated timber made of different species with various lamina thickness and combinations". In: *Construction and Building Materials* 240 (Jan. 2, 2020), p. 117924. DOI: 10.1016/j.conbuildmat.2019.117924. URL: https://doi.org/10.1016/j.conbuildmat.2019.117924.

[17] Klaudia Śliwa-Wieczorek et al. "Creep Behavior of CLT Beams with Finite Thickness Layers of Flexible Adhesives". In: *Materials* 16.12 (June 20, 2023), p. 4484. DOI: 10.3390/ma16124484. URL: https://doi.org/10.3390/ma16124484.

[18] Wen Gang Hu, Hui Yuan Guan, and Nanjing Forestry University. *STUDY ON COMPRESSIVE STRESS RELAXATION BEHAVIOR OF BEECH BASED ON THE FINITE ELEMENT METHOD*. 1. 2019, pp. 15–24. DOI: 10.4067/S0718-221X2019005000102.

[19] Tomasz Socha, Krzysztof Kula, and Arkadiusz Denisiewicz. *Linear Viscoelastic Wood Creep Models*. 2025, pp. 5348–. URL: https://doi.org/10.3390/ma18235348.

[20] Tu T. Nguyen et al. "Numerical Model for Creep Behavior of Axially Loaded CLT Panels". In: *Journal of Structural Engineering* 145.1 (Oct. 19, 2018). DOI: 10.1061/(asce)st.1943-541x.0002219. URL: https://doi.org/10.1061/(asce)st.1943-541x.0002219.

[21] Xiaowei Li et al. "Research on stress relaxation behavior of confined Chinese fir subjected to compression". In: *Wood Science and Technology* 58.4 (July 1, 2024), pp. 1381–1408. DOI: 10.1007/s00226-024-01572-z. URL: http://doi.org/10.1007/s00226-024-01572-z.

[22] Weinan Wang and Jinxin Gong. "New relaxation function and age-adjusted effective modulus expressions for creep analysis of concrete structures". In: *Engineering Structures* 188 (Mar. 12, 2019), pp. 1–10. DOI: 10.1016/j.engstruct.2019.03.009. URL: https://doi.org/10.1016/j.engstruct.2019.03.009.

[23] Wei Feng, Zheng Li, and Minjuan He. "Comparison of the tension and shear performance of CLT wall-to-foundation screwed connections: Experimental and theoretical analyses". In: *Structures* 83 (Dec. 11, 2025), p. 110885. DOI: 10.1016/j.istruc.2025.110885. URL: https://doi.org/10.1016/j.istruc.2025.110885.

[24] Jörg Dietsch and Milan Šejnoha, eds. *Design of Connections in Timber Structures*. COST Action FP1402. Aachen: Shaker Verlag, 2018. ISBN: 978-3-8440-5954-8.

[25] CEN. *EN 1995-1-1: Eurocode 5 – Design of timber structures – Part 1-1: General – Common rules and rules for buildings*. Including A1:2008 and A2:2014. Brussels: European Committee for Standardization, 2004.

[26] J.W.G. van de Kuilen, Delft University of Technology, and CNR Trees and Timber Research Institute. *Creep of timber joints*. 3. 2008, pp. 133–136.

[27] Yufei Wu, D.J. Oehlers, and M.C. Griffith. *Partial Interaction Analysis of Composite Beam/Column Members*. Feb. 14, 2017.

[28] Mahboobeh Fakhrzarei, Hossein Daneshvar, and Ying Hei Chui. "Numerical parametric study of cross-laminated timber diaphragms under in-plane loading". In: *Construction and Building Materials* 429 (May 1, 2024), p. 136387. DOI: 10.1016/j.conbuildmat.2024.136387. URL: https://doi.org/10.1016/j.conbuildmat.2024.136387.

[29] Sepideh Ashtari. "In-plane Stiffness of Cross-laminated Timber Floors". Oct. 2012.

[30] S.L. Chan and Department of Civil and Structural Engineering, Hong Kong Polytechnic University. *Non-linear behavior and design of steel structures*. 2001, pp. 1217–1231. URL: www.elsevier.com/locate/jcsr.

[31] CEN. *EN 1993-1-1:2005 Eurocode 3 – Design of steel structures – Part 1-1: General rules and rules for buildings*. Including A1:2014. Brussels: European Committee for Standardization, 2005.

[32] CEN. *EN 1990: Eurocode – Basis of structural design*. Including A1:2005 and A1:2005/AC:2010. Brussels: European Committee for Standardization, 2002.

[33] Bettina Franke et al. *Long-term behaviour of moisture content in timber constructions – Relation to service classes*. INTER / 49-09-01. 2016.

[34] Michele Mirra et al. "An analytical model describing the in-plane behaviour of timber diaphragms strengthened with plywood panels". In: *Engineering Structures* 235 (Mar. 10, 2021), p. 112128. DOI: 10.1016/j.engstruct.2021.112128. URL: https://doi.org/10.1016/j.engstruct.2021.112128.

[35] CEN. *EN 1991: Eurocode 1 – Actions on structures*. Multiple parts (EN 1991-1 to EN 1991-4). Brussels: European Committee for Standardization, 2002.

[36] Rothoblaas. *HBS – Technical Data Sheet*. Rothoblaas. n.d. URL: https://www.rothoblaas.com/attachments/288905-product-241/hbs-en-technical-data-sheet.pdf (visited on 02/27/2026).

A

Case study details

A.1. Materials and members

The numerical model consists of a reinforced concrete core, glulam timber beams and columns, and CLT floor slabs. All materials are modelled as linear elastic.

A.1.1. Materials

Table A.1 summarises the material properties adopted in the model. The concrete core is modelled using a reduced elastic modulus to account for cracking effects in a simplified manner. Timber beams and columns are modelled as isotropic material, whereas the CLT floors are modelled as orthotropic surface elements.

Table A.1: Material properties used in the numerical model

Material	Application	E_{mean} [N/mm^2]	$G_{x,y,mean}$ [N/mm^2]	ν [-]	γ [kN/m^3]
C30/37	Concrete core	15 000	5 769	0.20	25.0
GL24h	Beams and columns	11 500	650	0.30	4.2
CLT (Stora Enso)	Floor slabs	11 000	690	–	5.0

A.1.2. Structural members

Timber beams and columns are modelled using beam elements, while the CLT floors are modelled using surface elements. The concrete core is modelled using vertical surface elements extending over the full height of the building. An overview of the adopted member dimensions is given in Table A.2.

Table A.2: Structural members and cross-sections

Member type	Location / function	Cross-section [mm]
Columns	Typical	400×400
Columns	Facade	400×240
Columns	Adjacent to acoustic cut	240×400
Beams	All floor beams	360×360
Concrete core	Core walls	$t = 300$

CLT floor panels

The floor system consists of five-layer CLT panels with a total thickness of 200 mm. Each layer has a thickness of 40 mm, resulting in the lay-up:

$$0° - 90° - 0° - 90° - 0°$$

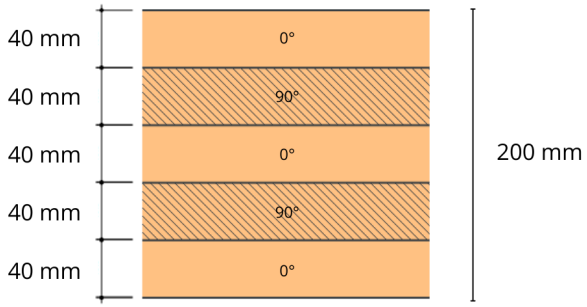

Figure A.1: CLT lay-up

The CLT slabs are modelled as orthotropic linear elastic surface elements, allowing different stiffness characteristics in the principal material directions. This modelling approach enables realistic diaphragm behaviour and in-plane load transfer towards the concrete core.

A.2. Connections

Connections are idealised to represent the intended global behaviour of the hybrid system. Beam–column and column base connections are modelled as pinned, such that the timber framing does not develop significant frame action and the core remains the primary stabilising element. In-plane load transfer within the floor system is represented by *line hinges* between CLT panels and along the CLT–core interface. These line hinges use smeared stiffness properties (per unit length/area). The specific in-plane connection details considered in this thesis are introduced and discussed in Chapter 5.

A.3. Imperfections

Geometric imperfections are included to account for both global sway effects and initial member out-of-straightness. In accordance with EN 1995-1-1 [25], equivalent sway imperfections are introduced as initial rotational imperfections applied per member.

The global imperfection angle ϕ is defined as

$$\phi = \pm \frac{1}{200} \tag{A.1}$$

which is applicable for member lengths and structural heights not exceeding 5 m. These imperfections are applied in the global horizontal directions and included in the stability analysis to ensure a conservative representation of second-order effects.

In addition, member bow imperfections are taken into account to represent initial local out-of-straightness of the columns. The bow imperfection is defined as

$$e_0 = \frac{L}{1000} \tag{A.2}$$

where L is the member length. This imperfection is included in the member verification to account for the influence of initial curvature on column stability.

A.4. Loads

Permanent actions consist of the self-weight of all structural elements (included automatically based on the assigned material densities) and additional permanent loads applied as idealised surface and line loads. Variable actions are represented by imposed (live) loads on floors and roof. Wind actions are determined according to EN 1991-1-4 [35] using global external pressure coefficients for rectangular plan buildings. The peak velocity pressure is evaluated for the building height and the selected terrain

category, after which equivalent wind line loads are applied along the floor edges to represent the global wind effect on the diaphragm levels.

Table A.3: Summary of applied loads and wind parameters

Category	Application / parameter	Value
Permanent and imposed loads		
Self-weight	All structural elements	Automatic
Permanent load g_k	Floors (surface load)	4.25 kN/m^2
Permanent load g_k	Roof (surface load)	kN/m^2
Permanent load g_k	Facade (line load)	1.00 kN/m
Imposed load q_k	Floors (surface load)	2.25 kN/m^2
Imposed load q_k	Roof (surface load)	kN/m^2
Wind (EN 1991-1-4)		
Building height h	Parameter	40 m
Terrain category	Parameter	III
Storey height h_{storey}	Parameter	3.2 m
Peak velocity pressure $q_p(z)$	Parameter	1.07 kN/m^2
Equivalent wind line load q_w	Pressure (windward)	2.739 kN/m
Equivalent wind line load q_w	Suction (leeward)	1.712 kN/m

B

Failure modes

B.1. Connection geometry and screw characteristics

This section summarises the geometric definitions and screw properties used for the resistance checks.

B.1.1. Connection layouts

Figure B.1 shows the connection configurations used in this thesis. The selected screw types and connection geometries are based on the manufacturer specifications provided in the Rothoblaas technical catalogue [36]. The member thicknesses t_1 and t_2 denote the embedment depths of the fastener in member 1 and member 2, respectively, measured along the fastener axis projection normal to the shear plane. For steel-to-timber joints, the steel plate thickness is denoted t_s.

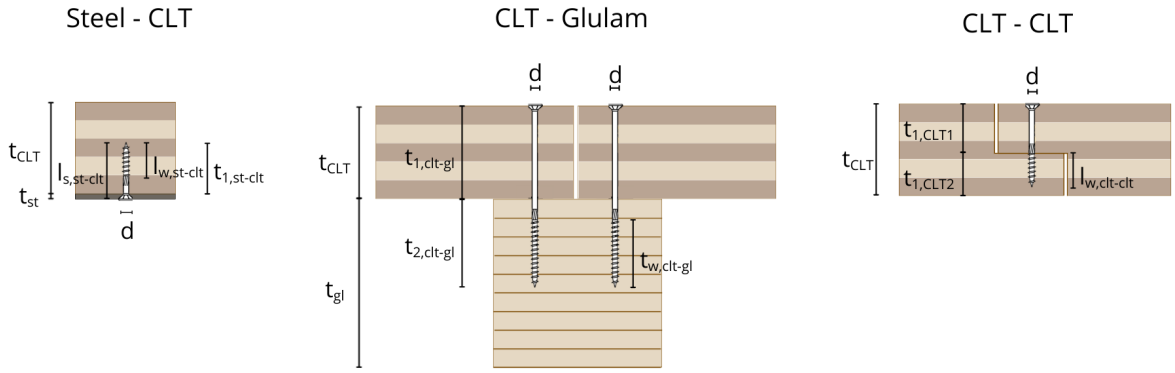

Figure B.1: Connection geometries and definition of embedment and withdrawal lengths used in the resistance checks.

Table B.1: Geometric input values for the resistance checks.

Connection	d [mm]	t_s [mm]	L_{screw} [mm]	t_1 [mm]	t_2 [mm]	l_w [mm]
Steel–CLT	10	10	120	110	–	60
CLT–glulam	10	–	380	200	180	100
CLT–CLT	10	–	160	100	60	60

B.2. Lateral resistance of dowel-type fasteners

This appendix presents the resistance expressions used to evaluate the ultimate capacity of laterally loaded self-drilling screws. All formulations follow prEN 1995-1-1, except for steel-to-timber joints,

which are assessed using EN 1995-1-1 since the steel-to-timber joint provisions are not explicitly provided in the draft version of the revised Eurocode 5.

Embedment strength (not predrilled).
The characteristic embedment strength is taken as:

$$f_{h,\varepsilon,k} = \frac{0.082\,\rho_k\,d^{-0.3}}{2.5\cos^2\varepsilon + \sin^2\varepsilon}, \tag{B.1}$$

where ρ_k is the characteristic timber density, d is the outer screw diameter, and ε is the angle between load direction and grain.

Inner diameter and yield moment.
The inner diameter d_1 is:

$$d_1 = \begin{cases} 0.60d, & 3.5 \le d \le 5.0 \text{ mm}, \\ 0.65d, & 5.0 < d \le 10.0 \text{ mm}, \\ 0.60d, & 10.0 < d \le 14.0 \text{ mm}, \\ 0.75d, & d > 14.0 \text{ mm}. \end{cases} \tag{B.2}$$

The characteristic yield moment is:

$$M_{y,k} = 0.3\,f_{u,k}\,d_1^{2.6}, \tag{B.3}$$

with $f_{u,k}$ the characteristic tensile strength of the screw steel.

Withdrawal strength parameter and withdrawal resistance.
For rope effect, the characteristic axial resistance is obtained from the characteristic withdrawal resistance. The withdrawal strength parameter is:

$$f_{w,k} = k_{\text{screw}}\;k_w\;k_{\text{mat}}\;d^{-0.33}\;\left(\frac{\rho_k}{350}\right)^{k_\rho}, \tag{B.4}$$

where $k_{\text{screw}} = 8.2$ and:

$$k_w = \begin{cases} 1.0, & 30^\circ \le \varepsilon \le 90^\circ, \\ 0.3 + 0.7\,\dfrac{\varepsilon}{30^\circ}, & 0^\circ \le \varepsilon < 30^\circ, \end{cases} \tag{B.5}$$

$$k_{\text{mat}} = \min\left(1 + \frac{\ln(n_p)}{12},\; 1.15\right), \tag{B.6}$$

and the density exponent k_ρ is taken as:

$$k_\rho = \begin{cases} 0.7, & \text{softwood and } \varepsilon \le 5^\circ, \\ 1.1, & \text{softwood and } 5^\circ < \varepsilon \le 90^\circ, \\ 1.6, & \text{hardwood and } 0^\circ \le \varepsilon \le 90^\circ. \end{cases} \tag{B.7}$$

The characteristic withdrawal resistance is then:

$$F_{w,k} = \pi\,d\,l_w\,f_{w,k}. \tag{B.8}$$

For rope effect, the characteristic axial resistance is taken as:

$$F_{ax,Rk} = F_{w,k}. \tag{B.9}$$

Rope effect limitation.
If rope effect is allowed, its contribution is limited to:

$$F_{\text{rope}} \le \frac{F_{ax,Rk}}{4}. \tag{B.10}$$

B.2.1. Steel-to-timber joints

A distinction is made between thin and thick steel plates:

- **Thin steel plate:** $t_s \leq 0.5d$,
- **Thick steel plate:** $t_s \geq d$.

For intermediate plate thicknesses, linear interpolation is applied.

For a thin steel plate, the characteristic lateral resistance per fastener per shear plane is:

$$F_{v,Rk} = \min \begin{cases} 0.4\, f_{h,k}\, t_1\, d, & \text{(a)} \\ 1.15 \sqrt{2\, M_{y,k}\, f_{h,k}\, d} + \dfrac{F_{ax,Rk}}{4} & \text{(b)} \end{cases} \tag{B.11}$$

where t_1 is the embedment depth in the timber member.

For a thick steel plate, the characteristic lateral resistance per fastener per shear plane is:

$$F_{v,Rk} = \min \begin{cases} f_{h,k}\, t_1\, d, & \text{(c)} \\ f_{h,k}\, t_1\, d \left[\sqrt{2 + \dfrac{4 M_{y,k}}{f_{h,k}\, d\, t_1^2}} - 1 \right] + \dfrac{F_{ax,Rk}}{4} & \text{(d)} \\ 2.3 \sqrt{M_{y,k}\, f_{h,k}\, d} + \dfrac{F_{ax,Rk}}{4} & \text{(e)} \end{cases} \tag{B.12}$$

B.2.2. Timber-to-timber joints

For timber-to-timber joints, the relative embedment strengths of the connected members are defined as:

$$\beta = \frac{f_{h,2,k}}{f_{h,1,k}}. \tag{B.13}$$

For fasteners loaded in single shear, the characteristic lateral resistance per fastener per shear plane is taken as the minimum value over the relevant failure modes:

$$F_{v,Rk} = \min \begin{cases} f_{h,1,k}\, t_1\, d & \text{(a)} \\ f_{h,2,k}\, t_2\, d & \text{(b)} \\ \dfrac{f_{h,1,k}\, t_1\, d}{1+\beta} \left[\sqrt{\beta + 2\beta^2 \left(1 + \dfrac{t_2}{t_1} + \left(\dfrac{t_2}{t_1} \right)^2 \right) + \beta^3 \left(\dfrac{t_2}{t_1} \right)^2} - \beta \left(1 + \dfrac{t_2}{t_1} \right) \right] + \dfrac{F_{ax,Rk}}{4} & \text{(c)} \\ 1.05\, \dfrac{f_{h,1,k}\, t_1\, d}{2+\beta} \left[\sqrt{2\beta(1+\beta) + \dfrac{4\beta(2+\beta)\, M_{y,k}}{f_{h,1,k}\, d\, t_1^2}} - \beta \right] + \dfrac{F_{ax,Rk}}{4} & \text{(d)} \\ 1.05\, \dfrac{f_{h,1,k}\, t_2\, d}{1+2\beta} \left[\sqrt{2\beta^2(1+\beta) + \dfrac{4\beta(1+2\beta)\, M_{y,k}}{f_{h,1,k}\, d\, t_2^2}} - \beta \right] + \dfrac{F_{ax,Rk}}{4} & \text{(e)} \\ 1.15 \sqrt{\dfrac{2\beta}{1+\beta}} \sqrt{2\, M_{y,k}\, f_{h,1,k}\, d} + \dfrac{F_{ax,Rk}}{4} & \text{(f)} \end{cases} \tag{B.14}$$

C

Analytical derivation of restraint forces in 1D beam models

This appendix derives the restraint-force expressions used in Section 5.4 for the simplified one-dimensional beam models.

Throughout the derivations, N is treated as the magnitude of the compressive axial force. In the final compact expressions, a negative sign is introduced to match the sign convention adopted in the main text, where compression is taken as negative.

C.1. Situation 2: Beam restrained by panel–core connections

Consider a beam of length L_p subjected to a free shrinkage strain $\Delta\varepsilon_{sh}$. Both ends are connected to axial springs with equal stiffness $K_{PC,\text{fin}}$. Due to the finite spring stiffness, the beam is only partially restrained and develops a compressive axial force N.

If the beam were unrestrained, the free shrinkage would result in a total shortening

$$u_{sh,\text{free}} = \Delta\varepsilon_{sh} L_p. \tag{C.1}$$

Because the shrinkage is restrained, the developed axial force produces an elastic strain in the beam

$$\varepsilon_{el} = \frac{N}{E_{\text{fin}} A}, \tag{C.2}$$

which corresponds to an elastic shortening

$$u_{el} = \varepsilon_{el} L_p = \frac{N L_p}{E_{\text{fin}} A}. \tag{C.3}$$

The actual shortening of the beam therefore equals the free shrinkage shortening minus the elastic shortening associated with the restraint force:

$$u = u_{sh,\text{free}} - u_{el} = L_p \left(\Delta\varepsilon_{sh} - \frac{N}{E_{\text{fin}} A} \right). \tag{C.4}$$

Thus, the free shrinkage shortening is partly accommodated by elastic shortening of the beam and partly by deformation of the end springs.

Because the system is symmetric, the total shortening is shared equally between the two springs. The deformation of each spring is therefore

$$u_s = \frac{u}{2}. \tag{C.5}$$

The reaction force in each spring follows as

$$R = K_{PC,\text{fin}}\, u_s. \tag{C.6}$$

From axial equilibrium, the axial force in the beam must be equal in magnitude to the spring reaction:

$$N = R. \tag{C.7}$$

Substituting $u_s = u/2$ gives

$$N = K_{PC,\text{fin}} \frac{1}{2} L_p \left(\Delta\varepsilon_{sh} - \frac{N}{E_{\text{fin}} A} \right). \tag{C.8}$$

Rearranging yields

$$N = \frac{K_{PC,\text{fin}} L_p}{2} \Delta\varepsilon_{sh} - \frac{K_{PC,\text{fin}} L_p}{2 E_{\text{fin}} A} N, \tag{C.9}$$

$$N \left(1 + \frac{K_{PC,\text{fin}} L_p}{2 E_{\text{fin}} A} \right) = \frac{K_{PC,\text{fin}} L_p}{2} \Delta\varepsilon_{sh}. \tag{C.10}$$

Solving for N gives

$$N = \frac{\dfrac{K_{PC,\text{fin}} L_p}{2} \Delta\varepsilon_{sh}}{1 + \dfrac{K_{PC,\text{fin}} L_p}{2 E_{\text{fin}} A}}. \tag{C.11}$$

Equivalently,

$$N = -\frac{\Delta\varepsilon_{sh} L_p}{\dfrac{2}{K_{PC,\text{fin}}} + \dfrac{L_p}{E_{\text{fin}} A}}, \qquad R = N. \tag{C.12}$$

The expression can be interpreted as the shrinkage strain multiplied by the equivalent stiffness of the system, consisting of the axial stiffness of the beam and the stiffness of the two end connections acting in series.

C.2. Situation 3: Beam restrained by panel–core and panel–beam connections

This configuration follows the same mechanical reasoning as Situation 2, but the beam is now restrained by two springs with different stiffnesses. The left end is connected to a spring with stiffness $K_{PC,\text{fin}}$, representing the panel–core connection, while the right end is connected to a spring with stiffness $K_{PB,\text{fin}}$, representing the panel–beam connection.

If the beam were unrestrained, the free shrinkage would again produce a total shortening

$$u_{sh,\text{free}} = \Delta\varepsilon_{sh} L_p. \tag{C.13}$$

As in Situation 2, the restraint induces a compressive axial force N, which produces an elastic strain

$$\varepsilon_{el} = \frac{N}{E_{\text{fin}} A}, \tag{C.14}$$

and an elastic shortening

$$u_{el} = \varepsilon_{el} L_p = \frac{N L_p}{E_{\text{fin}} A}. \tag{C.15}$$

The actual shortening of the beam therefore becomes

$$u = u_{sh,\text{free}} - u_{el} = L_p \left(\Delta\varepsilon_{sh} - \frac{N}{E_{\text{fin}} A} \right). \tag{C.16}$$

This shortening is accommodated by deformation of the two springs. Let u_{PC} and u_{PB} denote the deformations of the panel–core and panel–beam springs, respectively. Compatibility requires

$$u_{PC} + u_{PB} = u. \tag{C.17}$$

The corresponding spring reactions are

$$R_{PC} = K_{PC,\text{fin}} u_{PC}, \qquad R_{PB} = K_{PB,\text{fin}} u_{PB}. \tag{C.18}$$

Since the beam carries a uniform axial force, equilibrium requires

$$N = R_{PC} = R_{PB}. \tag{C.19}$$

The spring deformations can therefore be written as

$$u_{PC} = \frac{N}{K_{PC,\text{fin}}}, \qquad u_{PB} = \frac{N}{K_{PB,\text{fin}}}. \tag{C.20}$$

Substituting these expressions into the compatibility condition gives

$$\frac{N}{K_{PC,\text{fin}}} + \frac{N}{K_{PB,\text{fin}}} = L_p \left(\Delta\varepsilon_{sh} - \frac{N}{E_{\text{fin}} A} \right). \tag{C.21}$$

Rearranging leads to

$$N \left(\frac{1}{K_{PC,\text{fin}}} + \frac{1}{K_{PB,\text{fin}}} \right) = L_p \Delta\varepsilon_{sh} - \frac{L_p}{E_{\text{fin}} A} N, \tag{C.22}$$

$$N \left(\frac{1}{K_{PC,\text{fin}}} + \frac{1}{K_{PB,\text{fin}}} + \frac{L_p}{E_{\text{fin}} A} \right) = L_p \Delta\varepsilon_{sh}. \tag{C.23}$$

Hence

$$N = \frac{L_p \Delta\varepsilon_{sh}}{\dfrac{1}{K_{PC,\text{fin}}} + \dfrac{1}{K_{PB,\text{fin}}} + \dfrac{L_p}{E_{\text{fin}} A}}. \tag{C.24}$$

In compact form, this becomes

$$N = -\frac{\Delta\varepsilon_{sh} L_p}{\dfrac{1}{K_{PC,\text{fin}}} + \dfrac{1}{K_{PB,\text{fin}}} + \dfrac{L_p}{E_{\text{fin}} A}}, \qquad R_{PC} = R_{PB} = N. \tag{C.25}$$

This expression again reflects a system of stiffnesses acting in series, consisting of the beam stiffness and the stiffnesses of the two different connections.

C.3. Situation 4: Continuously restrained beam

Consider a beam of length L_w subjected to a shrinkage strain $\Delta\varepsilon_{sh}$ and continuously restrained by an elastic foundation with stiffness $k_{PC,\text{fin}}$. The restrained edge is modelled as a continuous line of axial springs. Both beam ends are free, implying

$$N(0) = N(L_w) = 0.$$

Let $u(x)$ denote the axial displacement along the restrained edge. Axial equilibrium of an infinitesimal beam segment requires

$$N'(x) + q_R(x) = 0, \tag{C.26}$$

where $q_R(x)$ is the distributed reaction force from the elastic foundation. Using a Winkler-type foundation model, this reaction is proportional to the local displacement:

$$q_R(x) = -k_{PC,\text{fin}}\, u(x). \tag{C.27}$$

The axial force in the beam follows from

$$N(x) = E_{\text{fin}} A \left[u'(x) - \Delta\varepsilon_{sh}\right]. \tag{C.28}$$

Differentiating gives

$$N'(x) = E_{\text{fin}} A\, u''(x). \tag{C.29}$$

Substituting into the equilibrium equation yields

$$E_{\text{fin}} A\, u''(x) - k_{PC,\text{fin}}\, u(x) = 0. \tag{C.30}$$

Introducing

$$\lambda = \sqrt{\frac{k_{PC,\text{fin}}}{E_{\text{fin}} A}}, \tag{C.31}$$

the equation becomes

$$u''(x) - \lambda^2 u(x) = 0. \tag{C.32}$$

The general solution is

$$u(x) = C_1 \cosh(\lambda x) + C_2 \sinh(\lambda x). \tag{C.33}$$

Applying the boundary conditions $N(0) = N(L_w) = 0$ leads to

$$u'(0) = \Delta\varepsilon_{sh}, \qquad u'(L_w) = \Delta\varepsilon_{sh}.$$

At $x = 0$, this gives

$$\lambda C_2 = \Delta\varepsilon_{sh}, \qquad C_2 = \frac{\Delta\varepsilon_{sh}}{\lambda}. \tag{C.34}$$

At $x = L_w$, substitution gives

$$\lambda \left[C_1 \sinh(\lambda L_w) + C_2 \cosh(\lambda L_w)\right] = \Delta\varepsilon_{sh}. \tag{C.35}$$

Using $C_2 = \Delta\varepsilon_{sh}/\lambda$:

$$\lambda C_1 \sinh(\lambda L_w) = \Delta\varepsilon_{sh} \left[1 - \cosh(\lambda L_w)\right]. \tag{C.36}$$

Hence

$$C_1 = \frac{\Delta\varepsilon_{sh}}{\lambda} \frac{1 - \cosh(\lambda L_w)}{\sinh(\lambda L_w)}. \tag{C.37}$$

Using the hyperbolic half-angle identities, this can be rewritten as

$$C_1 = -\frac{\Delta\varepsilon_{sh}}{\lambda} \frac{\sinh\left(\frac{\lambda L_w}{2}\right)}{\cosh\left(\frac{\lambda L_w}{2}\right)}. \tag{C.38}$$

Substitution into the general solution leads to the centred form

$$u(x) = \frac{\Delta\varepsilon_{sh}}{\lambda} \frac{\sinh\left(\lambda\left(\frac{L_w}{2} - x\right)\right)}{\cosh\left(\frac{\lambda L_w}{2}\right)}. \tag{C.39}$$

This expression makes the symmetry of the problem explicit, with $u(L_w/2) = 0$.
The distributed reaction force then follows directly as

$$q_R(x) = k_{PC,\text{fin}} \frac{\Delta\varepsilon_{sh}}{\lambda} \frac{\sinh\left(\lambda\left(\frac{L_w}{2} - x\right)\right)}{\cosh\left(\frac{\lambda L_w}{2}\right)}. \tag{C.40}$$

To obtain the axial force distribution, the displacement field is differentiated:

$$u'(x) = -\Delta\varepsilon_{sh} \frac{\cosh\left(\lambda\left(\frac{L_w}{2} - x\right)\right)}{\cosh\left(\frac{\lambda L_w}{2}\right)}. \tag{C.41}$$

Substituting this into the axial-force relation gives

$$N(x) = -E_{\text{fin}} A \, \Delta\varepsilon_{sh} \left[1 - \frac{\cosh\left(\lambda \left(\frac{L_w}{2} - x\right)\right)}{\cosh\left(\frac{\lambda L_w}{2}\right)} \right]. \tag{C.42}$$

This shows that the axial force is zero at the free ends and reaches its maximum at midspan, while the distributed reaction force is largest near the edges and decreases towards the centre.

D

Restrained forces verification

This appendix verifies the analytical expressions for shrinkage-induced restraint forces derived in Appendix C against numerical results obtained with RFEM. To ensure a direct comparison, the RFEM models are kept consistent with the analytical idealisations: a 1D axial member subjected to an imposed shrinkage strain and restrained by either fixed end conditions, discrete axial springs representing connection stiffness, or a continuous elastic foundation representing a distributed line connection.

All verification cases use the same shrinkage input, based on a moisture change $\Delta MC = 7\%$ and a shrinkage coefficient $\beta_x = 0.00015$, resulting in a free shrinkage strain

$$\Delta\varepsilon_{sh} = \beta_x \, \Delta MC.$$

In RFEM, the shrinkage is introduced as an equivalent axial strain e_x; the input value $e_x = -1.05$ is rounded by RFEM to $e_x = -1.1$. The elastic modulus is taken as $E = 11{,}000$ N/mm^2 for all models. Per situation, the effective strip width is set to $b_{\text{eff}} = 100$ mm and the relevant restraint parameters (member length and spring stiffness) are defined as listed in the corresponding section.

For each situation, the analytical formula is evaluated using the above input, and the resulting restraint force (and where applicable, its distribution) is compared to the RFEM output shown in the accompanying figures.

D.1. Situation 1: Fully restrained beam.

This configuration represents the limiting case of a member that is fully prevented from axial shortening. The imposed shrinkage strain is therefore fully converted into axial stress. For a linear-elastic material, the axial force follows directly from Hooke's law:

$$N = -E \, A \, \Delta\varepsilon_{sh}, \tag{D.1}$$

with $A = b_{\text{eff}} t$ the cross-sectional area of the considered strip.

Input.

$$\beta_x = 0.00015, \qquad \Delta MC = 7\%, \qquad \Delta\varepsilon_{sh} = \beta_x \Delta MC = 0.00015 \cdot 7 = 1.05 \times 10^{-3}.$$

RFEM rounds the imposed strain from $e_x = -1.05 \times 10^{-3}$ to $e_x = -1.10 \times 10^{-3}$. The modulus is $E = 11{,}000$ N/mm^2 and $b_{\text{eff}} = 100$ mm. In the RFEM verification model, the strip thickness equals $t = 200$ mm, hence

$$A = b_{\text{eff}} t = 100 \cdot 200 = 20{,}000 \text{ mm}^2.$$

Analytical result. Using the unrounded strain value:

$$N = -(11{,}000)(20{,}000)(1.05 \times 10^{-3}) = -231{,}000 \text{ N} = -231.0 \text{ kN}.$$

Using the rounded RFEM input $e_x = -1.10 \times 10^{-3}$:

$$N = -(11{,}000)(20{,}000)(1.10 \times 10^{-3}) = -242{,}000 \text{ N} = -242.0 \text{ kN}.$$

Comparison with RFEM. RFEM reports a uniform axial force of $N = 242.0$ kN (compression), see Figure D.1. The analytical solution matches exactly when the same rounded strain value is used in the calculation; the difference between 231 kN and 242 kN originates solely from the rounding of e_x in RFEM.

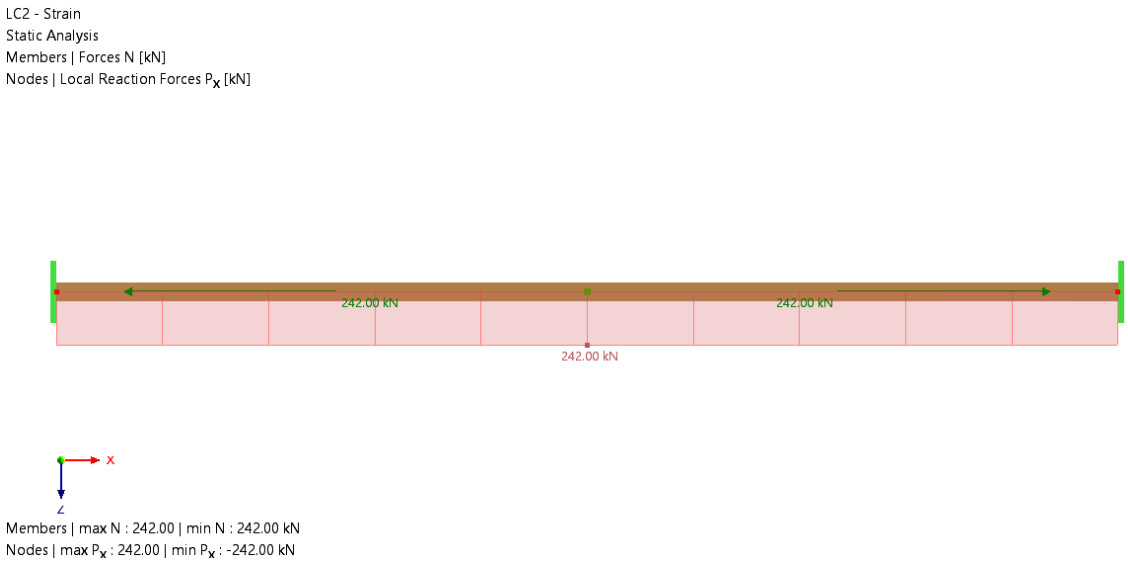

Figure D.1: RFEM check for fully restrained beam.

D.2. Situation 2: Beam restrained by panel–core connection.

In this configuration the beam is restrained by a panel–core connection at both ends, modelled as two identical axial springs with stiffness $K_{PC,\text{fin}}$. Because the restraint stiffness is finite, shrinkage is only partially restrained and the axial force follows from the series deformation of (i) the two springs and (ii) the axial stiffness of the beam strip.

The restrained axial force (equal to the reaction force in each end spring) is

$$N = \frac{-\Delta\varepsilon_{sh}}{\dfrac{2}{K_{PC,\text{fin}}L} + \dfrac{1}{EA}}. \tag{D.2}$$

Input. The imposed shrinkage strain in RFEM is $e_x = -1.1 \times 10^{-3}$. The modulus is $E = 11{,}000$ N/mm^2. For the effective strip width $b_{\text{eff}} = 100$ mm and strip thickness $t = 200$ mm (same as Situation 1),

$$A = b_{\text{eff}}t = 100 \cdot 200 = 20{,}000 \text{ mm}^2, \qquad EA = 11{,}000 \cdot 20{,}000 = 220 \times 10^6 \text{ N} = 220{,}000 \text{ kN}.$$

The spring stiffness is taken from the RFEM support definition:

$$K_{PC,\text{fin}} = 2313.2 \text{ kN/m}.$$

The member length in the RFEM verification model is $L = 11.0$ m.

Analytical result. Substitution into Equation D.2 gives

$$\frac{2}{K_{PC,\text{fin}}L} = \frac{2}{2313.2 \cdot 11.0} = 7.861 \times 10^{-5}\ \text{kN}^{-1}, \qquad \frac{1}{EA} = \frac{1}{220{,}000} = 4.545 \times 10^{-6}\ \text{kN}^{-1},$$

$$N = \frac{-1.1 \times 10^{-3}}{(7.861 \times 10^{-5}) + (4.545 \times 10^{-6})} = -13.23\ \text{kN}.$$

Comparison with RFEM. RFEM reports a uniform axial force of $N = 13.23$ kN and nodal reactions $P_x = \pm 13.23$ kN (see Figure D.2). The analytical result matches the RFEM output for identical input parameters.

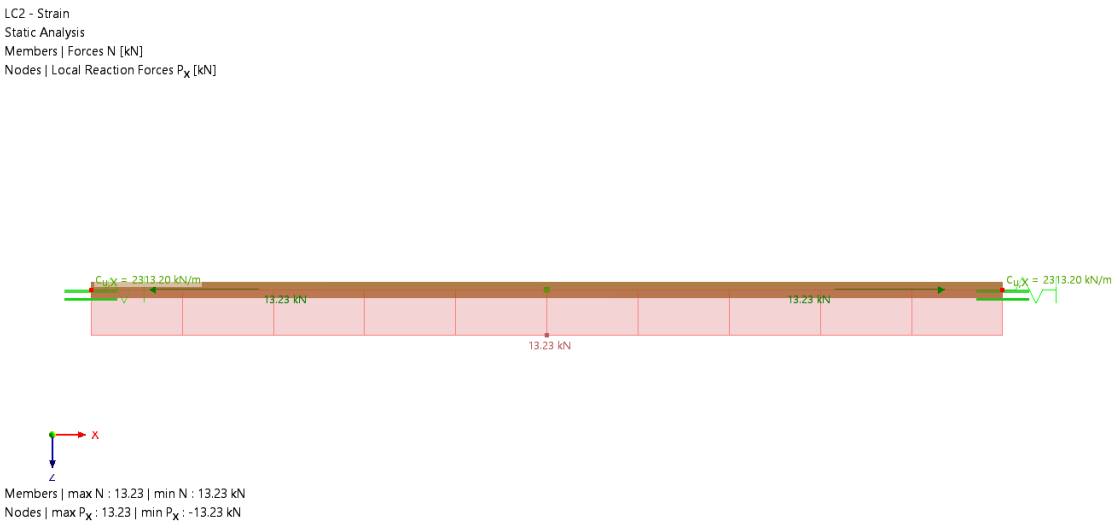

Figure D.2: RFEM check for beam on steel-to-timber connections.

D.3. Situation 3: Beam restrained by panel–core and panel-beam connection.

In this configuration the beam is restrained by two different connections: a panel–core connection at one end and a panel–beam connection at the other. These restraints are modelled as axial springs with stiffness $K_{PC,\text{fin}}$ and $K_{PB,\text{fin}}$, respectively. The restrained axial force follows from the compatibility of deformations of the two springs and the axial deformation of the beam strip.

The axial force (equal to the reaction force in both springs) is

$$N = \frac{-\Delta\varepsilon_{sh}}{\dfrac{1}{K_{PC,\text{fin}}L} + \dfrac{1}{K_{PB,\text{fin}}L} + \dfrac{1}{EA}}. \tag{D.3}$$

Input. The imposed shrinkage strain in RFEM is $e_x = -1.1 \times 10^{-3}$. The modulus is $E = 11{,}000$ N/mm^2. With $b_{\text{eff}} = 100$ mm and $t = 200$ mm,

$$A = b_{\text{eff}}t = 100 \cdot 200 = 20{,}000\ \text{mm}^2, \qquad EA = 11{,}000 \cdot 20{,}000 = 220 \times 10^6\ \text{N} = 220{,}000\ \text{kN}.$$

The member length is $L = 11.0$ m. Spring stiffness values are taken from the RFEM support definitions:

$$K_{PC,\text{fin}} = 2313.2\ \text{kN/m}, \qquad K_{PB,\text{fin}} = 1156.6\ \text{kN/m}.$$

Analytical result. Substitution into Equation D.3 gives

$$\frac{1}{K_{PC,\text{fin}}L} = \frac{1}{2313.2 \cdot 11.0} = 3.931 \times 10^{-5}\ \text{kN}^{-1}, \qquad \frac{1}{K_{PB,\text{fin}}L} = \frac{1}{1156.6 \cdot 11.0} = 7.861 \times 10^{-5}\ \text{kN}^{-1},$$

$$\frac{1}{EA} = \frac{1}{220{,}000} = 4.545 \times 10^{-6}\ \text{kN}^{-1},$$

$$N = \frac{-1.1 \times 10^{-3}}{(3.931 \times 10^{-5}) + (7.861 \times 10^{-5}) + (4.545 \times 10^{-6})} = -8.98\ \text{kN}.$$

Comparison with RFEM. RFEM reports a uniform axial force of $N = 8.98$ kN and nodal reactions $P_x = \pm 8.98$ kN (see Figure D.3). The analytical result matches the RFEM output for identical input parameters.

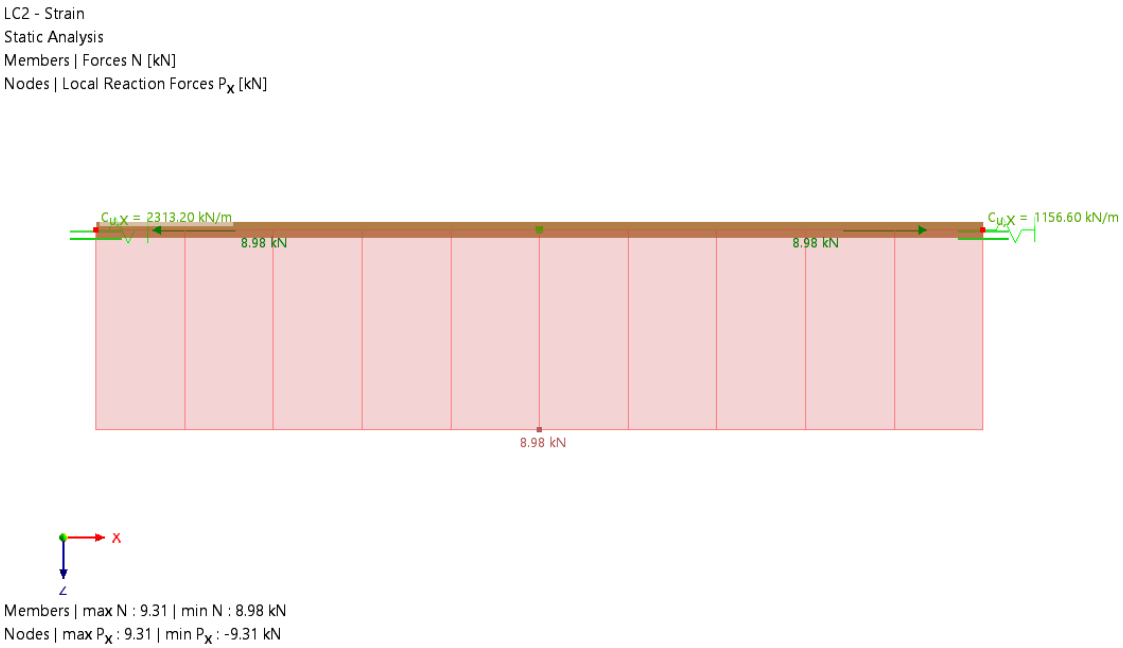

Figure D.3: RFEM check for beam on steel-to-timber and timber-to-timber connection.

D.4. Situation 4: Continuously restrained beam.

This verification case considers shrinkage of a beam strip that is restrained *continuously* along its length by a line connection. In RFEM this is modelled as a distributed elastic support ("continuous springs") with line stiffness $k_{PC,\text{fin}}$ in kN/m^2. The purpose of this check is twofold: (i) verify the analytical expressions for $q(x)$ and $N(x)$ for a beam on an elastic foundation, and (ii) verify that the continuous support can be approximated by discretised nodal springs with a spacing of 100 mm.

Input.

$$L = 8.0\ \text{m}, \qquad b_{\text{eff}} = 100\ \text{mm}, \qquad t = 200\ \text{mm} \Rightarrow A = b_{\text{eff}}t = 20{,}000\ \text{mm}^2,$$

$$E = 11{,}000\ \text{N/mm}^2 \Rightarrow EA = 220 \times 10^6\ \text{N} = 220{,}000\ \text{kN}, \qquad \Delta\varepsilon_{sh} = |e_x| = 1.1 \times 10^{-3},$$

$$k_{PC,\text{fin}} = 23{,}132\ \text{kN/m}^2.$$

For a shrinking member on a continuous elastic foundation, the characteristic parameter is

$$\lambda = \sqrt{\frac{k_{PC,\text{fin}}}{EA}} \qquad [\lambda] = \text{m}^{-1}. \tag{D.4}$$

With the above input:

$$\lambda = \sqrt{\frac{23{,}132}{220{,}000}} = 0.324\ \text{m}^{-1}, \qquad \frac{\lambda L}{2} = 0.324 \cdot 4.0 = 1.297.$$

Using the closed-form solution (cf. Appendix C), the axial displacement field, distributed reaction (shear flow), and axial force are

$$u(x) = \frac{\Delta\varepsilon_{sh}}{\lambda} \frac{\sinh\left(\lambda\left(\frac{L}{2} - x\right)\right)}{\cosh\left(\frac{\lambda L}{2}\right)}, \qquad q(x) = k_{PC,\text{fin}}\, u(x), \tag{D.5}$$

$$N(x) = -EA\,\Delta\varepsilon_{sh}\left[1 - \frac{\cosh\left(\lambda\left(\frac{L}{2} - x\right)\right)}{\cosh\left(\frac{\lambda L}{2}\right)}\right]. \tag{D.6}$$

The peak distributed reaction occurs at the ends ($x = 0$ and $x = L$):

$$q_{\max} = \sqrt{k_{PC,\text{fin}}\, EA}\,\Delta\varepsilon_{sh}\,\tanh\left(\frac{\lambda L}{2}\right). \tag{D.7}$$

Substitution gives

$$q_{\max} = \sqrt{(23{,}132)(220{,}000)}\,(1.1 \times 10^{-3})\,\tanh(1.297) = 67.6\ \text{kN/m}.$$

The peak axial force occurs at midspan ($x = L/2$):

$$N_{\max} = EA\,\Delta\varepsilon_{sh}\left(1 - \frac{1}{\cosh\left(\frac{\lambda L}{2}\right)}\right), \tag{D.8}$$

which yields

$$N_{\max} = 220{,}000\,(1.1 \times 10^{-3})\left(1 - \frac{1}{\cosh(1.297)}\right) = 119\ \text{kN}.$$

Comparison with RFEM. RFEM shows the characteristic distributions and peak values of $q(x)$ and $N(x)$ for the continuous support model (see Figure D.4). The analytical results closely reproduce the RFEM response for identical input parameters.

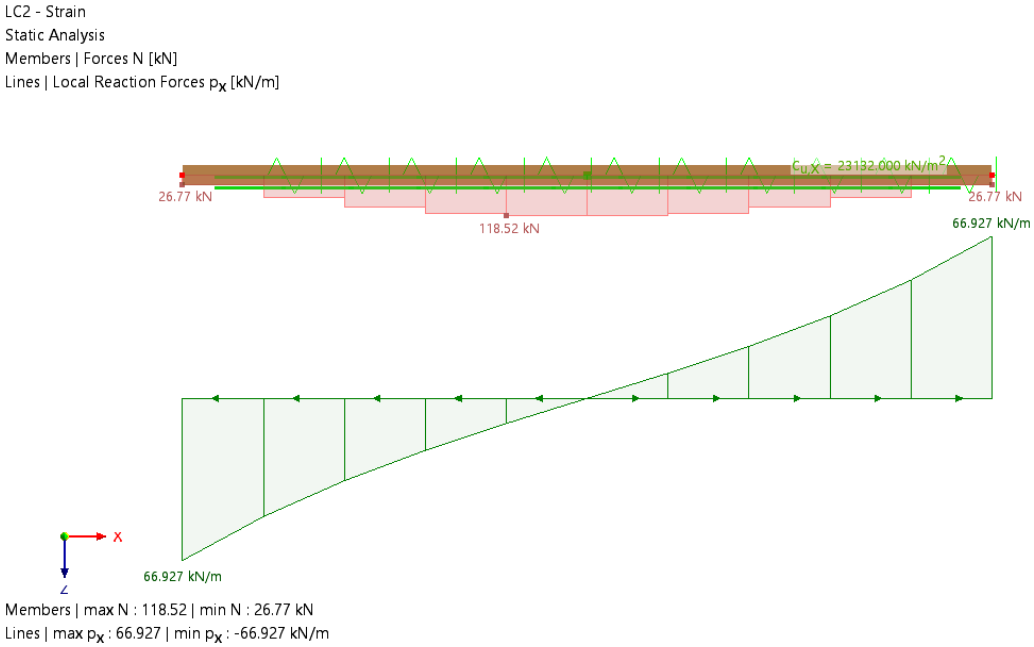

Figure D.4: RFEM check for beam on distributed springs.

To verify discretisation, the continuous foundation is replaced by nodal springs with spacing $s = 100\,\text{mm}$ (= 0.10 m). The equivalent nodal spring stiffness $K_{PC,\text{fin}} = 2313.2$ is used.

The force in a discrete spring at position x_i is approximated by integrating the distributed reaction over the tributary length. With uniform spacing this reduces to

$$R_i \approx q(x_i)\, s. \tag{D.9}$$

Using the peak reaction:

$$R_{\max} \approx q_{\max} s = 67.6 \times 0.10 = 6.76\ \text{kN}.$$

Comparison with RFEM. In the discretised RFEM model the nodal reactions reach approximately $P_{x,\max} \approx 6.66$ kN (see Figure D.5), which is in close agreement with $R_{\max} \approx 6.76$ kN from the analytical approximation.

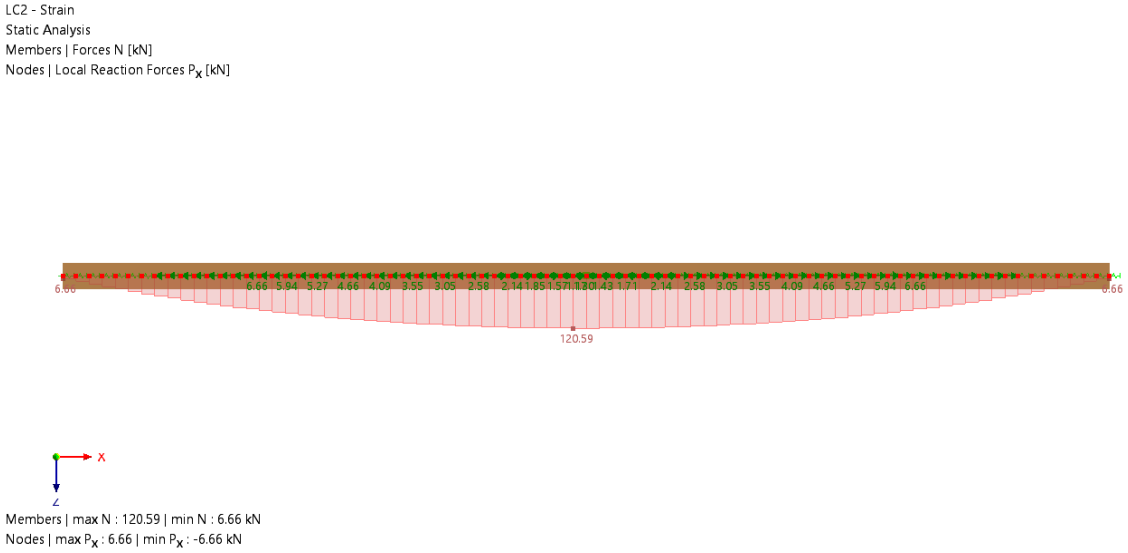

Figure D.5: RFEM check for beam on distributed springs, discretized.

E

Effective width distributed spring model

In this appendix, the effective widths determined from the RFEM analyses are verified using the analytical beam–spring formulation presented in Section **??**.

For a beam on a distributed elastic foundation, the maximum line reaction at the restrained edge is given by:

$$q_{\max} = k_{\text{line}} \frac{\varepsilon}{\lambda} \tanh\left(\frac{\lambda L}{2}\right), \tag{E.1}$$

with

$$\lambda = \sqrt{\frac{k_{\text{line}}}{E\,A}}, \qquad A = b_{\text{eff}}\, t. \tag{E.2}$$

Here:

- k_{line} is the line stiffness of the connection,
- E is the Young's modulus of the CLT panel,
- t is the panel thickness,
- b_{eff} is the calibrated effective width,
- L is the length of the restrained edge,
- ε is the imposed shrinkage strain.

The following two cases are verified.

E.1. Situation 4a: short edge

- $L = 2000\,\text{mm}$
- $\beta_y = 0.00035$
- $b_{\text{eff}} = 190\,\text{mm}$
- $t = 200\,\text{mm}$
- $q_{\text{RFEM}} = 45.140\,\text{N/mm}$

The axial stiffness becomes:

$$A = b_{\text{eff}} t = 190 \times 200 = 38{,}000\,\text{mm}^2. \tag{E.3}$$

The parameter λ is:

$$\lambda = \sqrt{\frac{k_{\text{line}}}{EA}}. \tag{E.4}$$

Substitution into the expression for $q_{\max}$ yields:

$$q_{\max} = k_{\text{line}} \frac{\varepsilon}{\lambda} \tanh\left(\frac{\lambda L}{2}\right) = 45.15\,\text{N/mm}, \tag{E.5}$$

which matches the RFEM result.

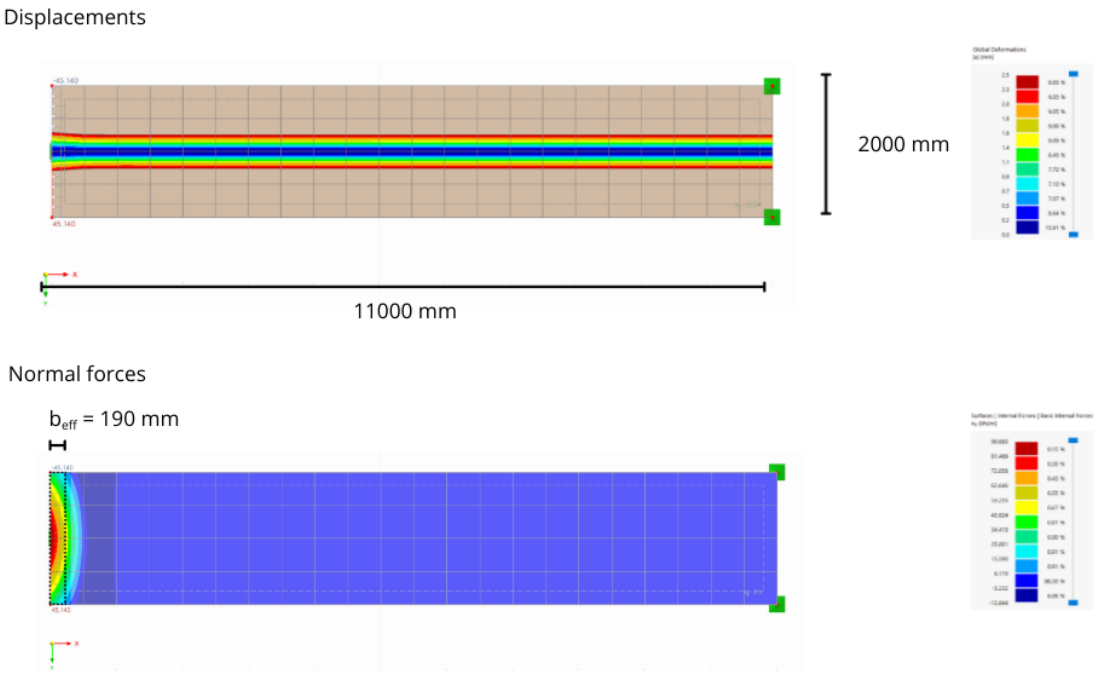

Figure E.1: Effective width for shrinkage along the short edge (situation 4a).

E.2. Situation 4b: long edge

- $L = 8000\,\text{mm}$
- $\beta_x = 0.00015$
- $b_{\text{eff}} = 455\,\text{mm}$
- $t = 200\,\text{mm}$
- $q_{\text{RFEM}} = 70.809\,\text{N/mm}$

The axial stiffness becomes:

$$A = b_{\text{eff}} t = 455 \times 200 = 91{,}000\,\text{mm}^2. \tag{E.6}$$

The parameter λ is:

$$\lambda = \sqrt{\frac{k_{\text{line}}}{EA}}. \tag{E.7}$$

Substitution into the analytical expression results in:

$$q_{\max} = k_{\text{line}} \frac{\varepsilon}{\lambda} \tanh\left(\frac{\lambda L}{2}\right) = 70.79\,\text{N/mm}, \tag{E.8}$$

which is in agreement with the RFEM analysis.

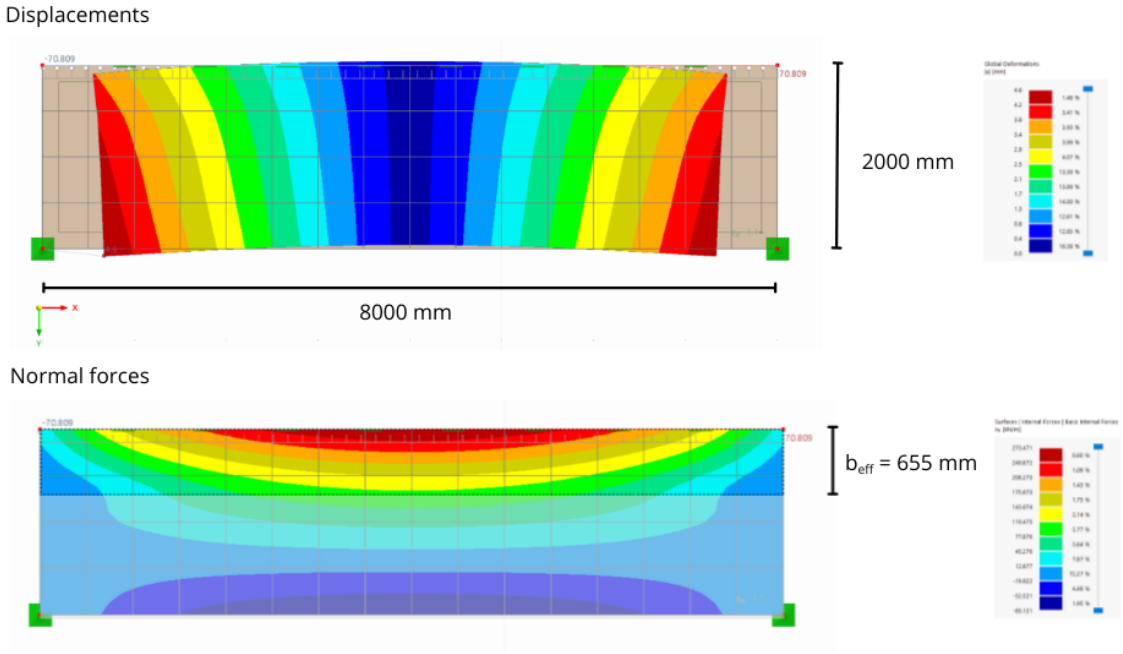

Figure E.2: Effective width for shrinkage along the long edge (situation 4b).

F

Critical load spring supported column

This appendix derives the critical axial load P_{cr} for a (nearly) rigid column of length L with a pinned base and a lateral translational spring of stiffness k at the top. The result is compared with the RFEM linear eigenvalue buckling analysis.

F.1. Analytical derivation

Figure F.1 shows the idealised model. The column is pinned at the base and loaded in compression by P at the top. The top node is laterally restrained by a linear spring with stiffness k. The column is assumed very stiff in bending, so the deformed shape is approximated as a rigid rotation by a small angle φ (limiting case $EI \to \infty$). The stability problem then has one degree of freedom: the rotation φ.

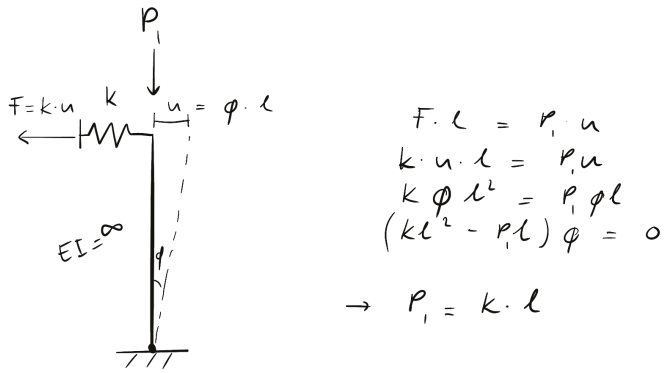

Figure F.1: Spring-supported column idealisation.

For a small rotation φ, the lateral displacement at the top is

$$u = \varphi L. \tag{F.1}$$

The spring force follows as

$$F = ku = k\varphi L. \tag{F.2}$$

Taking moments about the base gives:

$$M_k = FL = k\varphi L^2, \tag{F.3}$$

$$M_P = Pu = P\varphi L. \tag{F.4}$$

At neutral equilibrium the net moment is zero:

$$M_k - M_P = 0 \quad \Rightarrow \quad k\varphi L^2 - P\varphi L = 0. \tag{F.5}$$

For $\varphi \neq 0$, the critical load is

$$P_{\text{cr}} = kL. \tag{F.6}$$

This expression applies to the rigid-rotation limit. For finite bending stiffness EI, the critical load also depends on EI and approaches classical Euler-type behaviour.

F.2. Numerical verification column-spring model

Figure F.2 shows the first eigenmode from RFEM for the same system. The column cross-section is 400×400 mm and the material stiffness is taken as

$$E = 11{,}500 \text{ N/mm}^2, \tag{F.7}$$

corresponding to GL24c. In RFEM, a reference load $P_{\text{ref}} = 100$ kN is applied and the software reports a critical load factor λ_{cr}:

$$P_{\text{cr,RFEM}} = \lambda_{\text{cr}} P_{\text{ref}}. \tag{F.8}$$

For the RFEM model:

$$k = 1000 \text{ kN/m}, \qquad L = 3.2 \text{ m}, \qquad P_{\text{ref}} = 100 \text{ kN}. \tag{F.9}$$

The analytical result gives

$$P_{\text{cr}} = kL = 1000 \cdot 3.2 = 3200 \text{ kN}, \tag{F.10}$$

so the expected eigenvalue factor is

$$\lambda_{\text{cr}} = \frac{P_{\text{cr}}}{P_{\text{ref}}} = \frac{3200}{100} = 32. \tag{F.11}$$

This matches the first eigenvalue factor reported by RFEM (Mode Shape No. 1: $\lambda_{\text{cr}} = 32.000$), confirming consistency with $P_{\text{cr}} = kL$ for this idealisation.

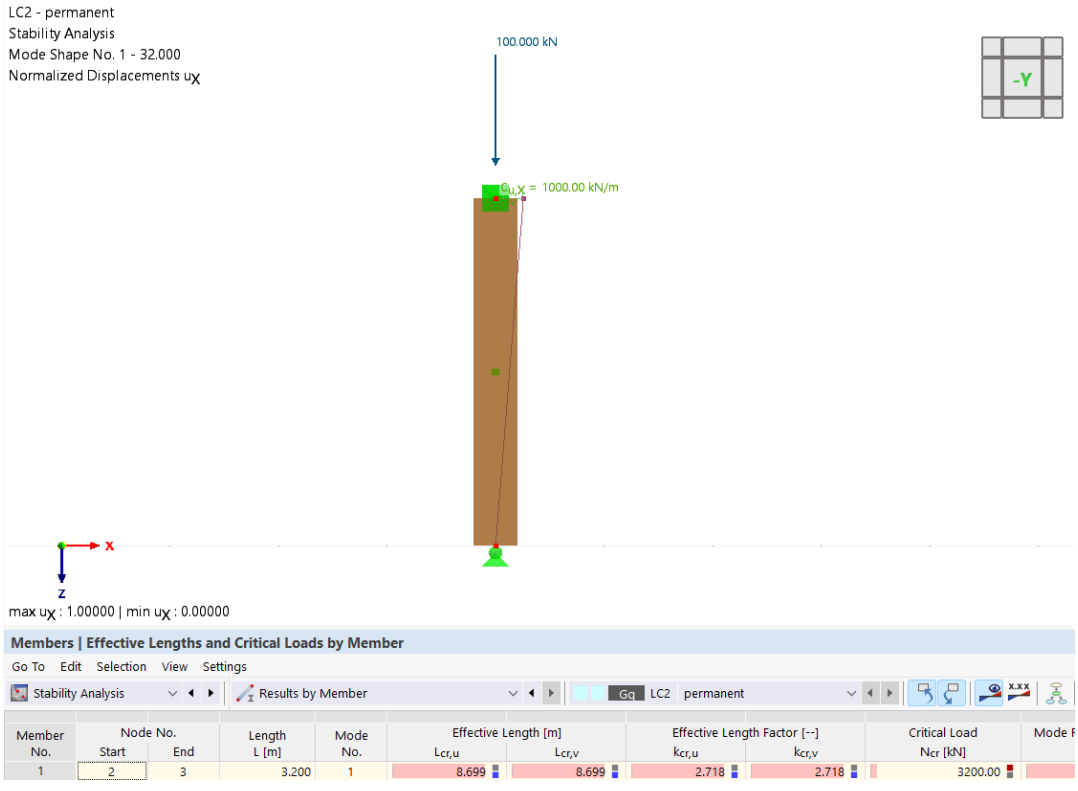

Figure F.2: RFEM linear eigenvalue buckling analysis of the spring-supported column.

G

Diaphragm deformation mechanisms: rocking, segmentation and grout

This appendix supports subsection 7.2.1 by combining an analytical breakdown of the monolithic cantilever-segment displacement into mechanism contributions and RFEM illustrations of how rocking behaviour changes with floor segmentation and grout at the floor–core interface.

The figures show the in-plane displacement field u of the segment (contours, in mm) and the line force resultants v_y along the floor–core interface and the panel–panel line hinges (in kN/m). The black markers (RC) indicate the rotation centre(s) identified from the displacement field.

G.1. Deformation components

This section evaluates the displacement components from Eqs. (7.1)–(7.5) for the monolithic cantilever segment. The goal is to quantify the displacement contribution of each mechanism and to compare the analytical total displacement to the RFEM result for the same segment. The input parameters are:

$$
\begin{aligned}
&L_p = 11000\ \text{mm}, \qquad L_{\text{core}} = 8000\ \text{mm}, \qquad t = 200\ \text{mm},\\
&E = 11000\ \text{N/mm}^2, \qquad G_{xy,\text{mean}} = 690\ \text{N/mm}^2,\\
&q = 4.451\ \text{N/mm}, \qquad s_c = 100\ \text{mm}, \qquad K_c = 1892.7\ \text{N/mm}.
\end{aligned}
$$

The section properties are taken as

$$
I = \frac{1}{12}\, t\, L_{\text{core}}^3, \qquad EI = EI, \qquad A_s = L_{\text{core}}\, t.
$$

For the monolithic floor–core interface, the translational and rotational stiffnesses are

$$
k_c = \frac{K_{c,\text{ser}}}{s_c} \quad [\text{N/mm}^2], \qquad K_A = L_{\text{core}}\, k_c \quad [\text{N/mm}], \qquad K_R = k_c\, \frac{L_{\text{core}}^3}{12} \quad [\text{N mm}].
$$

The displacement contributions are:

$$u_A = \frac{qL_p}{K_A} = 0.32 \text{ mm},$$
$$u_R = \frac{qL_p^3}{2K_R} = 3.67 \text{ mm},$$
$$u_B = \frac{qL_p^4}{8EI} = 0.09 \text{ mm},$$
$$u_S = \frac{qL_p^2}{2\,G_{xy,\text{mean}}\,A_s} = 0.24 \text{ mm}.$$

This gives a total displacement

$$u_{\text{tot}} = u_A + u_R + u_B + u_S = 4.32 \text{ mm}.$$

Rocking is the dominant contribution ($u_R \approx 85\%$ of u_{tot}), rocking governs the in-plane deformation for the monolithic segment. The analytical result $u_{\text{tot}} = 4.32$ mm is of the same order as the RFEM displacement for the monolithic segment, $u_Y = 4.4$ mm.

G.2. Effect of panel–panel rotational coupling

Figure G.1 compares a monolithic floor to a segmented floor with rigid panel–panel coupling ($K_p \to \infty$). Both cases show an almost identical deformation pattern: one global rocking mode with a rotation centre near the mid-width of the segment. In this configuration, the rocking moment is resisted with a relatively large lever arm, which limits both displacements and interface demands. For the monolithic reference, $u_{\max} = 4.7$ mm and $\max(v_y) = 25.46$ kN/m. The segmented case with $K_p \to \infty$ shows essentially the same displacement field.

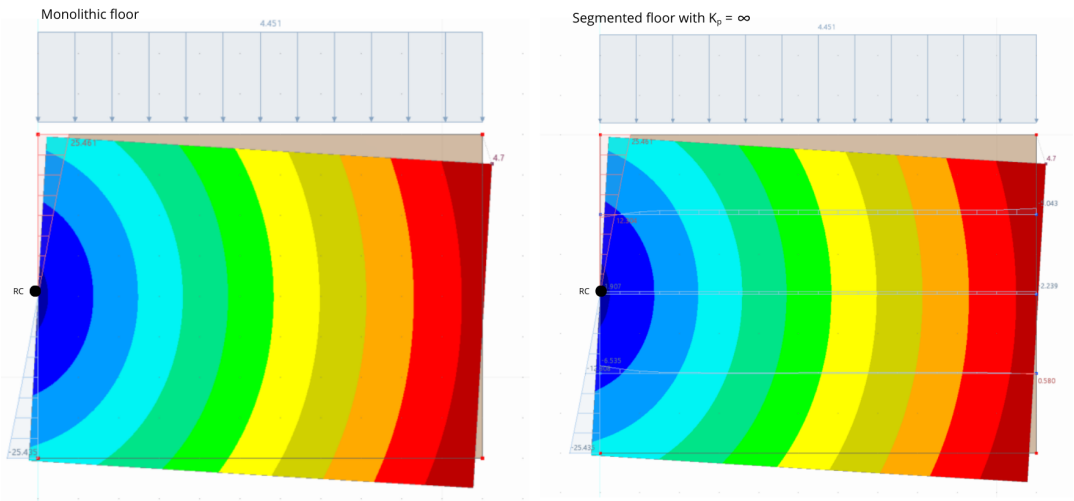

Figure G.1: In-plane displacement u (mm) for (left) a monolithic floor and (right) a segmented floor with rigid panel–panel coupling.

Figure G.2 shows the effect of reducing the panel–panel rotational stiffness. For $K_p = 0$, panels are uncoupled in rotation and moment transfer across the panel interfaces vanishes. The global rocking mode disappears and each panel rocks more independently, leading to multiple rotation centres. As the effective lever arm to mobilise a resisting couple reduces, both displacements and interface demands increase strongly. Here, $u_{\max} = 56.0$ mm and $\max(v_y) = 89.53$ kN/m.

For finite stiffness ($K_p = 12000\,\text{kN/m}^2$), panels are partly coupled and the response becomes intermediate. Panels rotate in groups, resulting in multiple rotation centres depending on the value of K_p (ranging

from several centres at low K_p to one centre for $K_p \to \infty$). Relative panel rotation remains visible as kinks in the displacement field and as local jumps in v_y along the panel–panel hinges. In this case, $u_{\max} = 6.2$ mm and $\max(v_y) = 28.04$ kN/m.

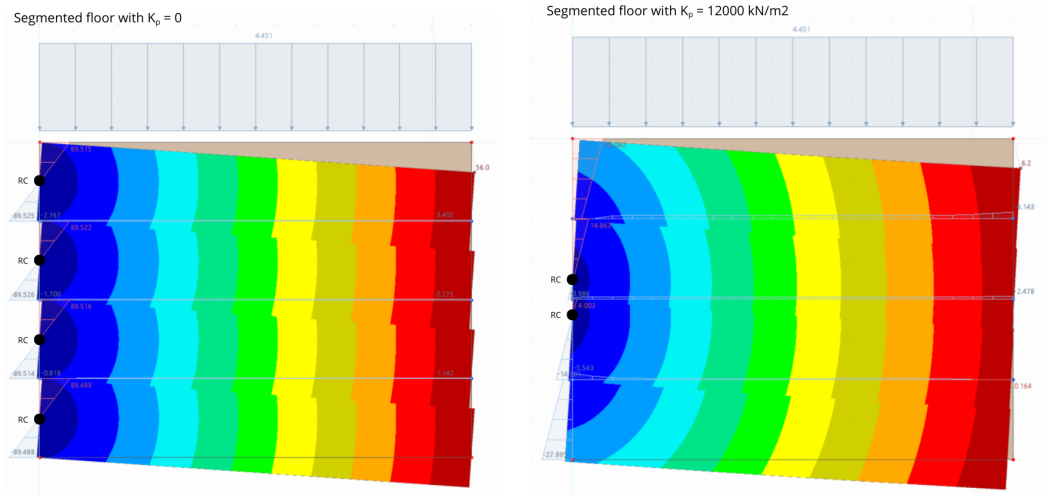

Figure G.2: Segmented floors with (left) K_{PP} and (right) $K_{PP} = 12000$ kN/m^2. Contours show in-plane displacement u (mm).

G.3. Effect of grout at the floor–core interface

Figure G.3 shows the effect of grout in the floor–core gap. With grout, rocking tends to activate contact at the interface. A compression zone forms along the core boundary and provides a stiff restoring couple, which reduces the rocking displacement.

For the monolithic floor with grout, $u_{\max} = 2.2$ mm. The interface response becomes compression-dominated, with $v_y^{\min} = -81.93$ kN/m and $v_y^{\max} = 15.66$ kN/m. This indicates that the rocking couple is carried primarily through compression transfer at the contact zone, while the fasteners on the opposite side carry a smaller share.

For the segmented floor with grout, $u_{\max} = 3.5$ mm, with $v_y^{\min} = -114.72$ kN/m and $v_y^{\max} = 18.36$ kN/m. Segmentation still influences the kinematics and local force concentrations, although the grout contact reduces the overall rocking deformation compared to the ungrouted configuration.

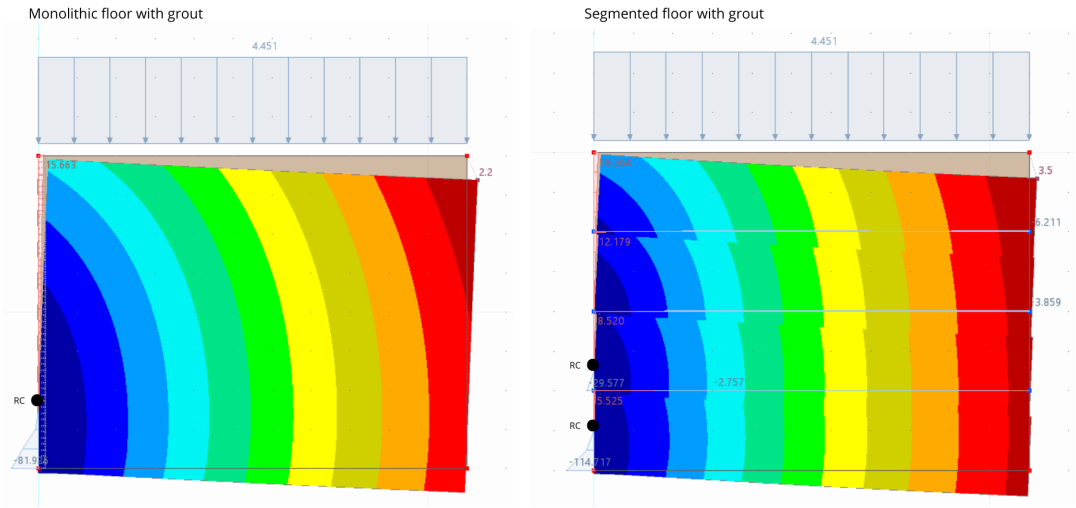

Figure G.3: Effect of grout at the floor–core interface: (left) monolithic floor with grout and (right) segmented floor with grout. Contours show in-plane displacement u (mm).

H

ULS connection checks

This appendix reports the detailed ULS checks for the diaphragm connections in Part III. RFEM line-hinge resultants are reported per unit length [kN/m] and are converted to fastener-level design forces using the fastener spacing of each variant. Results are shown for both first- and second-order analyses; variants labelled as *unstable* did not converge in second-order analysis.

Fastener-level conversion and utilisation

For fastener checks, the governing RFEM normal-force line resultant is converted to a design force per fastener as

$$F_{Ed} = |n_{Ed}|\ s, \tag{H.1}$$

where n_{Ed} is the relevant line resultant [kN/m] and s is the fastener spacing [m]. The utilisation ratio is evaluated as

$$\eta = \frac{F_{Ed}}{F_{Rd}}. \tag{H.2}$$

Panel–core fastener checks

For all variants, the panel–core fastener demand is reported using the peak normal-force line resultant $n_{\mathrm{PC,max}}$:

$$F_{Ed,\mathrm{PC}} = |n_{\mathrm{PC,max}}|\ s_{\mathrm{PC}}. \tag{H.3}$$

The derived fastener-level forces and utilisation ratios are reported in Table H.1.

Panel–panel fastener checks

For the panel–panel connections, the demand is governed by the peak normal-force line resultant $n_{\mathrm{PP,max}}$:

$$F_{Ed,\mathrm{PP}} = |n_{\mathrm{PP,max}}|\ s_{\mathrm{PP}}. \tag{H.4}$$

The derived fastener-level forces and utilisation ratios are reported in Table H.2.

Table H.1: Derived fastener-level ULS checks for the **panel–core (PC)** connection (a- and b-series), based on the peak normal-force line resultant $n_{\mathrm{PC,max}}$.

Case	s_{PC} [m]	$\lvert n_{\mathrm{PC,max},1}\rvert$ [kN/m]	$F_{Ed,1}$ [N]	η_1	$\lvert n_{\mathrm{PC,max},2}\rvert$ [kN/m]	$F_{Ed,2}$ [N]	η_2
C0	fixed	–	–	–	–	–	–
C1a1	0.10	10.5	1050	0.40	13.0	1300	0.49
C1b1	0.10	8.0	800	0.30	8.5	850	0.32
C1a2	0.10	10.0	1000	0.38	13.7	1370	0.52
C1b2	0.10	8.1	810	0.31	9.3	930	0.35
C1a3	0.10	9.7	970	0.37	15.7	1570	0.59
C1b3	0.10	8.2	820	0.31	10.0	1000	0.38
C1a4	0.10	9.5	950	0.36	unstable	–	–
C1b4	0.10	8.1	810	0.31	11.1	1110	0.42
C2a1	0.20	10.3	2060	0.78	27.2	5440	2.06
C2b1	0.20	6.8	1360	0.51	8.0	1600	0.60
C2a2	0.20	10.0	2000	0.76	unstable	–	–
C2b2	0.20	7.3	1460	0.55	9.3	1860	0.70
C2a3	0.20	9.7	1940	0.73	unstable	–	–
C2b3	0.20	7.5	1500	0.57	10.8	2160	0.82
C2a4	0.20	9.6	1920	0.73	unstable	–	–
C2b4	0.20	7.5	1500	0.57	13.0	2600	0.98
C3a1	0.30	10.0	3000	1.13	unstable	–	–
C3b1	0.30	6.0	1800	0.68	7.4	2220	0.84
C3a2	0.30	9.9	2970	1.12	unstable	–	–
C3b2	0.30	6.6	1980	0.75	9.3	2790	1.05
C3a3	0.30	9.8	2940	1.11	unstable	–	–
C3b3	0.30	6.8	2040	0.77	12.0	3600	1.36
C3a4	0.30	9.6	2880	1.09	unstable	–	–
C3b4	0.30	4.6	1380	0.52	unstable	–	–

Table H.2: Derived fastener-level ULS checks for the **panel–panel (PP)** connection, based on the peak normal-force line resultant $n_{\mathrm{PP,max}}$.

Case	s_{PP} [m]	$\lvert n_{\mathrm{PP,max},1}\rvert$ [kN/m]	$F_{Ed,1}$ [N]	η_1	$\lvert n_{\mathrm{PP,max},2}\rvert$ [kN/m]	$F_{Ed,2}$ [N]	η_2
C0	fixed	–	–	–	–	–	–
C1a1	0.10	6.5	650	0.23	8.4	840	0.30
C1b1	0.10	5.4	540	0.19	6.4	640	0.23
C1a2	0.20	5.6	1120	0.40	8.2	1640	0.58
C1b2	0.20	4.3	860	0.31	5.4	1080	0.38
C1a3	0.30	8.0	2400	0.85	8.9	2670	0.95
C1b3	0.30	6.6	1980	0.70	8.2	2460	0.87
C1a4	0.40	4.6	1840	0.65	unstable	–	–
C1b4	0.40	3.5	1400	0.50	5.2	2080	0.74
C2a1	0.10	6.8	680	0.24	20.4	2040	0.72
C2b1	0.10	5.0	500	0.18	6.4	640	0.23
C2a2	0.20	6.0	1200	0.43	unstable	–	–
C2b2	0.20	4.8	960	0.34	7.0	1400	0.50
C2a3	0.30	5.4	1620	0.57	unstable	–	–
C2b3	0.30	4.1	1230	0.44	6.4	1920	0.68
C2a4	0.40	5.0	2000	0.71	unstable	–	–
C2b4	0.40	3.7	1480	0.53	7.1	2840	1.01
C3a1	0.10	6.9	690	0.24	unstable	–	–
C3b1	0.10	5.0	500	0.18	6.8	680	0.24
C3a2	0.20	6.1	1220	0.43	unstable	–	–
C3b2	0.20	5.2	1040	0.37	6.9	1380	0.49
C3a3	0.30	5.6	1680	0.60	unstable	–	–
C3b3	0.30	4.1	1230	0.44	8.8	2640	0.94
C3a4	0.40	5.2	2080	0.74	unstable	–	–
C3b4	0.40	2.5	1000	0.35	unstable	–	–

Table H.3: Derived fastener-level ULS checks for the **panel–core (PC)** shear connection (a-series), based on the peak shear-force line resultant $v_{y,\mathrm{PC,max}}$.

Case	s_{PC} [m]	$\lvert v_{y,\mathrm{PC,max},1}\rvert$ [kN/m]	$F_{Ed,1}$ [N]	η_1	$\lvert v_{y,\mathrm{PC,max},2}\rvert$ [kN/m]	$F_{Ed,2}$ [N]	η_2
C0	fixed	–	–	–	–	–	–
C1a1	0.10	15.3	1530	0.58	18.7	1870	0.71
C1a2	0.10	16.8	1680	0.64	22.9	2290	0.87
C1a3	0.10	17.9	1790	0.68	28.9	2890	1.09
C1a4	0.10	18.9	1890	0.71	unstable	–	–
C2a1	0.20	12.8	2560	0.97	34.8	6960	2.63
C2a2	0.20	13.8	2760	1.04	unstable	–	–
C2a3	0.20	14.6	2920	1.10	unstable	–	–
C2a4	0.20	15.2	3040	1.15	unstable	–	–
C3a1	0.30	11.8	3540	1.34	unstable	–	–
C3a2	0.30	12.5	3750	1.42	unstable	–	–
C3a3	0.30	13.0	3900	1.47	unstable	–	–
C3a4	0.30	13.5	4050	1.53	unstable	–	–

Timber bearing check for grouted panel–core interfaces

For the grouted variants (b-series), rocking activates local contact at the panel–core interface and a compression zone forms. The RFEM shear resultant $v_{y,\mathrm{PC}}$ becomes highly localised near the contact region (see Fig. 8.8 and Appendix G). To obtain a conservative estimate of the timber bearing stress, the peak shear resultant is converted to a compressive stress using an effective bearing width $b_{\mathrm{eff}} = 0.25$ m:

$$\sigma_{c,t,Ed} = \frac{|v_{y,\mathrm{PC,Ed}}|}{b_{\mathrm{eff}}}. \tag{H.5}$$

The utilisation is evaluated as

$$\eta_\sigma = \frac{\sigma_{c,t,Ed}}{f_{c,t,k}}, \tag{H.6}$$

with $f_{c,t,k} = 21$ MPa. The derived stresses and utilisations are reported in Table H.4.

Table H.4: Derived timber bearing stress for grouted panel–core variants (b-series), based on the peak panel–core shear resultant $v_{y,\mathrm{PC,max}}$ from RFEM.

Case	$v_{y,\mathrm{PC,max},1}$ [kN/m]	$\sigma_{c,t,Ed,1}$ [MPa]	$\eta_{\sigma,1}$ [-]	$v_{y,\mathrm{PC,max},2}$ [kN/m]	$\sigma_{c,t,Ed,2}$ [MPa]	$\eta_{\sigma,2}$ [-]
C1b1	-821.8	3.29	0.16	-821.8	3.29	0.16
C1b2	-1175.4	4.70	0.22	-1177.8	4.71	0.22
C1b3	-1416.3	5.67	0.27	-1423.8	5.70	0.27
C1b4	-1625.1	6.50	0.31	-1635.7	6.54	0.31
C2b1	-853.3	3.41	0.16	-853.3	3.41	0.16
C2b2	-1254.1	5.02	0.24	-1254.1	5.02	0.24
C2b3	-1526.7	6.11	0.29	-1531.2	6.12	0.29
C2b4	-1747.8	6.99	0.33	-2095.7	8.38	0.40
C3b1	-857.5	3.43	0.16	-857.4	3.43	0.16
C3b2	-1275.3	5.10	0.24	-1275.3	5.10	0.24
C3b3	-1559.6	6.24	0.30	-2227.3	8.91	0.42
C3b4	-1287.7	5.15	0.25	unstable	–	–

I

RFEM case study model verification

I.1. Model verification strategy

This appendix documents the verification checks performed on the baseline RFEM model (Case C0: monolithic floor, PC0+PP0+PB0). The aim is not to reproduce all results by hand, but to demonstrate that the model is representative of the structural problem and that the global mechanisms and load paths are understood. Checks are performed risk-driven and in increasing order of model complexity, starting from individual load cases in a first-order linear-elastic analysis.

Unless stated otherwise, checks are first carried out for the individual load cases ($LC1$, $LC2$, $LC3$, $LC5$) using a 1st-order static analysis. Only after the individual load cases are validated are the governing load combinations for result extraction evaluated in both 1st- and 2nd-order analysis (CO15/CO8 for SLS and CO14/CO4 for ULS).

I.2. Global equilibrium checks

kijken hier naar het hele gebouw.

I.2.1. Global vertical equilibrium

Table I.1: Verification check: global vertical equilibrium.

Load case	$LC1 + LC2 + LC3$
RFEM output	Sum of vertical support reactions, $\sum R_z$
Expected outcome	$\sum R_z$ matches total applied vertical load
Purpose	Confirms vertical load magnitudes and load transfer to supports

Hand calculation:
The gross floor area is $A = 19 \cdot 24 - 8 \cdot 8 = 392$ m^2. For 10 typical floors, $q_{LC2} = 4.25$ kN/m^2 and $q_{LC3} = 2.25$ kN/m^2 are applied. For the roof (1 floor), reduced loads $q_{LC2,\text{roof}} = 1.5$ kN/m^2 and $q_{LC3,\text{roof}} = 1.9$ kN/m^2 are used. A facade line load of 1.0 kN/m over 42 m is included at each of the 11 levels.

Self-weight per storey is estimated from one CLT floor ($t = 0.20$ m), 30 glulam beams (0.36×0.36 m, $L = 4$ m), (iii) 40 column segments (0.40×0.40 m, $h = 3.2$ m), 8 concrete core wall segments ($L = 4$ m, $h = 3.2$ m, $t = 0.30$ m), and one concrete core slab ($8 \times 8 \times 0.30$ m). Using $\gamma_{\text{CLT}} = 5$ kN/m^3, $\gamma_{\text{glulam}} = 4.2$ kN/m^3, and $\gamma_{\text{conc}} = 25$ kN/m^3, this gives $W_{LC1,1} \approx 1791$ kN per storey, hence $W_{LC1,\text{tot}} \approx 11 \cdot 1791 = 19.7$ MN.

The applied surface loads sum to $W_{LC2+LC3} = 10 \cdot A \cdot (4.25 + 2.25) + A \cdot (1.5 + 1.9) + 11 \cdot (1.0 \cdot 42) \approx 27.3$ MN. Therefore, $W_{\text{tot,hand}} \approx 47.0$ MN.

RFEM reports $W_{\text{tot,RFEM}} = 46.83$ MN, i.e. the hand estimate differs by approximately 0.33%, confirming global vertical equilibrium and correct load implementation.

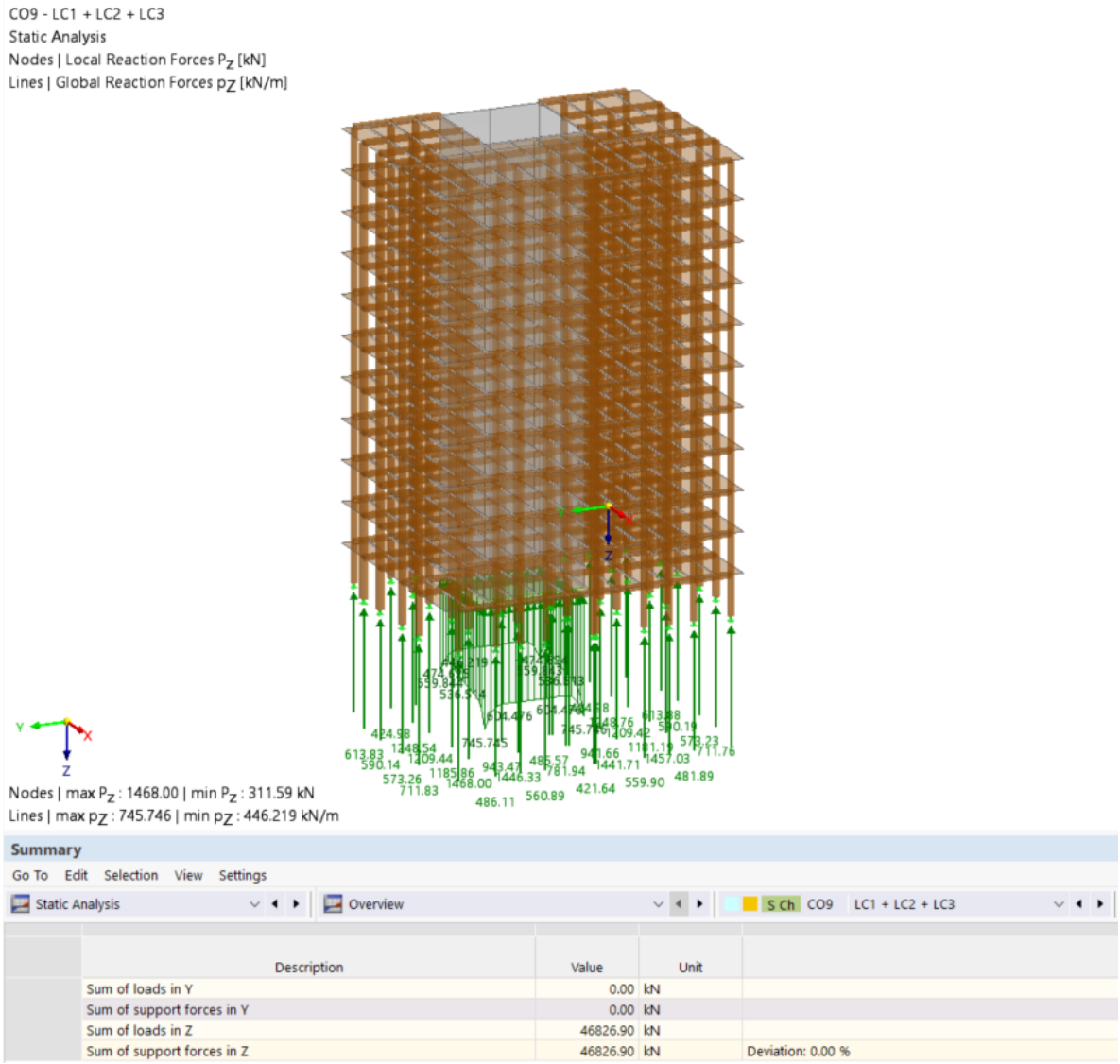

Figure I.1: RFEM: sum of loads and sum of support forces in Z.

I.2.2. Horizontal equilibrium under wind loading

Table I.2: Verification check: horizontal equilibrium under wind loading.

Load case	$LC5$ (wind in global Y)
RFEM output	Sum of applied loads in Y and sum of horizontal support reactions in Y, $\sum R_y$
Expected outcome	$\sum R_y$ equals the applied wind resultant in Y (global equilibrium)
Purpose	Verifies wind load input, sign convention and global lateral equilibrium

Hand calculation:
Wind is applied as a line load along the facade edges. From the load input, the wind line loads are $w_1 = 2.739$ kN/m and $w_2 = 1.712$ kN/m acting over a characteristic facade length of $L = 19$ m. The total wind resultant per level is therefore estimated as:

$$F_{y,\text{level}} \approx (w_1 + w_2)\, L = (2.739 + 1.712) \cdot 19 = 84.6 \text{ kN}. \tag{I.1}$$

For 11 levels, this gives:

$$F_{y,\mathrm{tot}} \approx 11 \cdot 84.6 = 931 \text{ kN}. \tag{I.2}$$

RFEM reports $\sum$ loads in $Y = 930.26$ kN and $\sum$ support forces in $Y = 930.26$ kN (deviation 0.00%), which agrees well with the hand estimate.

Observed behaviour (Figure I.2):
The horizontal support reactions are concentrated primarily at the core supports, indicating that lateral wind loads are transferred through the floor diaphragms to the concrete core as the main stability system. Only minor horizontal reactions occur at the column supports under wind-only loading.

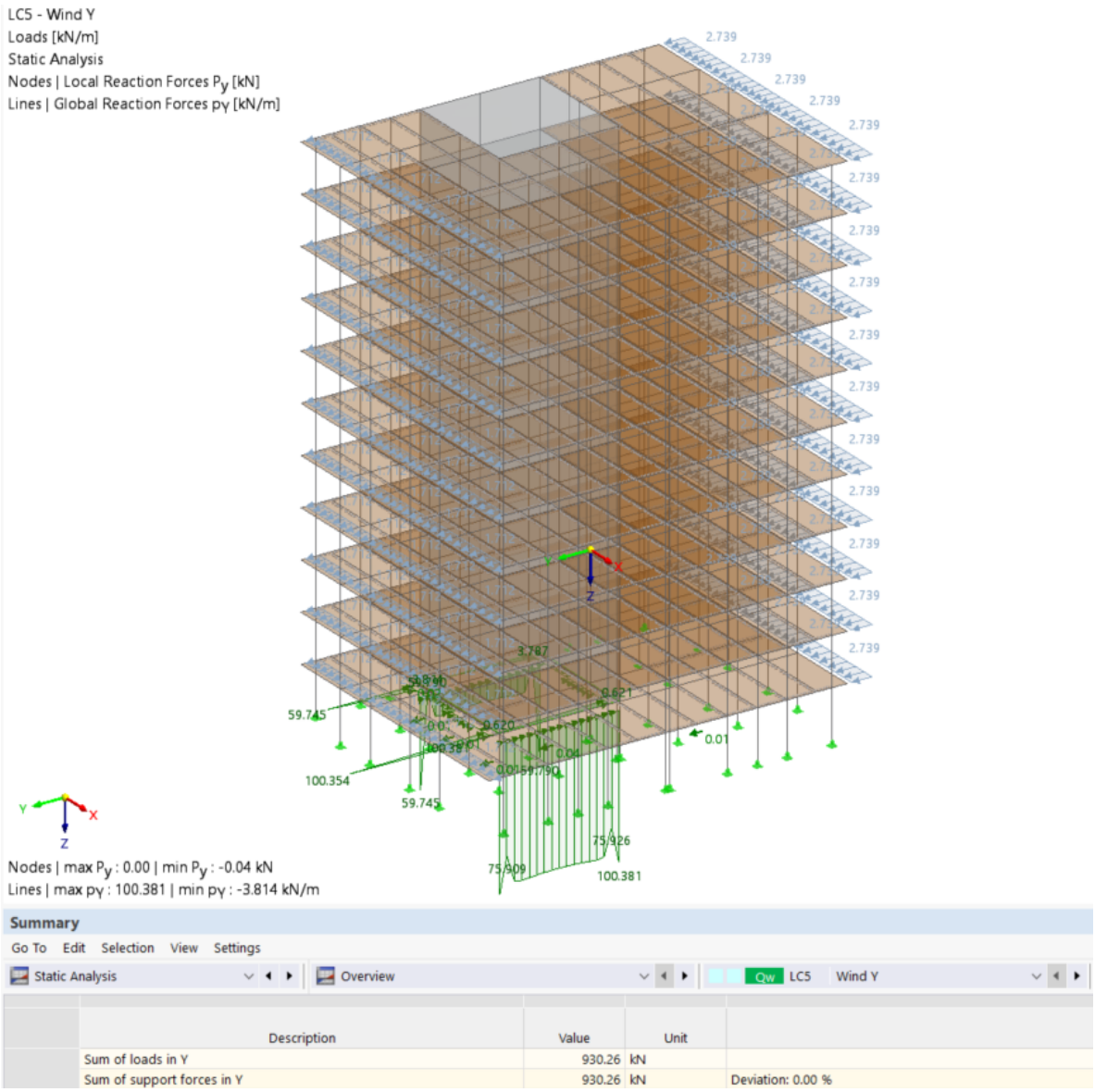

Figure I.2: RFEM: wind in global Y (LC5) and corresponding support reactions in Y.

The distribution of core support reactions is non-uniform and shows local concentrations near core corners. This is expected, because the core resists wind through a combination of base shear, overturning and torsional effects, which produce shear-flow transfer around the corner. As a result, noticeable r_y components may also occur in the wall segment perpendicular to the wind direction at locations where it is coupled to the wind-parallel wall.

I.3. Load path and reaction distribution

To obtain clear figures, the reactions are shown for the first floor level only. Therefore, nodal support reactions appear at the core nodes at this level, whereas in the full-building model the reactions are all transferred to the base supports at foundation level.

I.3.1. Wind load transfer to the stability system

Table I.3: Verification check: wind load transfer to the core.

Load case	$LC5$ (wind in global Y)
RFEM output	Horizontal support reactions at core and column supports (R_x, R_y); resultant support moment about Z, M_z
Expected outcome	Majority of base shear carried by the core; negligible horizontal reactions at column supports; non-zero torsional moment M_z due to plan asymmetry
Purpose	Confirms load path "wind → diaphragm → core" and verifies torsional response due to plan asymmetry

Observed behaviour:
For wind-only loading, horizontal reactions in the wind direction are concentrated at the core, while the column supports exhibit negligible nodal reactions. This confirms that the floor diaphragm transfers the lateral wind load primarily to the concrete core as the stability system. In addition, the core reactions exhibit a resultant moment about the global Z-axis, which is consistent with torsional response caused by plan asymmetry (i.e. an eccentricity between the wind resultant and the model reference point).

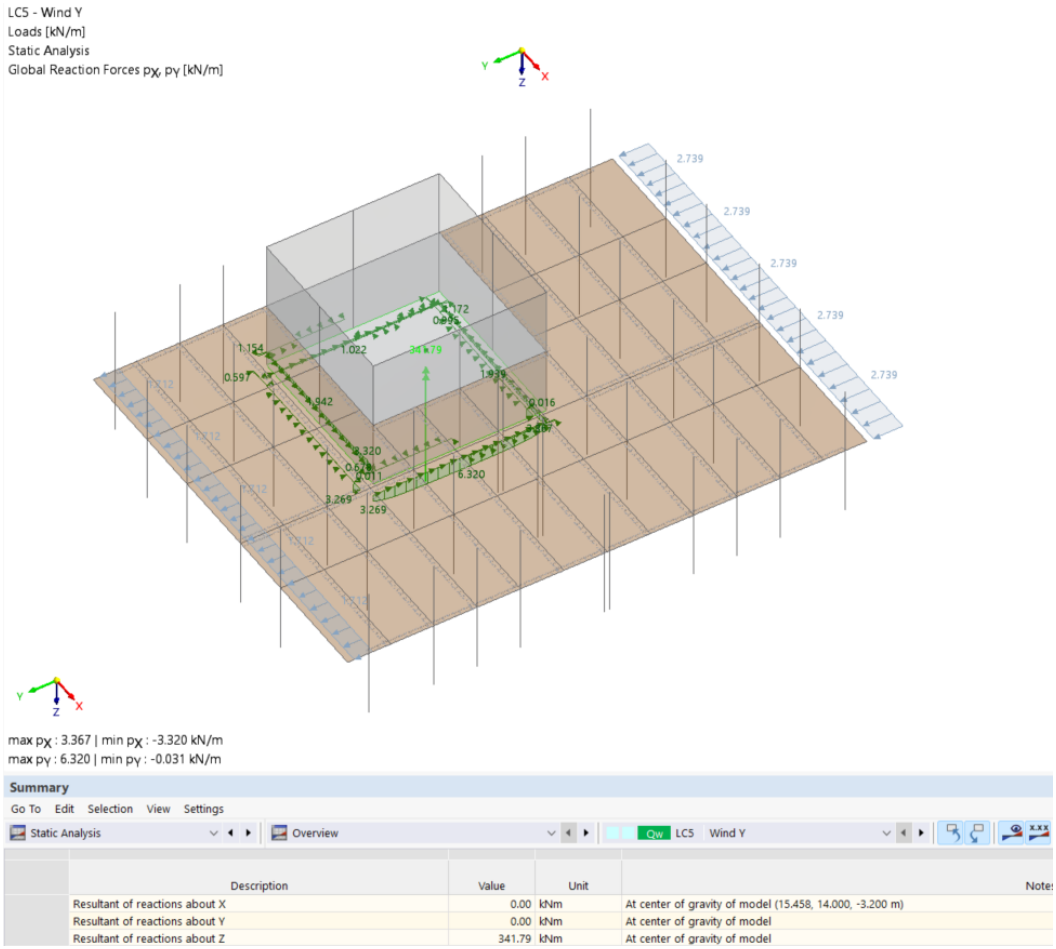

Figure I.3: RFEM: core support reactions in X and Y under $LC5$, showing a torsional moment about the global Z-axis.

Hand calculation:
RFEM reports a resultant support moment about the global Z-axis of $M_{z,\mathrm{RFEM}} = 341.79$ kNm for the first floor level. The wind resultant on the same level is $F_{y,\mathrm{level}} = 84.57$ kN. An effective torsional eccentricity (with respect to the RFEM reference point used for the reported resultant moment) follows as:

$$e_{\mathrm{eff}} = \frac{M_{z,\mathrm{RFEM}}}{F_{y,\mathrm{level}}} = \frac{341.79}{84.57} = 4.04 \text{ m}. \tag{I.3}$$

This indicates that the line of action of the wind resultant is offset by approximately 4 m in the direction perpendicular to the wind, which is consistent with the observed torsional response.

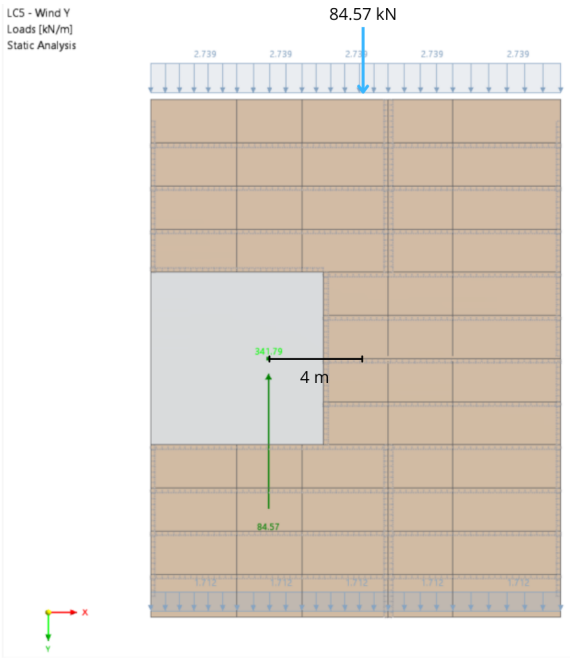

Figure I.4: Wind resultant on the first floor level and corresponding torsional moment about the global Z-axis.

I.3.2. Verification of pinned column behaviour

Table I.4: Verification check: pinned column behaviour.

Load case	$LC1 + LC2 + LC5$
RFEM output	Column end moments and column bending moments (M_x, M_y)
Expected outcome	Column end moments are negligible (hinged behaviour)
Purpose	Confirms that pendulum columns and releases are modelled correctly

Observed behaviour:
The plotted moment distribution shows bending carried primarily by the beams, while the columns do not develop bending moments under the combined gravity and wind loading, which is consistent with the intended hinged column behaviour.

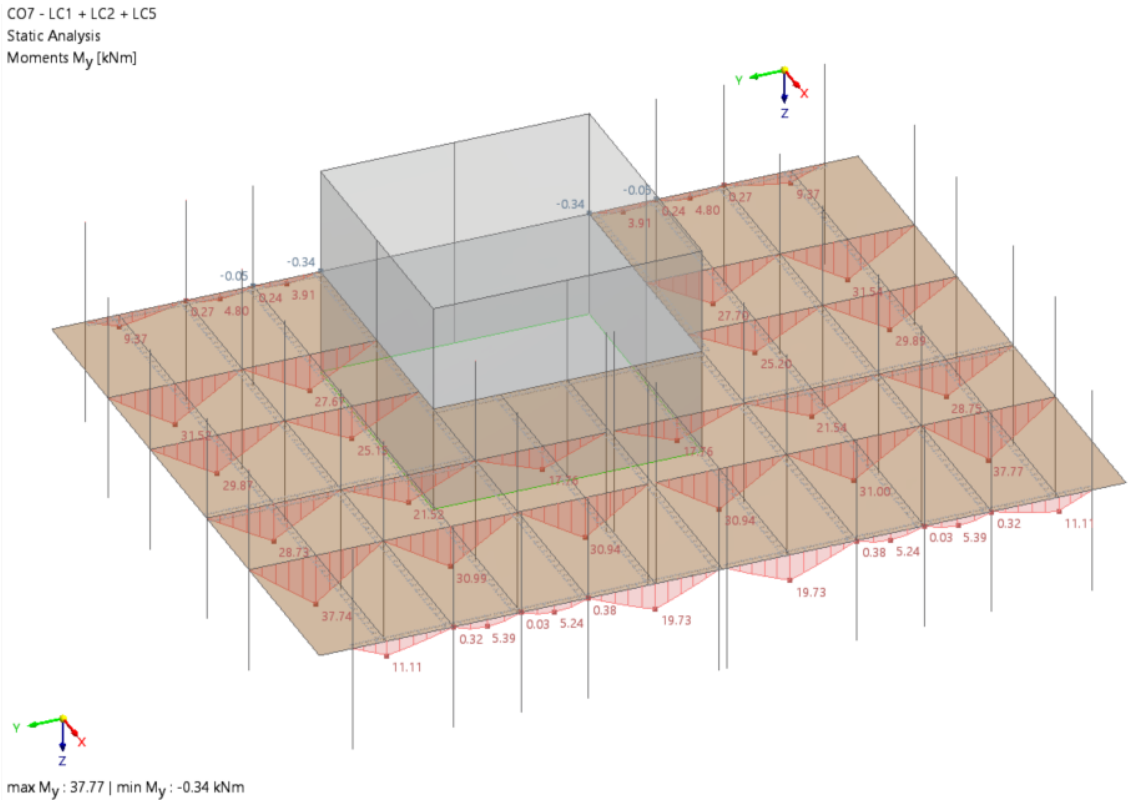

Figure I.5: RFEM: example moment distribution for $LC1 + LC2 + LC5$ (visual check of pinned column behaviour).

I.4. Deformed shape inspection

I.4.1. Global displacements

Table I.5: Verification check: deformed shape under wind (direction and torsion).

Load case	$LC5$ (wind in global Y)
RFEM output	Deformed shape and displacement magnitude $\|u\|$
Expected outcome	Global drift in the wind direction with a torsional component due to plan asymmetry
Purpose	Confirms correct wind direction and checks for unintended restraints or modelling artefacts

Observed behaviour:
The global deformed shape under $LC5$ shows lateral drift in the wind direction. The displacement field is not uniform across the plan, indicating a torsional response of the floor diaphragms, which is consistent with plan asymmetry and an eccentric load path to the core.

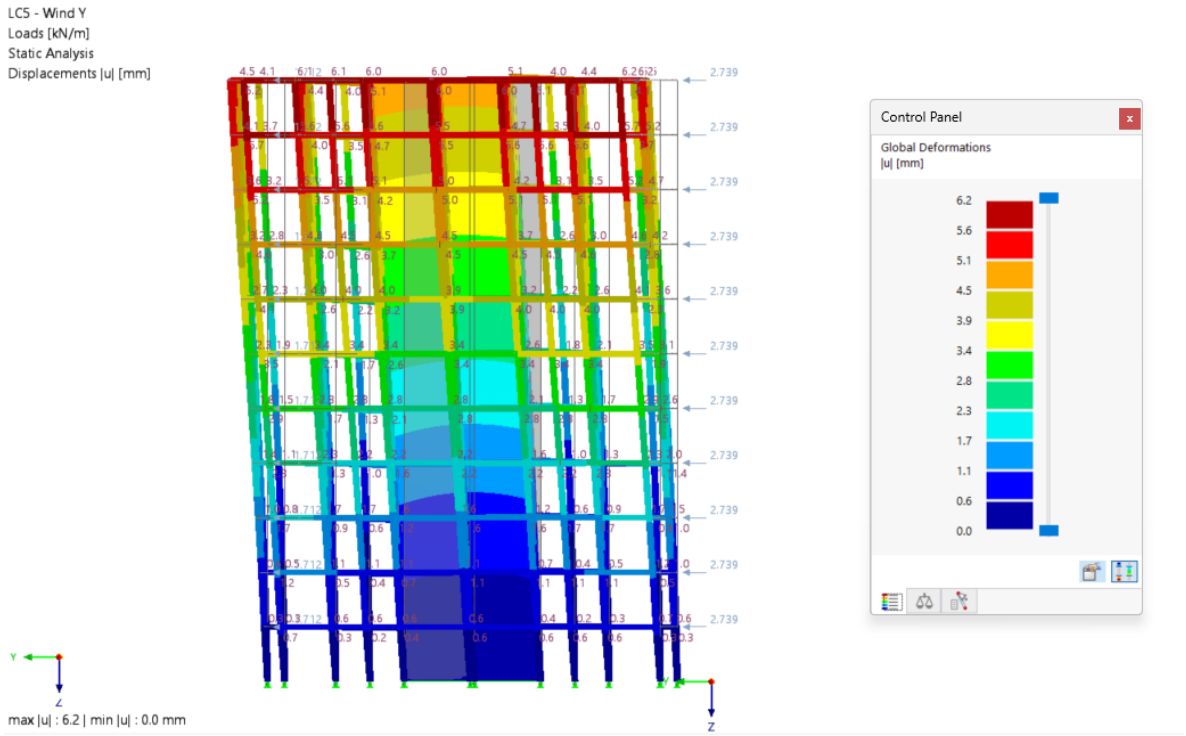

Figure I.6: RFEM: global deformed shape and displacement magnitude under wind in global *Y* (*LC*5).

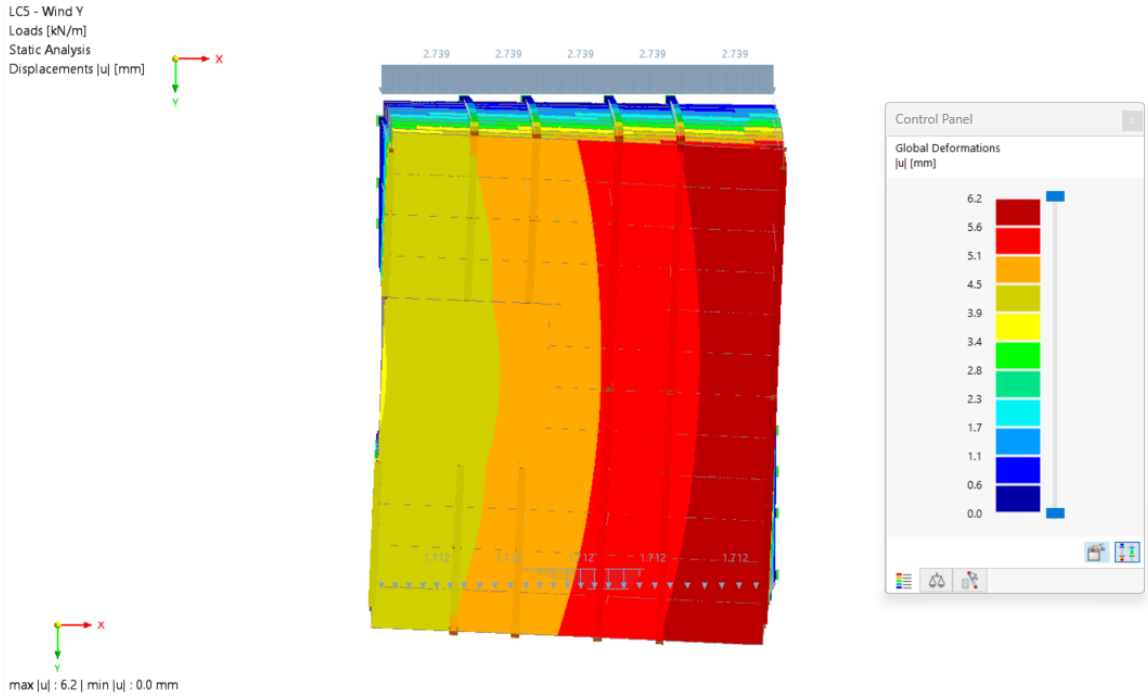

Figure I.7: RFEM: plan view of the displacement magnitude under *LC*5, illustrating non-uniform deformation across the floor and thus torsion.

I.4.2. Floor out-of-plane deflection

Table I.6: Verification check: floor out-of-plane deflection under gravity.

Load case	$LC1 + LC2 + LC3$
RFEM output	Floor vertical displacement field u_z
Expected outcome	Small displacements near supports; largest deflections in spans; smooth field for the monolithic baseline (no spurious jumps)
Purpose	Validates slab behaviour, support modelling and continuity of the floor system

Observed behaviour:
The deformed shape shows maximum downward deflection in the most flexible regions of the floor (largest spans), while displacements remain small in the vicinity of column supports and along the core boundary. The deformation pattern is symmetric, which is consistent with the symmetric gravity loading and indicates that the loads are applied correctly.

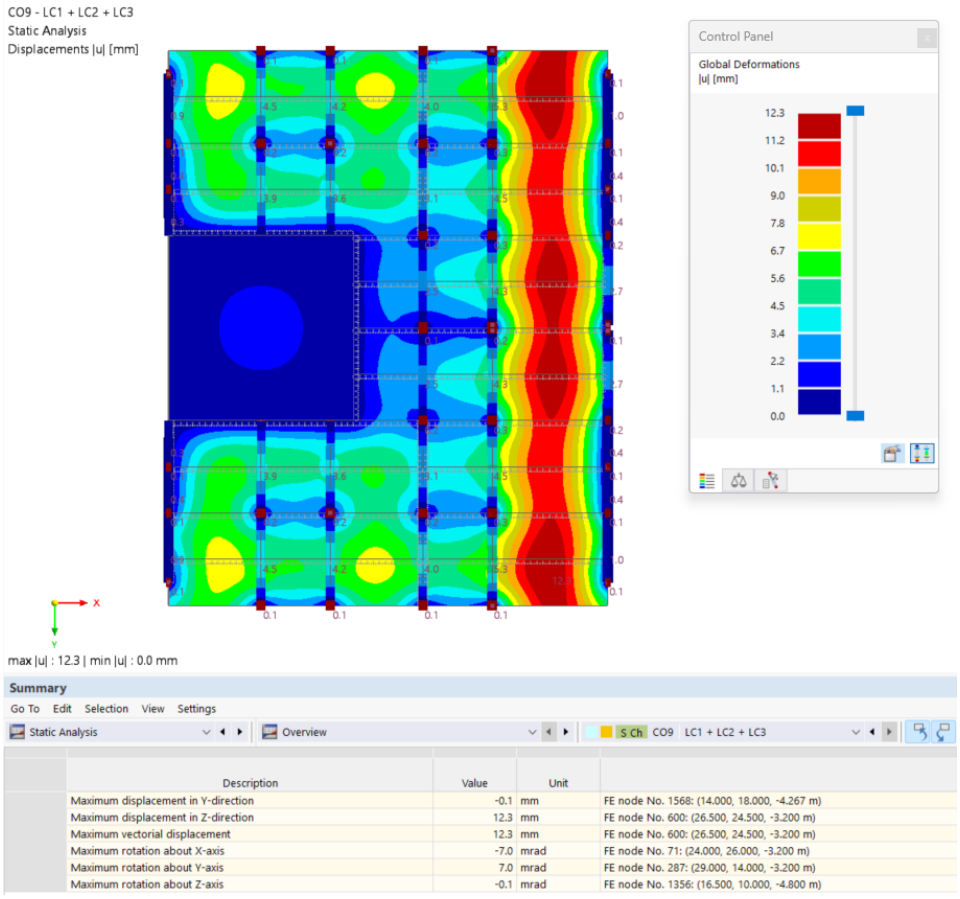

Figure I.8: RFEM: floor out-of-plane deflection under gravity loading ($LC1 + LC2 + LC3$).

I.4.3. Member–surface compatibility

Table I.7: Verification check: member–surface compatibility (beam–floor coupling).

Load case	$LC1 + LC2 + LC3$
RFEM output	Vertical displacement u_z along a beam line and at an adjacent floor surface point
Expected outcome	Compatible deflections where beams are connected to the floor surface (no offsets or gaps)
Purpose	Detects incorrect coupling, rigid links or unintended releases between members and surfaces

Observed behaviour:
At a representative location, the displacement extracted on the beam line matches the displacement at the adjacent floor grid point (both 5.3 mm), indicating that the member–surface coupling is consistent and that no unintended release exists in the vertical direction.

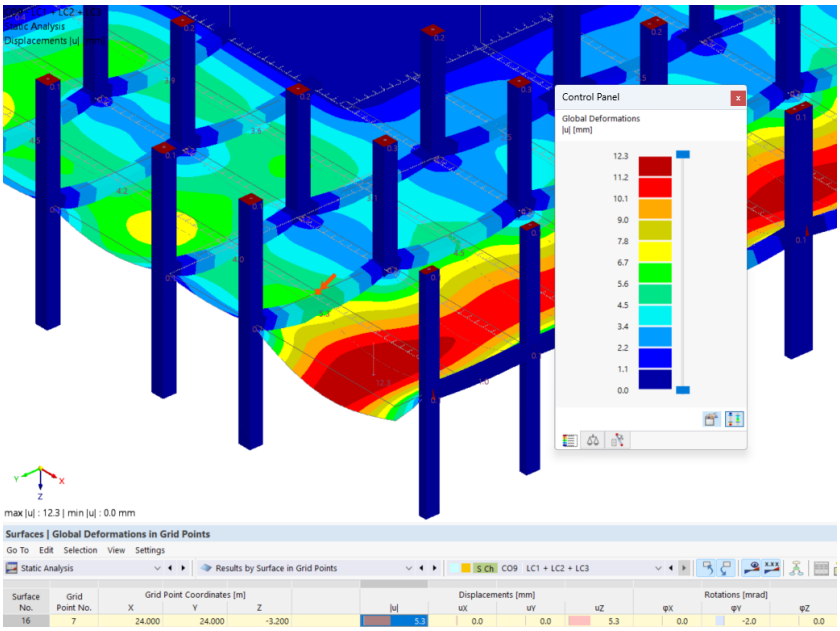

Figure I.9: RFEM: example check of member–surface compatibility showing matching vertical displacements on a beam and the connected floor surface.

I.5. Diaphragm action

To keep interpretation clear, line-hinge checks are evaluated on the bottom floor diaphragm. The baseline case C0 uses fully rigid in-plane connections at the panel–core and panel–panel interfaces; therefore, relative slip should be minimal and results should primarily reflect global equilibrium and load path.

I.5.1. Diaphragm shear transfer under wind

Table I.8: Verification check: diaphragm shear transfer to the core (line-hinge forces).

Load case	$LC5$ (wind in global Y)
RFEM output	Line-hinge resultants along the panel–core interface (bottom floor): in-plane shear v_y and in-plane normal force N [kN/m]
Expected outcome	The panel–core interface carries the majority of the diaphragm shear required to transfer wind to the core; non-uniform v_y and non-zero N may occur due to torsion and force redirection around core corners
Purpose	Verifies intended load transfer mechanism and confirms torsional load effects at the floor–core interface

Observed behaviour:
Figures I.10–I.11 show the in-plane normal forces n in the line hinges along the floor–core interface. Although the applied wind acts in global Y, the diaphragm load path is not a pure shear transfer: due to plan asymmetry and the core geometry, the shear flow in the diaphragm is redirected around core corners. This produces local axial forces along parts of the interface, which appear as non-zero n in the line hinges. The largest magnitudes occur near corners and at locations where force flow turns or where collector beams connect to the diaphragm.

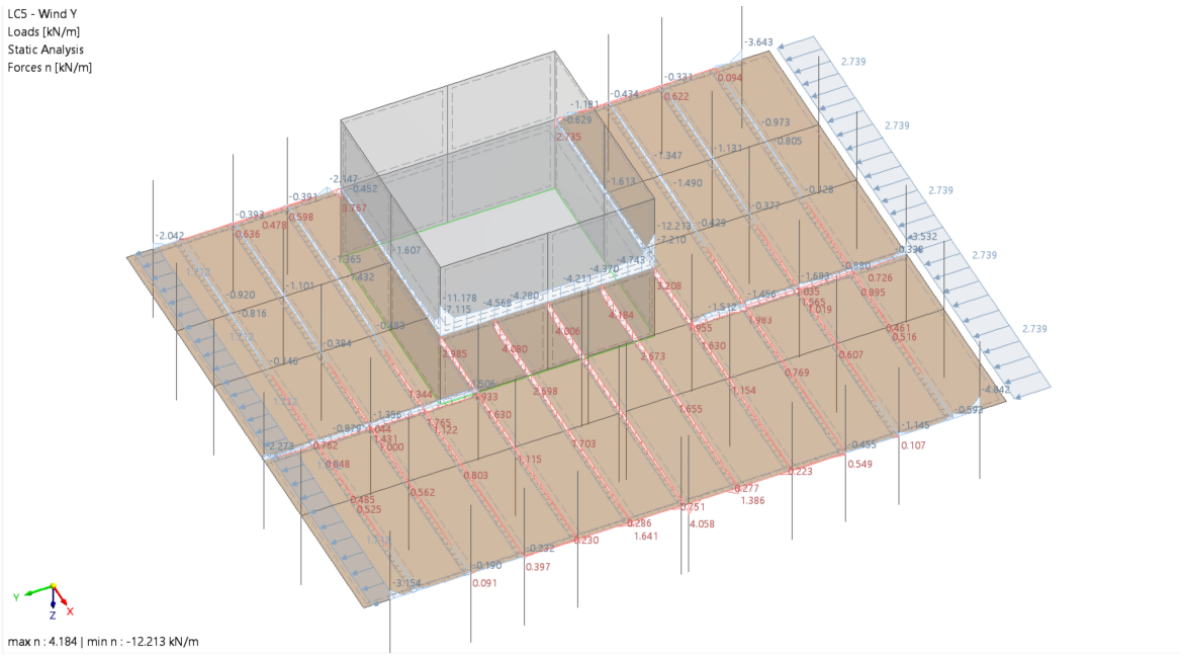

Figure I.10: RFEM: in-plane normal forces N in the panel–core line hinges on the bottom floor under $LC5$.

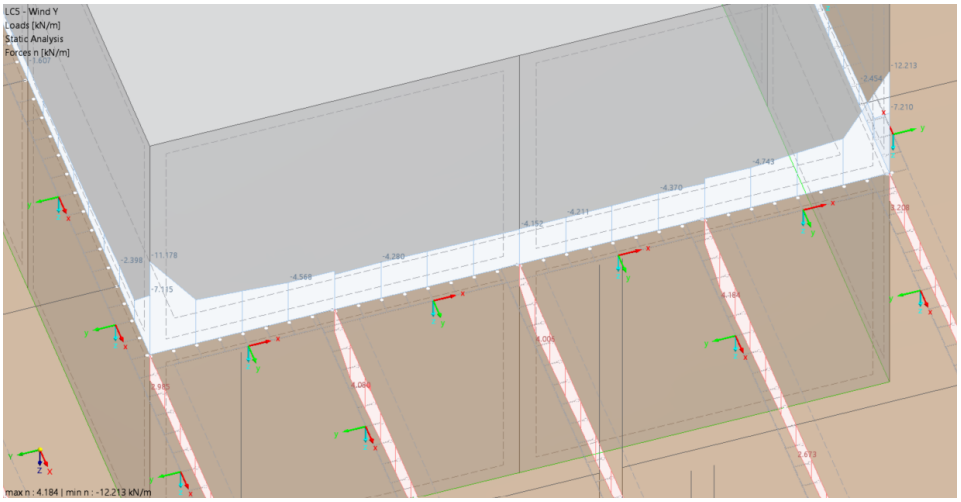

Figure I.11: RFEM: close-up of in-plane normal forces N near the core interface, highlighting local peaks near corners/discontinuities.

Figure I.12 shows that the shear transfer along the panel–core interface is not uniform, which reflects the torsional diaphragm response. Along the upper core wall, a small zone of tension (left) is followed by predominantly compression along the remainder of the interface. Along the core wall parallel to the wind direction, the sign change and gradual variation in v_y indicate that the diaphragm rotates approximately about a point near the centre of the floor plan (consistent with the eccentricity-based torsion check presented earlier). At the lower core wall, the pattern reverses: a dominant tension zone develops on the right side, with only a small compression region on the left. Overall, the opposite sign patterns at the upper and lower interfaces, combined with the varying distribution along the wind-parallel wall, are consistent with a torsional shear flow around the core.

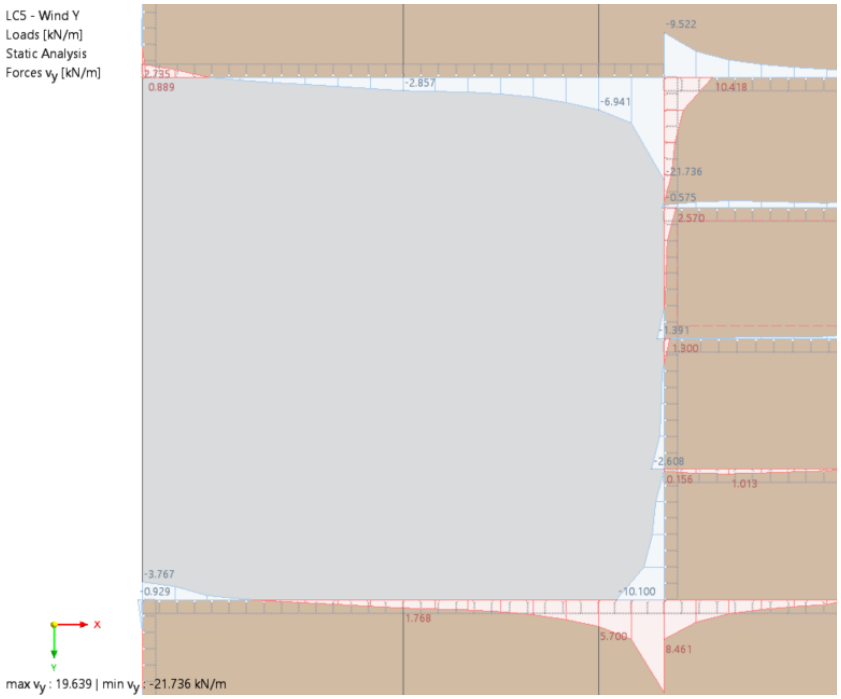

Figure I.12: RFEM: in-plane shear forces v_y along the panel–core line hinges on the bottom floor under $LC5$. The non-uniform distribution and sign changes indicate torsional diaphragm action.

I.6. Second-order analysis

After the above checks are satisfied for the individual load cases in a 1st-order linear-elastic analysis, the governing SLS and ULS combinations are evaluated using both 1st-order and 2nd-order (P–Δ) static analysis settings: CO15/CO8 (SLS) and CO14/CO4 (ULS).

For the baseline case C0, the in-plane stiffness is high and global displacements are small; consequently, the difference between 1st- and 2nd-order results is limited. To verify that the 2nd-order analysis settings are applied correctly and to assess sensitivity to geometric non-linearity, the comparison is therefore illustrated using a more flexible connection configuration (PC1a+PP1, with PB1), for which P–Δ effects are expected to be more pronounced.

I.6.1. Second-order displacements

Table I.9: Verification check: second-order displacement amplification.

Load combinations	CO15 (1st order) vs CO8 (2nd order)
RFEM output	Global displacement component in wind direction, u_y
Expected outcome	$u_{y,2} \geq u_{y,1}$ due to P–Δ amplification; largest differences in lower storeys
Purpose	Confirms correct implementation of 2nd-order analysis settings and provides a sensitivity check for geometric non-linearity

Observed behaviour:
Figures I.13 and I.14 show the global displacement field u_y for the governing SLS combination in 1st- and 2nd-order analysis, respectively. The overall displacement pattern remains similar, while the 2nd-order results show a small increase in lateral displacements, most noticeable in the lower storeys. This behaviour is consistent with modest P–Δ effects under serviceability loading.

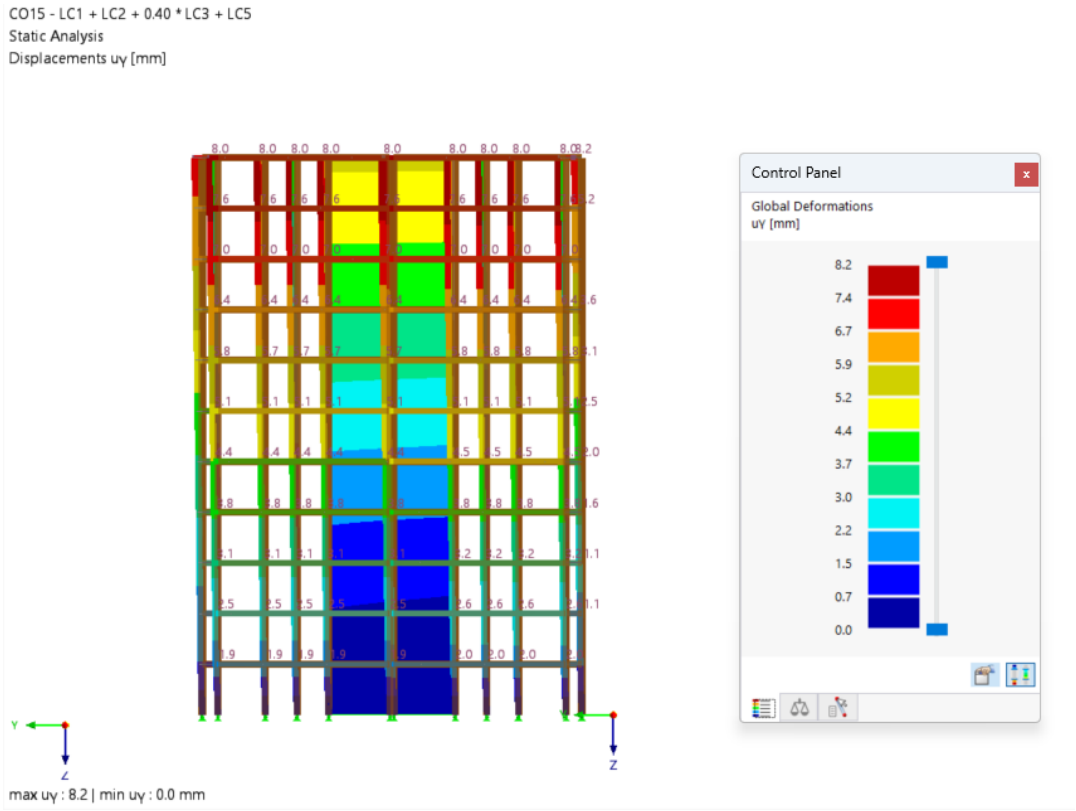

Figure I.13: RFEM: u_y displacements for SLS CO15 (1st-order analysis) for the flexible configuration (PC1a+PP1, PB1).

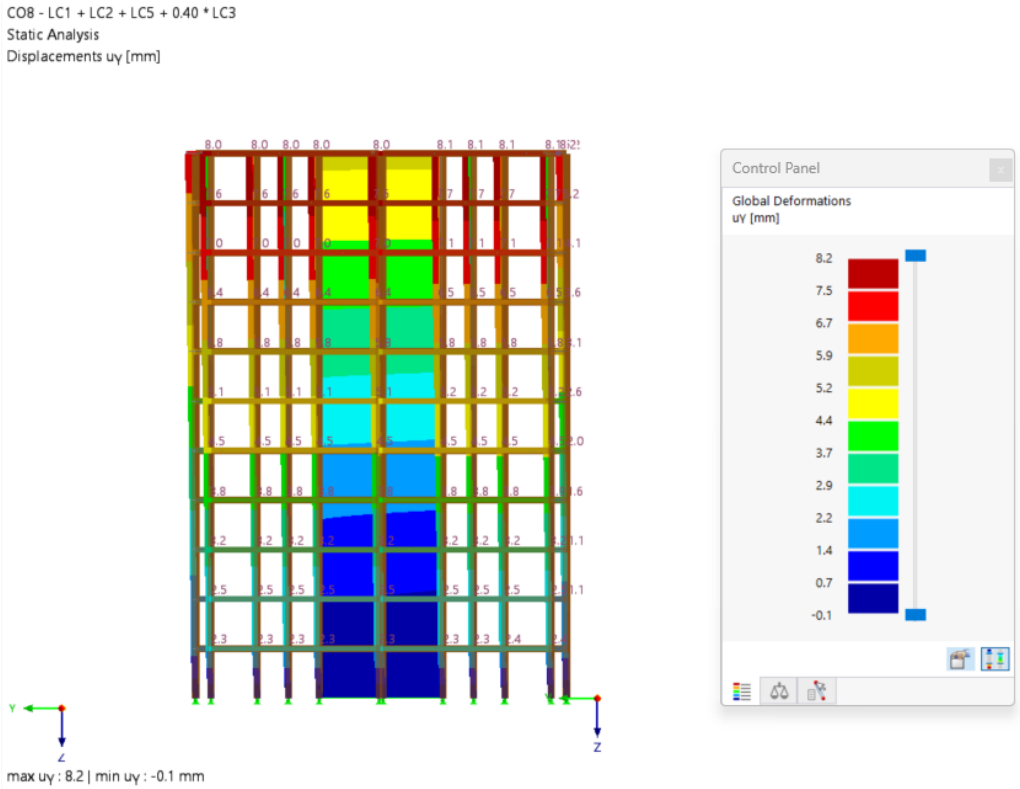

Figure I.14: RFEM: u_y displacements for SLS CO8 (2nd-order analysis) for the flexible configuration (PC1a+PP1, PB1).

I.6.2. Second-order forces

Table I.10: Verification check: second-order amplification of diaphragm interface forces.

Load combinations	CO14 (1st order) vs CO4 (2nd order)
RFEM output	Line-hinge resultants in diaphragm interfaces (panel–core and panel–panel): in-plane normal force N and in-plane shear v_y [kN/m]
Expected outcome	Second-order analysis yields equal or larger interface demands due to P–Δ amplification; differences most pronounced in lower storeys
Purpose	Confirms correct implementation of 2nd-order analysis settings and verifies that force amplification follows the expected global behaviour under ULS loading

In-plane normal forces in panel–core

The maximum compressive normal force in the panel–core interface increases in 2nd-order analysis, from $N_{\mathrm{PC,min}} = -10.50$ kN/m (CO14) to $N_{\mathrm{PC,min}} = -12.98$ kN/m (CO4). The amplification is primarily visible in the lower storeys, consistent with P–Δ effects.

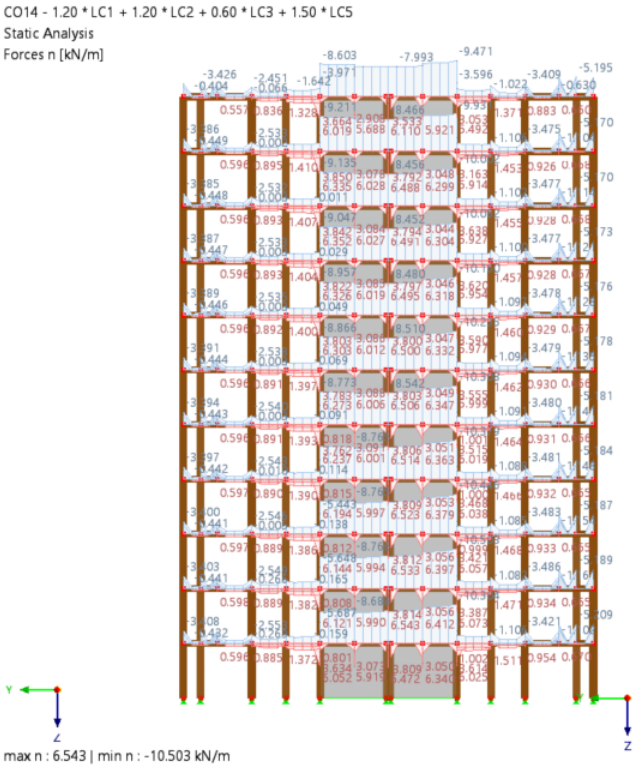

Figure I.15: RFEM: panel–core line-hinge normal forces N for ULS CO14 (1st order).

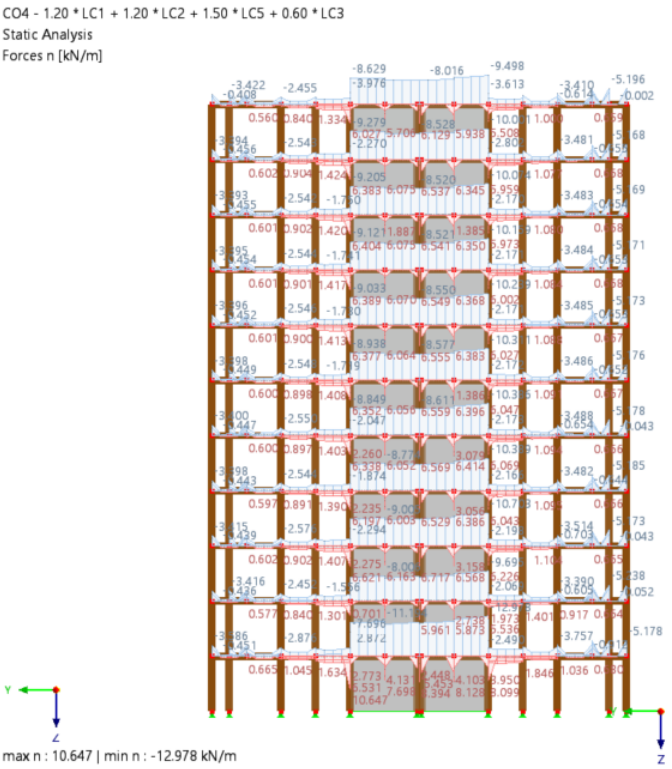

Figure I.16: RFEM: panel–core line-hinge normal forces N for ULS CO4 (2nd order).

In-plane normal forces in panel–panel

The maximum panel–panel normal force increases in 2nd-order analysis from $N_{PP,max}$ = 6.47 kN/m (CO14) to $N_{PP,max}$ = 8.39 kN/m (CO4), again with the largest differences occurring in the lower storeys.

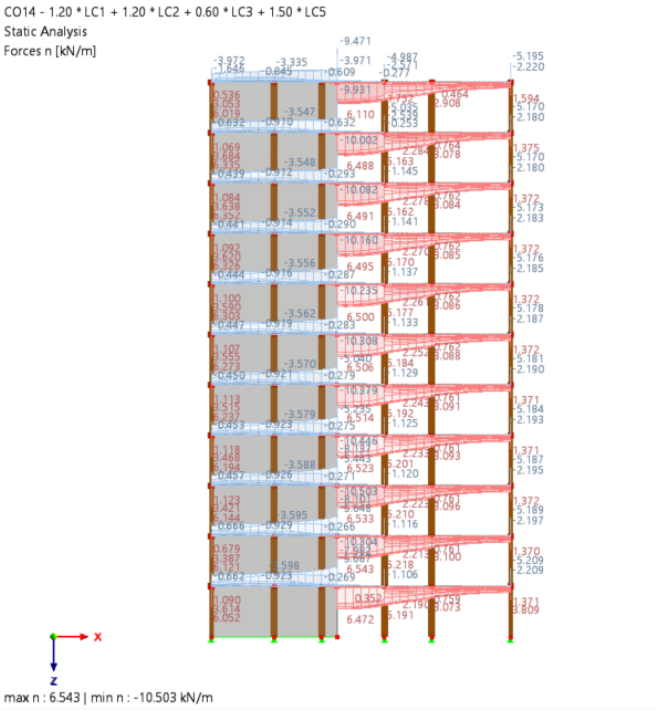

Figure I.17: RFEM: panel–panel line-hinge normal forces N for ULS CO14 (1st order).

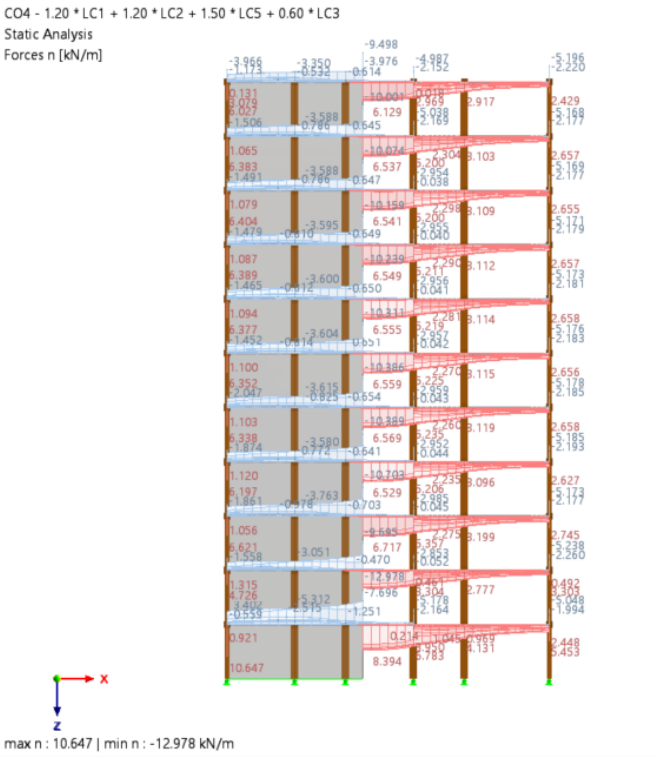

Figure I.18: RFEM: panel–panel line-hinge normal forces N for ULS CO4 (2nd order).

In-plane shear forces V_y in panel–core

The shear force distribution along the core interface reflects the combined diaphragm shear transfer and torsional effects. In 2nd-order analysis, the extreme values increase from $V_{y,\min} = -15.32$ kN/m (CO14) to $V_{y,\min} = -18.67$ kN/m (CO4), with differences most apparent in the lower storeys. This trend is consistent with P–Δ amplification of lateral response and associated connection demands.

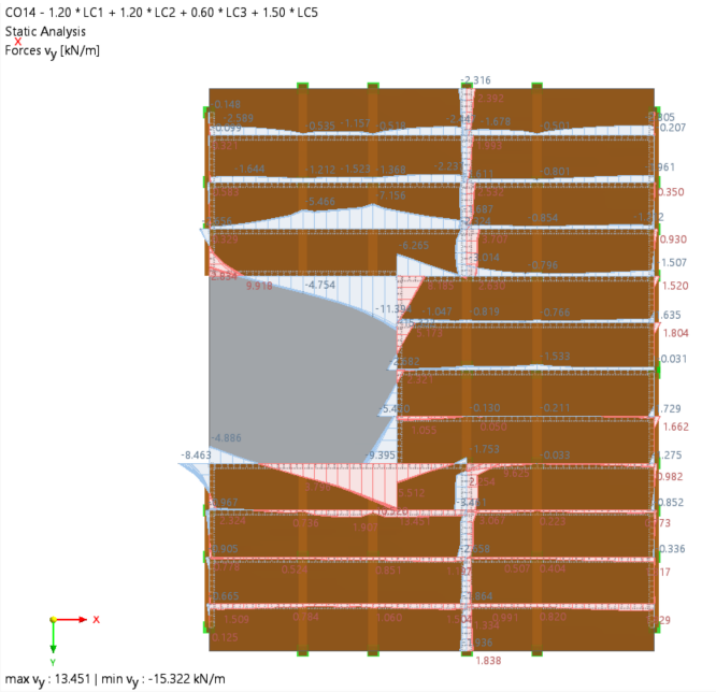

Figure I.19: RFEM: panel–core line-hinge shear forces V_y for ULS CO14 (1st order).

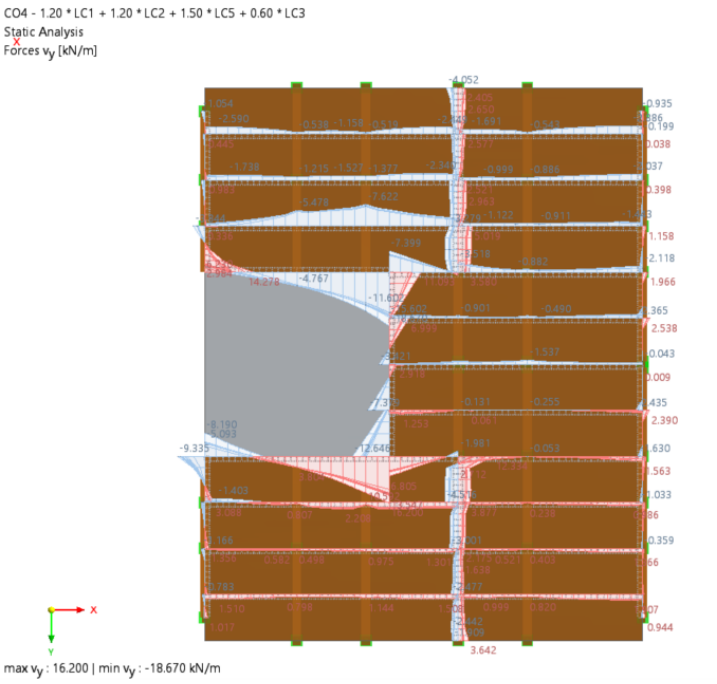

Figure I.20: RFEM: panel–core line-hinge shear forces V_y for ULS CO4 (2nd order).